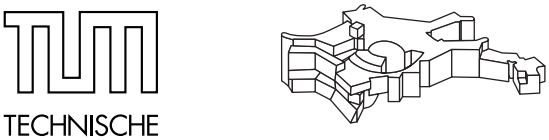

Max-Planck-Institut für Astrophysik

Turbulent Thermonuclear Combustion in Degenerate Stars

Wolfram Schmidt

Vollständiger Abdruck der von der Fakultät für Physik der Technischen Universität München zur Erlangung des akademischen Grades eines

Doktors der Naturwissenschaften

genehmigten Dissertation.

Vorsitzender:	Univ.-Prof. Dr. L. Oberauer
Prüfer der Dissertation:	1. Hon.-Prof. Dr. W. Hillebrandt
	2. Univ.-Prof. Dr. M. Lindner

Die Dissertation wurde am 19. 1. 2004 bei der Technischen Universität München eingereicht und durch die Fakultät für Physik am 20. 2. 2004 angenommen.

'Forgive my ignorance of stellar physics, but I've been studying, so let me see if I get this right.'

'When that big, whirling cloud of dross and corpses finally collapses, it's going to dump a tenth of a solar mass onto the hot, dense surface of that white dwarf. A dwarf that's already near its Chandrasekhar limit. Much of the new material will compress to incredible density and undergo superfast nuclear fusion, triggering–'

'What Earthlings used to call a "type one" supernova,' the Niss Machine cut in, unable to resist an inbuilt yen to interrupt.

'Normally, this happens when a large amount of matter is tugged off a giant star, falling rapidly onto a neighboring white dwarf. In this case, however, the sudden catalyzing agent will be the flesh of once living beings! Their body substance will help light a pyre that should briefly outshine this entire galaxy, and be visible to the boundaries of the the universe.'

D. Brin, **Heaven's Reach**

Motivation and Objectives

This Thesis is mainly concerned with turbulence and its significance for thermonuclear burning processes in degenerate stars. Contrary to main sequence stars such as the Sun, in which a feed-back mechanism between reaction rates, expansion and cooling moderates thermonuclear burning, the physical conditions in a white dwarf of nearly critical mass entail a thermonuclear runaway, once density and temperature rise above a certain threshold. The critical mass of a white dwarf is known as Chandrasekhar mass. In the course of the run-away, carbon and oxygen is rapidly burned to heavier elements, in particular, nickel, and the star explodes due to the enormous energy release. According to our present understanding, burning in these thermonuclear supernovae progesses as deflagration, which means that ignition is caused by heat conduction rather than shock compression. Since the intrinsic propagation speed of a deflagration front is much less than the speed of sound, there must be something acting to accelerate the burning process. The agent is thought to be turbulence, which folds and wrinkles flames and thereby increases the rate of burning. A major difficulty of describing turbulent burning in numerical simulations stems from the fact that it is impossible to resolve the whole range of dynamical scales, even with the most powerful of currently available computers. This restriction leads to the concept of a large-eddy simulation, in which only the largest scales are numerically resolved. However, since the burning process is susceptible to turbulent velocity fluctuations on scales smaller than the numerical resolution, a model which accounts for effects on these scales is indispensable. The investigation of several options for such a subgrid scale model is the research subject of this Thesis. As testing and comparing different subgrid scale models systematically in full supernova simulations would be quite hard, a simplified scenario was chosen, where turbulence is artifically produced by a stochastic force field in a cubic domain. In the beginning, pure hydrodynamical turbulence was investigated, and then thermonuclear burning was added. The research goal has been to some extent a phenomenological understanding of turbulence and turbulent burning, but eventually it aims at a subgrid scale model, which makes physically sound predictions and is applicable to simulations of thermonuclear supernovae.

Acknowledgements

First of all, I thank my advisors *W. Hillebrandt* and *J. C. Niemeyer* for their support. I am indepted to Wolfgang, who offered me the opportunity of doing a doctoral thesis in the supernova team of the Max-Plack-Institute for Astrophysics. Jens initiated my research with a paper on dynamical subgrid scale modelling, and the idea of using stochastic stirring in a cubic box is also his. I thank my colleague *F. Röpke* for many discussions and, particularly, *M. Reinecke* for answering a plethora of questions regarding the code and running simulations on various platforms. Without Martin's help I would hardly have managed to get it going! Valuable last minute input came from *F. Kupka*, who has already played an influencial role in the course of my diploma thesis. The research presented in this Thesis would not have been possible at all without high-end computing resources. The required computing power was provided by the Hitachi SR-8000 supercomputer of the Leibniz Computing Centre in Munich and the IBM p690 supercomputer of the Computing Centre of the Max-Planck-Society in Garching.

There are always people behind the scenes, whose support is nonetheless indispensable. Most of all, I am grateful for the continual encouragement and financial aid of my parents. Without naming them individually, I finally thank many friends of mine for their share in recreational activities, which rank highly among the preconditions for creative work of any kind.

Contents

Chapter 1

White Dwarfs and Thermonuclear Supernovae

Der wichtigste Stern ist α CMa, Sirius, der Hundsstern; bei den Ägyptern stand der Große Hund für Anubis, den schakalköpfigen Wächter der Totenstadt. Sirius ist mit $-1^{\mathrm{m}}.4$ der hellste Stern am Himmel, ein A1-Stern in weniger als 9 Lichtjahren Entfernung; er hat einen kleinen Belgeiter, der ihn in einem Abstand von 2,9 Milliarden Kilometer in rund 50 Jahren einmal umrundet: Sirius B mit einer Helligkeit von $9^{\mathrm{m}}.1$ ist der erste Weiße Zwerg, den man beobachtet hat.

Baker and Hardy, **Der Kosmos-Sternführer**

The mountain smoked beneath the moon;
The dwarves, they heard the tramp of doom.

J. R. R. Tolkien, **The Hobbit**

In 1862, A. G. Clarke found the dim companion of the bright star Sirius A, after F. W. Bessel had deduced from parallax measurements that Sirius, in fact, is a binary star system. It came as a great surprise to astronomers when in 1915 W. Adams discovered that Sirius B is a blue-white star, much too hot for its luminosity $L \approx 0.03 L_\odot$. Indeed, the startling consequence inferred from the Stefan-Boltzmann law was that Sirius B must be extraordinarily compact, a result first dismissed by astronomers as being absurd. Later the temperature of Sirius B was determined to be $2.7 \cdot 10^4$ K, implying a radius of a mere 5500 km and a density of about $3 \cdot 10^6\,\mathrm{g\,cm^{-3}}$. The mystery was lifted by R. H. Fowler in 1926. He applied the newly discovered exclusion principle of Pauli and was able to show that a star like Sirius B must be entirely supported by *electron degeneracy pressure* against gravity. Today a great variety of these *white dwarfs* are known, with masses typically in the range from 0.4 to $0.8\,M_\odot$ and an average density of $4.7 \cdot 10^5\,\mathrm{g\,cm^{-3}}$ [1].

[1] Sirius B has a mass of about $1\,M_\odot$ which is larger than the mass of most known white dwarfs. More on the phenomenology of white dwarfs can be found in Liebert [1980] or Carroll and Ostlie [1996, Section 15.2].

The formation of a white dwarf is the final stage in the evolution of a star less massive than about $8M_\odot$, which does not cease in a core collapse supernova. Isolated white dwarfs are cooling over many billions of years. Eventually, they will fade and become dark. White dwarfs which are members of close binary star systems, on the other hand, may accrete mass from their companions and thereby go through violent evolutionary changes. Such events are observable as *novae*. They belong to the class of *cataclysmic variables*, which are characterised by short outbursts of radiation following long quiescent intervals. These outbursts are caused by the explosive thermonuclear burning of a hydrogen surface layer, which is accumulated through accretion from the companion star [cf. Carroll and Ostlie, 1996, Section 17.4]. In the course of nova, most of the accreted mass is ejected into space. However, under certain circumstances a white dwarf can gradually accrete material without entering a nova phase. In this case, the mass will steadily increase and finally approach the *Chandrasekhar limit*, which is the largest mass that can be supported by the degeneracy pressure of electrons. Close to the Chandrasekhar mass, the density and temperature in the core of the white dwarf reach a critical threshold. At this point, the rate of thermonuclear reactions increases rapidly and a catastrophic runaway sets in, which incinerates and disrupts the whole star within a few seconds. The released energy is of the order 10^{51} erg and gives rise to one of the most luminous events in the universe, a *type Ia supernova*. Although alternative progenitor systems have been suggested, the best match between observational properties and predictions from numerical simulations is found for the scenario outlined above, which is known as the *single degenerate* (SD) scenario. The physics of thermonuclear supernova explosions is introduced in the first part of this Chapter. In particular, it is shown that turbulence plays a crucial role in the modelling of thermonuclear burning. Furthermore, theory and observations of type Ia supernovae are discussed in a broader astrophysical context in the second part.

1.1 Physical Foundations

Our current theoretical understanding of thermonuclear supernovae in the SD scenario rests on three fundamental pillars. Firstly, the physics of degenerate matter, secondly, hydrodynamics including turbulence and, finally, thermonuclear combustion physics. The underlying principles and some of the most important facts are outlined in the following.

1.1.1 Degeneracy

Degeneracy pressure is a *non-thermal* property of a fermion gas. In the limit of *zero temperature*, each fermion occupies the state of lowest energy available without violating Pauli's exclusion principle. Let us consider a gas consisting of electrons and ignore electrostatic interactions. According to Heisenberg's uncertainty relation, the minimal phase space volume occupied by any electron is $(2\pi\hbar)^3/g$, where g is the multiplicity given by the number of possible spin orientations. For electrons, which are spin-1/2 particles, $g = 2$. In the ground state, all electrons occupy states within a sphere of radius p_F in momentum space. p_F is called the *Fermi momentum*. It is related to the

number density n_e of electrons through the equation

$$n_e = \frac{2}{(2\pi\hbar)^3}\int_0^{p_F} 4\pi p^2\,\mathrm{d}p = \frac{2}{(2\pi\hbar)^3}\frac{4\pi p_F^3}{3}. \tag{1.1}$$

The non-vanishing momentum of electrons in the ground state gives rise to pressure and a corresponding energy density [cf. Shapiro and Teukolsky, 1983, Section 2.3],

$$P_F = \frac{2}{3(2\pi\hbar)^3}\int_0^{p_F}\frac{4\pi p^4c^2\mathrm{d}p}{\sqrt{p^2c^2+m_e^2c^4}} = \frac{m_ec^2}{\lambda_e^3}\phi(x), \tag{1.2}$$

$$E_F = \frac{2}{(2\pi\hbar)^3}\int_0^{p_F} 4\pi p^2\sqrt{p^2c^2+m_e^2c^4}\,\mathrm{d}p = \frac{m_ec^2}{\lambda_e^3}\chi(x), \tag{1.3}$$

where $x = p_F/m_ec$ and

$$\phi(x) = \frac{1}{8\pi^2}\left[x\sqrt{1+x^2}\left(\frac{2x^2}{3}-1\right)+\ln\left(x+\sqrt{1+x^2}\right)\right], \tag{1.4}$$

$$\chi(x) = \frac{1}{8\pi^2}\left[x\sqrt{1+x^2}\left(1+2x^2\right)-\ln\left(x+\sqrt{1+x^2}\right)\right]. \tag{1.5}$$

P_F is called the *degeneracy pressure* and E_F the *Fermi energy* of the electron gas. The characteristic energy and length scale associated with these quantities are, respectively, the rest energy $m_ec^2 \approx 8.187\cdot10^{-7}$ erg and the Compton wavelength $\lambda_e = \hbar/m_ec \approx 3.862\cdot10^{-11}$ cm of the electron. Thus, the order of magnitude of the degeneracy pressure is given by

$$P_F \approx 1.422\cdot10^{25}\phi(x)\,\mathrm{dyne\,cm^{-2}}. \tag{1.6}$$

In the limit $x \to 0$, the Fermi gas becomes *non-relativistic*, whereas $x \gg 0$ corresponds to *ultra-relativistic* degenerate electrons.

At finite temperature, the simple distribution function of the electrons in the ground state, $f(E) = \theta(E_F - E)$, is smeared out in the vicinity of the Fermi energy, because a certain fraction of electrons occupies excited states. In general, the integrals defining energy and pressure of the free electrons in white dwarf matter of finite temperature must be solved numerically. A parameter which measures the degree of degeneracy is the ratio of the Fermi energy to the thermal energy, $\eta = E_F/n_ek_BT$. Complete degeneracy is asymptotically approached in the limit $\eta \to \infty$. Defining the *Fermi temperature* by $T_F = E_F/n_ek_B$, this limit is equivalent to $T/T_F \to 0$. The Fermi temperature depends on the mass density. For example, $T_F \propto \rho^{2/3}$ for non-relativistic particles. This is why degeneracy is hugely dominated by thermal effects in matter under typical terrestial conditions. In stellar matter, the phase space volume occupied by an electron is of the order $180(2\pi\hbar)^3(M/M_\odot)^{1/2}(R/R_\odot)^{3/2}$, as estimated by Shapiro and Teukolsky. Hence, electrons in a star of one solar mass become degenerate if the star contracts to a radius of roughly $0.03R_\odot$. Indeed, $T_F \sim 10^{10}$K in the interior of a white dwarf, while the central temperature is of the order 10^8 K. Consequently, the degeneracy pressure exceeds the pressure due to thermal motions of the particles and, thus, it maintains hydrodynamical equilibrium.

The equation of state (EOS) of the degenerate electron gas in a white dwarf is modified by several additional effects. An early account of the EOS was given, for instance,

by Baym et al. [1971]. At rather low densities ($\rho \lesssim 10^4\,\mathrm{g\,cm^{-3}}$), electrostatic corrections due to the attraction of electrons by ions are important [cf. Shapiro and Teukolsky, 1983, Section 2.4]. Chemical equilibrium at high densities ($\rho \gtrsim 10^8\,\mathrm{g\,cm^{-3}}$), on the other hand, is heavily influenced by the *neutronisation* caused by inverse β-decays [cf. Shapiro and Teukolsky, 1983, Section 2.5]. For thermonuclear supernovae, pair creation at temperatures of the order 10^{10} K must be taken into account. The nuclei, on the other hand, constitute in very good approximation a perfect gas. Further discussion of the full EOS can be found in Balberg and Shapiro [2000] and explicit formulae in Reinecke [2001].

As the mass of a white dwarf increases, the number of electron states and the Fermi momentum becomes ever larger. At a certain threshold, $p_\mathrm{F} \sim m_\mathrm{e}c$ and the degenerate electrons become relativistic. Since $p_\mathrm{F} \propto n_\mathrm{e}^{1/3}$ according to equation (1.1), the Fermi energy in the relativistic regime is of the order

$$E_\mathrm{F} \sim \hbar c n_\mathrm{e}^{4/3} \sim \frac{\hbar c N^{4/3}}{R^4}, \tag{1.7}$$

where R is the radius of the star and $N \sim n_\mathrm{e}R^3$ the total number of particles. The mass of the white dwarf can be expressed as $M = Nm_\mathrm{B}$, where m_B is the mean mass of the baryons in the nuclei, and the gravitational potential energy per unit volume is given by

$$E_\mathrm{G} \sim -\frac{GN^2m_\mathrm{B}^2}{R^4}. \tag{1.8}$$

If $E_\mathrm{F} > -E_\mathrm{G}$, expansion of the white dwarf will lower the Fermi energy to the point where the electrons become non-relativistic and $E_\mathrm{F} \propto R^{-5}$. Eventually, the total energy E becomes negative and the star settles into hydrodynamical equilibrium. On the other hand, if N and, consequently, M exceeds a certain threshold, then $E_\mathrm{G} < -E_\mathrm{F}$, and E becomes smaller with *decreasing* radius. In this case, no stable configuration exists and gravitational collapse sets in[2]. The critical mass is called the *Chandrasekhar mass*. Modelling the white dwarf as a polytrope, a more elaborate analysis yields

$$M_\mathrm{Ch} = \frac{\sqrt{3\pi}}{2m_\mathrm{B}^2}\left(\frac{\hbar c}{G}\right)^{3/2} Y_\mathrm{e}^2\left[-\lambda\frac{\mathrm{d}\Theta_3}{\mathrm{d}\lambda}\right]_{\lambda=\lambda_1} \approx 5.76 Y_\mathrm{e}^2 M_\odot, \tag{1.9}$$

where λ_1 is the first zero point of the *Lane-Emden function* $\Theta_3(\lambda)$ for the $n = 3$ polytrope [cf. Müller, 2002, Section 2.4]. For matter with equal fractions of protons and neutrons, $Y_\mathrm{e} = n_\mathrm{e}/n_\mathrm{B} = 0.5$ and, thus, $M_\mathrm{Ch} \approx 1.44\,M_\odot$. However, an accreting white dwarf which gradually approaches the Chandrasekhar limit does not necessarily end in a collapse. The fate of the star depends on its composition and the accretion rate. For white dwarfs which are composed of oxygen, neon and magnesium, electron capture at sufficiently high density triggers the collapse to a neutron star, provided that the accretion rate is large enough to circumvent helium detonations [cf. Nomoto and Kondo, 1991]. For the more common carbon and oxygen white dwarfs, on the other hand, a thermonuclear runaway under ultra-relativistically degenerate conditions is likely to preceed the collapse and to cause a supernova explosion, as will be discussed further in Section 1.2.1.

[2]The argument for a maximal mass of white dwarfs as outlined above was given by Landau [1932]. Originally, it was calculated by Chandrasekhar [1931].

1.1.2 Turbulence

The dynamics of fluids in the continuum approximation is governed by a set of five partial differential equations (PDEs) for the mass density ρ, the three components of the velocity $\boldsymbol{v}$ and the specific energy e [cf., for instance, Warsi, 1993, Section 3.2][3]:

$$\frac{\mathrm{D}\rho}{\mathrm{D}t} + \rho\boldsymbol{\nabla}\cdot\boldsymbol{v} = 0, \tag{1.10}$$

$$\rho\frac{\mathrm{D}\boldsymbol{v}}{\mathrm{D}t} = -\boldsymbol{\nabla}P + \rho(\boldsymbol{a}+\boldsymbol{g}) + \boldsymbol{\nabla}\cdot\boldsymbol{\sigma}, \tag{1.11}$$

$$\rho\frac{\mathrm{D}e}{\mathrm{D}t} + \boldsymbol{\nabla}\cdot(P\boldsymbol{v} - \boldsymbol{\sigma}\cdot\boldsymbol{v} - \rho c_\mathrm{P}\chi\boldsymbol{\nabla}T) = \rho(\boldsymbol{a}+\boldsymbol{g})\cdot\boldsymbol{v}. \tag{1.12}$$

The operator $\mathrm{D}/\mathrm{D}t$ is the *Lagrangian derivative*,

$$\frac{\mathrm{D}}{\mathrm{D}t} = \frac{\partial}{\partial t} + \boldsymbol{v}\cdot\boldsymbol{\nabla}, \tag{1.13}$$

which, acting upon a dynamical quantity, gives the rate of change with respect to the flow. The spatial derivative in the direction of the velocity, $\boldsymbol{v}\cdot\boldsymbol{\nabla}$, accounts for *advection*. It gives rise to a non-linearity, $(\boldsymbol{v}\cdot\boldsymbol{\nabla})\boldsymbol{v}$, in the equation of momentum conservation. Motion is induced by any mechanical force $\rho\boldsymbol{a}$ acting on the fluid, as well as the gravitational force $\rho\boldsymbol{g}$ and the pressure gradient $\boldsymbol{\nabla}P$. Dissipation of kinetic energy $e_\mathrm{kin} = \frac{1}{2}|\boldsymbol{v}|^2$ into internal energy $e_\mathrm{int} = e - e_\mathrm{kin}$ is caused by *viscous dissipation*. In the momentum equation, the dissipation term is given by the divergence of the symmetric tensor $\boldsymbol{\sigma}$, which is called the *viscous stress tensor*. Both the pressure P and the temperature T are coupled to ρ and e_int through the equation of state. The product of the heat capacity c_P and thermal diffusivity χ yields the specific conductivity of the fluid. In the following, the phenomenology emerging from the above set of equations is discussed.

Strain and Vorticity: On the Way to Turbulence

For *Newtonian fluids* of constant viscosity $\rho\nu$, the viscous stress tensor is proportional to the trace-free part of the *rate-of-strain tensor*:

$$\sigma_{ik} = 2\rho\nu S^*_{ik} \equiv 2\rho\nu\left(S_{ik} - \frac{1}{3}\delta_{ik}\right), \tag{1.14}$$

where

$$S_{ik} = v_{(i,k)} \equiv \frac{1}{2}\left(\frac{\partial v_i}{\partial x_k} + \frac{\partial v_k}{\partial x_i}\right). \tag{1.15}$$

The total contraction $|S| = 2S_{ik}S_{ik}$ is the scalar rate of strain, and the trace $d = \mathrm{Tr}\,\boldsymbol{S} = S_{ii}$ is the *divergence* of the velocity field. If the dissipation term in equation (1.11) is comparable to the advection term, i. e., $2\nu S^*_{ik,k} \sim v_k v_{i,k}$, then viscosity dominates the fluid dynamics and the flow is said to be *laminar*. In this case, the flow is completely characterised by the boundary conditions, the spatial structure and temporal evolution of the force fields $\boldsymbol{a}$ and $\boldsymbol{g}$. For *characteristic scales* of spatial and temporal variations

[3] Basically, the continuum approximation holds if the mean free path of particles is much smaller than the dynamically relevant length scales of bulk motion. In this case, a separation into internal energy due to random thermal motions and kinetic energy due to bulk motion is possible.

L and T, respectively, we have $S_{ik,k} \sim L^{-1}T^{-1}$, $v_k v_{i,k} \sim LT^{-2}$ and, thus, $\nu \sim L^2T^{-1}$. On the other hand, if $\nu \ll L^2T^{-1}$ or, equivalently,

$$\mathrm{Re} = \frac{LV}{\nu} \gg 1, \tag{1.16}$$

where $V = L/T$ is the characteristic velocity, then the strain increases to the point where velocity fluctuations on scales much smaller than L are produced. The dimensionless number Re is called the *Reynolds number*. It was originally introduced as a phenomenological parameter which characterises the state of a flow. For large Reynolds numbers, the dynamics of the fluid becomes increasingly *non-linear*. Beyond $\mathrm{Re} \sim 10^3$, the flow usually enters the *turbulent* regime, in which the dynamics is fully chaotic and sensitivity on initial conditions as well as mixing emerge as the hallmarks of chaos. This means that two realisations of a turbulent flow with nearly the same initial and boundary conditions diverge rapidly with time, and the trajectories of test particles in the fluid tend to fill an increasing fraction of the accessible phase space volume. The transition from a non-linear to a fully turbulent flow is beautifully illustrated by the photographs of a grid flow with immersed soap films in Figure 1.1.

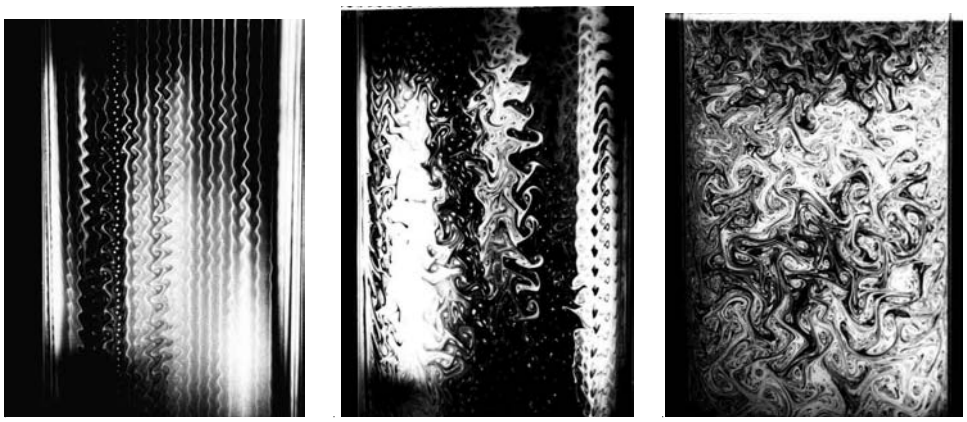

Figure 1.1: The onset of two-dimensional grid generated turbulence in flowing soap films [Rutgers, Wu, and Goldburg, 1996].

Another aspect of the mixing property of turbulent flows is the mechanism of vortex stretching. The initially produced vortices are stretched out by the flow to form *vortex filaments* which become increasingly folded. A measure for the local strength of rotational motion is the *vorticity* of the velocity field, which is defined by

$$\omega = 2W_{ik}W_{ik}, \tag{1.17}$$

where

$$W_{ik} = v_{[i,k]} \equiv \frac{1}{2}\left(\frac{\partial v_i}{\partial x_k} - \frac{\partial v_k}{\partial x_i}\right). \tag{1.18}$$

From $\boldsymbol{\omega} = \boldsymbol{\nabla} \times \boldsymbol{v}$, it follows that $\boldsymbol{\omega} \cdot \boldsymbol{\omega} = \epsilon_{ikl}\epsilon_{imn}v_{l,k}v_{n,m} = \omega^2$. Iso-surfaces of vorticity which are tangential to the vector field $\boldsymbol{\omega}(\boldsymbol{x}, t)$ at each point are called vortex tubes. In

other words, vortex tubes are bundles of vortex lines that are integral curves of $\boldsymbol{\omega}(\boldsymbol{x}, t)$. Compact vortex tubes evolve into vortex filaments of small cross section and large circulation through stretching and folding. Different pieces of vortex filaments may connect and merge, a phenomenon called *vortex pairing*. Thereby, the flow structure becomes increasingly intricate. A bound on vortex stretching is set by the viscosity of the fluid, which inhibits rotational motion below a certain scale and drains energy from vortices of a size above that scale[4].

Kolmogorov's Theory: Self-Similar Developed Turbulence

Notwithstanding the complicated dynamics of vortex interaction, a phenomenological theory of developed isotropic turbulence can be formulated on grounds of very simple scaling arguments. This theory was put forward by Kolmogorov in the nineteenfourties and rests on three fundamental conjectures, which have a lasting impact on contemporary theories [cf. Pope, 2000, Section 6.1][5]:

Hypothesis of local isotropy: At sufficiently high Reynolds number, the dynamics on small scales $l \ll L$ tends to become statistically isotropic.

First similarity hypothesis: The statistics of isotropic velocity fluctuations on sufficiently small scales are universal and uniquely determined by the viscosity and the rate of kinetic energy dissipation.

Second similarity hypothesis: There is a subrange of scales for which the statistics of turbulent fluid motions are independent of the viscosity, i. e., the mechanism and the characteristic scale of dissipation.

The first hypothesis stems from the idea that anisotropies in large-scale motions due to boundary conditions or the forcing on length scales $l \sim L$ is lost in the chaotic dynamics on smaller scales. This is related to the notion of a *turbulence cascade*, which was originally proposed by Richardson [1922]. In a pictorial way, the largest vortices of size comparable to L pass on energy to smaller vortices which in turn act on yet smaller vortices and so on. Thus, energy is transferred from the largest to the smallest dynamical scales. In spectral space, the turbulence cascade corresponds to the interaction between Fourier modes, where energy is transferred from modes of smaller to those of larger wave numbers. Since energy is injected at the largest scales, corresponding to the wavenumber $k_0 \sim 1/L$, the spectral interactions become asymptotically independent of the external forces for $k \gg k_0$. This is the *universal equilibrium range*. There is an upper cutoff in wave number space and a lower cutoff with respect to length scales, beyond which viscosity damps fluid motions. The cutoff length is called the *Kolmogorov scale* and is given by

$$\pi/k_\mathrm{K} = \eta_\mathrm{K} = \left(\frac{\nu^3}{\langle\epsilon\rangle}\right)^{1/4}, \tag{1.19}$$

where $\langle\epsilon\rangle$ is the mean rate of dissipation of kinetic energy. Contracting the equation of momentum conservation (1.11) with the velocity and integrating the viscous term by

[4] More on the mechanism of vortex stretching can be found in Chorin [1994, Chapter 5].

[5] A refined version of the theory was later published by Kolmogorov [1962].

parts, one obtains

$$\langle \epsilon \rangle = \nu \langle |S^*|^2 \rangle = \nu \left[\langle |S|^2 \rangle - \frac{2}{3} \langle d^2 \rangle \right], \tag{1.20}$$

where brackets $\langle\ \rangle$ are used to denote the ensemble average. For a given driving force $\boldsymbol{f}$, the rate of strain $|S|$ becomes larger as the viscosity *decreases*, because the derivative of the velocity is mostly determined by fluctuations on the smallest scales $l \sim \eta_K$. For an incompressible flow, $|S^*|^2 = |S|^2 = \omega^2$. Thus, $\langle \epsilon_s \rangle = \nu \langle \omega^2 \rangle$ is called the *solenoidal* rate of dissipation.

As was shown by Landau, the ratio of the largest to the smallest dynamical length scale is of the order [cf. Landau and Lifshitz, 1991]

$$\frac{L}{\eta_K} \sim \mathrm{Re}^{3/4}. \tag{1.21}$$

For sufficiently high Reynolds number, there are intermediate length scales $\eta_K \ll l \ll L$ in the so-called *inertial subrange*. On these scales, neither viscous dissipation nor large-scale anisotropy affects the flow, and the dynamics is largely dominated by the non-linear turbulent energy transfer corresponding to the advection term. Consequently, turbulent fluid motions on scales within the inertial subrange are quasi *inviscid* and *isotropic*. Furthermore, the scaling law $v'(l) \propto l^{1/3}$ holds for velocity fluctuations $v'(l)$ at the length scale l. Kolmogorov found that this scaling law is equivalent to the kinetic energy spectrum function

$$E(k) = C \langle \epsilon \rangle^{2/3} k^{-5/3}, \tag{1.22}$$

which specifies the mean kinetic energy per wave number interval [cf. Pope, 2000, Section 6.5]. C is called the *Kolmogorov constant*. Data from numerous laboratory experiments and numerical simulations suggest that the Kolmogorov constant is nearly universal with $C \approx 1.5 \ldots 1.7$. However, deviations from universality may occur in *intermittent* flows, in which laminar and turbulent regimes are alternating. From round jet experiments, it was found that C decreases with the degree of intermittency, but the $k^{-5/3}$ scaling of the energy spectrum remains intact.

Heat Conduction and Buoyancy: Convectively Driven Turbulence

A particularly important kind of turbulence, which encompasses the weather on Earth as well as convection zones in stellar interiors, is found in *Rayleigh-Bénard systems*. The prerequisite is a thermally conducting fluid subject to gravity, with an incoming heat flux from below and an infinite heat reservoir of lower temperature on top. The mechanism producing turbulence works in the following way. As fluid is heated from below, its density decreases and the bottom layer becomes *Rayleigh-Taylor unstable* due to buoyancy. Thus, rising motion of warm fluid towards cooler layers sets in. Depending on the thermal and viscous properties of the fluid, besides the temperature gradient and the gravitational field, there are several possible outcomes. If the conductivity is very high, heated fluid will cool so quickly that the motion stalls and conduction persists as the sole mechanism of heat transport. On the other hand, if heat conduction is less efficient, plumes of hot fluid will rise all the way to the reservoir on top, where excess heat is disposed. If heat is added at a constant rate, this will

eventually result in a steady state of fluid circulation (or "flywheel" motion) called *convection*. With growing strength of buoyancy relative to viscous damping and thermal diffusion, convection becomes increasingly turbulent.

Rayleigh-Bénard systems are characterised by several dimensionless parameters. The relative strength of buoyancy compared with the inhibiting factors conduction and viscosity is specified by the *Rayleigh number*:

$$\mathrm{Ra} = \frac{g_{\mathrm{eff}} L^3}{\chi \nu}, \tag{1.23}$$

where $g_{\mathrm{eff}} = g\delta_P \Delta T / T_0$ is the *buoyant acceleration* due to the gravity g and the density contrast between hot and cold parcels of fluid. T_0 is the temperature of the heat reservoir and Δ_T is the temperature difference over the vertical length scale L of the system. The logarithmic gradient $\delta_P = -\langle \partial \log \rho / \partial \log T \rangle$ measures the thermal expansion of the fluid[6]. With increasing Ra, the fluid motion becomes ever more chaotic. Fully turbulent convection is usually found for $\mathrm{Ra} \gtrsim 10^8$ [cf. Kadanoff, 2001]. Even then, the flow is rather laminar inside rising convective plumes, while the strain exerted by fluid which has cooled and is dragged downwards produces turbulent vortices. Since the pattern of plumes and the turbulent down-drafts in between changes with time, a spatially fixed region experiences quiescent conditions alternating with turbulent phases. Evidence for the *intermittency* of convectively driven turbulence was inferred, for instance, from the observation of solar granulation by Nesis et al. [1999].

The *Prandtl number* relates the diffusive properties of the fluid:

$$\mathrm{Pr} = \frac{\nu}{\chi}. \tag{1.24}$$

In liquids, $\mathrm{Pr} \sim 1$ and even for air $\mathrm{Pr} \sim 0.1$. In white dwarf matter, however, the Prandtl number is much smaller than one. This is mainly a consequence of the high thermal conductivity of the degenerate electron gas. According to an estimate of the electron opacity by Woosley et al. [2003], $\rho c_P \chi \approx 3 \cdot 10^{18}\,\mathrm{erg\,cm^{-1}\,s^{-1}\,K^{-1}}$ for typical conditions in a white dwarf near the Chandrasekhar limit with $T \sim 10^8\,\mathrm{K}$ and $\rho \sim 10^9\,\mathrm{g\,cm^{-3}}$. The corresponding heat capacity is $c_P \approx 9 \cdot 10^6\,\mathrm{erg\,g^{-1}\,K^{-1}}$. The viscosity was calculated by Nandkumar and Pethick [1984]. They found $\nu \sim 1\,\mathrm{cm^2\,s^{-1}}$. Putting these values together, a Prandtl number of the order 10^{-3} is obtained. The product of Pr and Ra yields a squared ratio of time scales:

$$\mathrm{Pr\,Ra} = \frac{gL^3}{\chi^2} \frac{\delta_P \Delta T}{\langle T \rangle} = \left(\frac{\tau_\chi}{\tau_{\mathrm{B}}} \right)^2. \tag{1.25}$$

The time scale of thermal conduction is defined by $\tau_\chi = L^2/\chi$ and the time scale of buoyant motion is given by $\tau_{\mathrm{B}} = (LT_0 / g\delta_P \Delta T)^{1/2}$. Thus, Pr Ra is a measure of the *efficiency* of convection [cf. Canuto, 1996]. If $\tau_{\mathrm{B}} \ll \tau_\chi$, then convection is highly efficient compared to conduction and the gross of heat transport is non-conductive. On the other hand, if $\tau_\chi \sim \tau_{\mathrm{B}}$, thermal conduction significantly influences the dynamics of the system and tends to level super-adiabatic temperature gradients which support convection.

[6] In the context of stellar structure or atmospheres, it is customary to use the local *super-adiabatic* temperature gradient in the definition of the Rayleigh number. For conceptual simplicity, however, we use the absolute linear gradient here.

For the thermonuclear "smoldering phase" in a critical white dwarf shortly in advance of ignition, Woosley et al. [2003] estimated Ra $\sim 10^{25}$ and, hence, $\tau_\chi \sim 10^{11}\tau_\mathrm{B}$ [7]. This result indicates that convection is extremely efficient, despite the excellent conductivity of degenerate matter. The buoyant rise velocities are of the order $10^6\,\mathrm{cm\,s^{-1}}$. In combination with the integral scale $L \sim 10^8$ cm, which is given by the size of a Chandrasekhar-mass white dwarf, a Reynolds number of the order 10^{14} is implied. Once the thermonuclear runaway commences, heat is released in highly localised regions, namely, the flame fronts, and the dominating buoyancy forces are caused by the significantly larger density contrast between unburned and processed material.

1.1.3 Combustion

There are two fundamentally different modes of combustion. On the one hand, slow burning or *deflagration* and, on the other hand, *detonations* [cf. Landau and Lifshitz, 1991, Chapter XIV]. In the case of a deflagration, the temperature of unburned fluid (fuel) in the vicinity of the reaction zone rises due to thermal conduction. Once heat generation is balanced by diffusion, the burning zone is propagating at a steady subsonic speed, and pressure equilibrium is maintained across the reaction zone. Basically, this characterises what is commonly known as a *flame*[8]. The notion of a flame applies if fluid motions do not significantly disturb the burning process within the reaction zone, i. e., the time scale of burning is much smaller than the time scale of velocity fluctuations on scales comparable to the flame thickness. If the ignition of fuel is caused by compressive heating through a shock wave, the burning process is called a *detonation*. In this case, there is an overpressure in the burned material (ash) behind the supersonically propagating shock. Quantitatively, a classification of the burning regimes can be made by means of the conservation laws for momentum and the state variables across the reaction zones. In particular, if the thickness of the reaction zone is small compared with all dynamical length scales, it can be treated as a discontinuity and the variables hither and tither the burning front are linked by a set of simple algebraic equations which are called the *Rankine-Hugoniot jump conditions*. In particular, the conservation of the mass flux $j = \rho v$ across the flame front or detonation wave implies

$$P_\mathrm{b} - P_\mathrm{u} = -j^2\left(\frac{1}{\rho_\mathrm{b}} - \frac{1}{\rho_\mathrm{u}}\right) \tag{1.26}$$

for the pressure difference between burned and unburned fluid. This is known as the *Rayleigh criterion*. In a state diagram, the lines satisfying the Rayleigh criterion intersect with the *Hugenoit curve*, which accounts for energy conservation:

$$e_\mathrm{int,b} - e_\mathrm{int,u} = \varepsilon_\mathrm{nuc} - \frac{1}{2}\left(\frac{1}{\rho_\mathrm{b}} - \frac{1}{\rho_\mathrm{u}}\right)(P_\mathrm{b} + P_\mathrm{u}), \tag{1.27}$$

[7] Such an extraordinarily high Rayleigh number possibly indicates a regime of convection beyond the turbulent Rayleigh-Benard convection. Unfortunately, this regime is also far beyond anything that is accessible in laboratory experiments. Kraichnan argued that the convective cells might break up and fluid motion should become utterly chaotic [cf. Kadanoff, 2001].

[8] For chemical combustion, a distinction is made between *premixed* and *diffusive* flames. Thermonuclear flames, however, are trivially premixed, because no additional agent, like oxygen in most chemical burning processes, is required.

where $\varepsilon_{\rm nuc}$ is the energy released per unit of burned mass. There are two branches of intersection points at the Hugenoit curve which correspond to physical solutions. In one branch, the propagation speed is supersonic and $P_{\rm b} > P_{\rm u}$, and in the other branch $P_{\rm b} < P_{\rm u}$, with subsonic propagation speed. These solutions correspond to detonations and deflagrations, respectively. Usually, explosions are attributed to detonations. However, deflagration can also lead to an explosion, if most of the fuel is incinerated before the flames are quenched by the thermal expansion of the burning products. Indeed, degeneracy of the fuel in a thermonuclear supernovae implies that there is only little expansion while a significant fraction of carbon and oxygen has already been burned. However, since the flame propagation speed is very small compared to the speed of sound, *turbulence* is necessary to enhance the burning rate and, thus, to accelerate the deflagration. Therefore, it is probably the combination of degeneracy and turbulence which enables pure deflagration to cause an explosion. Nevertheless, there is an ongoing debate whether there might be a transition from the deflagration to a detonation at some point.

Laminar Burning and Flame Instability

To begin with, we shall consider laminar flames which are smooth on the smaller length scales being considered. For a *steady laminar flame*, the width of the reaction zone, $\delta_{\rm F}$, is determined by the equilibrium between energy generation due to nuclear reactions, B, and the rate of diffusion caused by thermal conduction [cf. Landau and Lifshitz, 1991, § 128]. The balance between these two processes can be expressed in terms of their characteristic time scales, $\tau_{\rm burn}$ and $\tau_{\rm cond}$. The former is given by $\tau_{\rm burn} \sim \rho\varepsilon_{\rm nuc}/B_{\rm nuc}$, where $\varepsilon_{\rm nuc}$ is the specific energy released by thermonuclear fusion. The time scale of diffusion, on the other hand, can be expressed as $\tau_{\rm cond} \sim \delta_{\rm F}^2/l_{\rm e}c$, where $l_{\rm e}$ is the mean free path of electrons, which contribute the largest part of the thermal conductivity. Setting these two time scales equal, one finds that the *flame thickness* $\delta_{\rm F}$ is approximately given by

$$\delta_{\rm F} \sim \sqrt{\frac{\rho\varepsilon_{\rm nuc} l_{\rm e} c}{B}}. \tag{1.28}$$

Defining the *laminar flame speed* by $s_{\rm lam} = \delta_{\rm F}/\tau_{\rm burn}$, we have

$$s_{\rm lam} \sim \sqrt{\frac{l_{\rm e} c B}{\rho\varepsilon_{\rm nuc}}}. \tag{1.29}$$

Thermonuclear combustion of degenerate carbon and oxygen in the laminar burning regime was investigated by Timmes and Woosley [1992]. They computed the conductive flame propagation with several methods and determined various parameters, in particular, the flame speed $s_{\rm lam}$ for a wide range of mass densities and nuclear compositions. For equal mass fractions of ^{12}C and ^{16}O at a density $\rho_0 = 10^9\,{\rm g\,cm^{-3}}$, for example, $s_{\rm lam} \approx 36\,{\rm km\,s^{-1}}$. The specific energy release is $\varepsilon_{\rm nuc} \approx 7 \cdot 10^{17}{\rm erg\,g^{-1}}$ [cf. Steinmetz et al., 1992], which is of the same order of magnitude as the Fermi energy per unit mass (see Section 2.3.2). Moreover, $GM_{\rm Ch}/R \sim \varepsilon_{\rm nuc}$ in a Chandrasekhar-mass white dwarf. For this reason, almost all matter must be burned to get the star gravitationally unbound, i. e., to produce an explosion. Assuming a spherical flame surface

propagating at laminar speed from the centre of the white dwarf outwards, the time required to burn the whole star would be of the order 10 s. As burning increases the internal energy by an amount comparable to the Fermi energy, degeneracy is lifted and expansion sets in. With decreasing density, this effect becomes even stronger. The scale on which the star adjusts itself to the rising internal energy is the sound crossing time τ_S. Initially, $\tau_S \sim 0.1\,\mathrm{s}$. Hence, the expansion would proceed too quickly and quench the burning process before an explosion could commence, if the flame would propagate more or less as a spherical surface. In conclusion, there must be surface-increasing processes caused by *flame instabilities*.

Starting with a nearly planar flame front, deviations from the perfectly planar geometry are amplified in the course of propagation. This is a consequence of the normal component of the velocity going through a jump across the flame front, while the tangential component is continuous. If there is a bulge towards the unburned material, the velocity at the crest is maximal and steadily increases with respect to those portions of the front lagging behind. Thus, the bulge grows, an effect which is called *Landau-Darrieus instability* [cf. Landau and Lifshitz, 1991]. However, as discovered by Zel'dovic [1966], the perturbations cannot grow indefinitely, because eventually cusps form between adjacent bulges, and the front assumes a stable cellular shape. Since the surface area of a cellular front is larger than a planar front, the total rate of burning is also higher. If the cellular structure of a flame cannot be resolved in a numerical simulation, it is possible to account for the increase of the burning rate by means of an an *effective propagation speed* $s_c = (A_c/A_0)s_{\mathrm{lam}}$. The surface ratio A_c/A_0 is determined by the density contrast ρ_b/ρ_u between burned and unburned material. Blinnikov and Sasorov [1995] argued that the emerging cellular surface is fractal within certain lower and upper cutoff scales. Implications of the cellular structure for deflagration fronts in thermonuclear supernovae were investigated by Niemeyer and Hillebrandt [1995a] and, furthermore, Niemeyer and Woosley [1997]. It became clear that the increase of the rate of burning due to the cellular structure is small and definitely not sufficient to produce an explosion. Röpke et al. [2003] have recently confirmed the mechanism of flame stabilisation for two-dimensional deflagration in degenerate C+O matter. The simulations performed with a fuel density of $\rho_u = 5 \cdot 10^7\,\mathrm{g\,cm^{-3}}$ indicated an increase of the propagation speed by about 25 %.

In the presence of a gravitational field, the evolution of the burning process becomes even more intricate, as the burned fluid has lower density than the unburned fuel and, hence, it is subject to buoyancy. Considering initially globular blobs of thermonuclear ash, they will rise and form convective plumes, while the surrounding unprocessed material is dragged downwards. The asymptotic rise velocity was experimentally found to be of the order $\sqrt{g_{\mathrm{eff}} L_{\mathrm{RT}}}$, where L_{RT} is the characteristic spatial scale (the "size of the bubble") and $g_{\mathrm{eff}} = \mathrm{At}\, g$ is the *effective acceleration* due to buoyancy [cf. Niemeyer and Woosley, 1997]. The *Atwood number* $\mathrm{At} = (\rho_u - \rho_b)/(\rho_u + \rho_b)$ is a measure of the density contrast between burned and unburned material. The corresponding time scale is given by

$$\tau_{\mathrm{RT}} \sim \sqrt{\frac{L_{\mathrm{RT}}}{g_{\mathrm{eff}}}} = \sqrt{\frac{L_{\mathrm{RT}}}{\mathrm{At}\, g}}, \tag{1.30}$$

which agrees with results obtained from linear stability analysis of sinusoidal pertur-

bations in a horizontal planar interface separating low-density fluid from high-density fluid on top [cf. Padmanabhan, 2000, Section 8.13.1]. The gravitational amplification of vertical density perturbations is called *Rayleigh-Taylor instability* and, in fact, is the driving mechanism of turbulence in supernova explosions.

Turbulent Deflagration

The energy being generated by thermonuclear burning in a white dwarf is driving convection. Thereby, heat is converted into mechanical energy. As the burned material of lower density penetrates the high-density fuel, strain is generated at the interface, which in turn gives rise to *Kelvin-Helmholtz instabilities*. In the beginning, the vortices distort the convective plumes into mushroom-like shapes. As mentioned above, the characteristic velocity of convection on the length scale l is $v_{\mathrm{RT}}(l) \sim \sqrt{g_{\mathrm{eff}} l}$. In principle, RT instabilities are generated on arbitrarily small length scales. However, nonlinear turbulent interactions among different scales will produces a cascade of vortices. The scaling behaviour of these vortices asymptotically approaches Kolmogorov's law $v'(l) \propto l^{1/3}$ [9]. Consequently, turbulent vortices will increasingly dominate RT instabilities on small length scales, provided that there is enough time for turbulence to develop. The time required to produce turbulence on the scale l, given a characteristic velocity $v_{\mathrm{RT}}(l)$, is of the order $\tau_{\mathrm{RT}} = l/v_{\mathrm{RT}}(l) \propto l^{1/2}$. This is the self-interaction time scale of convective plumes of size l. After the time τ_{RT} has elapsed, turbulence on scales $\lesssim l$ is developed. However, if the time scale τ_{RT} becomes comparable to the sound crossing time, the expansion of the star tends to inhibit the production of turbulent vortices. Consequently, $\tau_{\mathrm{S}} \sim 0.1\,\mathrm{s}$ sets an upper bound on the range of fully turbulent length scales. This is the integral length scale L of the turbulence cascade, which was estimated to be of the order 10^6 cm by Niemeyer and Woosley [1997]. On the largest length scales $l \gtrsim L$, buoyancy governs the dynamics, whereas turbulence dominates the smaller length scales $l \lesssim L$. This Thesis is exclusively concerned with the dynamics on the scales smaller than L.

In the figurative framework of a hierarchy of vortices or eddies, one can think of $v'(l)$ as being the typical velocity of an eddy of size l. The associated *eddy turn-over time* is $l/v'(l)$. If $v'(l)$ is small compared to the laminar flame speed s_{lam}, then the flame front will propagate through a region of size l in a time much faster than the turn-over time $l/v'(l)$. Thus, the turbulent flow appears to be more or less "frozen" with respect to the burning process on these scales. For $v'(l) \gtrsim s_{\mathrm{lam}}$, on the other hand, the front is significantly distorted while it is crossing a vortex of diameter l. Hence, there is a threshold scale on which burning decouples from turbulence. This is the *Gibson scale* l_{G}, which is defined by

$$\langle v'(l_{\mathrm{G}}) \rangle_{\mathrm{F}} = s_{\mathrm{lam}}. \tag{1.31}$$

The brackets denote the ensemble average of the velocity fluctuations over the whole region in which burning takes place. On length scales $l \gtrsim l_{\mathrm{G}}$, turbulence stretches and folds the flame and thereby increases the surface area A. Since the rate of energy generation is proportional to $A s_{\mathrm{lam}}$, ever more heat is released per unit time. This

[9] Niemeyer and Kerstein [1997] investigated the possibility of a different scaling law in the case of turbulence being driven by convection. As of today, however, most experimental results favour the validity of the Kolmogorov scaling law.

enhances convection and the production of turbulence. The flame front would tend towards a fractal, if it were not for the lower cut-off set by the Gibson scale[10].

In a *gedanken experiment*, one can imagine a flame front propagating through an infinite column subject to a vertical gravitational field. Initial perturbations of a horizontal flame will grow due to RT instability. Turbulence will increasingly distort the flame. A steady state will be approached asymptotically, in which the burning rate is statistically constant. We shall denote the maximum burning rate in the steady state by B_∞. Actually, this scenario was implemented numerically by Khokhlov [1995]. He found that the mean burning rate in the steady state is independent of the laminar flame speed $s_{\rm lam}$. In fact, it is only determined by the asymptotic rise velocity of RT instabilities and the length scale $L_{\rm RT}$:

$$B_\infty \propto \sqrt{g_{\rm eff} L_{\rm RT}}. \tag{1.32}$$

Setting the initial burning rate $B_0 \propto A_0 s_{\rm lam}$, where A_0 is the surface area of the horizontal planar front, the ratio B_∞/B_0 is equal to the ratio A_∞/A_0. A_∞ can be regarded as an ensemble average of the flame surface area in the steady state. The same rate of energy generation would be obtained, if the surface area was A_0, but the flame would be propagating at an *effective* speed

$$s_{\rm t}(L_{\rm RT}) = \frac{A_\infty}{A_0} s_{\rm lam} \sim \sqrt{g_{\rm eff} L_{\rm RT}}. \tag{1.33}$$

This is the *turbulent flame speed*. It captures the effects of turbulence in a purely statistical manner.

The notion of a turbulent flame speed can be applied at the level of any scale in between the Gibson and the integral scale of turbulence. The basic idea is that a front, which is smoothed on scales smaller than l, must propagate with an effective speed $s_{\rm t}(l)$ of the order $v'(l)$, because the dynamics of the flame on scales $\sim l$ is governed by turbulent vortices of size l. The relation $s_{\rm t}(l) \sim v'(l)$ was first proposed by Damköhler [1940], who studied Bunsen cones. Further evidence was found from other laboratory measurements on steady open flames [cf. Williams, 1994, Chapter 7]. Kerstein [1988] confirmed this relation on the basis of numerical studies. Invoking the Kolmogorov scaling law $v'(l) \propto l^{1/3}$, $s_{\rm t}(l)$ can be estimated on scales $l \lesssim L$ to be

$$s_{\rm t}(l) \sim v'(l) \propto l^{1/3}. \tag{1.34}$$

In order to conserve the burning rate, the implied scaling law for the surface area of the smoothed flame front is

$$A(l) \propto l^{1/3}. \tag{1.35}$$

The power law $A(l) \propto l^{D-2}$ is characteristic for a fractal of dimension D. In the Kolmogorov regime, $D = 7/3$, where the lower cut-off is given by the Gibson scale $l_{\rm G}$ and the upper cut-off by the integral scale L. For the larger, buoyancy-dominated scales $L \lesssim l \lesssim L_{\rm RT}$, the scaling law $v_{\rm RT}(l) \propto l^{1/2}$ implies a greater dimension, $D = 5/2$. Calculating the turbulent flame speed is of crucial importance for numerical simulations.

[10] Of course, there are also topological reasons for the flame surface being limited. Once different portions of the flame front collide and merge, the increase of the burning rate ceases, as pointed out by Khokhlov [1995].

Suppose that Δ is the length scale corresponding to the discretisation. In the case of a finite-volume scheme, Δ is the size of the grid cells. The unresolved scales $l \lesssim \Delta$ are called *subgrid scales*. For most turbulent combustion processes which are of physical or technological interest, $l_\mathrm{G} \ll \Delta$, given the power of contemporary computers. The effective propagation speed of the modelled flame front is $s_t(\Delta) \sim v'(\Delta)$. In conclusion, an approximative description of turbulence on scales $l \lesssim \Delta$, i. e., a *subgrid scale model*, is required. This is the very topic of this Thesis.

So far we have assumed that the flame front is merely advected by the turbulent flow but the internal structure of the reaction zone is not affected by turbulence. This is the case in the *flamelet regime* of burning. Once turbulent vortices disrupt the reaction zone itself, the notion of a flame front which locally propagates with a speed s_l relative to the fuel is not sensible, and one speaks of *distributed burning*. Traditionally, the criterion for the breakdown of the flamelet regime is considered to be $\mathrm{Ka} = \delta_\mathrm{F}/\eta_\mathrm{K} \sim 1$, where Ka is known as the *Karlovitz* number. However, Niemeyer and Kerstein [1997] pointed out that $\mathrm{Ka} \sim 1$ is not the appropriate criterion for $\mathrm{Pr} \ll 1$, i. e., if the diffusivity of turbulence energy is small compared to the thermal diffusivity of heat. In general, $\delta_\mathrm{F} \sim l_\mathrm{G}$ marks the transition to distributed burning, because turbulent vortices of size smaller than the Gibson scale do not affect the flame in any case. If $\mathrm{Pr} \sim 1$, $l_\mathrm{G} \sim \eta_\mathrm{K}$ and the conventional criterion is recovered. Since the Prandtl number is much smaller than unity in white dwarf matter, $\delta_\mathrm{F} \ll l_\mathrm{G}$ is the correct criterion for deflagration in a thermonuclear supernova. It appears that the flamelet regime breaks down if $\rho \lesssim 3 \cdot 10^7\,\mathrm{g\,cm^{-3}}$ [cf. Niemeyer and Woosley, 1997].

Detonations

For the initiation of a detonation, a certain critical mass must explode and produce a self-sustaining pressure wave. The fuel has to be heated up to the point of ignition in less than one sound crossing time. Otherwise, the pressure wave will be damped too quickly. It is thought that such pressure waves might be triggered by a local excess of energy, which cannot immediately be disposed through adiabatic cooling. Whether this *induction time gradient mechanism* can initiate a detonation depends on the level of temperature fluctuations, as the reaction rate and the associated burning time scale are largely determined by the temperature. According to Niemeyer and Woosley [1997], the temperature fluctuations are very tightly constrained for a detonation to be initiated in carbon and oxygen of density $3 \cdot 10^9\,\mathrm{g\,cm^{-3}}$. However, such *preconditioning* is virtually impossible under the condition of extremely high degeneracy, because even minute variations in the local state entail very large temperature fluctuations. This is probably the reason why prompt detonations of Chandrasekhar-mass white dwarfs are not observed.

At lower density, on the other hand, turbulent mixing is a possible agent of preconditioning. This led Khokhlov [1991] to the conjecture that a detonation might be triggered by turbulent deflagration, once the white dwarf has expanded considerably. Indeed, transitions from deflagrations to detonations are observed in combustion experiments with explosive gaseous mixtures. However, an objection inferred from scaling arguments persists. For instance, at a density of about $10^7\,\mathrm{g\,cm^{-3}}$, the minimal size of a preconditioned region for the initiation of a detonation would be roughly 2 km. However, this is still much larger than the heat diffusion scale δ_F (1.28). Since this is

the length scale on which significant temperature variations occur, the transition to a detonation seems very unlikely, as was pointed out by Niemeyer [1999]. Nevertheless, it is not entirely excluded once the deflagration enters the regime of distributed burning. In this regime, the burning process is not localised to flames but spread out by turbulence over regions much larger than δ_{F}. Then the preconditioning requirements for a detonation could be met. However, the modelling of burning in the distributed regime has not been attempted yet in the context of supernova explosions. For the time being, there is no conclusive evidence, and the transition from deflagration to a detonation remains hypothetical.

1.2 Models and Observations

Supernovae are classified according to their spectral properties. The category of type Ia supernovae (SNe Ia) is distinguished from those of type II by the absence of hydrogen lines. Contrary to type Ib/c, there is no helium seen in the spectra of type Ia supernovae but prominent silicon lines, in particular, a P-Cygni profile around 6100 Å. As an example, spectra for the type Ia SN 2002bo at various stages are shown in Figure 1.2. This classification scheme has grown historically form advances in the observation of supernovae. Unfortunately, it is completely detached from the theoretical understanding. At present, all but type Ia supernoave are thought to be caused by the gravitational collapse of the core of a massive star. For supernovae of type Ia, on the other hand, an entirely different mechanism was proposed by Hoyle and Fowler [1960]. They identified a thermonuclear runaway as the cause for an explosion of degenerate stars, namely, white dwarfs. This accounts well for another defining property of type Ia supernova, the large mass of ^{56}Ni which decays into ^{56}Fe and thereby powers the light curve. Since the original proposal, there has been vivid controversy of how such an explosion might come about and what the exact physical mechanism could be. No final answer can be given yet. The most likely scenario from our current point of view is the explosion of a Chandrasekhar-mass white dwarf, either being caused by pure deflagration of carbon and oxygen or an initial deflagration followed by a detonation. This is the aforementioned single-degenerate scenario. In the following, the astrophysical framework of the consensus model is discussed.

1.2.1 Progenitor Scenarios

The main difficulty with the SD scenario is the search for evolutionary channels which could produce a white dwarf of mass $M_{\mathrm{Ch}} \approx 1.4 M_{\odot}$. Since most white dwarfs are born with masses near $0.6\,M_{\odot}$, progenitors of thermonuclear supernovae presumably evolve in *semi-detached binary systems*, in which a C+O white dwarf accumulates mass by accretion of hydrogen form a companion star. However, if the mass-transfer rate is significantly less than $5 \cdot 10^{-7}\,M_{\odot}\,\mathrm{yr}^{-1}$, shell flashes burn most of the hydrogen layer on top of the C+O core, once a critical amount has been accreted. Such events can be observed as nova outbursts and are violent thermonuclear explosions, in which the outer layer of the white dwarf is expelled into space. Consequently, there is no significant gain in mass. For accretion rates just below $5 \cdot 10^{-7}\,M_{\odot}\,\mathrm{yr}^{-1}$, on the other hand, steady hydrogen-shell burning gradually increases the mass of the white dwarf. In between,

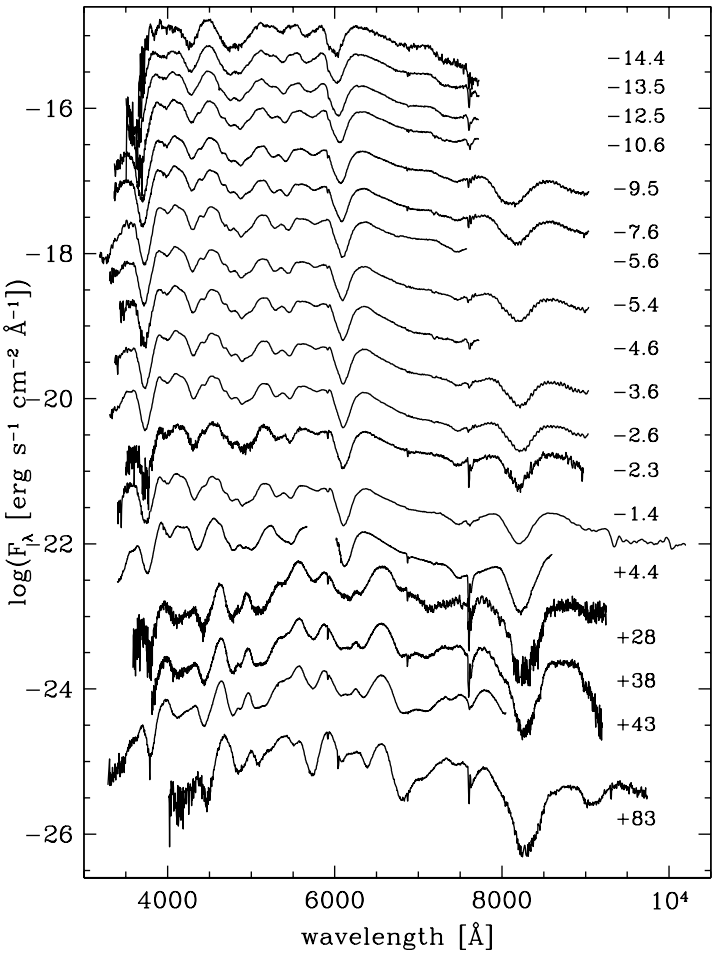

Figure 1.2: Spectral evolution of SN 2002bo [taken from Benetti et al., 2003].

weak shell flashes might occur. Contrary to the detonations at lower accretion rates, these flashes do not expel all the accreted matter, and so the white dwarf can grow. For still higher transfer rates, mass loss due to strong wind works against the accumulation of mass.

Basically, two possible evolutionary channels leading to the thermonuclear explosion of a Chandrasekhar-mass white dwarf in a semi-detached binary system have been identified. These channels are discussed, for instance, in Hachisu [2002], Nomoto et al. [2003] and Fedorova et al. [2003]. Although there is no agreement yet on the details of the binary evolution, the picture is more or less as follows. In one scenario, the binary system goes through a *common envelope* (CE) phase once the primary reaches the asymptotic giant branch. The CE gets ejected and the core of the primary star is left with a secondary main sequence (MS) star in close orbit. The former is either a C+O white dwarf or a helium star which subsequently becomes a white dwarf. The secondary fills its Roche lobe when it is still on the MS or as a subgiant. Then the white dwarf continuously accretes matter from the secondary and eventually approaches the

Chandrasekhar mass. This is the WD+MS channel. In the other scenario, the more massive star becomes a helium star after its first Roche lobe overflow, and helium core burning produces a C+O white dwarf. Mass accretion by the white dwarf starts when the secondary evolves into a red giant and fills its Roche lobe. Hence, this channel is labelled WD+RG. Observationally, binary star systems evolving towards a type Ia supernova are associated with *supersoft X-ray sources*, in which steady hydrogen burning produces the radiation. In the case of weak shell flashes, *recurrent novae* might also indicate possible progenitors. Moreover, *long-period dwarf novae* were suggested as an alternative route towards type Ia supernovae by King et al. [2003].

The minimal initial mass to produce a Chandrasekhar-mass white dwarf in the WD+MS channel was deduced from binary evolution calculations by Han and Podsiadlowski [2003]. It appears that white dwarfs born with a mass less than $0.67\,M_\odot$ cannot reach the Chandrasekhar limit. Since SNe Ia are quite rare events, this lower bound does not seem too restrictive. However, for initial masses in the range below $0.8\,M_\odot$, the constraints on the initial mass of the secondary and the orbital period are very tight. From binary population synthesis, Han and Podsiadlowski found a birth rate of roughly 10^{-3} type Ia supernovae in the Milky Way, which falls slightly short of the observationally estimated rate of at least $3\cdot10^{-3}\,\mathrm{yr}^{-1}$. As for the WD+RG channel, they inferred a negligible contribution to the Galactic supernova rate. Fedorova et al. [2003] presented an even more conservative estimate of $0.2\cdot10^{-2}\,\mathrm{yr}^{-1}$ from both channels in the SD scenario. This would clearly be insufficient to account for the observed supernova occurrence rate. Another problem which sheds doubt on the exclusiveness of the SD scenario is the lack of observational evidence for binary star systems with a substantially massive white dwarf component. So far only a single candidate for a type Ia supernova has been discovered, the recurrent nova *U Scorpii*. According to new radial velocity measurements by Thoroughgood et al. [2001], the white dwarf primary has a mass very close to the Chandrasekhar limit and is likely to undergo a thermonuclear supernova explosion in less than a million years. A further observational obstacle is the lack of hydrogen in the spectra of type Ia supernovae, actually, the defining feature. If there was a companion star, it should contaminate the supernova ejecta with hydrogen and possibly helium. An additional source of hydrogen could be residuals from a CE phase. However, evidence for hydrogen has only very recently been found in the single case of supernova 2002ic [Hamuy et al., 2003].

Of course, alternative progenitor scenarios have been proposed as well. One of those is the double degenerate (DD) scenario, in which two white dwarfs merge to a supercritical degenerate mass which explodes. The obvious difficulty encountered with the DD scenario is the remarkable observational homogeneity of type Ia supernovae regarding the explosion energy and the produced mass of ^{56}Ni. Apart from that, the merging of two white dwarfs could also result in the gravitational collapse to a neutron star [cf. Hillebrandt and Niemeyer, 2000, Sections 4.1 & 5.3]. Nevertheless, the DD scenario might explain some peculiar supernovae such as the extraordinarily bright SN 1991T which is hard to accommodate within the consensus model. Another possibility put forward is the detonation of an accreted degenerate helium layer, which might ignite the C+O core of a sub-Chandrasekhar mass white dwarf. In this case, burning proceeds from the outer helium layer inwards. However, predictions deduced from this scenario are in conflict with several observational properties of type Ia supernovae [cf. Hillebrandt and Niemeyer, 2000, Section 5.2].

1.2.2 Ignition and Explosion Models

The most poorly understood aspect of the SD scenario is the initiation of the deflagration phase, which is expected to occur at a temperature of roughly 10^9 K and a mass density around $2 \cdot 10^9$ g cm^{-3}. Once the mass of a C+O white dwarf approaches the Chandrasekhar limit, thermonuclear heating surpasses cooling by neutrinos and the core goes through a phase of strong convection. The convective turn-over time τ_B becomes ever smaller as the rate of thermonuclear reactions rises due to the increasing temperature. At a certain point, the time scale of thermonuclear burning becomes so small that a phase transition in the nuclear equilibria is initiated and microscopically thin, conductively propagating burning zones are formed. Within the flames, carbon and oxygen is completely burned to intermediate mass elements, which in turn are processed to ^{56}Ni and α particles by a multitude of reactions. The term *ignition* refers to the initial formation of flames rather than the gradual onset of thermonuclear reactions prior to the deflagration. Since the density contrast between fuel and the burning products is typically much more pronounced than the thermal density fluctuations in the convective regime, the initially formed bubbles of thermonuclear ash are lifted by buoyancy at a much higher speed than the convective plumes.

Phenomenological 1D models of the explosion appeared in the nineteen eighties, in particular, the well known deflagration model W7 by Nomoto et al. [1984]. Actually, this model is still in use for radiation transport calculations. For W7, the flame propagation speed is a free parameter which is adjusted such that observational properties can be fit. A decade later, attempts towards multidimensional computations were made. Assuming some arbitrary initial burning zones, these models evolve the hydrodynamical equations in combination with a simplified reaction network and some numerical treatment of flame propagation. As with the early 1D models, two distinct branches of models have been developing since then. On the one hand, Khokhlov [1991] picked up the idea of a *delayed detonation* (DDT), whereas Niemeyer and Hillebrandt [1995b] began with *pure deflagration* models. As discussed in Section 1.1.3, the transition from deflagration to a detonation is supposed to occur once the density of the expanding white dwarf has dropped to roughly 10^7 g cm^{-3}. Then the detonation would rapidly consume the remaining carbon and oxygen and enhance the explosion energy significantly. However, the mechanism which could trigger a detonation remains dubious. In deflagration models, on the other hand, turbulence is highlighted as the crucial factor producing enough energy for an explosion and the correct distribution of elements. Apart from these two variants of the explosion of a Chandrasekhar-mass white dwarf, the originally proposed *prompt detonation* model was dismissed, because no elements of intermediate mass such as silicon were produced. This was definitely contradicting observations [cf. Steinmetz et al., 1992]. Yet another flavour of the DDT model assumes a *pulsational delayed detonation*, with alternating detonation phases followed by a recollapse which triggers a further detonation, possibly, with re-ignition of deflagration in between. By now, however, this appears to be a rather unlikely scenario.

The main challenge encountered with the pure deflagration model is the very small propagation speed of the flame fronts, especially, once the white dwarf has expanded significantly and the density drops. As discussed in Section 1.1.3, turbulence aids to the acceleration of the burning process. As the mechanism producing turbulence

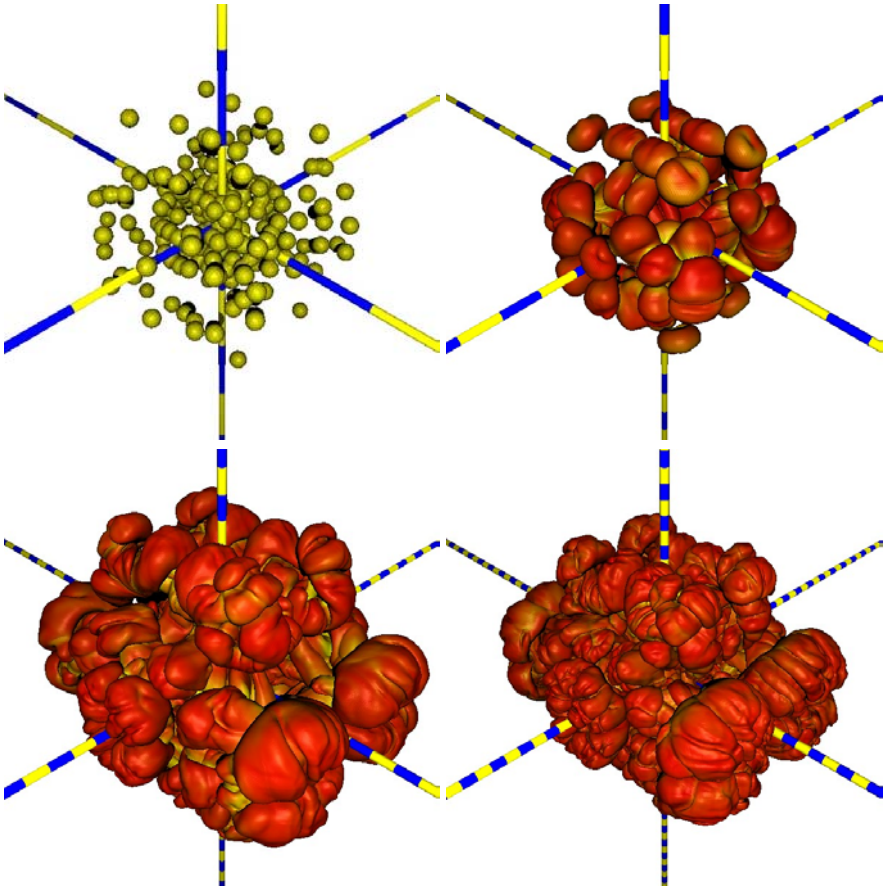

Figure 1.3: Evolution of the flame front in a 3D LES of a thermonuclear supernova with random multi-point ignition. The numerical resolution is 768^3 [taken from Niemeyer, Reinecke, Travaglio, and Hillebrandt, 2003].

is essentially three-dimensional, any sensible modelling of turbulent deflagration requires 3D computations. It is instructive to note that the early 2D deflagration models, which were computed by Niemeyer and Hillebrandt [1995b], Niemeyer et al. [1996] and Reinecke et al. [1999], in most cases failed to produce sufficient energy for an explosion. Apart from the deficiences in the modelling of turbulence, it was noted that the explosion energy sensitively depends on initial conditions. With a new generation of massively parallel supercomputers becoming accessible at the turn of the millennium, high-resolution 3D simulations of thermonuclear supernovae became feasible and, indeed, a total energy release on top of the gravitational binding energy of about $5 \cdot 10^{50}$ erg was achieved [Reinecke, Hillebrandt, and Niemeyer, 2002]. The evolution of the flame front in a recent 3D simulation is shown in Figure 1.3. With regard to the explosion energy and nucleosynthesis, the results are still not fully satisfactory, but at least it appears that the 3D deflagration models are on the right track [Niemeyer et al., 2003].

Independent simulations with adaptive mesh refinement (AMR) were carried out by Gamezo et al. [2003]. The most important difference in the methodology of the

two groups is the determination of the turbulent flame speed. Gamezo et al. calculated s_t from the asymptotic rise velocity associated with the RT instabilities, whereas a subgrid scale turbulence energy model was used by Reinecke et al. The first method is based upon the assumption that turbulent velocity fluctuations are mostly produced by buoyancy, even at the cut-off length scales of typical contemporary simulations. According to the discussion of turbulent deflagration in Section 1.1.3, however, this assumption seems very questionable. On the other hand, if SGS velocity fluctuations are indeed dominated by the turbulence cascade, in agreement with Kolmogorov's self-similarity theory, a subgrid scale model which accounts for the turbulent interactions between resolved and subgrid scales has to be implemented. However, the model utilised by Reinecke et al. is largely *ad hoc*. In any case, the subgrid scale model must be sound even in the extremely complex scenario of a thermonuclear supernova explosion. Actually, none of the aforementioned approaches meets this requirement, as will be demonstrated in this Thesis.

1.2.3 Lightcurves and Spectra

The first observed supernova which was possibly of type Ia is Kepler's supernova of AD 1604. It was discovered several days before maximum light and there is a remarkably accurate record of the variation in brightness over about one year. This made the reconstruction of the light curve possible [cf. Green and Richardson, 2003]. Since then, no type Ia supernova within the Galaxy has been observed. Today the light curves of type Ia supernovae are characterised by several phases, as described by Leibundgut [2000]. The earliest detections of type Ia supernovae were made about 16 days before the peak brightness. In the beginning, there is a steep rise of luminosity. In the maximum phase, $M_V \approx -19.5$ corresponding to roughly 10^{10} times the luminosity of the sun. The distance modulus required to calibrate the luminosity is usually determined by Cepheids. The spectra near maximum brightness are dominated by P-Cygni lines of elements in the intermediate mass range, particularly, Si, Ca and Mg, which indicate ejection velocities in the range $1.0 \ldots 1.5 \cdot 10^4\,\mathrm{km\,s^{-1}}$. There is also a second maximum in the infrared and red light between 20 and 40 days after the first maximum. Following a rapid decrease of luminosity past the maximum, the lightcurves finally enter a phase of exponential decline, with a rate that is roughly the same for most type Ia supernovae. During the decline, forbidden Fe and Co lines become increasingly prominent. From the relative intensities of these lines, it can be inferred that the tail of the light curve is powered by the radioactive decay of ^{56}Co, which in turn stems from the quickly decaying ^{56}Ni [cf. Hillebrandt and Niemeyer, 2000, Section 2.1].

The rather homogeneous properties of type Ia supernovae and their extraordinary brightness add up to a good cosmological distance indicator. According to Branch [1998], a one-parameter representation is sufficient to normalise the absolute brightness. Basically, less luminous events appear redder, and the light curve displays a faster post-maximum decline. Moreover, the ejection velocities inferred from the lines are smaller. A customary method of accounting for these variations is to calculate the decline rate Δm_{15}, i. e., the change in the magnitude over fifteen days in the aftermath of the peak luminosity [Phillips, 1993]. As a particular important application, the Hubble constant can be measured [Branch, 1998; Riess and Filippenko, 2001; Perlmutter and Schmidt, 2003]. In Figure 1.4, the current Hubble diagram for SNe Ia in the lo-

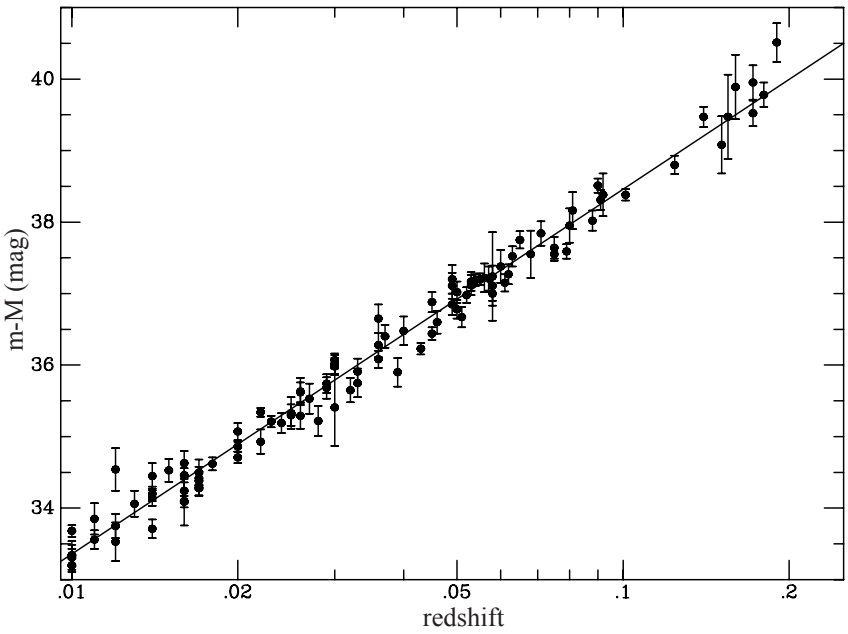

Figure 1.4: Hubble diagram for observed type Ia supernovae in the local universe [taken from Perlmutter and Schmidt, 2003].

cal universe is plotted. Moreover, data obtained by the Supernova Cosmology Project [Perlmutter et al., 1999] and the High-z Supernova Search [Schmidt et al., 1998] for the first time provided evidence that the expansion of the Universe is accelerating rather than decelerating. The luminosities of distant type Ia supernovae in a sample taken up to a redshift $z \approx 1$ appear too dim to be reconcilable with a matter-dominated universe. The fits of high redshift SN Ia data for several cosmological models are shown in Figure 1.5. In consequence, there must be a non-vanishing contribution from a *cosmological constant* or *dark energy*. This is, perhaps, both the most thrilling and the most puzzling discovery in contemporary astrophysics. In combination with measurements of the cosmic microwave background anisotropies and results from large-scale structure surveys, the composition of the universe is constraint to be about 30% matter and 70% dark energy [Perlmutter, 2003; Carroll, 2003]. Although the results have been confirmed recently by Tonry et al. [2003] and reddening by dust as well as evolutionary effects are quite likely ruled out as sources of systematic errors, it has also become clear that type Ia supernovae are actually more diverse than originally assumed [Leibundgut and Suntzeff, 2003; Ruiz-Lapuente, 2003; Filippenko, 2003; Benetti et al., 2003]. Apart from predicting light curves and spectral features, understanding the physical origin of variations in luminosity, the amount of produced nickel and the different decline rates is therefore the major challenge for the theory of thermonuclear supernovae.

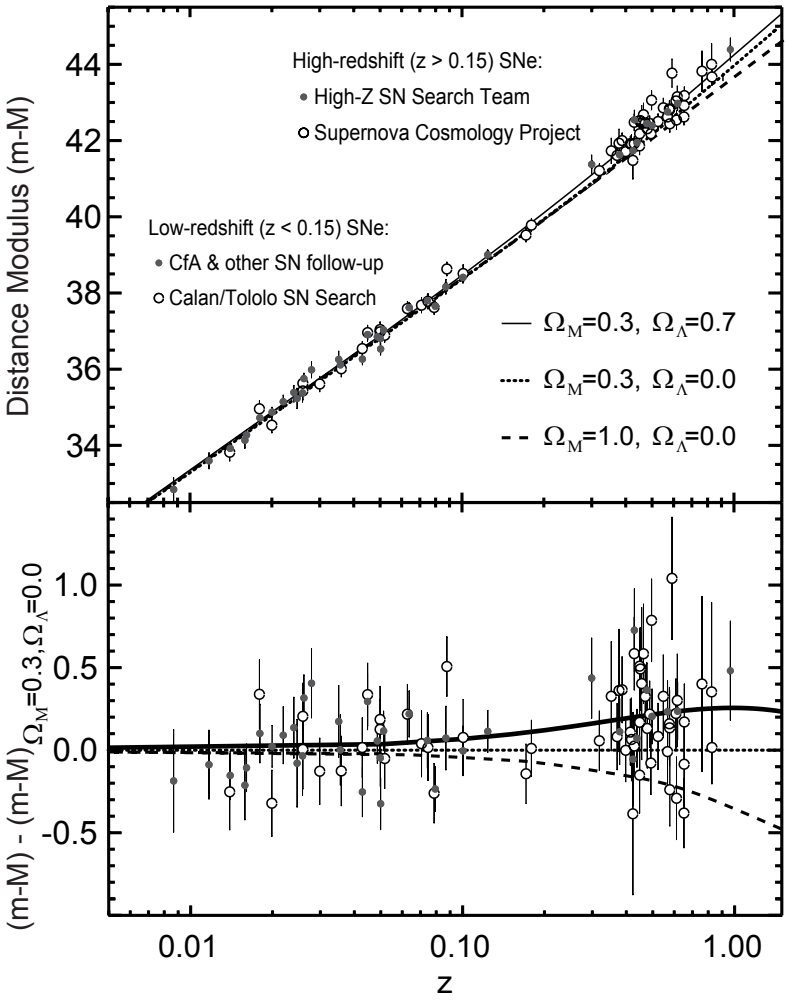

Figure 1.5: Luminosities of type Ia Supernovae, including those found at high redshifts, and the corresponding fits for three different cosmological models. The best agreement is found in the case of a flat universe with a non-zero cosmological constant [taken from Perlmutter and Schmidt, 2003].

Chapter 2

Forced Isotropic Turbulence

Fluid motion forces vortices to stretch, and a stretching vortex must fold to accommodate an increasing length in a fixed volume. To the extent that the flow is scaling, I conjecture the vortex tends toward a fractal.

B. B. Mandelbrot, **The fractal geometry of nature**

Telperion the one was called in Valinor, and Silpion, and Ninquelótë, and many other names.

J. R. R. Tolkien, **The Silmarillion**

The direct numerical simulation (DNS) of isotropic turbulence serves as a kind of virtual experiment for the study of various properties of turbulent flows. Typically, the compressible flow in a cubic domain subject to periodic boundary conditions is computed. The fluid is set into motion by a random force field and, if the forcing is statistically isotropic and stationary, the outcome is an almost perfect realisation of the mathematical paradigm of homogeneous and isotropic turbulence. Although such a scenario is highly artifical and could hardly be produced in any laboratory experiment, it is still a valuable utility to infer fundamental properties of turbulence, to study the behaviour of the numerical scheme in use and to evaluate structural information, which might be helpful in the context of subgrid scale modelling. In the first part of this Chapter, the methodology of computing numerical representations of isotropic turbulence is discussed. Then results from several high-resolution 3D simulations regarding statistics, flow structure, energy spectra and numerical dissipation are presented, and thereby a rich phenomenology of turbulence emerges. Each computation was carried out on the Hitachi SR-8000 supercomputer of the Leibniz Computing Center, with domain-decomposition using 512 processors in parallel.

2.1 Dynamical Equations and Spectral Representation

The hydrodynamical problem can be formulated as follows. There is no energy source except for a stochastic force field $\boldsymbol{a}(\boldsymbol{x}, t)$, which acts uniformly on the fluid. Forces due

to self-gravity and also energy flux due to thermal conduction are neglected. Moreover, we shall assume that viscous dissipation of physical origin is negligible compared to dissipation produced by the numerical scheme for solving the dynamical equations. One can formally account for this effect by including a putative *numerical damping* term $\mathfrak{R}(\boldsymbol{x}, t)$ in place of the viscous dissipation term in the momentum equation. The stripped conservation laws for momentum (1.11) and the total energy (1.12) are therefore

$$\frac{\partial}{\partial t}\rho v_i + \frac{\partial}{\partial x_k}\rho v_i v_k = -\frac{\partial}{\partial x_i}P + \rho a_i + \mathfrak{R}_i, \tag{2.1}$$

$$\frac{\partial}{\partial t}E + \frac{\partial}{\partial x_k}E v_k = \rho a_k v_k. \tag{2.2}$$

The pressure P and temperature T are determined for given E_{int} via the equation of state (EOS) of degenerate matter, which is outlined in Section 1.1.1. In the following, two numerical issues are discussed. First the numerical scheme is outlined, which is used to solve the above set of dynamical equations, and then some questions regarding the spectral representation of field quantities subject to periodic boundary conditions (BC) are addressed.

2.1.1 The Piece-Wise Parabolic Method

Contrary to the common approach of simulating homogeneous turbulence, which is the *pseudo-spectral method* of advancing the Fourier modes of the velocity field according to the Navier-Stokes equation in spectral space, we apply a finite-volume method to solve the dynamical equations in physical space, namely, the *piece-wise parabolic method* (PPM)[1]. Our implementation of the PPM originated from Fryxell, Müller, and Arnett [1989] and was adopted by Reinecke [2001] in a new modular Fortran 90 code featuring MPI for massively parallel computation on high-end platforms. We named this code Telperion to distinguish it from the original Prometheus implementation by Fryxell et al., which has been evolving into various branches by now.

The PPM is a finite-volume scheme based on the Godunov method for solving the Riemann problem at the cell interfaces, with higher-order interpolation between the cell-averaged variables. In addition, shocks are detected and treated with special techniques. Thereby, oscillations and smearing out over several cells are inhibited. The PPM is thus fully applicable to compressible and possibly supersonic flows, which makes this method especially attractive for astrophysical applications. The ability of the PPM to handle shocks particularly well is certainly not that important in the context of thermonuclear deflagration, because the Mach numbers are typically small (at least with respect to the bulk motion) and the flow remains strictly subsonic. Nevertheless, the significant density contrast between nuclear fuel and processed material makes the use of a hydrodynamical code applicable to compressible flows mandatory. Here we will discuss turbulence at various Mach numbers, ranging from subsonic to partially supersonic flows.

A crucial point in the application of the PPM is *numerical dissipation*. In a way, the usual categories of DNS versus large-eddy simulation (LES) are merged in the case

[1] An introduction to pseudo-spectral methods is given, for instance, in Pope [2000, Chapter 9]. The PPM was first proposed by Colella and Woodward [1984].

of a dissipative finite-volume scheme like the PPM. In this case, dissipation terms of purely numerical origin enter the conservation laws, which mimic on larger scales the action of viscous dissipation on smaller scales. Consequently, when the hydrodynamical equations are solved with the PPM, in fact, the Euler equation with an additional numerical dissipation term is evolved (see equation 2.1). The underlying assumption is that the damping force $\mathfrak{R}$ smoothes the flow on scales $l \sim \Delta$, where Δ is the size of the finite-volume cells. For scales $l \gg \Delta$, on the other hand, $\mathfrak{R}$ is negligible compared to the non-linear advection term and the forcing term, respectively. If, in addition, those scales which are largely unaffected by numerical dissipation encompass at least a fraction of the inertial subrange, then we can say that the numerically computed flow is a fair representation of the physical flow on scales much larger than *Delta*. Indeed, this is a tight constraint as we will see in Section 2.5. In this respect, applying the PPM in a hydrodynamical simulation is considered to be equivalent to a LES, in which the Navier-Stokes equations (NSE) with explicit subgrid scale dissipation are solved. If numerical dissipation is the exclusive source of energy dissipation, then we shall speak of a *direct numerical simulation*, regardless of whether the dissipation length scale is of the same order or much larger than the physical Kolmogorov scale. The term large-eddy simulation, on the other hand, will be used for any kind of computation including a subgrid scale model. In particular, this applies to simulations of turbulent burning, as the propagation speed of the flame front is determined by the unresolved part of the kinetic energy.

There is a long record of publications on testing the PPM in simulations of compressible turbulence. Particularly, in the series of papers by Porter, Pouquet, and Woodward [1992], Porter et al. [1994], Porter and Woodward [1994], Porter et al. [1998] as well as Sytine et al. [2000] a wealth of results from simulations of isotropic turbulence in an isothermal perfect gas with resolutions up to 1024^3 cells is discussed. All of these simulations are restricted to the case of decaying turbulence, where the fluid is not continually driven but only some initial perturbations at low wave numbers are set and the computation is advanced merely over a couple of large-eddy turnovers. Sytine et al. especially advocated the key idea of using DNS with the PPM as alternative to applying schemes based on the NSE. Convergence tests presented in their paper seem to indicate that a good approximation to the limit of infinite Reynolds number can be achieved with the PPM on grids of about 512^3 or more cells.

Although a slightly reduced resolution of 432^3 cells was used for the sake of optimal computational performance, the simulations which are presented here introduce several new features. Firstly, energy injection through a stochastic force field was applied over several large-eddy turnover times, starting with a uniform fluid at rest. Thereby, the complete evolution was computed, beginning with the production of turbulence, which is followed by equilibration and then passes over into decay when the forcing ceases. Secondly, the spectral composition of the random force field was varied, in particular, the weights of solenoidal components, which set the fluid into rotational motion, relative to the dilatational components, which act as compressive forces. Thirdly, the full EOS applicable to degenerate C/O matter was used and a comparison between simulations with different mass densities allowed the discrimination of EOS-dependent effects. Apart from the computationally demanding Riemann solver for the PPM, it was mainly the computational cost of solving the complicated EOS in combination with very long simulation runs, typically, over several thousand

time steps, which necessitated the aforementioned moderation in spatial resolution.

2.1.2 Fourier Transforms of Periodic Dynamical Variables

For the composition of the stochastic force which drives the turbulent flow as well as the computation of energy spectra, the formulation of a spectral representation of force and velocity fields is indispensable. Since the equations of motion (2.1) and (2.2) are solved in a cubic domain subject to periodic BCs, some care has to be taken in the treatment of Fourier transforms. Obviously, the solution of these equations must be spatially periodic and, consequently, the resulting fields are not absolutely integrable. For this reason, Fourier transforms in the form of integrals over all space, as usually found in the literature, are non-existent. For a mathematically sound formulation one must recognise that the Fourier transform of a field which is periodic in space is a generalised function which, naturally, leads to discrete spectral modes.

Assuming periodicity in (x, y, z) with wavelengths X, Y and Z, the Fourier transform $\hat{q}(\boldsymbol{k}, t)$ of a field variable $q(\boldsymbol{x}, t)$ can be defined by a normalised volume integral,

$$\hat{q}(\boldsymbol{k}, t) = \int_0^Z \frac{\mathrm{d}z}{Z} \int_0^Y \frac{\mathrm{d}y}{Y} \int_0^X \frac{\mathrm{d}x}{X}\, q(\boldsymbol{x}, t) \exp(-\mathrm{i}\boldsymbol{k} \cdot \boldsymbol{x}). \tag{2.3}$$

The spatial region spanned by (X, Y, Z) is usually called the *fundamental cell* of the periodic function. Here we will call it the *fundamental domain* which seems more suitable in a computational context and avoids confusion with the finite-volume cells associated with numerical discretisation. The inverse Fourier transform which is consistent with the above definition of $\hat{q}(\boldsymbol{k}, t)$ is given by

$$q(\boldsymbol{x}, t) = \frac{XYZ}{(2\pi)^3} \int \mathrm{d}^3k\, \hat{q}(\boldsymbol{k}, t) \exp(\mathrm{i}\boldsymbol{k} \cdot \boldsymbol{x}). \tag{2.4}$$

Periodicity in physical space induces a dual structure in spectral space in the form of an equipartition into cells of volume $(2\pi)^3/XYZ$. Each of these cells is associated with a wave vector $\boldsymbol{k}_{jlm} = 2\pi(j/X, l/Y, m/Z)$. To that effect, any periodic function can be expressed as a *discrete* Fourier series, i. e.,

$$q(\boldsymbol{x}, t) = \sum_{j,l,m} \hat{q}_{jlm}(t) \exp(\mathrm{i}\boldsymbol{k}_{jlm} \cdot \boldsymbol{x}), \tag{2.5}$$

where the *Fourier modes* are given by

$$\hat{q}_{jlm}(t) = \int_0^1 \mathrm{d}\tilde{z} \int_0^1 \mathrm{d}\tilde{y} \int_0^1 \mathrm{d}\tilde{x}\, q(\boldsymbol{x}, t) \exp[-2\pi\mathrm{i}(j\tilde{x} + l\tilde{y} + m\tilde{z})], \tag{2.6}$$

with the dimensionless coordinates $\tilde{x}_i = x_i/X_i \in [0, 1]$. In order to consolidate the notion of a Fourier transform and the existence of discrete Fourier modes, $\hat{q}(\boldsymbol{k}, t)$ has to be identified with the following generalised function:

$$\hat{q}(\boldsymbol{k}, t) = \frac{(2\pi)^3}{XYZ} \sum_{jlm} \hat{q}_{jlm}(t) \delta(\boldsymbol{k} - \boldsymbol{k}_{jlm}). \tag{2.7}$$

By substitution into equation (2.4), it can be verified that the Fourier expansion (2.5) of $q(\boldsymbol{x}, t)$ is recovered. We will find this identity helpful when it comes to the question of calculating an energy spectrum function from discrete Fourier modes.

2.2 Stochastic Forcing

The simulation of turbulent flows with homogeneous statistics both in space and time utilises random force fields. In mathematical terms, the temporal evolution of the driving force at any spatial point is determined by a *random function* or *stochastic process*. It is actually easier to compose these random fields in spectral space, in which additional constraints such as vanishing divergence can be invoked. Apart from spatial homogeneity, the evolution of the stirring field should be statistically stationary. If this is the case, the flow will asymptotically approach an equilibrium state, in which production of turbulence is balanced by dissipation. To that end, the spectral modes of the stirring field are modelled by a certain flavour of *diffusive* stochastic processes, the so-called *Ornstein-Uhlenbeck process*. In order to compose solenoidal fields, which produce rotational fluid motion, one has to modify the spectral modes by means of projection operators, a method that was suggested by Eswaran and Pope [1988] and, for example, applied by Niemeyer et al. [1999].

2.2.1 The Ornstein-Uhlenbeck Process

The type of stochastic process which can be utilised to model a physically reasonable random force is constrained by several mathematical properties. To begin with, let us consider the simplest case of a scalar random force $f(t)$. Firstly, the statistics of the process should be completely determined by some initial statistics at time t_0. More precisely, given the probability distribution function $F(f(t); t|f(t_0); t_0)$ of $f(t)$ at time t conditioned on the value $f(t_0)$ at an earlier time t_0, we have a complete specification of the corresponding stochastic process. Such a process is called a *Markov process*. Secondly, the simplest assumption one can make about the statistics of the random function is that it is Gaussian. A fundamental Markov process which has Gaussian statistics is the *Wiener process* $\mathcal{W}_t(f)$ on a variable f, for which

$$\Delta_h \mathcal{W}_t = \mathcal{W}_{t+h} - \mathcal{W}_t = \mathcal{N}(0, h). \tag{2.8}$$

This means that the distribution of the increment $\Delta_h \mathcal{W}_t$ of the Wiener process over a time step h is normal with mean zero and variance equal to h. A realization $f(t)$ of $\mathcal{W}_t(f)$ is a path fluctuating around zero, where the magnitude of the fluctuations scales with their duration.

As for driving turbulence, a process with certain temporal correlation properties is is called for. This leads us to the more general concept of a *diffusion process* $\mathcal{D}_t(f)$, which is characterised as a Markov process with a *continuous* sample path and statistics that is specified by two functions $a(f, t)$ and $b(f, t)$, called the *drift coefficient* and the *diffusion coefficient*, respectively. Since $\lim_{h\to 0} \mathcal{N}(0, h) = 0$, any sample path of $\mathcal{W}_t$ is, in fact, continuous and the Wiener process is therefore a normalised diffusion process with $a(f, t) = 0$ and $b(f, t) = 1$. The infinitesimal increment $\mathrm{d}\mathcal{W}_t$ can formally be written as

$$\mathrm{d}\mathcal{W}_t = \mathcal{W}_{t+\mathrm{d}t} - \mathcal{W}_t = \mathcal{N}(0, \mathrm{d}t). \tag{2.9}$$

Using the Wiener process as building block, a general diffusion process can be defined by the following stochastic differential equation (SDE):

$$\mathrm{d}\mathcal{D}_t = a[\mathcal{D}_t, t]\mathrm{d}t + b[\mathcal{D}_t, t]\mathrm{d}\mathcal{W}_t = \mathcal{N}(a[\mathcal{D}_t, t]\mathrm{d}t, b^2[\mathcal{D}_t, t]\mathrm{d}t). \tag{2.10}$$

Yet another property we have to observe is statistical stationarity. The archetypical statistically stationary diffusion process is defined by

$$a(f,t) = -\frac{f}{t}, \qquad b^2(f,t) = \frac{2\sigma^2}{T}. \tag{2.11}$$

Substituting the above drift and diffusion coefficients, the SDE (2.10) becomes the *Langevin equation*

$$\mathrm{d}\mathcal{U}_t = -\mathcal{U}_t \frac{\mathrm{d}t}{T} + \left(\frac{2\sigma^2}{T}\right)^{1/2} \mathrm{d}\mathcal{W}_t. \tag{2.12}$$

The process $\mathcal{U}_t(f)$ is called the *Ornstein-Uhlenbeck process*. It has the conditional distribution function

$$F(f_2;t_2|f_1;t_1) = \mathcal{N}\left(f_1 \mathrm{e}^{-(t_2-t_1)/T}, \sigma^2\left[1-\mathrm{e}^{-2(t_2-t_1)/T}\right]\right). \tag{2.13}$$

This implies that T is the *autocorrelation time scale* of the Ornstein-Uhlenbeck process, i. e., given any value f_1 at time t_1, the memory of this value will be largely erased after an elapse of time $\sim T$. If $t_2 - t_1 \ll T$, on the other hand, there is a high probability that the change from f_1 to f_2 will be small.

The mean of $\mathcal{U}_t$ is given by $\langle\mathcal{U}_t\rangle = \langle\mathcal{U}_0\rangle e^{-t/T}$. Therefore, any information about the initial configuration is exponentially damped. Using the properties $\langle\mathcal{U}\mathrm{d}\mathcal{W}_t\rangle = 0$ (statistical independence) and $\langle\mathrm{d}\mathcal{W}_t^2\rangle = \mathrm{d}t$ (variance equal to time increment), the infinitesimal change of the second moment of this process is given by

$$\begin{aligned}
\langle\mathcal{U}_{t+\mathrm{d}t}^2\rangle &= \langle\mathcal{U}_t^2\rangle + 2\langle\mathcal{U}_t\mathrm{d}\mathcal{U}_t\rangle + \langle\mathrm{d}\mathcal{U}_t^2\rangle \\
&\simeq \langle\mathcal{U}_t^2\rangle - \frac{2}{T}\langle\mathcal{U}_t^2\mathrm{d}t\rangle + \frac{2\sigma^2}{T}\langle\mathrm{d}\mathcal{W}_t^2\rangle \\
&= \langle\mathcal{U}_t^2\rangle + 2\left(-\langle\mathcal{U}_t^2\rangle + \sigma^2\right)\frac{\mathrm{d}t}{T}.
\end{aligned}$$

This is equivalent to the first-order linear DE

$$\frac{\mathrm{d}}{\mathrm{d}t}\langle\mathcal{U}_t^2\rangle = \frac{2}{T}\left(-\langle\mathcal{U}_t^2\rangle + \sigma^2\right) \tag{2.14}$$

which has the solution

$$\langle\mathcal{U}_t^2\rangle = \sigma^2 + \left(\langle\mathcal{U}_0^2\rangle - \sigma^2\right)e^{-2t/T}. \tag{2.15}$$

If $\langle\mathcal{U}_0^2\rangle = \sigma^2$, then $\langle\mathcal{U}_t^2\rangle = \sigma^2$ for all t. Otherwise, the deviation of $\langle\mathcal{U}_t^2\rangle$ from σ^2 is exponentially damped on a time scale $T/2$. In conclusion, the Ornstein-Uhlenbeck process is asymptotically stationary with $\langle\mathcal{U}_\infty^2\rangle = \sigma^2$.

2.2.2 Spectral Representation of the Force Field

In order to construct a vectorial random force field $\boldsymbol{a}(\boldsymbol{x},t)$ in physical space, we first determine the Fourier models $\hat{\boldsymbol{a}}_{jlm}(t)$. One can think of each mode as being the realization of a three-component complex stochastic process. In this Section, some of the

equations are formulated, for brevity, in terms of the components of the Fourier transform, $\hat{\boldsymbol{a}}(\boldsymbol{k},t)$. The evolution of $\hat{\boldsymbol{a}}(\boldsymbol{k},t)$ is given by a three-dimensional generalisation of the SDE (2.12) for scalar Ornstein-Uhlenbeck process:

$$\mathrm{d}\hat{\boldsymbol{a}}(\boldsymbol{k},t) = -\hat{\boldsymbol{a}}(\boldsymbol{k},t)\frac{\mathrm{d}t}{T} + F_0 \sum_{jlm} \left(\frac{2\sigma^2(\boldsymbol{k})}{T}\right)^{1/2} \delta(\boldsymbol{k}-\boldsymbol{k}_{jlm})\boldsymbol{P}_\zeta(\boldsymbol{k})\cdot \mathrm{d}\boldsymbol{\mathcal{W}}_t. \tag{2.16}$$

Recall that, according to equation (2.7), the Fourier transform is a generalised function. This is the origin of Dirac delta in the stochastic diffusion term on the right-hand side.

The functional form of the dimensionless variance $\sigma^2(\boldsymbol{k})$ determines the symmetries of the force field. In particular, if σ depends on the wave number $k = |\boldsymbol{k}|$ only, then the resulting stochastic force field will be *isotropic* in physical space. Moreover, it is usually assumed that the spectral density of turbulence energy for the smallest wave numbers within the energy containing range has the asymptotic form $E(k,t) \propto k^4$, which would imply $\sigma(\boldsymbol{k}) \propto k^2$. On the other hand, for wave numbers $k \gg k_0$, where k_0 is the characteristic scale of turbulence production, $\sigma(\boldsymbol{k})$ should decrease exponentially. Combining these two asymptotic expressions, we obtain $\sigma(\boldsymbol{k}) = \sigma_0(k/k_0)^2\mathrm{e}^{-k/k_0}$. However, the exponential tail of this function poses numerical difficulties, because one would require a spectral grid of the same resolution as the spatial grid and, consequently, the computation of the inverse Fourier would become prohibitively expensive. This can be avoided if the stochastic force spectrum is confined to a narrow interval of wave numbers corresponding to the largest scales of the system and is set identically zero for all wave numbers outside this interval. One possibility would be to use a certain cut-off wavenumber without altering the functional form of the spectrum. But here we prefer a modified spectral profile which is purely polynomial:

$$\sigma(\boldsymbol{k}) = \begin{cases} \sigma_0(k/k_0)^2\left[1-(k/k_0)^2\right] & \text{if } k \in [0, 2k_0], \\ 0 & \text{otherwise.} \end{cases} \tag{2.17}$$

Introducing the parameter $\alpha = k_0 X/2\pi$ which must be an integer, the number of non-zero modes is only $(2\alpha)^3$. This is by far less than the number of cells in the spatial grid. Making use of this fact, the inverse Fourier transform can be implemented very efficiently.

The symmetric tensor $\boldsymbol{P}_\zeta(\boldsymbol{k})$ is defined by the linear combination of the projection operators perpendicular and parallel to the wave vector. The components of $\boldsymbol{P}_\zeta(\boldsymbol{k})$ can be expressed as

$$(P_{ij})_\zeta(\boldsymbol{k}) = \zeta P^\perp_{ij}(\boldsymbol{k}) + (1-\zeta)P^\parallel_{ij}(\boldsymbol{k}) = \zeta\delta_{ij} + (1-2\zeta)\frac{k_i k_j}{k^2}, \tag{2.18}$$

where the spectral weight ζ determines whether the resulting stochastic force field is purely solenoidal or dilatational or a combination of both. This can be seen by taking, respectively, the divergence and the rotation of the dynamical equation in spectral space.

- The dilatational part of the stochastic force field is obtained by contracting equation (2.16) with the wave vector:

$$\boldsymbol{k}\cdot\mathrm{d}\hat{\boldsymbol{a}}(\boldsymbol{k},t) = -\boldsymbol{k}\cdot\hat{\boldsymbol{a}}(\boldsymbol{k},t)\frac{\mathrm{d}t}{T} + (1-\zeta)F_0 \sum_{jlm} \left(\frac{2\sigma^2(\boldsymbol{k})}{T}\right)^{1/2} \delta(\boldsymbol{k}-\boldsymbol{k}_{jlm})\boldsymbol{k}\cdot\mathrm{d}\boldsymbol{\mathcal{W}}_t. \tag{2.19}$$

In the case $\zeta = 1$, the contracted diffusion term vanishes and the stochastic force field has asymptotically zero divergence, i. e. it becomes purely *solenoidal* in the stationary regime. If $\zeta < 1$, there are components of the stochastic force field which produce compressive forces in physical space. One can see from the above equation that the ratio of the compressive or *dilatational* components to the solenoidal components is of the order $(1 - \zeta)$.

- On the other hand, taking the cross-product yields

$$\boldsymbol{k}\times \mathrm{d}\hat{\boldsymbol{a}}_l(\boldsymbol{k},t) = -\boldsymbol{k}\times\hat{\boldsymbol{a}}_l(\boldsymbol{k},t)\frac{\mathrm{d}t}{T} + \zeta F_0 \sum_{jlm}\left(\frac{2\sigma^2(\boldsymbol{k})}{T}\right)^{1/2} \delta(\boldsymbol{k}-\boldsymbol{k}_{jlm})\boldsymbol{k}\times \mathrm{d}\boldsymbol{\mathcal{W}}_t. \quad (2.20)$$

This equation demonstrates that in the case $\zeta = 0$ a completely rotation-free force field subject to the initial condition $\boldsymbol{k} \times \hat{\boldsymbol{a}}(\boldsymbol{k}, 0) = 0$ is obtained, i. e., a purely dilatational initial field remains dilatational. If the initial field has solenoidal components, they are damped out exponentially on the time scale T and, eventually, the field becomes purely dilatational as well.

Since different Fourier modes are completely uncorrelated, it follows that the mean square of $\hat{\boldsymbol{a}}_{jlm}(t)$ in the limit of $t/T \gg 1$ becomes

$$\langle \hat{\boldsymbol{a}}_{jlm}(t) \cdot \hat{\boldsymbol{a}}_{jlm}(t)\rangle \simeq \frac{1}{2}F_0^2\sigma^2(\boldsymbol{k}_{jlm})|P_\zeta(\boldsymbol{k}_{jlm})|^2 \quad (2.21)$$

$$= (1 - 2\zeta + 3\zeta^2)F_0^2\sigma^2(\boldsymbol{k}_{jlm}), \quad (2.22)$$

where $|P_\zeta|^2 = 2(P_{ij})_\zeta(P_{ij})_\zeta$ is the total contraction of the projection tensor. However, it is important to bear in mind that only a half-set of the Fourier modes can be evolved randomly, while the other half-set is determined by the constraint that each mode $\hat{\boldsymbol{a}}_{jlm}(t)$ must be Hermitian conjugate with respect to the wave number $k_0 = 2\pi\alpha/X$. Otherwise the corresponding physical force $\boldsymbol{a}(\boldsymbol{x}, t)$ would fail to be real. In consequence, we choose the normalisation

$$\sum_{jlm}\sigma^2(\boldsymbol{k}_{jlm}) = \frac{1}{2}, \quad (2.23)$$

with $j, l, m \in \{0, 1, \ldots, 2\alpha\}$. Summing up equation (2.21) for all modes, one obtains

$$\sum_{jlm}\langle \hat{\boldsymbol{a}}_{jlm}(t) \cdot \hat{\boldsymbol{a}}_{jlm}(t)\rangle \simeq (1 - 2\zeta + 3\zeta^2)F_0^2. \quad (2.24)$$

Let us now assume that the stochastic force field is identically zero for $t < 0$, and then it is set to the initial configuration

$$\hat{\boldsymbol{a}}(0, \boldsymbol{k}_{jlm}) = F_0\left(\frac{2\sigma^2(\boldsymbol{k}_{jlm})}{T}\right)^{1/2} \boldsymbol{P}_\zeta(\boldsymbol{k}_{jlm}) \cdot \boldsymbol{\mathcal{N}}_{jlm}(0, 1). \quad (2.25)$$

Here $\boldsymbol{\mathcal{N}}_{jlm}(0, 1)$ is a complex random three-vector for each spectral cell, where both the real and the imaginary part of each component are distributed normally, with mean zero and variance unity. In this case, the stochastic force process immediately starts in the

statistically stationary regime at $t = 0$. The subsequent evolution can be numerically calculated, based upon the conditional distribution function (2.13) of the Ornstein-Uhlenbeck process. Suppose, $\hat{\boldsymbol{a}}(t, \boldsymbol{k})$ is known at time t. Then $\hat{\boldsymbol{a}}(t + \delta t, \boldsymbol{k})$ can be approximated for a finite time step $\delta t \ll T$ in the following way:

$$\begin{aligned}\hat{\boldsymbol{a}}(t + \delta t, \boldsymbol{k}_{jlm}) \simeq \hat{\boldsymbol{a}}(t, \boldsymbol{k}_{jlm}) \underbrace{\mathrm{e}^{-\delta t/T}}_{\simeq 1-\delta t/T} \\ + F_0 \sigma(\boldsymbol{k}_{jlm}) \underbrace{\sqrt{1 - \mathrm{e}^{-2\delta/T}}}_{\simeq (2\delta t/T)^{1/2}} \boldsymbol{P}_\zeta(\boldsymbol{k}_{jlm}) \cdot \boldsymbol{\mathcal{N}}_{jlm}(0, 1).\end{aligned} \tag{2.26}$$

Implementing this equation with a Gaussian pseudo-random number generator, the Fourier modes of the force field can be advanced for each time step in a simulation.

2.2.3 The Physical Stochastic Force Field

In terms of the discrete stochastic Fourier modes $\hat{\boldsymbol{a}}_{jlm}(t)$, the force field $\boldsymbol{a}(\boldsymbol{x}, t)$ in physical space is given by

$$\boldsymbol{a}(\boldsymbol{x}, t) = \sum_{jlm} \hat{\boldsymbol{a}}_{jlm}(t) \exp\left[-\frac{2\pi \mathrm{i}}{\alpha L}(jx + ly + mz)\right], \tag{2.27}$$

where $j, l, m \in \{0, 1, \ldots, 2\alpha\}$. Utilising operator splitting, the source terms in the conservation laws (2.1) and (2.2) are numerically approximated by means of a simple Euler-forward scheme:

$$\delta \boldsymbol{v}^{(\mathrm{f})}(\boldsymbol{x}, t) \simeq \boldsymbol{a}(\boldsymbol{x}, t)\delta t, \tag{2.28}$$

$$\delta e^{(\mathrm{f})}_{\mathrm{kin}}(\boldsymbol{x}, t) \simeq \boldsymbol{v}(\boldsymbol{x}, t) \cdot \boldsymbol{a}(\boldsymbol{x}, t)\delta t + \frac{1}{2}|\boldsymbol{a}(\boldsymbol{x}, t)|^2 \delta^2 t, \tag{2.29}$$

where $\delta \boldsymbol{v}^{(\mathrm{f})}$ is the virtual displacement of the velocity caused by the acceleration $\boldsymbol{a}$ and the corresponding change in kinetic energy per unit mass is $\delta e^{(\mathrm{f})}_{\mathrm{kin}}$. Of course, this treatment is purely kinetic and does not account for changes of the mass density within the time step δt. Nevertheless, it seems to be a sensible approximation, because the stochastic force field acts on length scales L much larger than the size of the numerical cells and on time scales of the order $T \gg \delta t$.

According to Parseval's theorem, the ensemble average of the second moment of the stochastic force field at time $t \geq 0$ is equal to the sum of the mean squared Fourier modes, i. e.,

$$\int_0^1 \mathrm{d}\tilde{z} \int_0^1 \mathrm{d}\tilde{y} \int_0^1 \mathrm{d}\tilde{x} \, \langle \boldsymbol{a}(\boldsymbol{x}, t) \cdot \boldsymbol{a}(\boldsymbol{x}, t) \rangle = \sum_{jlm} \langle \hat{\boldsymbol{a}}_{jlm}(t) \cdot \hat{\boldsymbol{a}}_{jlm}(t) \rangle. \tag{2.30}$$

Therefore, equation (2.21) implies that the root mean square of the stochastic force is given by

$$a_{\mathrm{rms}} = (1 - 2\zeta + 3\zeta^2)^{1/2} F_0. \tag{2.31}$$

The statistical homogeneity and stationarity of the stochastic force field also suggests that the stochastic force process is *ergodic*, i. e., temporal and spatial averaging of a

particular realisation of the process should approach the ensemble average in the limit of infinite time:

$$\lim_{n\to\infty} \frac{1}{nT} \int_0^{nT} \mathrm{d}t \int_0^1 \mathrm{d}\tilde{z} \int_0^1 \mathrm{d}\tilde{y} \int_0^1 \mathrm{d}\tilde{x}\, |\boldsymbol{a}(\boldsymbol{x}, t)|^2 \simeq (1 - 2\zeta + 3\zeta^2) F_0^2. \tag{2.32}$$

In particular, the spatially averaged stochastic force force is itself a stochastic process with an expectation value of $a_{\mathrm{rms}} = (1 - 2\zeta + 3\zeta^2)^{1/2} F_0$.

In the limiting case $\zeta = 1$, which corresponds to a purely solenoidal stochastic force, we have $a_{\mathrm{rms}} = \sqrt{2} F_0$. This is a consequence of projecting the normally distributed random modes produced by the three-component Wiener process perpendicular to the corresponding wave vectors, which leaves only two from three degrees of freedom. On the other hand, if the modes were projected parallel to the corresponding wave vectors, the complementary single degree of freedom would be retrieved. In his case, the force is purely dilatational and, indeed, equation (2.31) shows that $a_{\mathrm{rms}} = \sqrt{1} F_0$ if $\zeta = 0$. Since F_0 has the physical dimension of acceleration, it can be expressed as the *characteristic velocity* of the flow divided by the *integral time scale* of turbulence production. It seems reasonable to set this integral time scale equal to the correlation time scale T, which was introduced in equation (2.16), because changes of the stochastic force field are expected to evolve on the same time scale as large-scale velocity fluctuations (the so-called *large eddies*). Hence, linking the time scale T to the large-scale properties of the flow, we set $T = L/V$ and $F_0 = V/T = LV^2$, where V is the characteristic velocity of the large eddies associated with the integral length scale $L = 2\pi/k_0$.

2.3 Physical Scales

As a first step in setting up a DNS of turbulence, appropriate values of the fundamental scales have to be chosen as simulation parameters. Starting with a uniform fluid at rest, there are only five independent parameters. One possible set is given by the initial mass density ρ_0 and temperature T_0, the integral length scale L, the characteristic velocity V and, finally, the spectral weight of the solenoidal component of the driving force, ζ. Then ρ_0 and T_0 fix the pressure P_0, the internal energy E_0 and the speed of sound c_0 over the equation of state (EOS), the integral time scale T is trivially given by $T = L/V$, and the properties of the stochastic driving force are completely specified by the magnitude $F_0 = LV^2$, the characteristic wave number $k_0 = 2\pi/L$ and the weighing parameter ζ. For the structural properties of the flow, the main parameter of concern is the ratio V/c_0, which is the *characteristic Mach number*. Of course, V/c_0 only gives an order of magnitude for the actual average Mach number encountered in the flow, once turbulence is fully developed. In this Section, typical values of the state variables are considered, which follow from approximations for non-relativistic and extremely relativistic degeneracy, and appropriate normalisations are introduced, in order to obtain dimensionless parameters. Moreover, the admissible range for the integral length scale L is determined.

2.3.1 Mass Density

A characteristic density scale of degenerate matter in white dwarfs is given by the mass density for which the Fermi momentum p_F of the electrons is equal to $m_\mathrm{e}c$. The relativistic Fermi momentum can be expressed as $p_\mathrm{F} = (3\pi^2)^{1/3}\hbar n_\mathrm{e}^{1/3}$, where $n_\mathrm{e} = Y_\mathrm{F}\rho_0/m_\mathrm{B}$ is the number density of electrons, given a mean baryon mass m_B and a fraction Y_F of electrons per nucleon [cf. Shapiro and Teukolsky, 1983, Section 2.3]. Setting $m_\mathrm{B} \approx m_\mathrm{p}$, the mass density corresponding to $p_\mathrm{F} = m_\mathrm{e}c$ is given by

$$\rho_\mathrm{c} = \frac{m_\mathrm{p}}{3\pi^2 Y_\mathrm{F}}\left(\frac{m_\mathrm{e}c}{\hbar}\right)^3 = \frac{m_\mathrm{p}}{3\pi^2 Y_\mathrm{F}\lambda_\mathrm{e}^3}. \tag{2.33}$$

This is the *critical density*, for which the particles of a Fermi gas become relativistic. From the last expression, it can be seen that the mean particle separation at the critical density is of the order of the Compton wavelength $\lambda_\mathrm{e} \approx 3.862 \cdot 10^{-11}\,\mathrm{cm}$. Thus, we shall adopt the constant $m_\mathrm{p}(m_\mathrm{e}c/\hbar)^3 \approx 2.903 \cdot 10^7\,\mathrm{g\,cm^{-3}}$ as the fundamental density scale and define the dimensionless density parameter

$$\tilde{\rho}_0 = \left(\frac{\hbar}{m_\mathrm{e}c}\right)^3 \frac{\rho_0}{m_\mathrm{p}}. \tag{2.34}$$

Now the ratio of density to critical density can be written in the form $\rho_0/\rho_\mathrm{c} = 3\pi^2 Y_\mathrm{F}\tilde{\rho}_0$.

$\tilde{\rho}_0$	$\rho_0[\mathrm{g\,cm^{-3}}]$	ρ_0/ρ_c	degenerate electrons
0.02	$5.805 \cdot 10^5$	0.30	marginally relativistic
1.0	$2.903 \cdot 10^7$	15.0	relativistic
50.0	$1.451 \cdot 10^9$	740	extremely relativistic

Table 2.1: Some values of the mass density and related parameters.

For the numerical simulations, a mixture of equal parts of ^{12}C and ^{16}O with $Y_\mathrm{F} \approx 0.5$ was used. The chosen mass densities are listed in Table 2.1. The lower density, $\rho_0 \approx 5.8 \cdot 10^5\,\mathrm{g\,cm^{-3}}$, is close to the observed average density of white dwarfs, $\bar{\rho}_0 \approx 4.7 \cdot 10^5\,\mathrm{g\,cm^{-3}}$. The higher density, $\rho_0 \approx 1.5 \cdot 10^9\,\mathrm{g\,cm^{-3}}$, on the other hand, is of the same order of magnitude as the central density in SN Ia progenitors close to the Chandrasekhar limit.

2.3.2 Fermi Energy and the Speed of Sound

The internal energy and the pressure are dominated by the degenerate electron gas, if the temperature is much lower than the Fermi temperature. In this case, $E_\mathrm{int} \simeq E_\mathrm{F} \sim P_\mathrm{F} \sim \rho_0 c_0^2$, and it is convenient to measure energy in units of $\rho_0 c_0^2$, i. e., we set $\tilde{E} = E/\rho_0 c_0^2$. The temperature $m_\mathrm{e}c^2/k_\mathrm{B} \approx 5.929 \cdot 10^9\,\mathrm{K}$, which is of the order of the Fermi temperature of relativistic electrons, provides a fundamental temperature scale. Approximations which apply to the limiting cases of non-relativistic and relativistic degeneracy are commonly known and, for instance, discussed in Shapiro and Teukolsky [1983, Section 2.3].

The Non-Relativistic Limit

If $\rho_0 \ll \rho_c$, the Fermi energy of the degenerate electron gas is given by

$$E_{\rm F}^{\rm (nr)} \simeq \frac{3h^2}{10m_{\rm e}}\left(\frac{3}{8\pi}\right)^{2/3}\left(\frac{Y_{\rm F}\rho_0}{m_{\rm p}}\right)^{5/3} \approx 1.49\cdot 10^{13}(Y_{\rm F}\rho_0)^{5/3}\,[\rm cgs]. \tag{2.35}$$

The speed of sound is readily obtained from $c_0 = (\gamma P_{\rm F}/\rho_0)^{1/2}$ with $\gamma = 5/3$, assuming that $P \simeq P_{\rm F}$ in the limit of high degeneracy. Substituting $P_{\rm F} = 2E_{\rm F}/3$, with the Fermi energy given by equation (2.35), we obtain

$$c_0^{\rm (nr)} \simeq \frac{h}{(3m_{\rm e})^{1/2}}\left(\frac{3}{8\pi}\right)^{1/3}\left(\frac{Y_{\rm F}}{m_{\rm p}}\right)^{5/6}\rho_0^{1/3} \approx 4.06\cdot 10^6 Y_{\rm F}^{5/6}\rho_0^{1/3}\,[\rm cgs]. \tag{2.36}$$

The normalised Fermi energy in the non-relativistic limit is therefore the constant $\tilde{E}_{\rm F}^{\rm (nr)} = 9/10$. The Fermi temperature $T_{\rm F} = E_{\rm F}/n_{\rm e}k_{\rm B}$ expressed in dimensionless form depends on the density:

$$\tilde{T}_{\rm F}^{\rm (nr)} \simeq \frac{3}{10}(3\pi^2 Y_{\rm F}\tilde{\rho}_0)^{2/3} = \frac{3}{10}\left(\frac{\rho_0}{\rho_{\rm c}}\right)^{2/3} \tag{2.37}$$

For $\tilde{\rho}_0 = 0.02$, the Fermi temperature according to equation (2.37) is about $\tilde{T}_{\rm F} \approx 0.13$ or $T_{\rm F} \approx 7.9\cdot 10^8$ K. However, this pushes the limit of validity of the non-relativistic approximation, as $\tilde{\rho}_0 \approx 0.3\tilde{\rho}_{\rm c}$. For the sound speed, equation (2.36) gives an estimated value of $c_0 \approx 1.9\cdot 10^8\,{\rm cm\,s^{-1}}$.

The Extremely Relativistic Limit

On the other hand, if $\rho_0 \gg \rho_c$, then the Fermi energy is approximately given by

$$E_{\rm F}^{\rm (er)} \simeq \frac{3}{4}\left(\frac{3}{8\pi}\right)^{1/3} hc\left(\frac{Y_{\rm F}\rho_0}{m_{\rm p}}\right)^{4/3} \approx 1.85\cdot 10^{15}(Y_{\rm F}\rho_0)^{4/3}\,[\rm cgs]. \tag{2.38}$$

Using $\gamma = 4/3$ and $P_{\rm F} = E_{\rm F}/3$ in the extremely relativistic limit, we obtain for the sound speed

$$c_0^{\rm (er)} \simeq \left(\frac{\pi}{3}\right)^{1/3}(\hbar c)^{1/2}\left(\frac{Y_{\rm F}}{m_{\rm p}}\right)^{2/3}\rho_0^{1/6} \approx 4.05\cdot 10^7 Y_{\rm F}^{2/3}\rho_0^{1/6}\,[\rm cgs]. \tag{2.39}$$

Hence, $\tilde{E}_{\rm F}^{\rm (er)} = 9/4$. The corresponding Fermi temperature is

$$\tilde{T}_{\rm F}^{\rm (er)} \simeq \frac{3}{4}(3\pi^2 Y_{\rm F}\tilde{\rho}_0)^{1/3} = \frac{3}{4}\left(\frac{\rho_0}{\rho_{\rm c}}\right)^{1/3}. \tag{2.40}$$

For the density $\tilde{\rho}_0 = 50.0$, the Fermi temperature is $\tilde{T}_{\rm F} \approx 6.8$ corresponding to $T_{\rm F} \approx 4.0\cdot 10^{10}$ K, and equation (2.39) yields a sound speed of $c_0 \approx 8.6\cdot 10^8\,{\rm cm/s}$.

2.3.3 Characteristic Velocity and Integral Length Scale

The magnitude of the stochastic force, F_0, is determined by the integral length scale L and the characteristic velocity V of the system. The dynamical properties of the flow mainly depend on the characteristic Mach number V/c_0. The initial sound speed c_0 is determined by the initial mass density and temperature. Thus, using the estimates of the sound speed form the previous Section, it is easy to estimate the characteristic Mach number for a given value of V. As for the integral length scale, there appears to be a large range of possible values and, as one would expect, scaling invariance of turbulence implies that we are free to use any value within that range. Since we are dealing with a system that, in principle, has no boundaries, there is no useful notion of self-gravity for the whole system. However, local density fluctuations produced by turbulence do, in fact, interact gravitationally. Of course, solving Poisson's equation for the gravitational field in a cubic domain would be computationally too expensive. Therefore, one has to ensure that the typical gravity exerted by the largest regions of density exceeding the average on the surrounding regions of lower density is dynamically insignificant.

An order-of-magnitude estimate can be made as follows. The excess mass related to a density fluctuation of size $\sim l$ is roughly $\delta m(l) \sim l^3 \delta\rho$. The magnitude of density fluctuations is given by the characteristic Mach number squared, i. e., $\delta\rho \sim [v'(l)/c_0]^2\rho_0$, where $v'(l)$ is the magnitude of turbulent velocity fluctuations on the length scale l. The corresponding gravitational energy per unit mass is $\delta e_G(l) \sim G\delta m/l \sim Gl^2\delta\rho$. The gravitational interactions produced by these density fluctuation will be dynamically negligible if the specific gravitational energy, $e_G(l)$, is small compared to the kinetic energy per unit mass, $v'(l)^2$. As $c_0^2 \sim E_F/\rho_0$, this constraint is equivalent to $G\rho_0^2 l^2 \ll E_F$, which is *independent* of the characteristic velocity $v'(l)$. In conclusion, gravitational interactions are dynamically insignificant on arbitrary scales of the simulated system, provided that

$$E_G(L) = G\rho_0^2 L^2 \ll E_F. \tag{2.41}$$

In the two limiting cases of non-relativistic and relativistic degeneracy, respectively, the resulting upper bounds on the integral length scale L are

$$L \ll \begin{cases} 8.4 \cdot 10^9 \rho_0^{-1/6}\,[\text{cgs}] & \text{if } \rho_0 \ll \rho_c, \\ 1.0 \cdot 10^{11} \rho_0^{-1/3}\,[\text{cgs}] & \text{if } \rho_0 \gg \rho_c. \end{cases} \tag{2.42}$$

For $\rho_0 \approx 5.8 \cdot 10^5\,\mathrm{g\,cm^{-3}}$, the above constraint becomes $L \ll 10^9\,\mathrm{cm}$, which is comparable to the size of a white dwarf of this density. On the other hand, in the case of $\rho_0 \approx 1.45 \cdot 10^9\,\mathrm{g\,cm^{-3}}$, the constraint is lower by an order of magnitude, $L \ll 10^8\,\mathrm{cm}$, which is about the size of a white dwarf close to the Chandrasekhar limit. For the simulations discussed in the following, $N = 432$ cells of size $\Delta = 10^3\,\mathrm{cm}$ were used in each dimension and a characteristic wavenumber of stochastic forcing $k_0 = 6\pi/N\Delta \approx 4.36 \cdot 10^{-5}\,\mathrm{cm^{-1}}$ corresponding to $\alpha = 3$. The resulting integral length scale is $L = N\Delta/3 = 1.44 \cdot 10^5\,\mathrm{cm}$, which is well below the upper bounds imposed by the constraints (2.42).

2.4 Global Statistics and Flow Structure

The evolution of statistically homogeneous flows is well described by spatial averages of dynamical quantities over the whole computational domain. Of particular interest are the root mean square magnitude of momentum and the averaged kinetic and internal energy. In addition, mean *structural invariants*, which can be constructed from the velocity derivative, play an important role in the investigation of turbulence. A more vivid impression of turbulence is received by means of 2D sections of the flow, which supplement the discussion in this Section.

2.4.1 Dimensionless Physical Quantities

It is commonly known that turbulence is a scale-invariant phenomenon. For example, the properties of the velocity field mainly depend on the ratio of the mean velocity to the speed of sound. The latter is determined by the equation of state and, in the case of degenerate matter, one finds values in the range $\sim 10^7 \ldots 10^9\,\mathrm{cm\,s^{-1}}$, which are quite large compared to typical speeds under terrestial conditions[2]. Nevertheless, if the velocity or other dynamical quantities are normalised with the corresponding characteristic scales, than the flow will look similar regardless of whether it is turbulence in air or in degenerate matter. Therefore, we shall exclusively use dimensionless quantities. In the following, normalisation is indicated by a tilde on top of the variable.

Dimensionless time is obviously given by $\tilde{t} = t/T$, with T being the integral time scale, and length is normalised in units of the integral length scale, i. e., $\tilde{x}_i = x_i/L$. As $v_i \sim V$, it seems appropriate to set $\tilde{v}_i = v_i/V$. For $v \lesssim c_0 \simeq 1$, a large contribution to the total energy comes from internal energy and, thus, $E_{\mathrm{int}} \sim P_{\mathrm{F}} \sim \rho_0 c_0^2$, which suggests $\tilde{E} = E/\rho_0 c_0^2$. The dimensionless total energy is then of the form

$$\tilde{E} = \frac{1}{2}\left(\frac{\rho}{\rho_0}\right)\left(\frac{V}{c_0}\right)^2 \tilde{v}^2 + \frac{E_{\mathrm{int}}}{\rho_0 c_0^2}. \tag{2.43}$$

The time derivative of energy, however, is more conveniently normalised with respect to the kinetic energy scale $\rho_0 V^2$, as we shall see below. Structural invariants of concern are the rate of strain $|S| = (2S_{ik}S_{ik})^{1/2}$, the vorticity $\omega = (2W_{ik}W_{ik})^{1/2} = |\boldsymbol{\nabla} \times \boldsymbol{v}|$ and the divergence of the velocity, $d = v_{i,i} = \boldsymbol{\nabla} \cdot \boldsymbol{v}$. Recall that $S_{ik} = v_{(i,k)}$ and $W_{ik} = v_{[i,k]}$ denote, respectively, the symmetric and antisymmetric parts of the Jacobian matrix of the velocity. The corresponding dimensionless counterparts follow immediately from $\tilde{v}_{i,k} = (L/V)v_{i,k} = Tv_{i,k}$. For instance, we have $\tilde{\omega} = T\omega$, which is a measure of the large-eddy turn-over time relative to time scales associated with the smallest eddies.

2.4.2 Solenoidal Forcing at Low Density

If the projection weight $\zeta = 1$ in equation (2.26), then the random force field $\boldsymbol{a}(\boldsymbol{x}, t)$ will be purely solenoidal, i. e., $\boldsymbol{\nabla} \cdot \boldsymbol{a}(\boldsymbol{x}, t) = 0$. Usually, one refers to this kind of forcing as stirring, because it is reminiscent of agitating the fluid into motion by mechanical stirring with randomly changing magnitude and spatial orientation.

[2] For example, the speed of sound in air is of the order $10^5\,\mathrm{cm\,s^{-1}}$

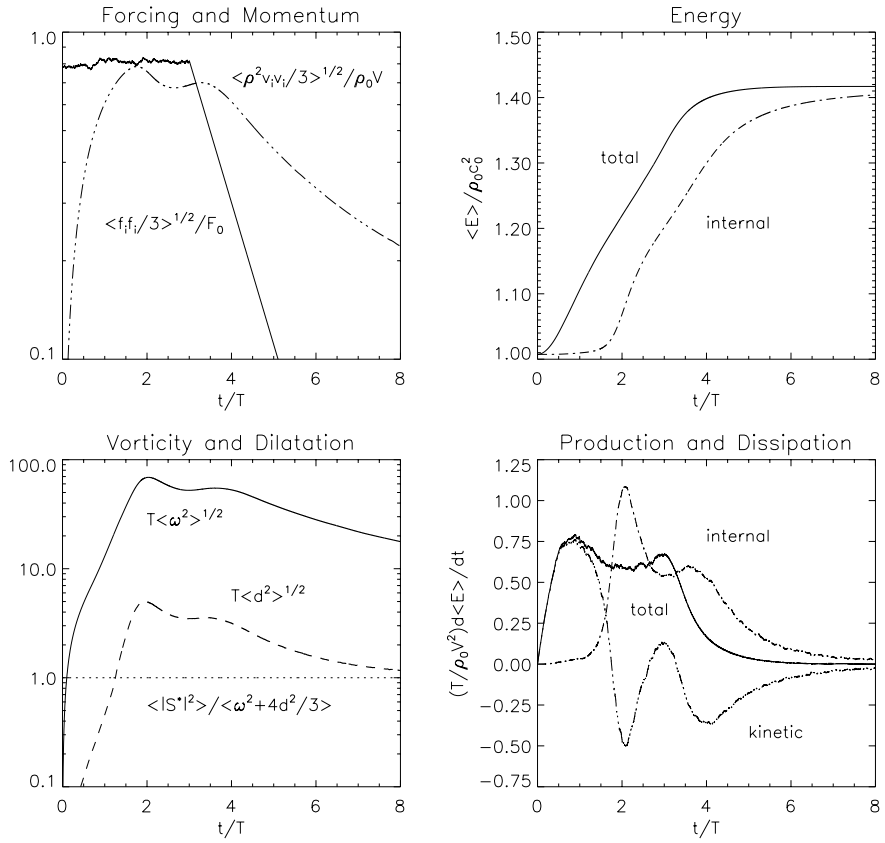

Figure 2.1: Evolution of dimensionless mean quantities for the simulation `dns432nrsl`. The panels show the RMS momentum, the mean total and internal energy, the RMS vorticity and divergence and the averaged rates of energy production and dissipation as functions of the normalised time $\tilde{t} = t/T$. The density parameter is $\tilde{\rho}_0 = 0.02$, the characteristic Mach number $V/c_0 = 0.42$, and the spectral weight of solenoidal forcing $\zeta = 1$.

We will first analyse the statistics of a simulation called `dns432nrsl` that was initialised with a mixture of equal mass fractions ^{12}C and ^{16}O of total mass density $\rho_0 = 5.805 \cdot 10^5\,\mathrm{g\,cm^{-3}}$ ($\tilde{\rho}_0 = 0.02$) and temperature $T_0 \approx 5.93 \cdot 10^6\,\mathrm{K}$ ($\tilde{T}_0 = 0.001$) at rest. Solenoidal stirring was applied over an interval of time $0.0 \le \tilde{t} \le 3.0$, and then the force field was decaying exponentially, according to equation (2.26) with the stochastic diffusion term switched off. The characteristic velocity and Mach number are, respectively, $V = 7.29 \cdot 10^7\,\mathrm{cm\,s^{-1}}$ and $V/c_0 = 0.42$. The computation was carried out over roughly 19 sound crossing times until $\tilde{t} = 8.0$.

The evolution of globally averaged quantities is shown in Figure 2.1. The root mean square acceleration $\tilde{a}_{\mathrm{rms}}/\sqrt{3} = \langle a_i a_i/3\rangle^{1/2}/F_0$ and momentum $\tilde{p}_{\mathrm{rms}}/\sqrt{3} = \langle \rho^2 v_i v_i/3\rangle^{1/2}/\rho_0 V$ are plotted in the upper left panel[3]. The factor $1/\sqrt{3}$ accounts for the statistical fraction corresponding to a single vector component. According to the

[3]The brackets $\langle\,\rangle$ are used quite generically here. The can either mean an ensemble average or a spatial average as well as a filter operation. In each case it should be clear from the context which operation is specifically in use.

discussion in Section 2.2.3, the expectation value of $|\boldsymbol{a}|/\sqrt{3}$ is $\sqrt{2/3} \approx 0.816$ in the statistically stationary regime. One would expect that $\tilde{p}_{\rm rms}/\sqrt{3}$ approaches the value $\sqrt{2/3}\rho_0 F_0 T \approx 0.8\rho_0 V$, after roughly one integral time scale has passed. Indeed, the plot of $\tilde{p}_{\rm rms}$ shows that a dimensionless momentum of about 0.8 is reached at $\tilde{t} \approx 1.5$, and then it approaches stochastic equilibrium with a value near 0.7 in advance of the exponential decay of turbulence from $\tilde{t} \approx 3.0$ onwards.

As one can see in the lower left panel of Figure 2.1, the root mean square vorticity $\tilde{\omega}_{\rm rms} = T\langle\omega^2\rangle^{1/2}$ grows exponentially, before it reaches a plateau at time $\tilde{t} \approx 2.0$. This marks the transition to *steady* turbulence with fully developed velocity fluctuations on the smallest scales. In the steady regime, stochastic equilibrium between turbulence production by the driving force and numerical dissipation is maintained. In the follow-up decay regime, vorticity decreases exponentially. The divergence (also called *dilatation* in the context of turbulence) is much smaller than vorticity, but in comparison still larger than the relative divergence of the stirring field, which is zero to a high degree of accuracy[4]. This is a consequence of appreciable compression effects at Mach numbers of the order unity. Furthermore, the numerical data evidence the identity

$$\frac{\langle|S^*|^2\rangle}{\langle\omega^2 + \frac{4}{3}d^2\rangle} = \frac{\langle S_{ik}S_{ik} - \frac{1}{3}d^2\rangle}{\langle W_{ik}W_{ik} + \frac{2}{3}d^2\rangle} \simeq 1. \tag{2.44}$$

In fact, this relation between the *globally averaged* rate of strain, vorticity and squared dilatation must hold, if the net flux through the boundaries of the computational domain is zero. This can be seen from the *local* relationship

$$|S^*|^2 = 2\partial_i(\partial_k u_i u_k - 2du_i) + \omega^2 + \frac{4}{3}d^2. \tag{2.45}$$

Volume integration over the whole domain implies equation (2.44) if the surface integral arising from the flux-divergence term vanishes, which is the case for periodic BCs.

The development of vorticity is clearly reflected in the change of energy with time, as can be seen in the right two panels in Figure 2.1. The initial value of mean internal energy $\langle\tilde{E}_{\rm int}\rangle$ is about 1.007 corresponding to $\langle E_{\rm int}(0)\rangle \approx 1.79 \cdot 10^{22}$ erg and increases only little before $\tilde{t} \approx 1.5$[5]. In the course of this initial phase, vortices on the smallest dissipative scales are not yet produced, and virtually all the injected energy is piled up in the form of kinetic energy in the turbulence cascade. This can be seen from the averaged rate of energy increase, also called the *rate of production*,

$$\tilde{\Pi} = \frac{T}{\rho_0 V^2}\frac{\mathrm{d}}{\mathrm{d}t}\langle E\rangle = \left(\frac{V}{c_0}\right)^{-2}\frac{\mathrm{d}}{\mathrm{d}\tilde{t}}\langle\tilde{E}\rangle, \tag{2.46}$$

which is plotted in the lower right panel. $\tilde{\Pi}$ is, of course, always positive and equal to the mean power exerted by the stirring force upon the fluid. For this reason, it shows the imprint of the stochastic variations in the stirring field. In between the time of

[4] Strictly speaking the term *dilatation* refers to the divergence of the velocity fluctuations. As there is no mean flow in the case of isotropic turbulence, however, dilatation and divergence can be identified.

[5] The actual value of $\langle\tilde{E}_{\rm int}(0)\rangle$ is by about 10 % larger than $\tilde{E}^{(\rm nr)} = 9/10$ (see Section 2.3.2). This indicates that the Fermi gas is already partially relativistic.

maximal momentum and the peak of vorticity at $\tilde{t} \approx 2.0$, the internal energy increases rapidly as the mean dissipation rate

$$\langle \tilde{\epsilon} \rangle = \frac{T}{\rho_0 V^2} \frac{\mathrm{d}}{\mathrm{d}t} \langle E_{\mathrm{int}} \rangle = \left(\frac{V}{c_0} \right)^{-2} \frac{\mathrm{d}}{\mathrm{d}\tilde{t}} \langle \tilde{E}_{\mathrm{int}} \rangle, \tag{2.47}$$

rises to a sharp peak. At the maximum of $\langle \tilde{\epsilon} \rangle$, more energy is dissipated than injected into the system. By $\tilde{t} \approx 2.5$, the turbulence energy increases slightly once more, but then the trend reverses when the exponential damping of the force field starts at $\tilde{t} = 3.0$.

The difference between production and dissipation is equal to the rate of change of the kinetic energy:

$$\tilde{\Pi} - \langle \tilde{\epsilon} \rangle = \frac{T}{\rho_0 V^2} \frac{\mathrm{d}}{\mathrm{d}t} \langle E - E_{\mathrm{int}} \rangle = \frac{1}{\rho_0} \frac{\mathrm{d}}{\mathrm{d}\tilde{t}} \langle \rho \tilde{v}^2 \rangle. \tag{2.48}$$

This rate becomes strongly negative when the dissipation rate approaches the peak near $\tilde{t} \approx 2.0$. Afterwards $\tilde{\Pi} - \langle \tilde{\epsilon} \rangle$ increases to a slightly positive value as the system equilibrates. At time $\tilde{t} = 3.0$, the rate of energy injection falls off exponentially and the graphs of total and internal energy gradually flatten and converge towards the same constant value when most of the kinetic energy is dissipated. The mean temperature in the final state is $\langle T \rangle_{\mathrm{f}} \approx 3.3 \cdot 10^8$ K ($\langle \tilde{T} \rangle_{\mathrm{f}} \approx 0.056$). This is still lower than the Fermi temperature $T_{\mathrm{F}} \approx 7.9 \cdot 10^8$ K estimated from the non-relativistic approximation (2.37), but only by a small margin. Hence, degeneracy more or less prevails against dissipative heating, however, with a significant fraction of thermal excitation.

An impression of the structure exhibited by the flow is given in Figure 2.2, which shows contour plots of various quantities in a horizontal 2D section at time $\tilde{t} = 1.5$, i. e., near the maximum of RMS momentum. At this stage, velocity fluctuations on the smallest numerically resolved scales are not fully developed yet, but quite a complex flow pattern has already evolved. In the left panel on the top, contours of the magnitude of the dimensionless velocity $\tilde{v} = (v_i v_i)^{1/2}/V$ are plotted. As $(V/c_0)^{-1} \approx 2.4$, it is clear that a significant fraction of the flow is supersonic. These regions appear in colours from dark blue to reddish and are separated by steep velocity gradients from the subsonic regions. As there are no extended strong shock fronts, the supersonic regions in this kind of flow at moderate Mach number are called *shocklets*. In the right top panel, which shows contours of the total energy $\tilde{E}$, shocklets can be seen even more clearly as bright thread-like regions of high energy, and the boundaries of shocklets are marked by a large rate of strain in the left panel on the bottom.

Furthermore, one can see that there are pronounced spots which are largely depleted of energy. These spots are associated with the central cross-sections of vortices, as is revealed by comparing the energy contour plot with the right bottom panel showing the contours of vorticity $\tilde{\omega}$ in logarithmic scaling. Here vortices appear bright, and one can see that there is a tight correlation to regions of low energy. In fact, the greater fraction of $\tilde{E}$ is internal energy, which is tightly coupled to the mass density. Due to the enormous under-pressure in the centre of a strong vortex, the density decreases quite significantly, a phenomenon similar to the eye of a Hurricane in Earth's atmosphere. It is intriguing to consider the actual physical scales: The largest vortices contain a total mass of about 10^{20} g, they are roughly 1 km in size, and the turn-over time is of the order about 10^{-3} s [6].

[6] The vortex mass is comparable to the mass of the asteroid whose impact caused mass extinction on

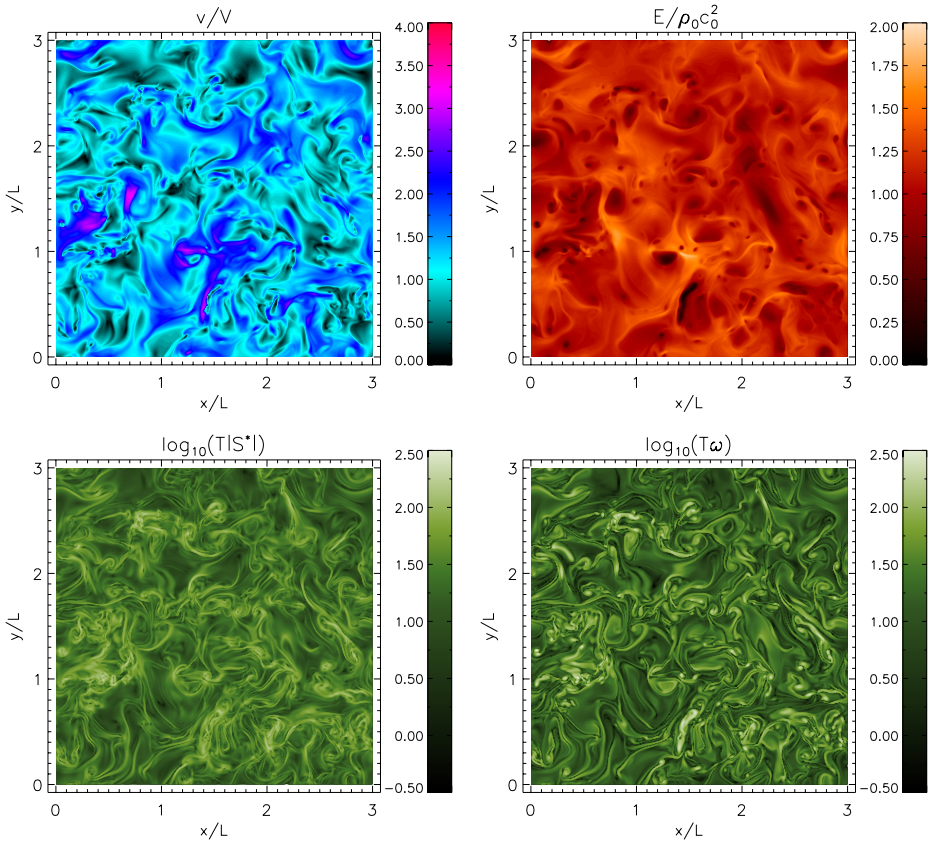

Figure 2.2: 2D contour sections of velocity, total energy, rate of strain and vorticity for model `dns432nrsl` in the plane $\tilde{z} = 2.0$ at time $\tilde{t} = 1.5$. The model parameters are as specified in Figure 2.1. Dimensionless scales are used for all quantities. Logarithmic contours are used both for the rate of strain $|S^*|$ and the vorticity ω in order to fully uncover the spatial variation.

2.4.3 Solenoidal Forcing at High Density

As a consequence of the equation of state (EOS) for degenerate matter, hydrodynamics is largely decoupled from thermodynamics, because the Fermi pressure of the electrons is independent of temperature. For this reason, the EOS solely influences the Euler equations through the relation between pressure and mass density. In order to see how far this affects the dynamics of turbulence, a reference simulation, `dns432ersl2`, was produced. For this simulation, the same characteristic Mach number as in the case of `dns432nrsl` was used, however, with a mass density in the extremely relativistic limit, $\tilde{\rho}_0 = 50.0$, which implies a characteristic velocity $V \approx 4.92 \times 7.29 \cdot 10^7 \,\mathrm{cm\,s^{-1}} \approx 3.59 \cdot 10^7 \,\mathrm{cm\,s^{-1}}$. The factor 4.92 is the ratio of the speed of sound for the density $\tilde{\rho}_0 = 50.0$ and $\tilde{\rho}_0 = 0.02$, respectively.

Comparing the statistics of the simulations `dns432nrsl` and `dns432ersl2` demonstrates that the differences are only minute. The evolution of mean momentum progresses, in fact, very closely for both models. The relative fluctuations in the mass

Earth about sixty five million years ago.

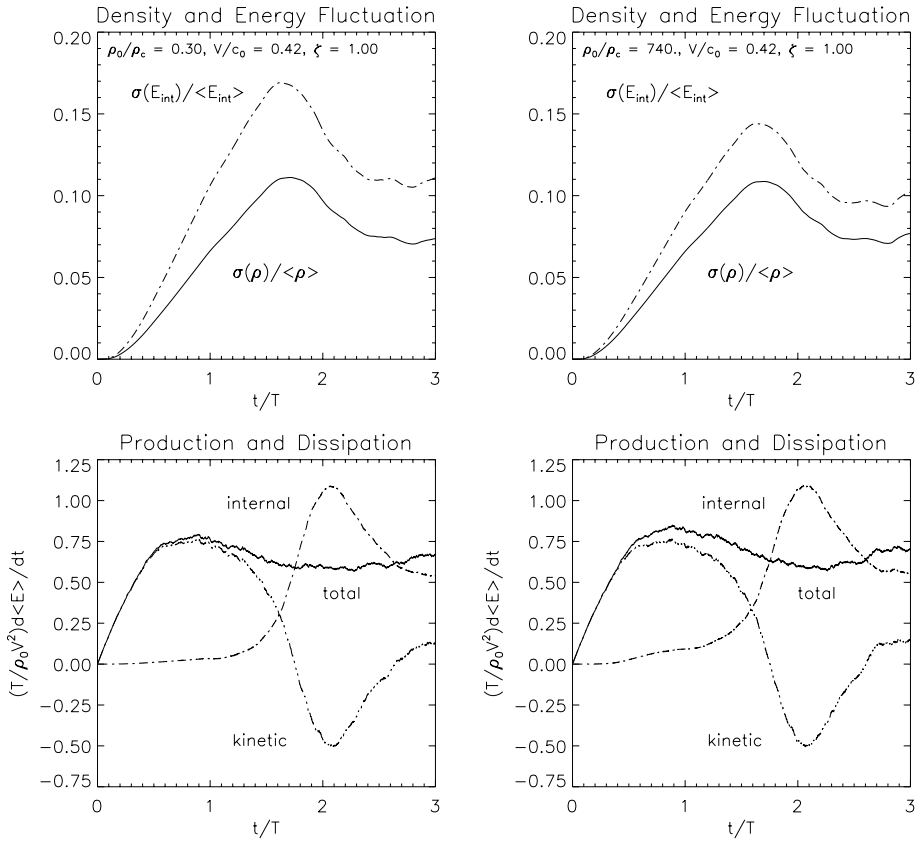

Figure 2.3: Comparison between the simulations `dns432nrsl` and `dns432ersl2` with $\tilde{\rho}_0 = 0.02$ and $\tilde{\rho}_0 = 50.0$, respectively. The top panels show the RMS fluctuations of internal energy and mass density, respectively. In the bottom panels, the rates of energy production and dissipation are plotted. The characteristic Mach number is $V/c_0 = 0.42$ and the spectral weight of the solenoidal forcing component $\zeta = 1$.

density as measured by $\sigma(\rho)/\langle\rho\rangle$, where $\sigma^2(\rho) = \langle\rho - \langle\rho\rangle\rangle^2$ is the variance of ρ, are not markedly different either, as one can see in the two top panels of Figure 2.3. However these panels also show that the magnitude of the relative fluctuations in the internal energy are systematically larger in the case of lower density. It appears that the variations in the mass density are virtually the same for both models as it can be expected on grounds of the equal characteristic Mach numbers. The fluctuations in pressure and internal energy induced by compression effects, however, are not quite the same and reflect the differences in the EOS. In the non-relativistic limit, $\delta E_F/E_F \approx (5/3)\delta\rho/\rho$ according to equation (2.35), whereas equation (2.38) implies $\delta E_F/E_F \approx (4/3)\delta\rho/\rho$ in the extremely relativistic limit. Actually, one finds for the ratio of the RMS fluctuations of energy and mass density at time $\tilde{t} = 3.0$ the value 1.32 for `dns432ersl2` and 1.51 for `dns432nrsl`. This behaviour verifies the statement that a thermodynamical quantity such as the internal energy, which is solely coupled via pressure to the momentum equation, have little influence on the evolution of hydrodynamical quantities, in particular, the mass density. The production and dissipation rates, which are plotted for both simulations the bottom panels of Figure 2.3, display some further dissimi-

larities between the two simulations. The increase of internal energy in the course of turbulence production is steeper in the case of higher density. Since the production rate is also larger, however, the kinetic energy budget is approximately the same for both models.

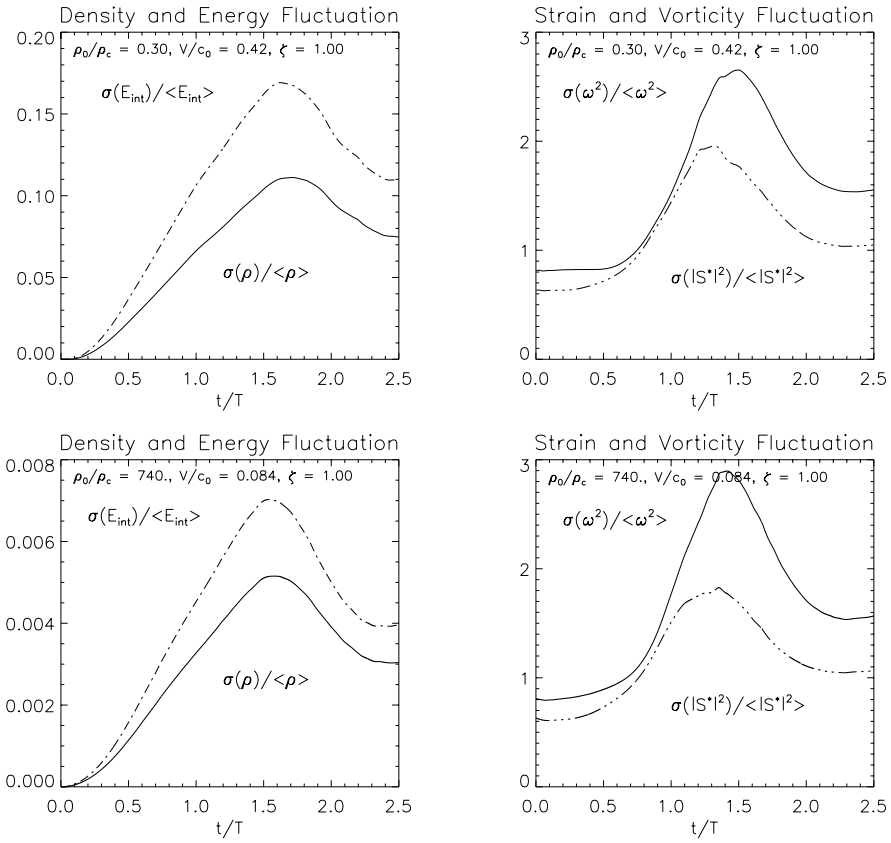

Figure 2.4: Comparison between `dns432nrsl` with $\tilde{\rho}_0 = 0.02$ and another simulation, `dns432ersl`, with the same characteristic velocity V and a higher density $\tilde{\rho}_0 = 50.0$. The characteristic Mach number of the low-density model is $V/c_0 = 0.42$, whereas $V/c_0 = 0.084$ for the high density model. The panels on the left show the RMS fluctuations of internal energy and mass density. The corresponding RMS fluctuations of vorticity and the rate of strain are plotted in the panels on the right.

As supplementary experiment, an additional simulation with density $\tilde{\rho}_0 = 50.0$ was carried out. This time, however, the same absolute magnitude of stirring as in simulation `dns432nrsl` was used. The outcome, `dns432ersl`, is a low Mach-number turbulence simulation with $V/c_0 = 0.084$ owing to the significantly higher sound speed in the extremely relativistic regime. A comparison of root mean square density and internal energy fluctuations for these two simulations can be found in the left-hand side panels of Figure 2.4. While the shape of the graphs for the density fluctuations is quite similar in both cases, the magnitude is found to scale with the square of the ratio of Mach numbers, $c_0^2(0.02, 10^{-3})/c_0^2(50.0, 0.1) \approx 0.041$, where the values in parentheses specify the dimensionless initial density $\tilde{\rho}_0$ and temperature $\tilde{T}_0$, respectively. Indeed, this scaling is implied by the Euler equations. Regarding the second moments of $\tilde{\omega}^2$

and $|\tilde{S}^*|^2$, both the evolution with time and the magnitude seem to be rather independent of density and Mach number, except for a slightly higher peak of $\sigma^{1/2}(\tilde{\omega}^2)/\langle\tilde{\omega}^2\rangle$ and a lower peak of $\sigma^{1/2}(|\tilde{S}^*|^2)/\langle|\tilde{S}^*|^2\rangle$ in the case of model `dns432ersl` as compared to `dns432nrsl`. Evaluating these quantities for the reference model `dns432ersl2`, one finds that the differences in the peak heights solely depend on the Mach number but not on the EOS. Moreover, note that the quasi-equilibrium values at $\tilde{t} = 2.5$ are almost the same both for the lower and the higher Mach number. This result also demonstrates the universality of turbulence.

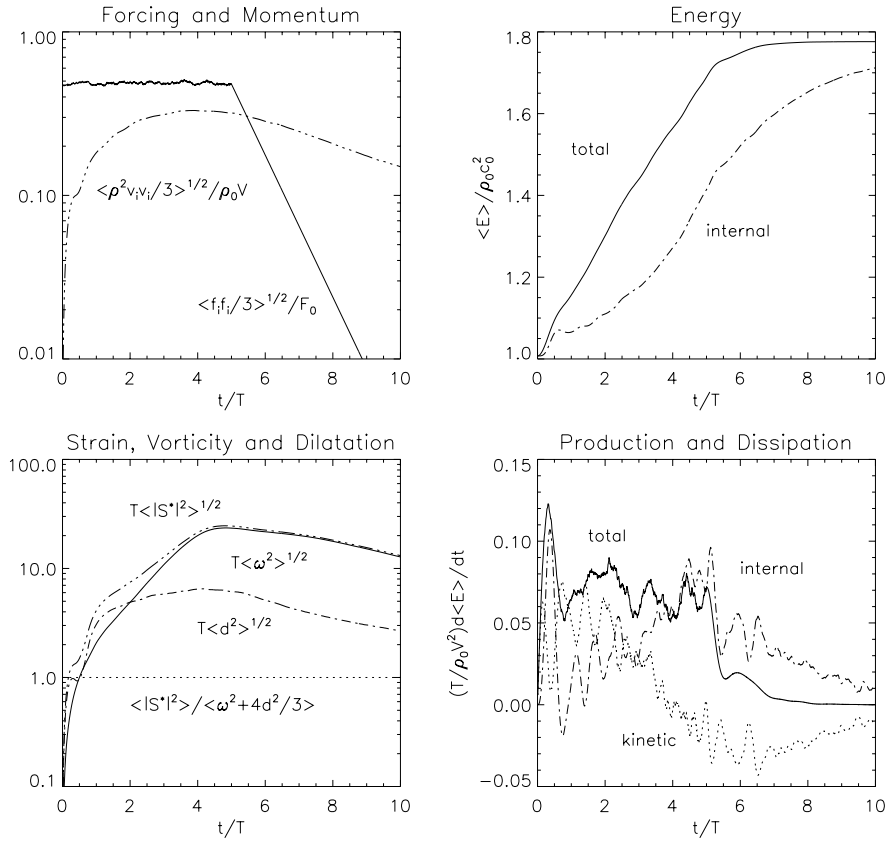

Figure 2.5: Evolution of dimensionless mean quantities for model `dns432nrh20`. The panels show the RMS momentum, the mean total and internal energy, the RMS vorticity and divergence and the averaged rates of energy production and dissipation as functions of the normalised time $\tilde{t} = t/T$. The density parameter is $\tilde{\rho}_0 = 0.02$, the characteristic Mach number $V/c_0 = 1.39$, and the spectral weight $\zeta = 0.2$.

2.4.4 Partially Dilatational Forcing

In the case $\zeta < 1$, the random force field $\boldsymbol{a}(\boldsymbol{x}, t)$ also has compressive or dilatational components which induce non-rotational motions in the fluid. In order to investigate the effects of dilatational forcing as opposed to the purely solenoidal stirring applied in the preceding simulations, we will now discuss two further simulations, `dns432nrh20` and `dns432nrh75`, with spectral weights $\zeta = 1/5$ and $\zeta = 3/4$, respec-

tively. The initial state is the same as in the case of simulation `dns432nrsl`. According to equation (2.31), the characteristic amplitude of the driving force is reduced from the value $\sqrt{2/3}F_0$, which applies to purely solenoidal forcing, to $\sqrt{19/48}F_0 \approx 0.63F_0$ for $\zeta = 3/4$ and $\sqrt{6/25}F_0 \approx 0.49F_0$ in the case of a mainly dilatational force with $\zeta = 1/5$. Apart from that, the dilatational component of the force field is less effective in producing turbulence, because it induces only small strain. Consequently, higher characteristic Mach numbers were chosen: $V/c_0 \approx 0.66$ for `dns432nrh75` and $V/c_0 \approx 1.39$ for `dns432nrh20`.

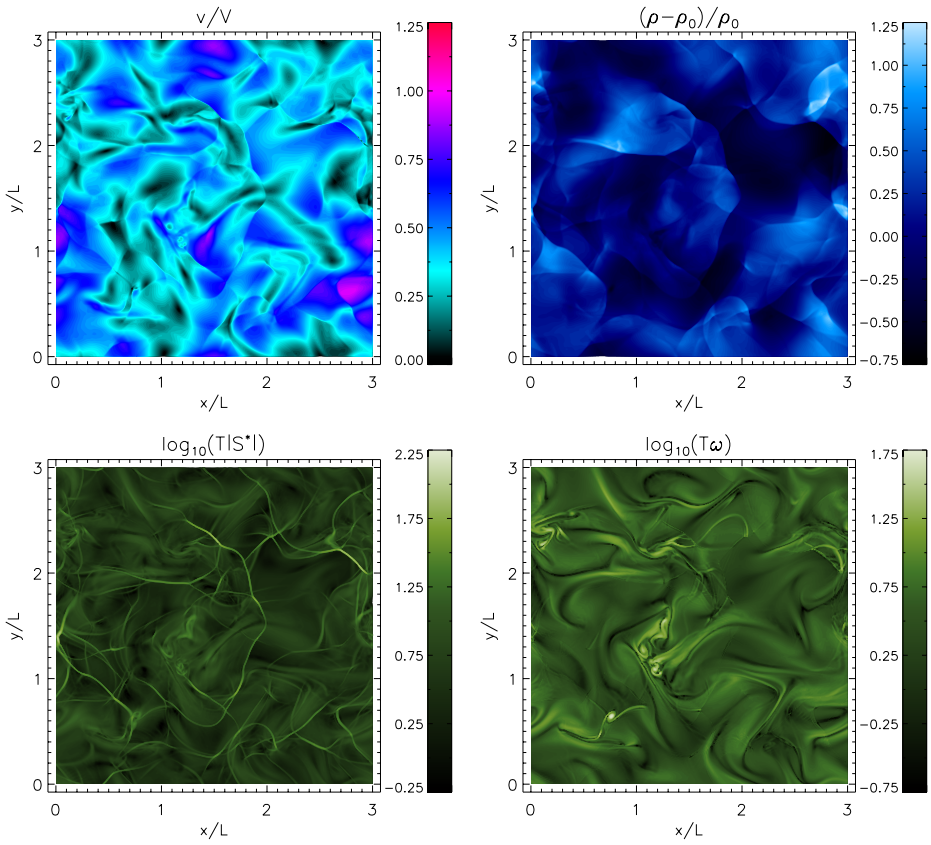

Figure 2.6: 2D contour sections of velocity, density fluctuations, rate of strain and vorticity for model `dns432nrh20` in the xy-layer with $\tilde{z} = 1.0$ at time $\tilde{t} = 2.0$. The model parameters are as specified in Figure 2.5. Also see the notes in the caption of Figure 2.2.

Let us consider the statistics obtained from the data of simulation `dns432nrh20`. Statistically stationary forcing was active in the interval $0 \leq \tilde{t} \leq 5.0$, and the decay of turbulence was computed over an interval of five integral time scales. The whole simulations encompasses about 7.2 sound crossing times. The various mean and RMS quantities are plotted in Figure 2.5. The left panel on the top shows that the maximal value of $\tilde{p}_{\rm rms}$ is significantly smaller than the expectation value $0.49F_0T$ in the stationary regime, and the maximum is not reached before $\tilde{t} \approx 3.5$. This confirms that the production of turbulence by dilatational forcing is reduced in comparison to

solenoidal stirring. From the panels on the right-hand side, some rather irregular evolution of energy becomes apparent. Prior to decay, the dimensionless rate of production $T\langle\dot{E}\rangle/\rho_0 V^2 \approx 0.07$, which falls about an order of magnitude short of the estimate $\dot{E} \sim \rho_0 F_0 V \sim \rho_0 V^2/T$. However, if the reduced magnitude of the characteristic force and the RMS momentum as well as the prolonged phase of production are taken into account, the estimate becomes $\dot{E} \sim 0.05\rho_0 F_0 V \sim \rho_0 V^2/T$ in good agreement with the actual values found in the simulation. Furthermore, one can observe a rapid increase of energy very early in the production phase, which suddenly drops at $\tilde{t} \approx 0.4$ followed by pronounced oscillations. This is a consequence of the formation of shocks which efficiently dissipate energy. Indeed, the contour sections shown in Figure 2.6 demonstrate that steep shock fronts are present at time $\tilde{t} = 2.0$, which extend over a length comparable to L and are much more pronounced than the borders of the shocklets encountered in the simulation `dns432nrsl`. The correlation between minimal dissipation and maximal increase of kinetic energy and vice versa indicates an alternating conversion of internal energy into mechanical energy and the other way around. This mechanism is entirely different from the turbulence cascade and is caused by *pressure-dilatation*, which will be discussed in more detail in Section 2.5.2. Beyond $\tilde{t} \approx 3.0$, the oscillations are vanishing, the rate of dissipation is rising, and a balance between production and dissipation is approached near $\tilde{t} \approx 4.0$.

Shock fronts are clearly identified as the locus of a large rate of strain in the left bottom panel of Figure 2.6. The right panel on the bottom, on the other hand, shows that there is no appreciable vorticity at the shock fronts. Moreover, the left bottom panel of Figure 2.5, in which the evolution of the averaged structural invariants $\langle|S^*|^2\rangle$, $\langle\omega^2\rangle$ and $\langle d^2\rangle$ is plotted, makes clear that the mean dilatation $\tilde{d}_{\mathrm{rms}} = T\langle d^2\rangle^{1/2}$ is significant in comparison to the vorticity $\tilde{\omega}_{\mathrm{rms}}$ in the early phase production. This is characteristic for the shock-dominated regime, in the course of which kinetic energy is mostly dissipated by shock waves and the flow structure is largely influenced by shock compression. From $\tilde{t} \approx 3.0$ onwards, however, the RMS rate-of-strain converges towards the RMS vorticity, the ratio $d_{\mathrm{rms}}/\omega_{\mathrm{rms}}$ becomes small compared to unity and the graphs of $\langle\tilde{\epsilon}\rangle$ and $\tilde{\Pi}$ resemble what is seen for lower Mach numbers. In this phase, the dynamics is finally governed by the turbulence cascade and the system approaches stochastic equilibrium. The transition from a phase of shock formation to the regime dominated by turbulence cascade has previously been observed, for instance, by Porter, Pouquet, and Woodward [1992] in a simulation of decaying turbulence with initial Mach number one. One can think of this transition as changing from an initial violent phase governed by shock-fronts to a shocklet regime.

The specific properties of the flow in the simulation `dns432nrh20` are also highlighted by a comparison with simulation `dns432nrh75`, in which the force field is dominated by solenoidal components with the weight $\zeta = 0.75$ and the characteristic Mach number is $V/c_0 \approx 0.66$. Apart from lucid differences in the magnitude of density and internal energy fluctuations, the panels on the left-hand side of Figure 2.7 show qualitative differences in the evolution which are noteworthy. During the production phase, the graphs for model `dns432nrh75` are quite similar in shape compared to those in the corresponding panels of Figure 2.4. In the case of `dns432nrh20`, on the other hand, the RMS density fluctuations are first growing rapidly, and then abruptly settle onto a plateau at time $\tilde{t} \approx 0.5$, which coincides with the drop in energy production shown in the right bottom panel of Figure 2.5. Beyond that point, the magnitude

of density fluctuations remains nearly constant until decay sets in, despite the metamorphosis which the flow is experiencing meanwhile. A contour plot of the density fluctuations at time $\tilde{t} = 2.0$ is shown in the right panel on the top of Figure 2.6.

From the plots of the relative RMS fluctuations of $|S^*|^2$ and ω^2, which are shown in the right panel on the bottom of Figure 2.7, the transition form the phase of shock formation to the Kolmogorov regime can be identified as well. Whereas initially a very sharp rise in strain and vorticity fluctuations occurs near$\tilde{t} = 1.0$, the magnitude of these fluctuations is quickly decreasing afterwards. Eventually, it approaches the same asymptotic values as for solenoidal forcing at lower Mach numbers. Moreover, there is crossing-over of the two graphs at$\tilde{t} \approx 2.9$. This indicates that the large strain, which is locally induced by shock fronts, declines in comparison to the strength of vortices built up by the turbulence cascade.

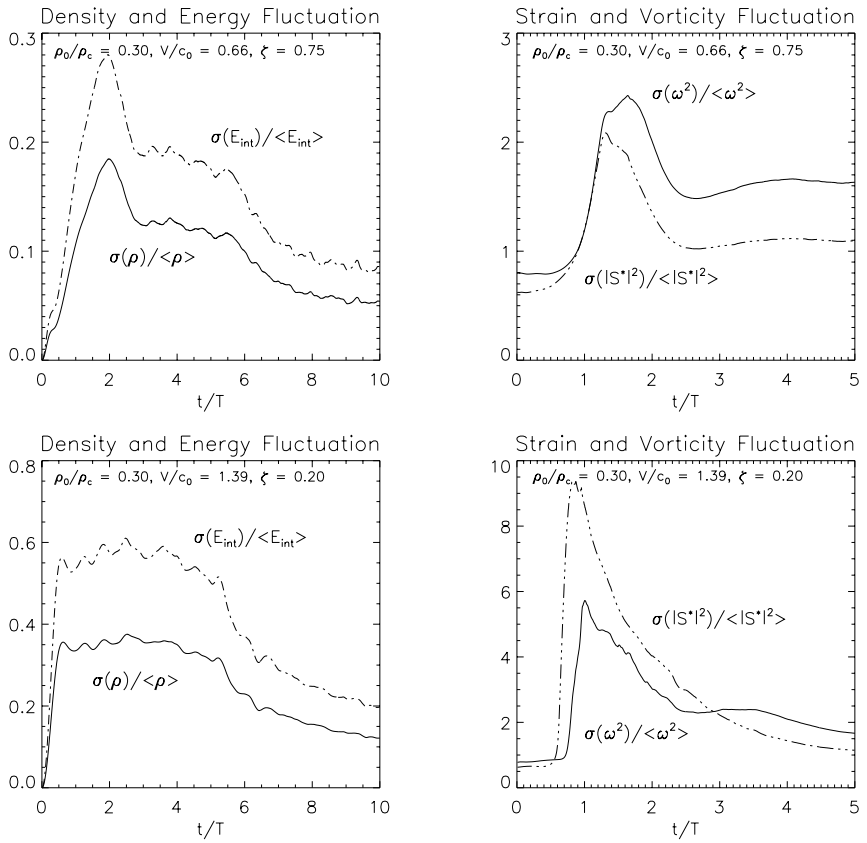

Figure 2.7: Comparison between the simulations `dns432nrh75` with a spectral weight of solenoidal forcing of $\zeta = 0.75$ and `dns432nrh20` with $\zeta = 0.2$. The characteristic Mach numbers are, respectively, $V/c_0 = 0.66$ and $V/c_0 = 1.39$. The panels panels on the left show the RMS fluctuations of internal energy and mass density, respectively, and the corresponding RMS fluctuations of vorticity and the rate of strain are plotted in the panels on the right.

2.5 Spectral Analysis

The quintessence of isotropic turbulence is found in the energy spectrum which describes the distribution of kinetic energy over the various wave numbers. From the turbulence spectrum, three subranges of wave numbers can be identified, firstly, the energy-containing range at the lowest wave numbers in the vicinity of k_0, secondly, an inertial range in which the Kolmogorov cascade of vortices reigns and, finally, the dissipation range of wave numbers, where numerical dissipation dominates the dynamics. In this Section, a discrete formulation of the turbulence energy spectrum is devised and then applied to numerical data from the simulations discussed in Section 2.4.

2.5.1 The Energy Spectrum Function

According to the discussion of Fourier transforms in Section 2.1.2, the spectral representation of the velocity field is given by the generalised function

$$\hat{\boldsymbol{v}}(\boldsymbol{k},t) = \frac{(2\pi)^3}{XYZ}\sum_{jlm}\hat{\boldsymbol{v}}_{jlm}(t)\delta(\boldsymbol{k}-\boldsymbol{k}_{jlm}), \tag{2.49}$$

where the discrete Fourier modes $\hat{\boldsymbol{v}}_{jlm}(t)$ are defined by

$$\hat{\boldsymbol{v}}_{jlm}(t) = \int_0^1 \mathrm{d}\tilde{z}\int_0^1 \mathrm{d}\tilde{y}\int_0^1 \mathrm{d}\tilde{x}\,\boldsymbol{v}(\boldsymbol{x},t)\exp[-2\pi\mathrm{i}(j\tilde{x}+l\tilde{y}+m\tilde{z})]. \tag{2.50}$$

Note that $\hat{\boldsymbol{v}}_{jlm}$ has the dimension of velocity. The dimensionless spatial coordinates are defined by $\tilde{x}_i = x_i/\alpha L$, where the integer α specifies the ratio of the linear size of the fundamental domain to the integral length scale of the flow.

The kinetic energy associated with a mode $\hat{\boldsymbol{v}}_{jlm}(t)$ is given by $\frac{1}{2}\hat{\boldsymbol{v}}_{jlm}(t)\hat{\boldsymbol{v}}^*_{jlm}(t)$. A representation of kinetic energy in the spectral continuum can be constructed as follows. Assuming statistically homogeneous turbulence, the Fourier transform $\hat{\boldsymbol{v}}(\boldsymbol{k},t)$ of the velocity field is uncorrelated except for conjugate wave vectors, i. e., the ensemble average $\langle\hat{\boldsymbol{v}}(\boldsymbol{k},t)\cdot\hat{\boldsymbol{v}}(\boldsymbol{k}',t)\rangle$ is non-zero only for $\boldsymbol{k}+\boldsymbol{k}'=0$. If the velocity field were absolutely integrable, this would motivate a velocity spectrum tensor of the form $\boldsymbol{\Phi}(\boldsymbol{k},t) = \langle\hat{\boldsymbol{v}}(\boldsymbol{k},t)\otimes\hat{\boldsymbol{v}}^*(\boldsymbol{k},t)\rangle$, and half of the trace of $\boldsymbol{\Phi}(\boldsymbol{k},t)$ would yield the kinetic energy. The periodic velocity fields which are considered here, however, necessitate a different approach.

Inspired by Parseval's theorem, let us invoke the *condition* that the total kinetic energy of all discrete Fourier modes must be equal to the mean kinetic energy in physical space:

$$\begin{aligned}\langle e_{\mathrm{kin}}(t)\rangle &= \int_0^1 \mathrm{d}\tilde{z}\int_0^1 \mathrm{d}\tilde{y}\int_0^1 \mathrm{d}\tilde{x}\,\frac{1}{2}|\boldsymbol{v}(\alpha L\tilde{\boldsymbol{x}},t)|^2\\ &= \sum_{jlm}\frac{1}{2}\hat{\boldsymbol{v}}_{jlm}(t)\cdot\hat{\boldsymbol{v}}^*_{jlm}(t).\end{aligned} \tag{2.51}$$

Obviously, this identity expresses the requirement of energy conservation. Now the velocity spectrum tensor can be defined implicitly by the integral relation

$$\int \mathrm{d}^3(\alpha\tilde{k})\,\boldsymbol{\Phi}(\alpha\tilde{k},t) = \sum_{jlm}\langle\hat{\boldsymbol{v}}_{jlm}(t)\otimes\hat{\boldsymbol{v}}^*_{jlm}(t)\rangle, \tag{2.52}$$

where $\alpha\tilde{\boldsymbol{k}} = (\alpha L/2\pi)\boldsymbol{k} = (X/2\pi)\boldsymbol{k}$ is the normalised wave vector which is dual to the dimensionless vector $\tilde{\boldsymbol{x}}/\alpha = \boldsymbol{x}/X$ in physical space.

In the case of statistically isotropic turbulence, $\boldsymbol{\Phi}(\alpha\tilde{k}, t)$ is independent of angular directions in spectral space and, hence, it is of the form [cf. Pope, 2000, Section 6.5.1]

$$\Phi_{ij}(\alpha\tilde{k}, t) = \frac{V^2\tilde{E}(\alpha\tilde{k}, t)}{4\pi\alpha^2\tilde{k}^2}\left(\delta_{ij} - k_i k_j/k^2\right), \tag{2.53}$$

where $\tilde{E}(\alpha\tilde{k}, t)$ is a dimensionless function. Substituting the above expression for $\Phi_{ij}(\alpha\tilde{k}, t)$ on the left-hand side of equation (2.52) and integrating over all angles, we obtain

$$\int \mathrm{d}^3(\alpha\tilde{k})\Phi_{ij}(\alpha\tilde{k}, t) = \frac{2}{3}V^2\int_0^\infty \mathrm{d}(\alpha\tilde{k})\tilde{E}(\alpha\tilde{k}, t)\delta_{ij} \tag{2.54}$$

The velocity spectrum of isotropic turbulence is therefore completely determined by the trace $\Phi_{ii}(\alpha\tilde{k}, t)$ and the tensor equation (2.52) can be contracted to yield the scalar equation

$$\int_0^\infty \mathrm{d}(\alpha\tilde{k})\tilde{E}(\alpha\tilde{k}, t) = \frac{1}{V^2}\sum_{jlm}\frac{1}{2}\langle\hat{\boldsymbol{v}}_{jlm}(t)\cdot\hat{\boldsymbol{v}}^*_{jlm}(t)\rangle = \langle\tilde{e}_{\mathrm{kin}}(t)\rangle. \tag{2.55}$$

Here $\tilde{e}_{\mathrm{kin}}(t) = v_i v_i/2V^2$ is the dimensionless specific kinetic energy. It is the function $E(k, t) = (\alpha L/2\pi)V^2\tilde{E}(\alpha\tilde{k}, t)$ which is called the *energy spectrum function*.

For periodic flows, we face the difficulty that $\tilde{E}(\alpha\tilde{k}, t)$ is a generalised function. This can be seen if the sum over all modes in equation (2.55) is expressed as an integral,

$$\sum_{jlm}\frac{1}{2}\langle\hat{\boldsymbol{v}}_{jlm}(t)\cdot\hat{\boldsymbol{v}}^*_{jlm}(t)\rangle = \int_0^\infty \mathrm{d}(\alpha\tilde{k})\sum_{jlm}\frac{1}{2}\langle\hat{\boldsymbol{v}}_{jlm}(t)\cdot\hat{\boldsymbol{v}}^*_{jlm}(t)\rangle\delta[\alpha(\tilde{k} - \tilde{k}_{jlm})], \tag{2.56}$$

where $\alpha\tilde{k}_{jlm} = (j^2 + l^2 + m^2)^{1/2}$. Hence,

$$\tilde{E}(\alpha\tilde{k}, t) = \frac{1}{V^2}\sum_{jlm}\frac{1}{2}\langle\hat{\boldsymbol{v}}_{jlm}(t)\cdot\hat{\boldsymbol{v}}^*_{jlm}(t)\rangle\delta[\alpha\tilde{k} - (j^2 + l^2 + m^2)^{1/2}]. \tag{2.57}$$

In this form, the energy spectrum function is certainly not suitable for numerical evaluation. Consequently, a discrete counterpart of $\tilde{E}(\alpha\tilde{k}, t)$ is essential to proceed.

To that end, let us introduce a staggered mesh of wave numbers,

$$\mathcal{K} = \{0, k_{1/2}, k_1, k_{3/2}, \ldots\} = \{k_{(n-1)/2} | n \in \mathbb{N}\},$$

and define a discrete measure

$$\mu_n = \sum_{\alpha^2\tilde{k}^2_{n-1/2}\le\alpha^2\tilde{k}^2\le\alpha^2\tilde{k}^2_{n+1/2}}\sum_{jlm}\left(\frac{2\pi}{\alpha L}\right)^3\delta^{\alpha^2\tilde{k}^2}_{j^2+l^2+m^2}, \tag{2.58}$$

associated with the wave number k_n. Note that the principal summation index $\alpha^2\tilde{k}^2 \in \mathbb{N}$. As one can see from the definition, μ_n is the total volume of all spectral cells of wavenumber k_{jlm} within the interval $[k_{n-1/2}, k_{n+1/2}]$. The normalised measure $\tilde{\mu}_n = (\alpha L/2\pi)^3\mu_n$ is just the corresponding number of cells. The average kinetic energy of modes with wave number $k_{n-1/2} \le k_{jlm} \le k_{n+1/2}$ at time t is thus given by

$$\Phi_n(t) = \frac{1}{\tilde{\mu}_n}\sum_{\alpha^2\tilde{k}^2_{n-1/2}\le\alpha^2\tilde{k}^2\le\alpha^2\tilde{k}^2_{n+1/2}}\sum_{jlm}\frac{1}{2}\hat{\boldsymbol{v}}_{jlm}(t)\cdot\hat{\boldsymbol{v}}^*_{jlm}(t)\delta^{\alpha^2\tilde{k}^2}_{j^2+l^2+m^2}. \tag{2.59}$$

For small wave numbers $\tilde{k}_n \sim 1$, $\Phi_n(t)$ depends on the instantaneous state of the system. For large wave numbers $\tilde{k}_n \gg 1$, on the other hand, the above summation will cover a great number of cells, even if the interval $[\tilde{k}_{n-1/2}, \tilde{k}_{n+1/2}]$ is quite narrow, i. e., $\tilde{k}_{n+1/2} - \tilde{k}_{n-1/2} \ll 1$. Hence, in the case of isotropic and statistically stationary turbulence, it can be expected that $\Phi_n(t)$ approaches the ensemble average of $\frac{1}{2}\hat{\boldsymbol{v}}_{jlm}(t) \cdot \hat{\boldsymbol{v}}^*_{jlm}(t)$ in the corresponding region of spectral space.

For this reason, we may conjecture that quasi-integration of $\Phi_h(t)$ over the spherical shell of wave number k_n yields an approximation to the energy spectrum at least in the limit of large wave numbers. Defining

$$\tilde{E}_n(t) = \frac{4\pi k_n^2}{V^2}\Phi_n(t), \tag{2.60}$$

we have

$$\int_0^\infty \mathrm{d}(\alpha\tilde{k}) \sum_n \tilde{E}_n(t)\frac{\tilde{\mu}_n}{4\pi k_n^2}\delta[\alpha(\tilde{k} - \tilde{k}_n)] = \frac{1}{V^2}\sum_{jlm}\frac{1}{2}\langle\hat{\boldsymbol{v}}_{jlm}(t) \cdot \hat{\boldsymbol{v}}^*_{jlm}(t)\rangle. \tag{2.61}$$

It is by the meaning of this identity, that we will subsequently call $\tilde{E}_n(t)$ the *instantaneous discrete energy spectrum function*. On grounds of the ergodicity argument mentioned above, $\sum_n \tilde{E}_n(t)\delta[\alpha(\tilde{k} - \tilde{k}_n)]$ can be regarded as approximation to the normalised energy spectrum function,

$$\tilde{E}(\alpha\tilde{k}) = \frac{2\pi}{\alpha L} \cdot \frac{1}{V^2}\, E(k), \tag{2.62}$$

where $\tilde{\mu}_n \mathrm{d}(\alpha\tilde{k})/4\pi k_n^2$ is to be taken as the appropriate measure for the integration[7]. Averaging $\tilde{E}_n(t)$ for steady turbulence over many integral time scales, the approximation is expected to match the exact spectrum asymptotically as $n \to \infty$.

The energy spectrum function can be separated into a longitudinal and a transversal part, in discrete form denoted by $E_n^{\parallel}(t)$ and $E_n^{\perp}(t)$, respectively. The longitudinal spectrum function is computed according to equations (2.59) and (2.60), with the Fourier modes $\hat{\boldsymbol{v}}_{jlm}(t)$ replaced by the modes projected parallel to the wave vector $\boldsymbol{k}_{jlm}$,

$$\hat{\boldsymbol{v}}^{\parallel}_{jlm} = \left(\frac{\boldsymbol{k}_{jlm} \cdot \hat{\boldsymbol{v}}_{jlm}}{|\boldsymbol{k}_{jlm}|^2}\right)\boldsymbol{k}_{jlm}. \tag{2.63}$$

The transversal part of the spectrum function, on the other hand, is obtained by setting $\hat{\boldsymbol{v}}^{\perp}_{jlm}(t) = \hat{\boldsymbol{v}}_{jlm}(t) - \hat{\boldsymbol{v}}^{\parallel}_{jlm}(t)$ in place of $\hat{\boldsymbol{v}}_{jlm}(t)$. Since

$$|\hat{\boldsymbol{v}}^{\parallel}_{jlm}|^2 + |\hat{\boldsymbol{v}}^{\perp}_{jlm}|^2 = |\hat{\boldsymbol{v}}_{jlm}|^2, \tag{2.64}$$

the sum of $E_n^{\parallel}(t)$ and $E_n^{\perp}(t)$ gives the total spectrum function $E_n(t)$.

According to the *second similarity hypothesis* of Kolmogorov, the so-called compensated spectrum function $\Psi(k) = \langle\epsilon\rangle^{-2/3}k^{5/3}E(k)$ is approximately constant for an

[7] Only by means of this measure, the discrete and continuous points of view are reconciled. As an alternative, one might use $\mathrm{d}(\alpha\tilde{k})$ as the right measure in both cases and renormalise the discrete energy spectrum function such that the correct integral is obtained. In this case, however, consistency would come at the cost of changing the energy in a certain wave number bin by a factor depending on the particular choice of the wave number grid $\mathcal{K}$ and the energy spectrum itself.

incompressible flow in the inertial subrange of wave numbers [cf. Pope, 2000, Section 6.5]. This suggests the definition of a *compensated discrete spectrum function*,

$$\Psi_n(t) = \left[\frac{\alpha}{2\pi}\langle\tilde{\epsilon}(t)\rangle\right]^{-2/3} (\alpha\tilde{k}_n)^{5/3}\tilde{E}_n^{\perp}(t), \tag{2.65}$$

as an indicator of Kolmogorov scaling. Note that only the transversal part of the energy spectrum is compensated, because it is the incompressible fraction of turbulence energy which *a priori* fulfils Kolmogorov scaling. For the calculation of $\Psi_n(t)$, the mean dissipation rate has to be determined, and so we face the problem of numerical dissipation.

2.5.2 Numerical Dissipation

The paradigm of turbulence put forward by Kolmogorov is based on the balance between energy injection and dissipation in equilibrium, regardless of the detailed mechanism of dissipation. For isotropic incompressible turbulence, this implies the scaling relation $E(k) = C\langle\epsilon\rangle^{2/3}k^{-5/3}$ in the inertial subrange. The universality of Kolmogorov scaling was confirmed in many laboratory experiments and numerical simulations. For example, Cao et al. [1996] performed high-resolution 3D numerical simulations of Navier-Stokes turbulence with normal viscosity and so-called hyper-viscosity and found more or less the same scaling independent of the spectral dissipation profile.

The details of the numerical dissipation produced by the PPM are basically unknown, but it is possible to infer the net mean dissipation rate from the globally averaged energy conservation laws. Since the BCs are periodic, the total flux through the boundary surfaces cancels out, and the equations governing the time evolution of the mean total and internal energy are of the following simple form:

$$\langle\Pi\rangle = \frac{\mathrm{d}}{\mathrm{d}t}\langle E_{\mathrm{tot}}\rangle = \langle\rho v_i a_i\rangle, \tag{2.66}$$

$$\rho_0\langle\epsilon\rangle = \frac{\mathrm{d}}{\mathrm{d}t}\langle E_{\mathrm{int}}\rangle = \rho_0\epsilon_{\mathrm{num}} - \langle Pd\rangle, \tag{2.67}$$

$$\langle\Pi\rangle - \rho_0\langle\epsilon\rangle = \frac{\mathrm{d}}{\mathrm{d}t}\langle K\rangle = \langle\Pi\rangle - \rho_0\epsilon_{\mathrm{num}} + \langle Pd\rangle. \tag{2.68}$$

Of course, no dissipation becomes apparent in the averaged equation for the total energy because the PPM is a conservative scheme. But the mean rate of numerical dissipation $\rho_0\epsilon_{\mathrm{num}}$ contributes to the increase of internal energy at the expense of kinetic energy.

In fact, there are two distinct mechanisms of dissipation in a compressible fluid. On the one hand, *pressure-dilatation* accounts for the conversion of internal energy into mechanical energy and vice versa as the fluid, respectively, expands or contracts. Although pressure-dilatation might locally produce mechanical work, it is effectively a dissipative irreversible process, and the net rate of heat production is given by $-\langle Pd\rangle$. If pronounced shocks are present, however, there might be transient phases in which $\langle Pd\rangle$ becomes positive. All dissipation apart from the explicitly resolved pressure-dilatation, on the other hand, must be of numerical origin, i. e.,

$$\tilde{\epsilon}_{\mathrm{num}} = \frac{T}{\rho_0 V^2}\left(\frac{\mathrm{d}}{\mathrm{d}t}\langle E_{\mathrm{int}}\rangle + \langle Pd\rangle\right) \tag{2.69}$$

Representative values of $\tilde{\epsilon}_{\text{num}}$ and the ratio $-\langle Pd\rangle/\epsilon_{\text{num}}$ are listed in the Tables 2.2, 2.3 and 2.4. Invoking Kolmogorov's similarity hypothesis, we can say that ϵ_{num} corresponds to the rate of energy transfer through the turbulence cascade on a scale $l \sim \Delta$ in the physical counterpart of the simulated flow. Thus, a reasonable approximation to the compensated spectrum should be obtained if $\tilde{\epsilon}_{\text{num}}$ was taken to be the mean dissipation rate in equation (2.65).

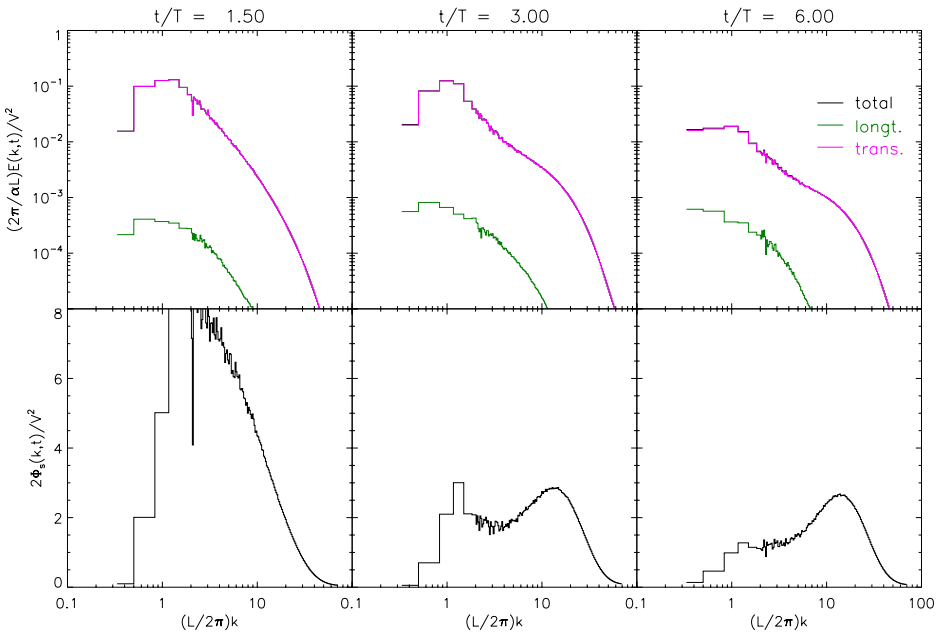

Figure 2.8: Turbulence energy spectra for the simulation `dns432nrsl`. The panels in the row on the top show the instantaneous discrete energy spectrum functions at representative stages in the advanced production regime, near equilibrium and in the late decay regime. In the bottom panels, the corresponding compensated spectrum functions are plotted.

$\tilde{t}$	$\langle\tilde{e}_{\text{kin}}\rangle$	$\langle e^{\parallel}_{\text{kin}}\rangle/\langle e_{\text{kin}}\rangle$	$\tilde{\epsilon}_{\text{num}}$	$-\langle Pd\rangle/\rho_0\epsilon_{\text{num}}$	η_{eff}/Δ	β	l_{p}/L
1.5	0.891	$3.74 \cdot 10^{-3}$	0.130	0.422	0.229	1.82	
2.0	0.885	$6.74 \cdot 10^{-3}$	0.985	0.073	0.250	1.57	0.0659
2.5	0.706	$7.56 \cdot 10^{-3}$	0.660	0.095	0.264	1.59	0.0587
3.0	0.728	$8.16 \cdot 10^{-3}$	0.474	0.107	0.261	1.62	0.0674
4.0	0.574	$9.41 \cdot 10^{-3}$	0.498	0.053	0.264	1.61	0.0615
6.0	0.168	$2.13 \cdot 10^{-2}$	0.088	0.051	0.285	1.69	0.0644

Table 2.2: Energy, dissipation and characteristic length scales for `dns432nrsl`

2.5.3 Turbulence Energy Spectra

Using the definition of a discrete energy spectrum function (2.60), a number of spectra were computed from the full 3D dumps of the simulation data at selected times.

Moreover, by evaluating the mean pressure-dilatation and using the time derivative of internal energy from the statistical data, the mean dissipation rate ϵ_{num} was determined for the calculation of compensated spectrum functions. Some of the obtained spectra are shown in Figures 2.8, 2.9 and 2.10 for the low-density simulations `dns432nrsl`, `dns432nrh75` and `dns432nrh20`, respectively. For each spectrum, a coarse equidistant wave number mesh was used in the energy containing range, $0 \leq \tilde{k} \leq 2$, and a logarithmic mesh with narrow bins for the larger wave numbers. Mean values of the turbulence energy and the numerical dissipation are listed in the Tables 2.2, 2.3 and 2.4.

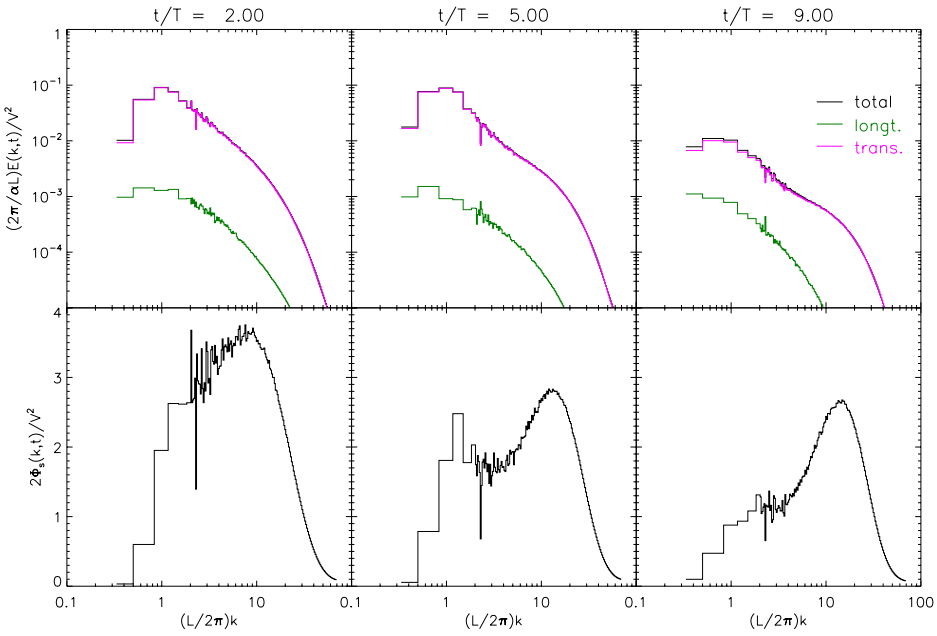

Figure 2.9: Turbulence energy spectra for the simulation `dns432nrh75`.

$\tilde{t}$	$\langle \tilde{e}_{\text{kin}} \rangle$	$\langle e^{\parallel}_{\text{kin}} \rangle / \langle e_{\text{kin}} \rangle$	$\tilde{\epsilon}_{\text{num}}$	$-\langle Pd \rangle / \rho_0 \epsilon_{\text{num}}$	η_{eff}/Δ	β	l_{p}/L
2.0	0.668	$2.25 \cdot 10^{-2}$	0.322	0.158	0.244	1.66	0.0830
4.0	0.544	$2.10 \cdot 10^{-2}$	0.305	0.106	0.261	1.62	0.0601
5.0	0.571	$1.87 \cdot 10^{-2}$	0.350	0.070	0.260	1.61	0.0659
7.0	0.252	$2.75 \cdot 10^{-2}$	0.170	0.059	0.268	1.61	0.0601
9.0	0.092	$6.72 \cdot 10^{-2}$	0.037	-0.150	0.283	1.69	0.0644

Table 2.3: Energy, dissipation and characteristic length scales for model `dns432nrh75`

The panels on the top of Figure 2.8 show, from left to right, the discrete energy spectrum function $\tilde{E}_n(t)$ at representative stages in the production regime, close to equilibrium and, finally, in the advanced decay regime for the simulation `dns432nrsl`. In addition, the corresponding longitudinal spectrum functions $\tilde{E}^{\parallel}_n(t)$ are plotted. The corresponding bottom panels show plots of the compensated spectrum function $\tilde{\Psi}_n(t)$. From these spectra, it becomes clear that a resolution of $N = 432$ is just at the brink

where an inertial subrange begins to take shape. Even in the quasi-equilibrium state, there is merely a narrow window of wave numbers in the vicinity of $\tilde{k} = 3.0$, in which nearly Kolmogorov scaling with $C \approx 1.7$ is found. In the second and third row of panels, there is a pronounced maximum of the compensated spectrum function at $\tilde{k} \approx 15$ corresponding to a flattening of the energy spectrum in comparison to the Kolmogorov law. This so-called *bottleneck effect* was observed in many numerical simulations, for instance, by Cao et al. [1996] and Sytine et al. [2000]. At time $\tilde{t} = 1.5$, on the other hand, the spectrum does not show a bump at higher wave numbers. In the production phase, the cascade of eddies is still building up and the small-scale features, which cause the distortion of the spectrum seen at later time, are not yet developed.

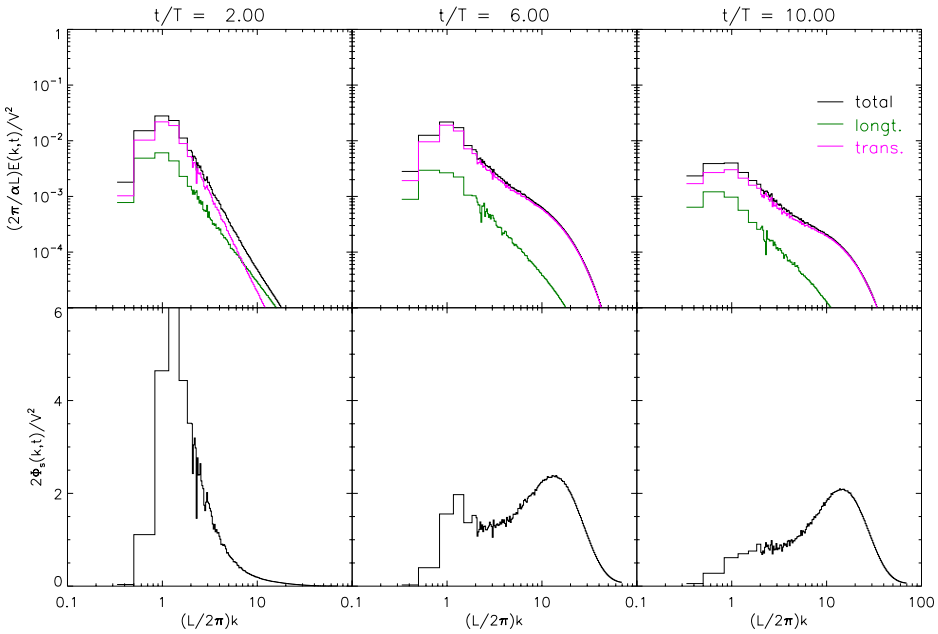

Figure 2.10: Turbulence energy spectra for the simulation `dns432nrh20`.

$\tilde{t}$	$\langle \tilde{e}_{\mathrm{kin}} \rangle$	$\langle e^{\parallel}_{\mathrm{kin}} \rangle / \langle e_{\mathrm{kin}} \rangle$	$\tilde{\epsilon}_{\mathrm{num}}$	$-\langle Pd \rangle / \rho_0 \epsilon_{\mathrm{num}}$	$\eta_{\mathrm{eff}}/\Delta$	β	l_{p}/L
2.0	0.103	0.250	0.0105	0.663	0.811	5.57	0.323
3.5	0.157	0.195	0.0278	0.940	0.359	2.24	0.229
5.0	0.147	0.189	0.0618	0.147	0.300	1.75	0.066
6.0	0.121	0.134	0.0443	0.198	0.288	1.71	0.063
9.0	0.045	0.158	0.0141	-0.078	0.282	1.68	0.060

Table 2.4: Energy, dissipation and characteristic length scales for model `dns432nrh20`

More or less the same results are found in the case of `dns432nrh75`. Due to the higher characteristic Mach number $V/c_0 \approx 0.66$, the gap between the total and the longitudinal energy spectrum functions is smaller, but the spectra are very similar in shape to those of simulation `dns432nrh20`. Once more, a value $C \approx 1.7$ is found for the compensated spectrum function around $\tilde{k} = 3.0$ at time $\tilde{t} = 5.0$. As for `dns432nrh20`,

differences can evidently be seen in Figure 2.10. There is a significant fraction of turbulence energy in the longitudinal components of the Fourier modes, particularly, in the early phase which is dominated by shock waves. The scaling appears to deviate markedly from the Kolmogorov law with a steeper fall-off. In the course of the transition to the shocklet-regime the spectra change in shape and become similar to those of simulation `dns432nrh75`, apart from a significantly lower value of the Kolmogorov constant, $C \approx 1.3$, at time $\tilde{t} = 5.0$. Therefore, it appears that the universality of the Kolmogorov law faces its limitations at transonic Mach numbers and for velocity fields with significant non-rotational components.

The origin of the bottleneck in turbulence energy spectra is not fully understood yet. To a certain extent, it might be a genuine feature of isotropic turbulence, a point of view which is supported by She and Jackson [1993], who reported that experimental data seemingly indicate a k^{-1} power law behaviour of the energy spectrum function in the vicinity of the wave number of maximum dissipation. They attributed the anomalous scaling to dynamical peculiarities on scales which are significantly influenced by dissipation, whereas Dobler et al. [2003] suggested that it might be a generic feature of three-dimensional spectra, which is less prominent in one-dimensional spectra. However, they do not clarify how the occurrence of this effect comes about in the three-dimensional spectra. In any case, the peaks of $\tilde{\Psi}_n(t)$ at the bottleneck wave number $\tilde{k} \approx 15$ are quite distinct. There is certainly a significant pile-up of energy at wave numbers $\tilde{k} \gtrsim 10$, once turbulence is fully developed. This might be caused at least in part by differences between the numerical dissipation produced by the PPM and viscous dissipation of physical origin (or the action of SGS stresses).

2.5.4 Dissipation Length Scales

The effect of numerical dissipation is equivalent to an *implicit filter* which smoothes out the flow on a certain length scale, say, Δ_{eff}. Fourier modes of wave number larger than $\pi/\Delta_{\mathrm{eff}}$ are suppressed by the filter. It is common to assume a sharp cutoff corresponding to the numerical discretisation. If a grid of resolution $\Delta = \alpha L/N$ is used, then the summation over the modes in equation (2.7) is truncated for indices $j, l, m \geq N - 1$. As the Fourier modes of a real function are Hermitian conjugate, it follows that the smallest wave number which can be resolved in all spatial directions is π/Δ and, thus, $\Delta_{\mathrm{eff}} = \Delta$. The corresponding dimensionless cutoff wave number is $\tilde{k}_{\mathrm{c}} = N/2\alpha = 72$ [8].

An improved estimate of the effective length scale Δ_{eff}, which accounts for the dissipation produced by the PPM, is based upon the notion of a characteristic filter scale [Lund, 1997]. For a one-dimensional filter of explicitly known functional form, a characteristic length scale can be calculated from the second moment of the Fourier transform of the filter kernel, the so-called *transfer function*. Since the implicit filter associated with the PPM is three-dimensional and the corresponding transfer function is unknown, we have to resort to the numerically computed energy spectra. Using Kolmogorov's law as reference spectrum function, let us introduce an *effective transfer function*

$$\hat{G}^2_{\mathrm{eff}}(k,t) = \frac{E(k,t)}{E_\infty(k,t)} = \frac{1}{C}\Psi(k,t), \tag{2.70}$$

[8] Since the diagonal of a cubic domain is larger by a factor $\sqrt{3}$ than the edges, modes in diagonal direction can be resolved up to a wave number $72\sqrt{3}$.

where $E_\infty(k,t) = C\epsilon_{\rm num}^{2/3}(t)k^{-5/3}$, and $C = 1.65$ [cf. Gotoh and Fukayama, 2001]. The second moment of the squared transfer function is defined by[9]

$$M^{(2)}[\hat{G}^2_{\rm eff}] = \int_0^\infty k^2 \hat{G}^2_{\rm eff}(k,t){\rm d}k. \tag{2.71}$$

Of course, $E(k,t)$ is not conform with the Kolmogorov law at wave numbers comparable to $k_0 = 2\pi/L$, because of energy injection on the largest length scales. However, the contribution of these wave numbers to the above integral is small due to the factor k^2. Thus, we shall ignore this error. Discretising the transfer function according to the procedure outlined in Section 2.5.1 and cutting off at wavelength π/Δ, the following approximation to the second moment is obtained:

$$M^{(2)}[\hat{G}^2_{\rm eff}] \simeq \frac{1}{C}\left(\frac{2\pi}{\alpha L}\right)^3 \int_0^{N/2} {\rm d}(\alpha\tilde{k}) \sum_n \Psi_n(t)\frac{\tilde{\mu}_n}{4\pi}\delta[\alpha(\tilde{k}-\tilde{k}_n)]. \tag{2.72}$$

The second moment of the filter transfer function has the dimension of inverse length cubed. Hence, a length scale is given by $(M^{(2)}[\hat{G}^2])^{-1/3}$, which is usually normalised by referring to the second moment of the sharp cutoff filter. The transfer function of this filter is given by $\hat{G}_\Delta(k) = \theta(\pi/\Delta - k)$, and the second moment is $M^{(2)}[\hat{G}^2_\Delta] = (\pi/\Delta)^3/3$. Setting $M^{(2)}[\hat{G}^2_{\rm eff}] = (\pi/\Delta_{\rm eff})^3/3$, the *effective filter scaling factor* of the PPM is therefore estimated to be

$$\beta = \frac{\Delta_{\rm eff}}{\Delta} = \frac{N}{2}\left[\frac{3}{C}\sum_{n=1}^{n_{\rm c}} \Psi_n(t)\frac{\tilde{\mu}_n}{4\pi}\right]^{-1/3}, \tag{2.73}$$

where $n_{\rm c} = \max\{n|\tilde{k}_n \le \tilde{k}_{\rm c}\}$. Numerically determined values of β for the three simulations with marginally relativistic Fermi gas are listed in the Tables 2.2, 2.3 and 2.4. It appears that β is more or less universal. For fully developed turbulence under stationary energy injection, we find $\Delta_{\rm eff} \approx 1.6\Delta$. As $\Delta_{\rm eff}$ is the smallest scale of the resolved flow, the *effective Reynolds number* is given by ${\rm Re}_{\rm eff} = (N/\alpha\beta)^{4/3} \approx 400$. Of course, the dependence of β on the numerical resolution should be investigated too. Changes can be expected towards lower resolution, because the energy-containing and the dissipation subrange will increasingly overlap. At higher resolution, on the other hand, β should asymptotically approach a value independent of N. Unfortunately, the attempt to validate this conjecture would require an undue amount of computational resources though.

In fact, $\Delta_{\rm eff}$ is much smaller than the length scale of maximum dissipation $l_{\rm p}$, which is given by the maximum of $\tilde{k}^2\tilde{E}_n(t) = \tilde{k}^{1/3}\tilde{\Psi}_n(t)$. For fully developed turbulence, the peak of dissipation is located close to the second maximum of $\tilde{\Psi}_n(t)$, with a typical value $l_{\rm p} \approx 0.065L$. This result is yet another indication of the very narrow range of inertial scales. In essence, the flow structure on these scales can be extracted by smoothing the velocity field with a filter of characteristic length larger than $l_{\rm p}$. In particular, a Gaussian filter of characteristic scale $\Delta_{\rm G} = 2l_{\rm p}$ was applied to the spectral

[9] Usually, filter length scales are defined by the second moment of $\hat{G}$ rather than $\hat{G}^2$. However, in the context of turbulence energy and in relation to the scale $\eta_{\rm eff}$ introduced below, it seems better motivated to use the square of the transfer function.

representation of the velocity data of model `dns432nrsl` at the end of the stationary regime ($\tilde{t} = 3.0$). The transfer function of the Gaussian filter is given by

$$\hat{G}_{\mathrm{G}}(\alpha\tilde{k}) = \exp\left[-\frac{\pi^2}{6}\left(\frac{\Delta_{\mathrm{G}}}{\alpha L}\right)^2 (\alpha\tilde{k})^2\right]. \tag{2.74}$$

The filtered Fourier modes are given by $\langle\hat{\boldsymbol{v}}_{jlm}\rangle_{\mathrm{G}} = \hat{G}_{\mathrm{G}}(\alpha\tilde{k}_{jlm})\hat{\boldsymbol{v}}_{jlm}$, and the corresponding velocity field $\langle\boldsymbol{v}\rangle_{\mathrm{G}}(\boldsymbol{x}, t)$ is obtained by computing the inverse Fourier transform. Basically, the filtering removes the more random velocity fluctuations on the smallest scales, while vortical structures in the inertial subrange are preserved. This is illustrated in Figure 2.11, which shows a planar section through the filtered velocity field in simulation `dns432nrsl` together with contours of the fully resolved velocity $v = (v_i v_i)^{1/2}$.

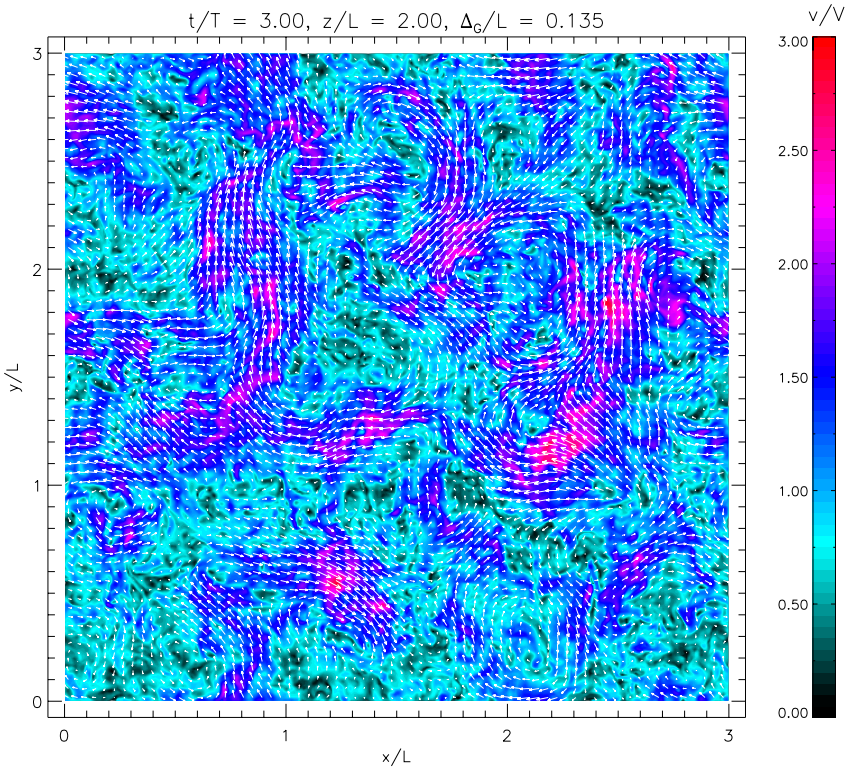

Figure 2.11: Flow map of the filtered velocity field $(\langle v_x\rangle_{\mathrm{G}}, \langle v_y\rangle_{\mathrm{G}})$ with contours of the fully resolved magnitude of the velocity, $\tilde{v} = (v_x^2 + v_y^2 + v_z^2)^{1/2}$, for the simulation `dns432nrsl`. The applied filter is Gaussian, with twice the length scale of maximum dissipation chosen as characteristic filter width. The arrows depicting the filtered velocity are normalised such that a length equal to the spacing $6\Delta/L$ between contiguous arrows corresponds to a magnitude $(\langle v_x\rangle_{\mathrm{G}}^2 + \langle v_y\rangle_{\mathrm{G}}^2)^{1/2} = V$.

Yet another approach is the calculation of the *effective* Kolmogorov scale η_{eff}, which marks the lower bound of the range of length scales dominated by dissipation. In the case of viscous dissipation, this scale is defined by $\eta = (\nu^3/\langle\epsilon\rangle)^{1/4}$. In fact, η is

usually much smaller than the length scale of maximum dissipation. In order to determine the scale η_{eff} from known properties of a numerically computed flow, the velocity derivatives $v_{i,k}$ can be utilised as a probe of the smallest turbulent velocity fluctuations. To that end, we consider the full contraction $v_{i,k}v_{i,k}$, which is represented by $\hat{v}_i k_k \hat{v}_i^* k_k$ in spectral space. The average of $v_{i,k}v_{i,k}$ in physical space can be expressed as the integral over the energy spectrum times k^2:

$$\langle v_{i,k}v_{i,k}\rangle = 2\int_0^\infty k^2 E(k,t)\mathrm{d}k. \tag{2.75}$$

Expressing the energy spectrum function $E(k,t)$ in terms of the effective transfer function according to equation (2.70), the integral on the right-hand side becomes

$$2\int_0^\infty k^2 \hat{G}_{\text{eff}}^2(k,t)E_\infty(k,t)\mathrm{d}k = 2C\epsilon_{\text{num}}^{2/3}(t)\int_0^\infty k^{1/3}\hat{G}_{\text{eff}}^2(k,t)\mathrm{d}k. \tag{2.76}$$

On the other hand, $\langle v_{i,k}v_{i,k}\rangle$ can be related to mean squared rate of strain, dilatation and vorticity:

$$\langle v_{i,k}v_{i,k}\rangle = \langle |S|^2 - d^2\rangle = \langle \omega^2 + d^2\rangle. \tag{2.77}$$

Putting together the different expressions for $\langle v_{i,k}v_{i,k}\rangle$, we obtain the equation

$$\left[2C\int_0^\infty k^{1/3}\hat{G}_{\text{eff}}^2(k,t)\mathrm{d}k\right]^{-3/2} = \frac{\epsilon_{\text{num}}}{\langle |S|^2 - d^2\rangle^{3/2}}, \tag{2.78}$$

where the expressions on both sides have the dimension of length squared.

The numerical evaluation of the integral on the left-hand side is prone to difficulties, because the contributions from small wave numbers, for which the notion of $\hat{G}_{\text{eff}}^2(k,t)$ is ill posed, are not suppressed as in equation (2.72). For this reason, we will define the effective Kolmogorov scale in terms of the mean dissipation rate and the averaged structural invariants, which are readily obtained from numerical data:

$$\eta_{\text{eff}} = \frac{\epsilon_{\text{num}}^{1/2}}{\langle |S|^2 - d^2\rangle^{3/4}} = \frac{\epsilon_{\text{num}}^{1/2}}{\langle \omega^2 + d^2\rangle^{3/4}}. \tag{2.79}$$

Motivated by the relation $\eta = (\nu^3/\langle\epsilon\rangle)^{1/4}$, an effective viscosity $\nu_{\text{eff}} = \eta_{\text{eff}}^2\langle |S|^2 - d^2\rangle^{1/2}$ can be formulated. However, this is only a formal definition because, *a priori*, it can not be assumed that numerical dissipation acts like viscous dissipation at all. For nearly incompressible flows, $d \ll |S|$. Then the Smagorinsky model is recovered, with the subgrid scale viscosity in place of the numerical viscosity and the Smagroinsky length l_{S} as effective Kolmogorov scale. This observation will be picked up as a key idea for SGS modelling. In stochastic equilibrium, once more a nearly universal value of $\eta_{\text{eff}} \approx 0.26\Delta$ is obtained from the simulation data. This value is by a factor of about 1.5 larger than the Smagorinsky length for the sharp cutoff filter, a factor which is quite close to the typical value of the effective filter scaling factor $\beta = \Delta_{\text{eff}}/\Delta \approx 1.6$. This seems to indicate that both the notion of an effective filter scale Δ_{eff} and an effective Kolmogorov scale η_{eff} are sensible and numerically sound. As a concluding remark, note that the typical value of η_{eff} indicates that numerical dissipation acts in such a way that the flow is actually under-resolved. This might in part explain the strong bottleneck effect observed in the spectra.

Chapter 3

Subgrid Scale Models

Formally, the filtering approach stands between the direct approach and the statistical approach and probably will produce in the future a unified theory linking the direct approach to the statistical one by a continuous interval of intermediate steps.

M. Germano, **Turbulence: the filtering approach**

Quantitative Unstimmigkeiten sind in der Wissenschaft an der Tagesordnung. Sie bilden ein "Meer von Anomalien", das jede einzelne Theorie umgibt.

P. Feyerabend, **Wider den Methodenzwang**

There is a substantial variety of subgrid scale (SGS) models which have been proposed by scientists and engineers in the last few decades. A discussion of some representative models can be found, for instance, in Lesieur and Métais [1996] or Meneveau and Katz [2000]. An extensive overview of SGS models for incompressible flows is given in the book of Sagaut [2001]. For the purpose of modelling the turbulent flame speed, above all we have to tackle the problem of determining the SGS turbulence energy, i. e., the integrated kinetic energy of SGS modes. Unfortunately, the non-linearity of the hydrodynamical conservation laws entails a major obstacle: there is no closed analytical expression or dynamical equation in terms of known quantities from which the turbulence energy could be computed. In consequence, either additional equations which determine SGS moments of higher order are formulated, or one resorts to more or less heuristic approximations which are called *closures*. In this Chapter, a subgrid scale model based on a conservation law for the turbulence energy is developed and the more common algebraic closures for this equation are discussed. For each of these closures a parameter has to be determined by means of an approximate turbulence theory or from DNS data. In any case, the self-similarity of turbulence in the inertial subrange implies scale invariance of the mean closure parameters. From the evaluation of DNS data, it became clear that the commonly used closures are merely crude devices of making the complicated turbulent interactions between different scales computationally accessible without explicitly resolving the whole range of scales. The outcome of

implementing the SGS models in large eddy simulations (LES) of turbulent burning will be discussed in the next Chapter.

3.1 The Filtering Approach

To begin with, let us introduce a separation of length scales into a range $l \gtrsim \Delta$, for which the flow is *numerically resolved*, and a complementary range of scales $l \lesssim \Delta$, which are called the *subgrid scales*. The range of resolved scales must encompass the whole energy-containing range. Then it can be assumed that $l \sim \Delta$ is within the inertial range of the physical flow. For brevity, we shall always refer to the numerically resolved quantities with the standard symbols, whereas the hypothetical exact solutions of the dynamical equations in the continuum limit, i. e., for infinite resolution, are indicated by the superscript ∞ on top of the corresponding symbol. Notwithstanding the deplorable lack of any proof of existence, we shall call the latter *ideal* quantities[1]. A customary device of relating the smoothed numerical solutions to the intended exact solutions is a *filter*, i. e., a convolution operation which satisfies certain properties, as outlined in Appendix A.1. Introducing an *implicit* or *effective filter* $\langle\,\rangle_{\text{eff}}$ which accounts for the combined effect of numerical discretisation and dissipation, the resolved velocity field $\boldsymbol{v}(\boldsymbol{x},t)$ can be related to the corresponding ideal field $\overset{\infty}{\boldsymbol{v}}(\boldsymbol{x},t)$ via[2]

$$\boldsymbol{v}(\boldsymbol{x},t) = \frac{\langle \overset{\infty}{\rho}(\boldsymbol{x},t)\overset{\infty}{\boldsymbol{v}}(\boldsymbol{x},t)\rangle_{\text{eff}}}{\rho(\boldsymbol{x},t)}, \tag{3.1}$$

where $\rho(\boldsymbol{x},t) = \langle \overset{\infty}{\rho}(\boldsymbol{x},t)\rangle_{\text{eff}}$ is the filtered mass density. Quantities such as the velocity or specific energy are therefore understood as mass-weighted averages over each grid cell. For a state variable like the pressure, on the other hand, we have

$$P(\boldsymbol{x},t) = \langle \overset{\infty}{P}(\boldsymbol{x},t)\rangle_{\text{eff}}. \tag{3.2}$$

Identifying the resolved velocity in LES of compressible flows with the mass-weighted filtered physical velocity, the dynamical equations assume the same form as those for the ideal quantities except for additional terms stemming from SGS turbulence [Moin et al., 1991]. In particular, the resolved momentum $p_i = \rho v_i = \langle \overset{\infty}{\rho}\overset{\infty}{v_i}\rangle$ is given by the *quasi-Navier-Stokes equation* (qNSE)

$$\frac{\partial}{\partial t}\rho v_i + \frac{\partial}{\partial x_k}\rho v_i v_k = -\frac{\partial P}{\partial x_i} + \rho(a_i + g_i) + \frac{\partial}{\partial x_k}(\sigma_{ik} + \tau_{ik}). \tag{3.3}$$

[1] According to Plato's Cave Analogy, the objects we experience in the world are related to their *ideals* like the silhouettes of outside things to someone trapped in a dark cave. In the same way, one can think of a numerically simulated flow as being merely a vague image of the corresponding physical flow or exact mathematical solution of the equations of motion.

[2] Of course, there is a twist due to sensitivity on initial conditions: inevitably, the numerically evolved field $\boldsymbol{v}(\boldsymbol{x},t)$ will increasingly deviate from the exact solution. Therefore, the notion of relating $\boldsymbol{v}(\boldsymbol{x},t)$ and $\overset{\infty}{\boldsymbol{v}}(\boldsymbol{x},t)$ via an effective filter holds only in a small temporal neighbourhood of some time $t' < t$ at which both fields are matched per definitionem. From an operational point of view, however, this difficulty does not spoil anything further on.

In comparison to equation (1.11), the viscous stress tensor is enhanced by the SGS *turbulence stress tensor*[3]

$$\tau_{ik} \equiv \tau(\overset{\infty}{v}_i, \overset{\infty}{v}_k) = -\langle \overset{\infty}{\rho}\overset{\infty}{v}_i\overset{\infty}{v}_k\rangle_{\text{eff}} + \rho v_i v_k, \tag{3.4}$$

This tensor accounts for the interaction between resolved and unresolved components the velocity field. Here the closure problem shows up. Various approaches of approximately computing τ_{ik} are the topic of this Section. Moreover, the notion of turbulence energy and the corresponding energy conservation law are considered in more detail.

3.1.1 Turbulence Energy

One possible definition of the SGS turbulence energy is made on grounds of *fluctuations* of the ideal velocity field with respect to the smoother resolved velocity field, $\boldsymbol{v}' = \overset{\infty}{\boldsymbol{v}} - \boldsymbol{v}$. The kinetic energy associated with these fluctuations is given by [cf. Canuto, 1997]

$$K'_{\text{sgs}} = \frac{1}{2}\langle \overset{\infty}{\rho}|\boldsymbol{v}'|^2\rangle_{\text{eff}} = \frac{1}{2}\left(\langle \overset{\infty}{\rho}\overset{\infty}{v}_i\overset{\infty}{v}_i\rangle_{\text{eff}} - \langle \overset{\infty}{\rho}\overset{\infty}{v}_i v_i\rangle_{\text{eff}} - \langle \overset{\infty}{\rho} v_i v'_i\rangle_{\text{eff}}\right) \tag{3.5}$$

Using this definition, the decomposition of the dynamical equation into a resolved part and a subgrid scale part turns out to be rather complicated and results in what is known as *Leonard's decomposition* [cf. Sagaut, 2001, Section 3.3.1]. Nevertheless, the notion of SGS turbulence energy being associated with the second moment of the unresolved velocity fluctuations has been used quite commonly in LES applications.

According to Germano [1992], on the other hand, a *generalised turbulence energy* can be defined in analogy to the form which the turbulence energy would assume if $\langle\ \rangle_{\text{eff}}$ were a *Reynolds operator*. A filter $\langle\ \rangle$ is called a Reynolds operator if it is a projector, i. e., $\langle \rho\boldsymbol{v} - \overset{\infty}{\rho}\overset{\infty}{\boldsymbol{v}}\rangle = 0$. Whereas local filters of finite characteristic length usually do not have this property, the global spatial average is a Reynolds operator. Thus, Reynolds operators are related to statistical theories of turbulence. Extending Germano's proposition to the case of compressible turbulence, we define the specific *subgrid scale turbulence energy* (SGSTE) in terms of the trace of the SGS turbulence stress tensor:

$$K_{\text{sgs}} = \rho k_{\text{sgs}} = -\frac{1}{2}\text{Tr}\,\boldsymbol{\tau} = \frac{1}{2}\left[\langle \overset{\infty}{\rho}|\overset{\infty}{\boldsymbol{v}}|^2\rangle_{\text{eff}} - \rho|\boldsymbol{v}|^2\right] \tag{3.6}$$

Now the mass-weighted filtered kinetic energy, $\rho^{-1}\langle \overset{\infty}{\rho}|\overset{\infty}{\boldsymbol{v}}|^2\rangle_{\text{eff}}$, is naturally decomposed into the resolved fraction, $k_{\text{res}} = \frac{1}{2}|\boldsymbol{v}|^2$, and a fraction associated with the subgrid scales. Moreover, as was pointed out by Germano, the algebraic structure of the closure is the same for every linear commuting filter. This is called the *averaging invariance* of the turbulence equations. Finally, we define the characteristic velocity of SGS turbulence by

$$q_{\text{sgs}} = \sqrt{2k_{\text{sgs}}}. \tag{3.7}$$

[3] Here the opposite sign as customary in most of the literature is used in order to make τ_{ik} a proper stress tensor, which enters the right-hand side of the equation for the resolved energy with positive sign.

3.1.2 A Non-Linear Algebraic Model

Given the definition of the generalised turbulence energy (3.6), a model for the SGS turbulence stress tensor with non-vanishing trace $\mathrm{Tr}\,\boldsymbol{\tau} = \tau_{ii}$ is called for. Simple algebraic closures such as the Smagorinsky model or even non-linear extensions like those of Lund and Novikov [1992] or Kosović [1997], in which τ_{ik} is expanded into a series of contractions of S_{ik} and W_{ik} of increasing order, do not meet this requirement. To the lowest order, the trace-free part of the SGS turbulence stress tensor is given by

$$\tau^*_{ik} \equiv \tau_{ik} - \frac{1}{3}\tau_{ii} \doteq 2\rho(C_\mathrm{S}\Delta)^2|S|S^*_{ik}. \tag{3.8}$$

This closure is known as the *Smagorinsky model*. The scalar factor $\nu_\mathrm{sgs} = (C_\mathrm{S}\Delta)^2|S|$ has the dimension of a viscosity and is usually interpreted as the *turbulent viscosity* due the interaction of SGS velocity fluctuations with the resolved flow. Thus, the form of τ_{ik} is analogous to the form of σ_{ik} and the *effective stress tensor* in the qNSE (3.3) can be written as

$$\sigma_{ik} + \tau^*_{ik} = \rho(\nu + \nu_\mathrm{sgs})S^*_{ik}. \tag{3.9}$$

The isotropic part of the SGS turbulence stress, τ_{ii}, can be absorbed into the pressure if the flow is incompressible. Hence, there is no notion of a turbulence energy in the framework of the Smagorinsky model.

Kosović et al. [2002] proposed a modification of the non-linear model which applies to moderately compressible flows and predicts a non-vanishing trace. There are two additional terms of higher order in the closure for the SGS turbulence stress tensor:

$$\tau_{ik} \doteq \rho(C_\mathrm{S}\Delta)^2\left[2|S|S^*_{ik} + C_1 S_{il}S_{lk} + C_2(S_{il}W_{lk} - W_{il}S_{lk})\right]. \tag{3.10}$$

Contracting this closure, an expression for the SGS turbulence energy is obtained, which agrees with the result calculated by Yoshizawa [1986] from an approximate analytical turbulence theory:

$$K_\mathrm{sgs} = -\frac{1}{2}\tau_{ii} \doteq -\frac{1}{2}\rho(C_\mathrm{S}\Delta)^2 C_1 S_{ik}S_{ik}. \tag{3.11}$$

The corresponding SGS turbulence velocity is given by

$$q_\mathrm{sgs} \doteq \sqrt{-\frac{C_1}{2}}C_\mathrm{S}\Delta|S|. \tag{3.12}$$

Note that $C_1 < 0$ is a necessary *realisability condition*. Speziale et al. [1988] pointed out that the above approximation of SGS energy is limited to the case of weakly compressible flows, for which $d \ll |S|$. Apart from that, the numerically resolved energy budget is not affected, because the non-linear model only yields an energy scale, but it does not predict the evolution of the SGS turbulence energy.

As we will see in Section 3.1.3, the contraction of τ_{ik} with the rate-of-strain tensor S_{ik} yields the rate of SGS turbulence energy production. Assuming *statistical equilibrium*, the mean rate of production is balanced by the mean dissipation rate:

$$\rho_0\langle\epsilon_\mathrm{sgs}\rangle = \langle\tau_{ik}S_{ik}\rangle. \tag{3.13}$$

Substituting the closure for τ_{ik}, the rate of dissipation can be written as the sum of two contributions, $\langle\epsilon_{\rm sgs}\rangle = \langle\epsilon_0\rangle + \langle\epsilon_1\rangle$, where

$$\langle\epsilon_0\rangle = (C_{\rm S}\Delta)^2 a_0 \langle|S|^2\rangle^{3/2}, \tag{3.14}$$

$$\langle\epsilon_1\rangle = (C_{\rm S}\Delta)^2 C_1 a_1 \langle|S|^2\rangle^{3/2} \tag{3.15}$$

and the coefficients a_0 and a_1 are solely determined by structural properties of the flow:

$$a_0 = \frac{\langle\rho|S^*|^2|S|\rangle}{\rho_0\langle|S|^2\rangle^{3/2}}, \tag{3.16}$$

$$a_1 = \frac{\langle\rho S_{ik}S_{jk}S_{kl}\rangle}{\rho_0\langle|S|^2\rangle^{3/2}} = \frac{1}{2\sqrt{2}}\mathrm{skew}(S_{ik}). \tag{3.17}$$

The last equation shows that a_1 is basically the *skewness* of the rate-of-strain tensor.

Introducing the fraction of non-linear dissipation to the total rate of dissipation, $C_{\rm nl} = \langle\epsilon_1\rangle/\langle\epsilon_{\rm sgs}\rangle$, as a free parameter, $C_{\rm S}$ and C_1 can be expressed as

$$C_{\rm S} = \sqrt{1 - C_{\rm nl}}\,\frac{\ell_{\rm S}}{\Delta}, \tag{3.18}$$

$$C_1 = \frac{a_0 C_{\rm nl}}{a_1(1 - C_{\rm nl})}. \tag{3.19}$$

The length scale

$$\ell_{\rm S} = \frac{\langle\epsilon_{\rm sgs}\rangle^{1/2}}{\langle|S|^2\rangle^{3/4}} \tag{3.20}$$

is the characteristic scale of the Smagorinsky model, which is obtained in the limit $C_{\rm nl} = 0$ under the assumption that $a_0 \simeq 1$. Since $a_1 \propto \mathrm{skew}(S_{ik}) < 0$ in isotropic turbulent flows, the coefficient C_1 is indeed negative, as required by the realisability of the stress tensor[4]. In conclusion, the SGS turbulence velocity is given by

$$q_{\rm sgs} \doteq \sqrt{-\frac{C_{\rm nl}}{2a_1}}\ell_{\rm S}|S| = \left[-\frac{\sqrt{2}C_{\rm nl}\langle\epsilon_{\rm sgs}\rangle}{\mathrm{skew}(S_{ik})}\langle|S|^2\rangle^{3/2}\right]^{1/2}|S|. \tag{3.21}$$

V/c_0	a_0	a_1	skew(S_{ik})	$\ell_{\rm S}/\Delta$
0.084	1.342	-0.1045	-0.296	0.298
0.42	1.339	-0.1041	-0.295	0.260
0.66	1.333	-0.1037	-0.293	0.258

Table 3.1: Parameters of the non-linear algebraic SGS model for fully developed turbulence in the simulations `dns432ersl`, `dns432nrsl` and `dns432nh75`.

Numerical values of the coefficients a_0 and a_1 can readily be calculated from DNS data. If there is a sufficiently wide range of resolved scales, one can expect that these

[4] According to Kosović et al. [2002], the $\langle\epsilon_1\rangle$ can be interpreted as rate of transfer due to the *backscattering* of energy from subgrid to resolved scales. However, this would imply that $C_{\rm nl} < 0$ and, thus, $C_1 > 0$ in contradiction to the realisability condition $C_1 < 0$. As it was not possible to trace back this inconsistency, we will simply ignore this interpretation and consider $C_{\rm nl}$ as a *positive* free parameter.

coefficients will be largely universal once turbulence is fully developed. This is indeed demonstrated by the values listed in Table 3.1, which were computed from full 3D structural data of the simulations `dns432ersl`, `dns432nrsl` and `dns432nh75`. For each model, a data set corresponding to nearly steady turbulence was chosen. It appears that the coefficients are well approximated by

$$a_0 \approx \frac{4}{3}, \text{ and } a_1 \approx -\frac{1}{10}. \tag{3.22}$$

The implied skewness of about -0.28 agrees with results of Kosović [1997]. Therefore, the closure for the SGS turbulence velocity becomes

$$q_{\text{sgs}} \triangleq \sqrt{5C_{\text{nl}}}\,\ell_{\text{S}}|S|. \tag{3.23}$$

Setting $\langle\epsilon\rangle$ equal the mean rate of numerical dissipation,

$$\rho_0\epsilon_{\text{num}} = \langle\Pi\rangle - \frac{\mathrm{d}}{\mathrm{d}t}\langle K\rangle + \langle Pd\rangle, \tag{3.24}$$

it is also possible to compute ℓ_{S} numerically. A sample of values is also listed in Table 3.1. $\ell_{\text{S}} \approx 0.26\Delta$ appears to be a typical value for characteristic Mach numbers $V/c_0 \sim 1$. On the other hand, for small Mach numbers, such as in the case of simulation `dns432ersl`, a slightly larger length scale of $\ell_{\text{S}} \approx 0.30\Delta$ is obtained. Thus, $\ell_{\text{S}}/\Delta_{\text{eff}} \approx 0.16$, which is about the value of the Smagorinsky constant obtained from analytical treatments [cf. Pope, 2000, Section 13.4].

3.1.3 Decomposition of the Kinetic Energy Conservation Law

Alternatively, a dynamical equation for the SGSTE can be found by decomposing the conservation laws for the ideal flow. Since we are mostly interested in the trace of the turbulence stress tensor, we shall start from the equation for the kinetic energy of the ideal flow, $\overset{\infty}{K} = \frac{1}{2}\overset{\infty}{\rho}|\overset{\infty}{\boldsymbol{v}}|^2$, which is obtained by multiplying the Navier-Stokes equation with the velocity and symmetrising:

$$\frac{\partial}{\partial t}\overset{\infty}{K} + \frac{\partial}{\partial x_i}\overset{\infty}{K}\overset{\infty}{v_i} = \overset{\infty}{v_i}\left[-\frac{\partial \overset{\infty}{P}}{\partial x_i} + \overset{\infty}{\rho}(a_i + g_i) + \frac{\partial}{\partial x_k}\overset{\infty}{\sigma}_{ik}\right]. \tag{3.25}$$

Note that the viscous dissipation term must not be neglected in this equation, regardless of how small the microscopic viscosity ν of the fluid is. Otherwise, there would be no dissipation of mechanical energy except for compression effects. If forcing were maintained indefinitely, the kinetic energy would increase to the point where the flow becomes supersonic and shock dissipation sets in. In an incompressible flow, dissipation would be nil, which is clearly inconsistent.

As mentioned previously, the *filtered* ideal kinetic energy can be split into two contributions,

$$\langle\overset{\infty}{K}\rangle_{\text{eff}} = \frac{1}{2}\langle\overset{\infty}{\rho}|\overset{\infty}{\boldsymbol{v}}|^2\rangle_{\text{eff}} \equiv \rho(k_{\text{res}} + k_{\text{sgs}}), \tag{3.26}$$

one being the resolved and the other the subgrid scale contribution. Thus, filtering and separating equation (3.25) yields a system of dynamical equations for the resolved

and the SGS kinetic energy, respectively, which is known as the *Germano consistent decomposition* (cf. Germano, 1992, and Sagaut, 2001, Section 3.3.2):

$$\rho\frac{\mathrm{D}}{\mathrm{D}t}k_{\mathrm{res}} = v_i\left[-\frac{\partial P}{\partial x_i} + \rho(a_i + g_i) + \frac{\partial}{\partial x_k}\tau_{ik}\right] \tag{3.27}$$

$$\rho\frac{\mathrm{D}}{\mathrm{D}t}k_{\mathrm{sgs}} - \mathfrak{D}_{\mathrm{sgs}} = \Pi_{\mathrm{sgs}} - \rho(\lambda_{\mathrm{sgs}} + \epsilon_{\mathrm{sgs}}). \tag{3.28}$$

In the first equation, the viscous dissipation term is neglected under the assumption that the flow is virtually unaffected by microscopic viscosity at the resolved scales. This is a good approximation if $\Delta \gg \eta_{\mathrm{K}}$, where η_{K} is the Kolmogorov scale introduced in Section 1.1.2. Consequently, the energy transfer from resolved to subgrid scales is solely mediated by turbulence stresses. The equation for k_{sgs} in the above form is valid provided that the specific force a_i and gravity g_i only inject energy on scales $l \gg \Delta$. Regarding gravity, it comes to the question of the range of scales for which turbulence is directly affected by buoyancy. For the time being, we will not pursue this troublesome point any further and conjecture that buoyancy is not significant on subgrid scales. The various abbreviated terms in equation (3.27) and (3.28) are defined as follows.

- The rate of turbulence energy *production* on subgrid scales is given by

  $$\Pi_{\mathrm{sgs}} = \tau_{ik}S_{ik}. \tag{3.29}$$

  In fact, τ_{ik} mainly depends on the Fourier modes associated with wave numbers in the vicinity of the cutoff $\pi/\Delta_{\mathrm{eff}}$ [cf. Sagaut, 2001, Section 4.1.2].

- The rate of SGS *dissipation*,

  $$\epsilon_{\mathrm{sgs}} = \langle\overset{\infty}{\sigma}_{ik}\overset{\infty}{S}_{ik}\rangle_{\mathrm{eff}} = \nu\langle|\overset{\infty}{S}^*|^2\rangle_{\mathrm{eff}} \tag{3.30}$$

  is determined by the second moment of the ideal rate-of-strain tensor. This poses severe difficulties for the closure of the dissipation term, because $\overset{\infty}{S}_{ik}$ mostly depends on velocity fluctuations at the smallest dynamical scales $l \sim \eta_{\mathrm{K}}$.

- SGS *pressure dilatation* accounts for compression effects on unresolved scales. It is defined by an expression analogous to the SGS turbulence stress:

  $$\rho\lambda_{\mathrm{sgs}} \equiv \tau(\overset{\infty}{P}, \overset{\infty}{d}) = -\langle\overset{\infty}{P}\overset{\infty}{d}\rangle_{\mathrm{eff}} + Pd. \tag{3.31}$$

  As was numerically confirmed by Gotoh and Fukayama [2001], the spectrum of turbulent pressure fluctuations is governed by a $k^{-7/3}$ power law. Given the $k^{-5/3}$ law for the turbulence energy spectrum, it follows that pressure-dilatation is small compared to kinetic effects for high wave numbers, and λ_{sgs} is likely to be negligible at sufficiently high resolution.

- The rate of SGS *transport* $\mathfrak{D}_{\mathrm{sgs}}$ is given by the gradient of the third-order moment (TOM) of the ideal velocity field and additional terms which accounts for diffusion due to pressure effects and viscous transport:

  $$\mathfrak{D}_{\mathrm{sgs}} = \frac{\partial}{\partial x_k}\left[\frac{1}{2}\tau_{iik} + \mu_k + \langle\overset{\infty}{v}_i\overset{\infty}{\sigma}_{ik}\rangle_{\mathrm{eff}}\right]. \tag{3.32}$$

The contracted TOM τ_{iik} is defined by

$$\tau_{iik} \equiv \tau(\overset{\infty}{v}_i, \overset{\infty}{v}_i, \overset{\infty}{v}_k) = -\langle \overset{\infty}{\rho} \overset{\infty}{v}_i \overset{\infty}{v}_i \overset{\infty}{v}_k \rangle_{\text{eff}} - 2\tau_{ik} v_i + \langle \overset{\infty}{\rho} \overset{\infty}{v}_i \overset{\infty}{v}_i \rangle_{\text{eff}} v_k, \tag{3.33}$$

and

$$\mu_k \equiv \tau(\overset{\infty}{P}, \overset{\infty}{v}_k) = -\langle \overset{\infty}{P} \overset{\infty}{v}_k \rangle_{\text{eff}} + P v_k. \tag{3.34}$$

The viscous term can be neglected, if the scale separation between η_K and Δ is sufficiently large.

At this point, we encounter the fundamental problem of SGS modelling: The various terms in the SGS turbulence energy equation depend on the ideal velocity field and state variables. However, these quantities are not computable. The problem could be tackled if turbulence theory provided closed analytic expression in terms of the *resolved* quantities. Alas, no such theory is at hand[5]. Therefore, putative approximations must be invoked, which are applicable to numerical computations. Such approximations are called *closures*. In essence, any complete set of closures substituted into equation (3.28) constitutes a *subgrid scale turbulence energy model* (SGSTE).

3.1.4 Closures for the Turbulence Energy Equation

Finding physically reasonable and computationally feasible approximations for τ_{ik}, ϵ_{sgs}, λ_{sgs} and $\mathfrak{D}_{\text{sgs}}$ is a highly non-trivial task. There are many proposals on the market. A universal model which includes the SGSTE equation merely as one building block was formulated by Canuto [1994]. Although satisfying from a purely theoretical point of view, Canuto's model is extremely complicated, with a system of many coupled PDEs to be solved. Consequently, the numerical implementation would be very demanding. The issue of stability has not been investigated at all. A more compact but still quite general model was proposed by Schmidt and Schumann [1989] for applications in the framework of convective boundary layers, i. e., atmospheres. For the problem of thermonuclear burning in degenerate matter, however, this model is not suitable either, because it includes turbulent temperature fluctuations which cannot be computed with reasonable precision in the limit of high degeneracy. Therefore, we will first consider a simple variant of the SGSTE model, in which neither thermal effects nor gravity are included.

Production: The *anisotropic* part of the SGS turbulence stress tensor,

$$\tau^*_{ik} = \tau_{ik} - \frac{1}{3}\tau_{ll}\delta_{ik} = \tau_{ik} + \frac{2}{3}K_{\text{sgs}}\delta_{ik}, \tag{3.35}$$

is modelled by virtue of a *turbulent-viscosity hypothesis* [cf. Pope, 2000, Section 10.1.]:

$$\tau^*_{ik} \doteq 2\rho\nu_{\text{sgs}} S^*_{ik} = 2\rho\nu_{\text{sgs}} \left(S_{ik} - \frac{1}{3} d\delta_{ik} \right). \tag{3.36}$$

This closure is formulated analogous to the viscous stress tensor in a Newtonian fluid. The turbulent viscosity ν_{sgs} is assumed to be proportional to the product of

[5] Actually, in the framework of Reynolds-stress models, a solution was presented by Canuto and Dubovikov [1996] for a restricted class of problems.

the characteristic length scale Δ_{eff} of the implicit filter $\langle\,\rangle_{\text{eff}}$ and the characteristic velocity of SGS turbulence (cf. Sagaut, 2001, Section 4.3, and Pope, 2000, Section 13.6.3), i. e.,

$$\nu_{\text{sgs}} \doteq C_\nu \Delta_{\text{eff}} k_{\text{sgs}}^{1/2} = \ell_\nu q_{\text{sgs}}. \tag{3.37}$$

The length scale $\ell_\nu = C_\nu \Delta_{\text{eff}} / \sqrt{2}$ is associated with SGS turbulence production.

Dissipation: Assuming a Kolmogorov spectrum for the ideal flow, the mean SGS turbulence energy corresponding to a sharp spectral cut-off can be related to the mean rate of SGS dissipation:

$$\langle k_{\text{sgs}} \rangle = \int_{\pi/\Delta}^{\infty} E(k)\mathrm{d}k = \frac{3}{2} C \langle \epsilon_{\text{sgs}} \rangle^{2/3} \left(\frac{\pi}{\Delta}\right)^{-2/3}. \tag{3.38}$$

The dissipation rate averaged over the whole domain of the flow is therefore given by

$$\langle \epsilon_{\text{sgs}} \rangle = \pi \left(\frac{3C}{2}\right)^{-3/2} \frac{\langle k_{\text{sgs}} \rangle^{3/2}}{\Delta} \approx 0.81 \frac{\langle k_{\text{sgs}} \rangle^{3/2}}{\Delta} \tag{3.39}$$

if $C \approx 1.65$. Conjecturing that the above relation also holds *locally* for any particular finite-volume cell [cf. Pope, 2000, Section 13.6.3], we have

$$\epsilon_{\text{sgs}} \doteq C_\epsilon \frac{k_{\text{sgs}}^{3/2}}{\Delta_{\text{eff}}} = \frac{q_{\text{sgs}}^3}{\ell_\epsilon}, \tag{3.40}$$

where $\ell_\epsilon = 2\sqrt{2}\Delta_{\text{eff}}/C_\epsilon$ and $C_\epsilon \sim 1$. Basically, equation (3.40) implies that SGS eddies of characteristic kinetic energy $\sim q_{\text{sgs}}^2$ are dissipated on a time scale $\sim \ell_\epsilon / q_{\text{sgs}}$.

Pressure-dilatation: For a turbulent deflagration, the flow velocity is strictly subsonic and local pressure equilibrium is maintained even across flame fronts. For this reason, a crude and, possibly, qualitative closure should do. A particularly simple relation was proposed by Deardorff [1973]:

$$\lambda_{\text{sgs}} \doteq C_\lambda k_{\text{sgs}} d. \tag{3.41}$$

For negative C_λ, kinetic energy is dissipated by pressure fluctuations on subgrid scales if $d < 0$, i. e., if the resolved flow is locally contracting. On the other hand, if the fluid is locally expanding ($d > 0$), internal energy is converted into mechanical energy which produces turbulence. The characteristic time scale of pressure dilatation is given by $-1/C_\lambda d$.

Diffusion: Apart from the pressure term in the SGS energy flux, one could attempt to model the contracted TOM τ_{iik} itself by an additional dynamical equation. Indeed, such an equation can be written down [cf. Canuto, 1994]. However, the solution of this equation would entail additional complications, in particular, further closure assumptions for yet higher-order moments. In cases where diffusion is weak in comparison to production and dissipation, it is customary to use the *gradient-diffusion hypothesis* [cf. Sagaut, 2001, Section 4.3][6]

$$\mathfrak{D}_{\text{sgs}} \doteq \frac{\partial}{\partial x_k} \rho C_\kappa \Delta_{\text{eff}} k_{\text{sgs}}^{1/2} \frac{\partial k_{\text{sgs}}}{\partial x_k} = \frac{\partial}{\partial x_k} \rho \ell_\kappa q_{\text{sgs}}^2 \frac{\partial q_{\text{sgs}}}{\partial x_k}. \tag{3.42}$$

[6] Also known as *Kolmogorov-Prandtl relation*.

The characteristic scale of diffusion is defined by $\ell_\kappa = C_\kappa \Delta_{\text{eff}} / \sqrt{2}$, and the SGS diffusivity is given by $\kappa_{\text{sgs}} = \ell_\kappa q_{\text{sgs}}$. The notion of a diffusivity of turbulent energy stems from the analogy to thermal diffusion. The diffusion equation is a macroscopic approximation which statistically describes the microscopic transport of some passive scalar such as heat. In the case of thermal diffusion, heat is transported due to molecular collisions, which appear to be random from the macroscopic point of view. Regarding turbulent diffusion, the agent of transport are turbulent velocity fluctuations on scales below the numerical resolution. The analogy to thermal diffusion suggests the definition of a *kinetic Prandtl number*,

$$\sigma_{\text{kin}} = \frac{\nu_{\text{sgs}}}{\kappa_{\text{sgs}}} = \frac{C_\nu}{C_\kappa}. \tag{3.43}$$

Summarising, we obtain the following SGSTE model:

$$\begin{aligned} \frac{\mathrm{D}}{\mathrm{D}t} k_{\text{sgs}} - \frac{1}{\rho} \boldsymbol{\nabla} \cdot \left(\rho C_\kappa \Delta_{\text{eff}} k_{\text{sgs}}^{1/2} \boldsymbol{\nabla} k_{\text{sgs}} \right) = \\ C_\nu \Delta_{\text{eff}} k_{\text{sgs}}^{1/2} |S^*|^2 - \left(\frac{2}{3} + C_\lambda \right) k_{\text{sgs}} d - C_\epsilon \frac{k_{\text{sgs}}^{3/2}}{\Delta_{\text{eff}}}. \end{aligned} \tag{3.44}$$

Alternatively, a dynamical equation for the SGS turbulence velocity q_{sgs} can be formulated:

$$\frac{\mathrm{D}}{\mathrm{D}t} q_{\text{sgs}} - \frac{1}{\rho} \boldsymbol{\nabla} \cdot \left(\rho \ell_\kappa q_{\text{sgs}} \boldsymbol{\nabla} q_{\text{sgs}} \right) - \ell_\kappa |\boldsymbol{\nabla} q_{\text{sgs}}|^2 = \ell_\nu |S^*|^2 - \left(\frac{1}{3} + \frac{C_\lambda}{2} \right) q_{\text{sgs}} d - \frac{q_{\text{sgs}}^2}{\ell_\epsilon} \tag{3.45}$$

Although in non-conservative form, the equation for q_{sgs} can be evolved starting with $q_{\text{sgs}} = 0$ for a fluid being initially at rest, which is appealing from a computational point of view. Moreover, non-integer powers of q_{sgs} do not occur, and the functional dependence on q_{sgs} is advantageous for the discretisation of the diffusion term. This is shown in Section A.2 of the Appendix. The closure parameters C_ν, C_ϵ, C_λ and C_κ are *a priori* unknown. In the case of stationary isotropic turbulence, values can be derived analytically. Particular examples are $C_\nu \approx 0.054$, $C_\epsilon \approx 1.0$ and $C_\kappa \approx 0.1$ [cf. Sagaut, 2001, Section 4.3]. For the Deardorff closure, it is customary to set $C_\lambda = -\frac{1}{5}$ [cf. Fureby et al., 1997]. Statistical closure parameters calculated from DNS data will be discussed in Section 3.2. Furthermore, one can apply so-called dynamical procedures to compute closure parameters *in situ* from structural properties of the resolved flow in a LES.

3.1.5 Dynamical Procedures

In turbulent flows which are intermittent or anisotropic, constant closure parameters are more or less inadequate. An archetypical example is turbulence near a wall, which is inherently anisotropic. Both the naïve Samgorinksy model and the SGSTE model with constant parameters fail already in this simple case. In astrophysics, anisotropy usually stems from the compressibility of the fluid. An obvious example are shock waves in supersonic flows. Steep density gradients in stratified media such as in stellar atmospheres can effectively act like walls, as was pointed out by Clement [1993].

Moreover, turbulence driven by convection is highly intermittent. A flame front also introduces anisotropy because of the density jump between burned and unburned material, even at very low Mach numbers. A step towards a more flexible SGS model is the determination of the production parameter C_ν from the local flow structure on the smallest resolved scales. Then the closure is said to be *localised*.

In the beginning, a localised Smagorinsky model for incompressible turbulence was suggested by Germano et al. [1991]. They utilised an identity relating the SGS turbulence stress and the stress associated with a larger length scale $\hat{\Delta} > \Delta$:

$$T_{ik} = \hat{\tau}_{ik} + L_{ik}, \tag{3.46}$$

where $L_{ik} = -\rho(\widehat{v_i v_k} - \hat{v}_i \hat{v}_k)$. The hat on top of a symbol indicates a filter operation with characteristic length $\hat{\Delta}$. This filter is called the *test filter*, and we can say that T_{ik} is the turbulence stress tensor at the level of the test filter. Germano et al. came up with the following hypothesis. Owing to scale-invariance, the turbulent-viscosity closure is expected to hold for the turbulence stress tensor associated with any length scale within the inertial subrange. In particular, for the discretisation scale Δ and the test filter length scale $\hat{\Delta}$, the closures for the corresponding stress tensors are given by

$$\tau^*_{ik} \doteq 2\rho C_\mathrm{S} \Delta^2 |S| S_{ik} \equiv C_\mathrm{S} \beta_{ik}, \tag{3.47}$$

$$T^*_{ik} \doteq 2\hat{\rho} C_\mathrm{S} \hat{\Delta}^2 |\hat{S}| \hat{S}_{ik}, \equiv C_\mathrm{S} \alpha_{ik}. \tag{3.48}$$

The rate-of-strain tensor $\hat{S}_{ik}$ at the test filter level is computed from the filtered resolved velocity field, i. e., $\hat{S}_{ik} = \hat{v}_{(i,k)}$. The parameter C_S is a function of position and time which is to be determined. Filtering the closure for the SGS stress tensor τ^*_{ik} and substituting the identity (3.46) for T_{ik}, it is possible to eliminate $\hat{\tau}_{ik}$, a tensor which is unknown. Then it follows that

$$L_{ik} \doteq \hat{\rho} C_\mathrm{S} \alpha_{ik} - \rho \widehat{C_\nu \beta_{ik}}. \tag{3.49}$$

Assuming $\widehat{C_\nu \beta_{ik}} \simeq C_\mathrm{S} \hat{\beta}_{ik}$ and minimising the residual error between L_{ik} and the corresponding closure expression, the Samgorinsky parameter is found to be[7]

$$C_\mathrm{S} = \frac{m_{ik} L_{ik}}{m_{ik} m_{ik}}, \tag{3.50}$$

where $m_{ik} = \alpha_{ik} - \hat{\beta}_{ik}$. Note that both m_{ik} and L_{ik} can be calculated from the numerically resolved flow. This method of localising the Samgorinsky model is known as the *Germano-Lilly dynamical procedure*.

LES of turbulent channel flows, for example, carried out by Piomelli [1993], contributed to confidence in the localised model. However, the dynamical procedure as outlined above suffers from several difficulties. First of all, the algorithm used to determine the Samgorinsky parameter is inconsistent because variations of C_S over the characteristic length of the test filter are neglected. This assumption was found to be violated significantly. The origin of this problem is the presumed scale-invariance of C_S in contradiction to the calculation from local properties of the resolved flow on a

[7] The original expression proposed by Germano et al. for C_S was slightly different but the basic idea remains unaltered.

certain scale that is given by the numerical cut-off. Apart from that, divergences can occur locally if m_{ik} vanishes. The simplest solution would be to average C_S in homogeneous directions of the flow, if there are any. A more sophisticated iterative scheme was discussed by Piomelli and Liu [1995]. This scheme was also meant to tackle numerical instabilities which are caused by persisting negative values of C_S. Ghosal et al. [1995] generalised the dynamical procedure and applied it to the SGS turbulence energy model including the local determination of the dissipation and diffusion parameters. They formulated a variational algorithm to calculate the model parameters even in completely inhomogeneous flows. Although the variational formalism turned out to be a powerful method which overcomes the mathematical inconsistency and numerical instability of the Germano-Lilly procedure, it is computationally very demanding, as integral equations have to be solved.

Liu, Meneveau, and Katz [1994] made a different proposition based on experimental data from velocity measurements in a round jet. They used a decomposition into wave number bands corresponding to a hierarchy of filters and investigated the correlation between explicit turbulence stresses and turbulent-visocisity closures at different levels for the Smagorinsky model. Although some correlation between the turbulent stresses at different filter levels was found, they verified significantly better correlation between the turbulent stress at a particular filter level and the stress associated with the intermediate scales in between two adjacent levels, i. e., the Leonards stress. Their observation can be understood as a consequence of most of the energy transfer across a certain wave number k being caused by interactions in the spectral band $[\frac{1}{2}k, 2k]$, which follows from a theoretical analysis by Kraichnan [cf. Sagaut, 2001, Section 4.1]. With regard to the Smagorinsky model, this implies that the turbulent-viscosity closure at the level of the test filter applies to L_{ik} in place of T_{ik}. Thus, the localised Smagorinsky parameter is given by

$$C_S = \frac{\alpha_{ik} L_{ik}}{\alpha_{ik}\alpha_{ik}}. \tag{3.51}$$

Obviously, the difficulties encountered with the original dynamical procedure proposed by Germano et al. [1991] are not encountered. The resulting closure for the SGS turbulence stress tensor is called the *similarity model*.

Following the spirit of the dynamical procedure for calculating the Smagorinsky parameter C_S, a localised closure for production in SGSTE model can be formulated as well. In this case, the expression for the parameter of production is analogous to equation (3.51):

$$C_\nu = \frac{\alpha_{ik} L^*_{ik}}{\alpha_{ik}\alpha_{ik}}, \tag{3.52}$$

where

$$\alpha_{ik} = 2\hat{\rho}\hat{\Delta} k_T^{1/2} \hat{S}^*_{ik} \tag{3.53}$$

and $k_T = L_{ii}/2\hat{\rho}$ is the resolved kinetic energy on scales smaller than Δ_T. The above expression for C_ν is part of the LDKM model proposed by Kim and Menon [1996]. It was also shown that the resulting closure for turbulence production preserves Galilean invariance and fulfils fundamental *realisability conditions*[8]. Moreover, they suggested

[8] In particular, these conditions ensure that the turbulence energy, which is determined by the trace of τ_{ik}, is always positive [cf. Sagaut, 2001, Section 3.3.5].

a localised closure for SGS dissipation,

$$C_\epsilon \frac{k_T^{3/2}}{\Delta_\mathrm{T}} = \nu_\mathrm{sgs} |\hat{S}^*|^2, \tag{3.54}$$

which is based upon the prejudice that viscous dissipation acting on subgrid scales is similar to the transfer of kinetic energy from resolved scales to scales below the cut-off Δ. Comparing the above relation with the closure (3.40), one can see that the SGS viscosity is put in place of the microscopic viscosity. This similarity assumption is certainly questionable and, indeed, it was later revised [cf. Kim et al., 1999]. Yet another, rather tentative method of determining C_ϵ will be discussed in Section 4.3.4 in the context of LES of turbulent burning.

3.2 The Self-Similarity of Turbulence

The notion of self-similarity plays an important role in the theory of turbulence. Particularly, Kolmogorov's theory of turbulence is, in essence, a self-similarity theory. Actually, there are several different flavours of self-similarity. Usually, the largest coherent structures in a flow are shaped by boundary conditions, the action of external forces etc. and, naturally, there is no similarity to smaller structures. But as we are looking on ever smaller length scales, a turbulent flow becomes *asymptotically* self-similar. Of course, even then a certain vortex or some turbulent patch is never exactly similar to another one. However, statistical moments of the velocity fluctuations in the turbulence cascade are *scale-invariant*. Therefore, turbulence is *statistically self-similar* on small scales, which bears important implications on SGS modelling. Furthermore, there is the question of correlation among different scales. For a cut-off scale Δ within the inertial subrange, the local dynamics of SGS turbulence should be mostly influenced by the dynamics of turbulence on resolved scales above the cut-off. Taking up this idea, Bardina et al. [1983] proposed that the statistical structure of the turbulence stress tensor constructed on the basis of the subgrid scales is similar to that of the equivalent evaluated on the basis of the smallest resolved scales. Indeed, this hypothesis by Barden was later extended by Liu et al. [1994] to a spectrum split into an arbitrary number of frequency bands, as mentioned in Section 3.1.5. The assumption of similarity was then applied to the flow structure in consecutive bands and led to the similarity model. In this Section, the self-similarity of turbulence with regard to SGS closures is investigated on grounds of numerical data from the DNS presented in the previous Chapter.

3.2.1 Hierarchical Filtering

To begin with, let us introduce an infinite series of *homogeneous* and *time-independent* filters $\langle\ \rangle_n$. The kernel of the n-th filter is denoted as $G_n(\boldsymbol{x})$. The corresponding *filter operation* on a dynamical quantity $q(\boldsymbol{x}, t)$ is defined by

$$q^{(n)}(\boldsymbol{x}, t) = \int \mathrm{d}^3 x'\, G_n(\boldsymbol{x}') q(\boldsymbol{x}', t) \tag{3.55}$$

and symbolically written as $q^{(n)} = \langle q \rangle_n$. In the limit $n \to \infty$, the identity operator is obtained. Setting $\Delta_0 = X$, where X is the size of the fundamental domain, $q^{(0)} = \langle q \rangle$ is

the global mean of the field $q(\boldsymbol{x}, t)$. Moreover, the series of filters $\langle\ \rangle_n$ is *self-similar* if

$$\forall n \in \mathbb{N}_0 : G_n(\boldsymbol{x}) = \gamma^3 G_{n-1}(\gamma \boldsymbol{x}). \tag{3.56}$$

Here we shall assume that $\langle\ \rangle_n$ is a Gaussian filter with a characteristic length Δ_n and wave number $k_n = \pi/\Delta_n$. The corresponding kernel is defined by [cf. Pope, 2000, Section 13.2]

$$G_n(\boldsymbol{x}) = \left(\frac{6}{\pi\Delta_n^2}\right)^{3/2} \exp\left(-\frac{6|\boldsymbol{x}|^2}{\Delta_n^2}\right). \tag{3.57}$$

In the following, we will mostly refer to a series of Gaussian filters with $\Delta_n = \{L/n\}_{n=1}^{\infty}$.

The velocity field $\boldsymbol{v}^{[n]}(\boldsymbol{x}, t)$ at the n-th filter level is defined by a *mass-weighted* filter operation:

$$\boldsymbol{v}^{[n]}(\boldsymbol{x}, t) = \frac{1}{\rho^{(n)}(\boldsymbol{x}, t)} \int \mathrm{d}^3x'\, G_n(\boldsymbol{x}')\overset{\infty}{\rho}(\boldsymbol{x}', t)\overset{\infty}{\boldsymbol{v}}(\boldsymbol{x}', t) \tag{3.58}$$

or, for brevity, $\boldsymbol{v}^{[n]} = \langle\overset{\infty}{\rho}\overset{\infty}{\boldsymbol{v}}\rangle_n / \langle\overset{\infty}{\rho}\rangle_n$. Filtering twice, we set

$$\boldsymbol{v}^{[m][n]}\rho^{(m)(n)} = \langle\rho^{(m)}\boldsymbol{v}^{[m]}\rangle_n = \langle\langle\overset{\infty}{\rho}\overset{\infty}{\boldsymbol{v}}\rangle_m\rangle_n, \tag{3.59}$$

where $\rho^{(m)(n)} = \langle\langle\overset{\infty}{\rho}\rangle_m\rangle_n$. If two filters of characteristic length scales Δ_m and $\Delta_n \gg \Delta_m$ are applied in succession, we have

$$\boldsymbol{v}^{[m][n]}\rho^{(m)(n)} = \langle\rho^{(m)}\boldsymbol{v}^{[m]}\rangle_n \simeq \langle\overset{\infty}{\rho}\overset{\infty}{\boldsymbol{v}}\rangle_n = \boldsymbol{v}^{[n]}\rho^{(n)}. \tag{3.60}$$

The validity of this approximation becomes immediately clear from the product of the kernels of the Gaussian filters in spectral space [cf. Pope, 2000, Section 13.2]:

$$\hat{G}_m(k)\hat{G}_n(k) = \exp\left[-\frac{k^2(\Delta_m^2 + \Delta_n^2)}{24}\right] \simeq \exp\left[-\frac{k^2\Delta_n^2}{24}\right] = \hat{G}_n(k). \tag{3.61}$$

Since the convolution with the filter kernel in physical space corresponds to the multiplication of the Fourier transforms in spectral space, it follows that $\langle\langle q\rangle_m\rangle_n \simeq \langle q\rangle_n$ if $\Delta_n \gg \Delta_m$.

The turbulence stress tensor associated with the n-th filter is defined by

$$\tau_{ik}^{[n]} = -\langle\overset{\infty}{\rho}\overset{\infty}{v_i}\overset{\infty}{v_k}\rangle_n + \rho^{(n)}v_i^{[n]}v_k^{[n]}. \tag{3.62}$$

Note that $\tau_{ik}^{[0]}$ is the Reynolds stress tensor in a purely statistical description of the flow. For two consecutive filter levels, say, n and $n-1$, there is a simple algebraic relation between the corresponding stress tensors,

$$\tau_{ik}^{[n][n-1]} = \langle\tau_{ik}^{[n]}\rangle_{n-1} + \tau^{[n,n-1]}(v_i^{[n]}, v_k^{[n]}), \tag{3.63}$$

where

$$\tau_{ik}^{[n][n-1]} = -\langle\langle\overset{\infty}{\rho}\overset{\infty}{v_i}\overset{\infty}{v_k}\rangle_n\rangle_{n-1} + \underbrace{\rho^{(n)(n-1)}v_i^{[n][n-1]}v_k^{[n][n-1]}}_{\frac{\langle\langle\overset{\infty}{\rho}\overset{\infty}{v_i}\rangle_n\rangle_{n-1}\langle\langle\overset{\infty}{\rho}\overset{\infty}{v_k}\rangle_n\rangle_{n-1}}{\langle\langle\overset{\infty}{\rho}\rangle_n\rangle_{n-1}}}. \tag{3.64}$$

and

$$\tau^{[n,n-1]}(v_i^{[n]}, v_k^{[n]}) = -\langle\rho^{(n)} v_i^{[n]} v_k^{[n]}\rangle_{n-1} + \frac{1}{\langle\rho^{(n)}\rangle_{n-1}}\langle\rho^{(n)} v_i^{[n]}\rangle_{n-1}\langle\rho^{(n)} v_k^{[n]}\rangle_{n-1} \tag{3.65}$$

is the *intermediate* stress tensor at the filter level n associated with the velocity field filtered at the level $n-1$. The above relation was originally formulated by Germano [1992] in the case of incompressible flows for which the filtered velocity field is not mass-weighted. The relation also applies to arbitrary filter levels, m and n, say. In the limit $\Delta_n \gg \Delta_m$, the contribution from $\langle\tau_{ik}^{[m]}\rangle_n$ becomes negligible and

$$\tau_{ik}^{[n]} \simeq \tau_{ik}^{[m][n]} \simeq \tau^{[m,n]}(v_i^{[m]}, v_k^{[m]}), \tag{3.66}$$

i. e., the turbulence stress associated with the scale Δ_n is not sensitive to the flow structure on much smaller scales. The asymptotic limit of the Germano relation is especially useful for the numerical evaluation of turbulence stresses from DNS data.

The generalised turbulence energy at the n-th filter level is defined by

$$K^{[n]} = \rho^{(n)} k^{[n]} = -\frac{1}{2}\tau_{ii}^{[n]}. \tag{3.67}$$

In particular, $K^{[0]}$ is the mean kinetic energy of the flow. Contracting the extended Germano identity (3.63), we obtain the relation

$$K^{[n][n-1]} = \langle K^{[n]}\rangle_{n-1} + K^{[n,n-1]}, \tag{3.68}$$

where

$$K^{[n,n-1]} = -\frac{1}{2}\tau^{[n,n-1]}(v_i^{[n]}, v_i^{[n]}) \tag{3.69}$$

is the intermediate turbulence energy, i. e., the kinetic energy of modes which are concentrated in the spectral band $[\pi/\Delta_{n-1}, \pi/\Delta_n]$. As opposed to the spectral filter, there are no sharp boundaries between adjacent bands associated with Gaussian filters. Nevertheless, the notion of turbulence energy as proposed by Germano is well-defined and unambiguously associates some energy contents with each band of wave numbers. Furthermore, the asymptotic self-similarity of turbulence implies that the closures defined in Section 3.1.4 are applicable to filters of characteristic length $\Delta_n \ll L$. Then the time evolution of $K^{[n]}$ is given by the generalisation of equation (3.44),

$$\begin{aligned}\frac{\mathrm{D}}{\mathrm{D}t}k^{[n]} - \frac{1}{\rho^{(n)}}\boldsymbol{\nabla}\cdot\left(\rho^{(n)} C_\kappa^{(n)}\Delta_n\sqrt{k^{[n]}}\boldsymbol{\nabla}k^{[n]}\right) = \\ C_\nu^{(n)}\Delta_n\sqrt{k^{[n]}}|S^{*[n]}|^2 - \left(\frac{2}{3} + C_\lambda^{(n)}\right)k^{[n]}d - C_\epsilon^{(n)}\frac{(k^{[n]})^{3/2}}{\Delta_n},\end{aligned} \tag{3.70}$$

where $S_{ik}^{*[n]} = v_{(i,k)}^{[n]} - \frac{1}{3}d^{[n]}\delta_{ik}$ are the components of the trace-free rate-of-strain tensor and $d^{[n]} = v_{(k,k)}^{[n]}$ is the divergence of the velocity field filtered at the level n. Now the question of self-similarity boils down to the scaling-behaviour of the parameters $C_\nu^{(n)}$, $C_\epsilon^{(n)}$ and $C_\kappa^{(n)}$ associated with the different filters in the hierarchy.

3.2.2 Production

The turbulent-viscosity closure (3.36) for the production of turbulence energy at the level of the n-th filter is given by

$$\tau_{ik}^{*[n]} S_{ik}^{[n]} \doteq \rho^{(n)} C_\nu^{(n)} \Delta_n \sqrt{k^{[n]}} |S^{*[n]}|^2. \tag{3.71}$$

In order to verify this closure *a priori*, DNS data can be filtered in the intermediate range of scales between the grid resolution and the integral scale. For the explicit evaluation of the turbulence stress tensor, an *enhanced viscosity approximation* is applied. This means that the ideal velocity field in definition (3.62) is replaced by the numerically computed field which is smooth on scales $l \lesssim \Delta$. One can think of the smoothness being caused by an effective filter of characteristic length Δ_{eff}, corresponding to a viscosity of numerical origin, which enhances the physical viscosity of the fluid. By the same line of reasoning as in the case of two filters with $\Delta_n \gg \Delta_m$, it follows that $\langle \overset{\infty}{q} \rangle_n \simeq \langle \langle \overset{\infty}{q} \rangle_{\text{eff}} \rangle_n = \langle q \rangle_n$ if $\Delta_n \gg \Delta_{\text{eff}}$. Moreover, $\exists N : \Delta_{N+1} < \Delta_{\text{eff}} \leq \Delta_N$. According to the asymptotic equation (3.66), $\tau_{ik}^{[n]}$ can be approximated by $\tau_{ik}^{[N,n]}$. This, in turn, implies

$$\tau_{ik}^{[n]} \simeq -\langle \rho v_i v_k \rangle_n + \rho^{(n)} v_i^{[n]} v_k^{[n]} \tag{3.72}$$

for a filter of much larger characteristic length than the the numerical scale Δ_{eff}.

V/c_0	ζ	t/T	Δ_6/l_{p}	$\langle C_\nu^{(6)} \rangle$	$C_\epsilon^{(6)}$	$C_\kappa^{(6)}$
0.084	1.0	2.5	2.25	0.0618	0.473	0.358
0.42	1.0	2.5	2.84	0.0615	0.424	0.369
0.66	0.75	2.0	2.00	0.0504		0.387
0.66	0.75	4.0	2.77	0.0574	0.461	0.390
0.66	0.75	6.0	2.53	0.0597	0.425	0.376
0.66	0.75	9.0	2.59	0.0570		0.512
1.39	0.20	3.5	0.73	0.0394		0.508
1.39	0.20	6.0	2.53	0.0548	0.474	0.484

Table 3.2: Mean production, dissipation and diffusion parameters calculated with a Gaussian filter is $\Delta_6 = L/6 = 24\Delta$ for different Mach numbers V/c_0, spectral weights ζ and varying time $\tilde{t} = t/T$.

However, the actual range of inertial scales in the DNS discussed in Section 2.4 is only marginal. From the turbulence energy spectra shown in Section (2.5.3), one can see that approximate Kolmogorov scaling is found for dimensionless wave numbers in the narrow range $2 \lesssim \tilde{k} \lesssim 5$. The dimensionless wave number associated with a Gaussian filter of characteristic length scale Δ_n is $\tilde{k}_n = (\pi/\Delta_n)(L/2\pi) = L/2\Delta_n$. Thus, only filters with $0.1 \lesssim \Delta_n/L \lesssim 0.25$ are more or less suitable for calculating $C_\nu^{(n)}$ from equation (3.71), with the turbulence stress given by the enhanced viscosity approximation (3.72). Notwithstanding these tight constraints, mean values of $C_\nu^{(n)}$ were calculated from a sample of 3D data sets using several different filters. The results are plotted as functions of the characteristic filter wave number in Figure 3.1. For the simulation `dens432ersl` with a characteristic Mach number of $V/c_0 \approx 0.084$, the plotted values seem to indicate a maximum of $\langle C_\nu^{(n)} \rangle$ near the wave number $\tilde{k} = 2.0$, which

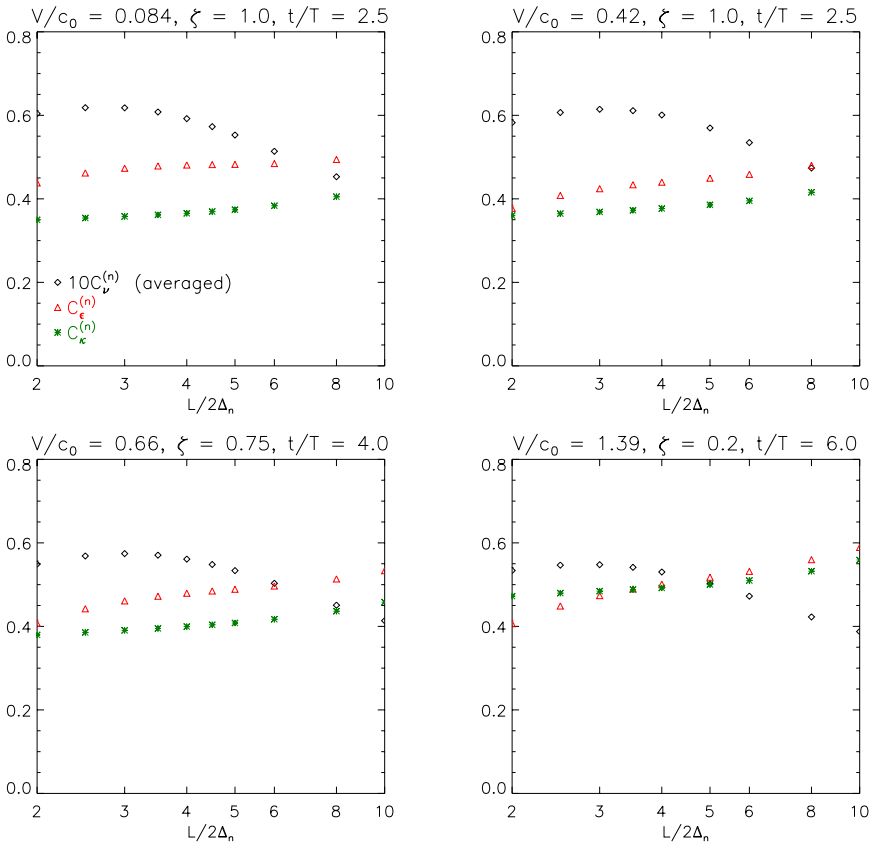

Figure 3.1: Statistical closure parameters $\langle C_\nu \rangle$, C_ϵ and C_κ as functions of the normalised wave number $\tilde{k}_n = L/2\Delta_n$ for a Gaussian filter of characteristic length Δ_n.

marks the upper bound of the energy-containing subrange. Towards higher wave numbers, i. e., for filters of smaller characteristic length, $\langle C_\nu^{(n)} \rangle$ decreases and eventually flattens in the vicinity of peak dissipation at the wave number $\tilde{k}_\mathrm{p} \approx 13.5$. Unfortunately, no pronounced self-similarity is apparent. This is probably an indication of insufficient resolution in the simulations. For the other models, a similar behaviour emerges, but there is a trend of smaller production parameters for higher Mach number and partially dilatational forcing. In any case, $\langle C_\nu \rangle \approx 0.06$ is adopted as an estimate for some of the LES discussed in the next Chapter. This choice is further supported by the selection of numerical values listed in Table 3.2. All of these values were calculated with the Gaussian filter of characteristic wave number $\tilde{k}_6 = 3$. Near this wave number, the compensated energy spectra in Section (2.5.3) go through a local minimum. Smaller values of $\langle C_\nu^{(n)} \rangle$ are found at early time when turbulence is still developing. Otherwise, $\langle C_\nu \rangle \approx 0.06$ appears to be a good value for fully developed turbulence.

Furthermore, let us contrast the statistical values for the production parameter with those obtained on grounds of the similarity hypothesis following the proposition of Liu et al. [1994]. To that end, the function $C_\nu^{(2n,n)}(\boldsymbol{x}, t)$ was determined from the intermedi-

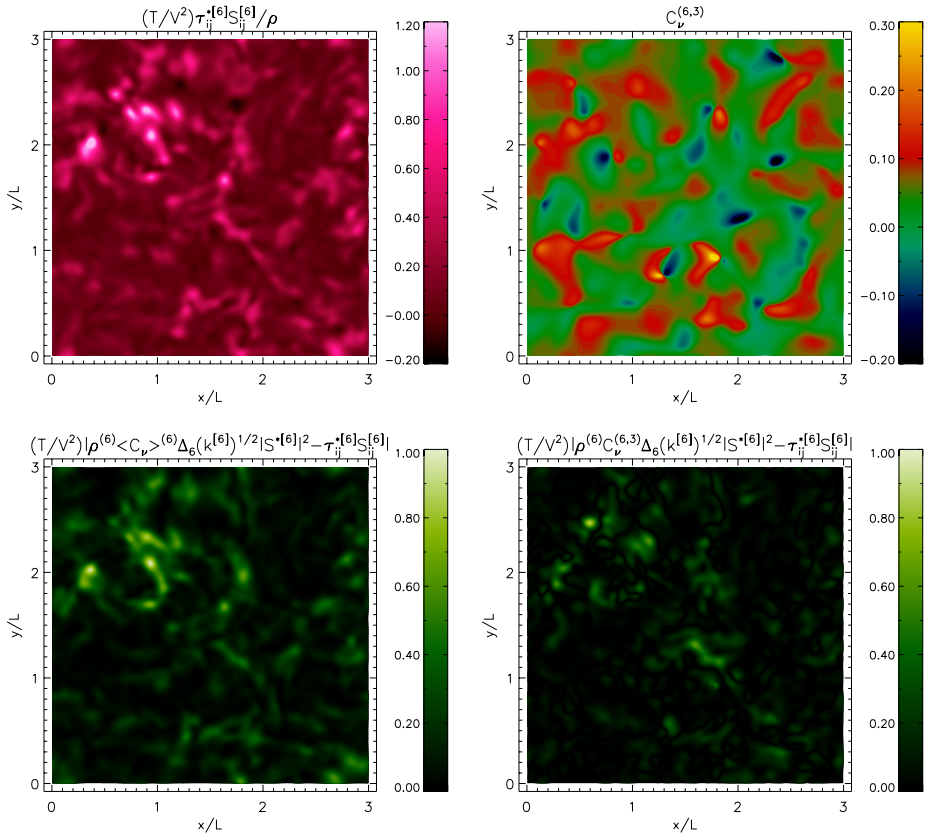

Figure 3.2: The rate of turbulence production evaluated from filtered data of simulation `dns432ersl` in the plane $z = 0$ at time $\tilde{t} = 2.5$ (left top panel) and the corresponding deviations of the statistical and the similarity turbulent-viscosity closure, respectively (bottom panels). The right panel on top shows the localised production parameter inferred from the similarity hypothesis.

ated stress tensor $\tau_{ik}^{[2n,n]}$ associated with the range of scales $\Delta_{2n} \lessapprox l \lessapprox \Delta_n = 2\Delta_{2n}$:

$$C_\nu^{(2n,n)} = \frac{\tau^{*\,[2n,n]}(v_i^{[2n]}, v_k^{[2n]}) S_{ik}^{[n]}}{\rho^{(n)} \Delta_n \sqrt{k^{[2n,n]}} |S^{*\,[n]}|^2} \tag{3.73}$$

The quantities in the above expression can be evaluated by filtering DNS data at two levels n and $2n$ in between the energy containing and the dissipation range, respectively. The *similarity closure* for the turbulence stress $\tau_{ik}^{[2n]}$ associated with the length scale Δ_{2n} is given by

$$\tau_{ik}^{*\,[2n]} S_{ik}^{[2n]} \triangleq C_\nu^{(2n,n)} \rho^{(2n)} \Delta_{2n} \sqrt{k^{[2n]}} |S^{*\,[2n]}|^2. \tag{3.74}$$

In order to validate the modelled rate of production given by equation (3.74), the turbulence stress tensor on the left-hand side has to be evaluated from the DNS data on grounds of the enhanced viscosity approximation.

The deviations of both the statistical and the similarity closure from the explicitly evaluated rate of production is illustrated in Figure 3.2. The top panel on the left is

a contour plot of $\tau^{*\,[6]} S_{ik}^{[6]}$, which was computed with a Gaussian filter of characteristic length $\Delta_6 = L/6$ from a 2D section of the flow in simulation `dns432ersl` at time $\tilde{t} = 2.5$. The corresponding turbulent-viscosity closure with the production parameter set equal to $\langle C_\nu^{(6)} \rangle \approx 0.0618$ is plotted in the panel panel below. Although the overall agreement is fairly good, some regions of pronounced production are not well reproduced. On the other hand, the similarity parameter $C_\nu^{(6,3)}$ was computed with equation (3.73). A contour plot is shown in the right panel on top of Figure 3.2. Obviously, $C_\nu^{(6,3)}$ is negative in several regions of the flow. The resulting negative turbulent viscosity is usually interpreted as *backscattering* of energy from smaller to larger scales. In fact, energy transfer upwards through the cascade is well known from turbulence theory and can only be described by a localised closure[9]. The outcome of inserting $C_\nu^{(6,3)}$ into the turbulent-viscosity closure for $\tau^{*\,[6]} S_{ik}^{[6]}$ is shown in the right bottom panel of Figure 3.2. The deviations from rate of production are clearly less than for the closure with the constant statistical parameter.

Δ_a/l_p	Δ_b/l_p	$\langle C_\nu \rangle$	$\rho(\tau_{ik}^* S_{ik})\|_{z=0}$
2.0	6.0	0.0401	0.769
2.0	5.0	0.0417	0.796
2.0	4.0	0.0426	0.825
2.0	3.5	0.0426	0.844
2.0	3.0	0.0421	0.865
1.5	5.25	0.0453	0.743
1.5	4.5	0.0465	0.760
1.5	3.75	0.0472	0.782
1.5	3.0	0.0469	0.814

Table 3.3: Mean production parameters computed from the intermediate turbulence stress associated with the length scales Δ_a and Δ_b. The data set was taken from simulation `dns432ersl` at time $\tilde{t} = 2.5$.

In a different numerical experiment, the influence of the width of the band for the intermediate turbulence stress was investigated. This time, two Gaussian filters with variable ratio of characteristic length scales Δ_b/Δ_a were applied. The results are summarised in Table 3.3. The parameter of production was calculated according to equation (3.73), with the correspondence $2n \leftrightarrow$ a and $n \leftrightarrow$ b. Both the global averages and the correlation coefficient between the explicitly evaluated rate of production and the modelled counterpart in the plane $z = 0$ are listed. The filter length is measured in units of the length scale of maximal dissipation, l_p. It appears that the mean production parameter is fairly robust with respect to the ratio Δ_b/Δ_a and the correlation coefficients are quite high, with a typical value of about 0.8 if $\Delta_b/\Delta_a \approx 2.0$ [10] . This agrees well with the comments on spectral transfer made in Section 3.1.5. However, corresponding

[9] Entirely different SGS models including backscattering processes are outlined in Sagaut [2001], Section 4.4.

[10] High levels of correlation are usually found with regard to the scalar rate of production $\tau_{ik} S_{ik}$. If the turbulence stress tensor τ_{ik} itself were compared to the corresponding closure, the correlation would be reduced due to the weak alignment of S_{ik} and τ_{ik}. This was recognised by Clark et al. [1979] from studies of DNS data.

values for the two different choices $\Delta_a = 1.5l_p$ and $\Delta_a = 2.0l_p$ are clearly different. This might be a consequence of the stronger influence of numerical dissipation on the scale $1.5l_p$ as compared to $2.0l_p$.

3.2.3 Dissipation

The rate of dissipation at the level of the n-th filter,

$$\epsilon^{(n)} = \nu\langle|\overset{\infty}{S}{}^*|^2\rangle_n, \tag{3.75}$$

is largely determined by velocity fluctuations on the smallest dynamical length scales near the microscopic Kolmogorov scale η_K, even if $\Delta_n \gg \eta_K$. For this reason, there is no way of explicitly evaluating $\epsilon^{(n)}$ from under-resolved numerical data. Alternatively, one could infer $\epsilon^{(n)}$ from the rate of energy transfer across the length scale Δ_n. However, the direct calculation of the rate of transfer is extremely complicated and was not attempted [cf. McComb, 1990, Section 2.7.1]. Consequently, a different approach is called for. A simple estimate can be made if the resolved flow is more or less in stochastic equilibrium. Taking the global average of the turbulence energy equation (3.70), the diffusion term cancels out and the mean time derivative is negligible in the case of steady turbulence. Hence,

$$0 \simeq \langle\tau_{ik}^{[n]}S_{ik}^{[n]} - \rho^{(n)}(\epsilon^{(n)} + \lambda^{(n)})\rangle. \tag{3.76}$$

Dropping the minor contribution of pressure dilatation and substituting the closures for production and dissipation, we obtain

$$C_\nu^{(n)}\Delta_n\langle|S^{*[n]}|^2\rangle - \frac{1}{3}\langle d^{[n]}q^{[n]}\rangle - \frac{1}{2}C_\epsilon^{(n)}\frac{\langle(q^{[n]})^2\rangle}{\Delta_n} \simeq 0. \tag{3.77}$$

From this averaged production–dissipation balance, a statistical estimate of the dissipation parameter $C_\epsilon^{(n)}$ can be calculated. Results obtained from DNS data are shown in Figure 3.1. It appears that the graphs of $C_\epsilon^{(n)}$ flatten near the transition to the range of wave numbers dominated by dissipation. For the simulation with the lowest Mach number, `dns432ersl`, $C_\epsilon^{(8)} \approx 0.48$ was found, and the corresponding values for the other models are not much different. A further sample of values for the dissipation parameter is listed in Table 3.2. In most cases, $C_\epsilon^{(n)}$ is slightly less than 0.5 for the filter levels $6 \le n \le 12$, which highlights the robustness of this parameter.

3.2.4 Diffusion

The turbulent flux of kinetic energy is given by

$$F_k^{[n]} = \frac{1}{2}\tau_{iik}^{[n]} + \mu_k^{(n)}, \tag{3.78}$$

where the contracted TOM $\tau_{iik}^{[n]}$ and the pressure-diffusion flux $\mu^{(n)}$ are defined analogously as in equations (3.33) and (3.34), respectively, with the effective numerical filter replaced by the filter $\langle\ \rangle_n$. In the gradient-diffusion closure, the flux is set equal to the mean product of kinetic diffusivity and the gradient of the turbulence energy:

$$\boldsymbol{F}^{[n]} \triangleq \rho^{(n)}C_\kappa^{(n)}\Delta_n\sqrt{k^{[n]}}\,\boldsymbol{\nabla}k^{[n]}. \tag{3.79}$$

This closure immediately reveals a consistency problem. The parameter $C_\kappa^{(n)}$ is overdetermined because there are three flux components. For a well defined solution, the gradient of $k^{[n]}$ has to be aligned with the flux vector $\boldsymbol{F}^{[n]}$. If this were the case, a least-square approach could be employed to calculate the closure parameter:

$$C_\kappa^{(n)} = \frac{\langle \boldsymbol{F}^{[n]} \cdot \boldsymbol{\nabla} k^{[n]} \rangle}{\langle \rho^{(n)} \Delta_n \sqrt{k^{[n]}} |\boldsymbol{\nabla} k^{[n]}|^2 \rangle}. \tag{3.80}$$

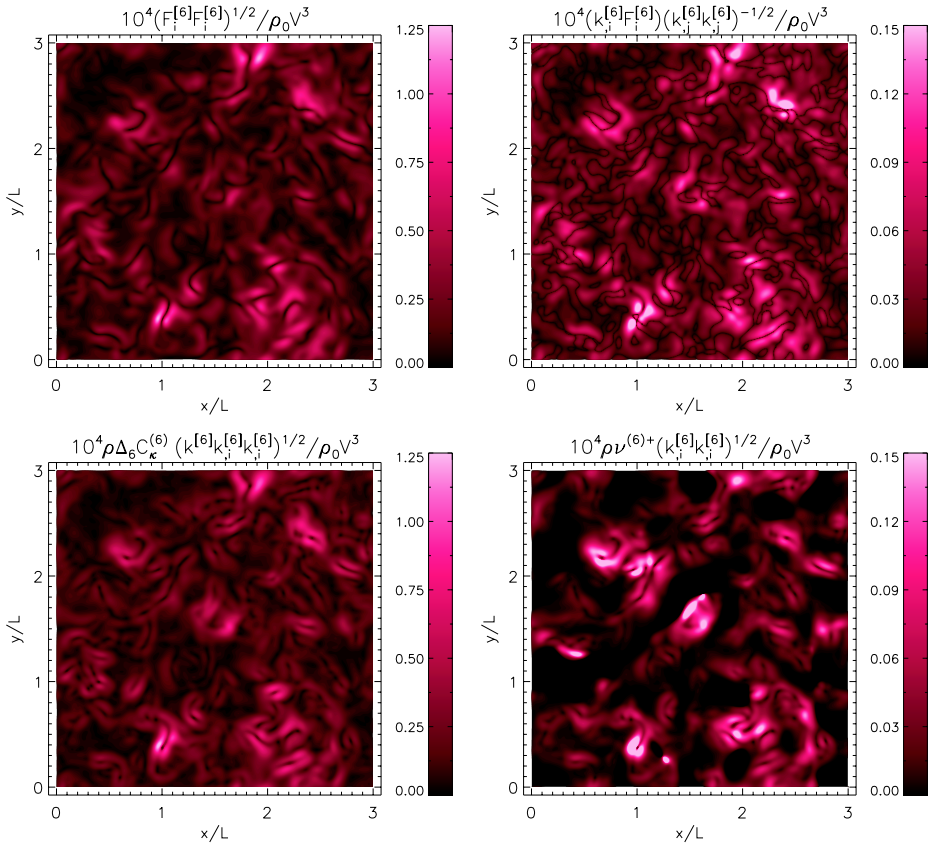

Figure 3.3: The turbulent flux magnitude computed with a Gaussian filter of characteristic length $\Delta_6 = L/6$ from data of simulation `dns432nrh75` at time $\tilde{t} = 5.0$. The left panel on the top shows the contours of the actual flux magnitude $|\boldsymbol{F}^{[6]}|$. The projection of the modelled flux as defined by equation (3.80) unto the actual flux is shown in the right top panel, and contours of differently modelled fluxes are plotted in the bottom panels.

The outcome of this ansatz was matched against the explicitly evaluated flux $F_k^{[6]}$ for a 2D section of the filtered flow in simulation `dns432nrh75` at time $\tilde{t} = 4.0$. The filtering length is $\Delta_6 = L/6 \approx 15\Delta_{\text{eff}}$. Equation (3.80) yields $C_\kappa^{(6)} \approx 0.0358$ from the full 3D data set. This is of the same order as the statistical parameter of production, $C_\kappa^{(6)} \approx 0.0574$, and appears to support a turbulent kinetic Prandtl number close to one. However, the overall agreement between the modelled and the explicitly evaluated turbulent flux is very poor, as the two panels on the top of Figure 3.3 reveal. Actually,

the typical magnitude of the flux is underestimated by a factor of about 8 according to the different scales for both plots. The discrepancy indicates that the assumption of turbulent transport in the direction of the turbulence energy gradient is not fulfilled. In particular, the dark wiggling ribbons in the right top panel, which basically shows contours of $\boldsymbol{\nabla} k^{[6]} \cdot \boldsymbol{F}^{[6]}$, correspond to those points where the turbulence energy gradient is oriented perpendicular to the turbulent flux vector.

Hence, we forsake the approach outlined so far and determine the diffusivity parameter through matching of the flux *magnitudes* in a scalar equation:

$$C_\kappa^{(n)} = \frac{\langle |\boldsymbol{F}^{[n]}| \rangle}{\langle \rho^{(n)} \Delta_n \sqrt{k^{[n]}} |\boldsymbol{\nabla} k^{[n]}| \rangle}. \tag{3.81}$$

With this equation, $C_\kappa^{(6)} \approx 0.390$ is obtained from the DNS data mentioned above. This is larger by about an order of a magnitude than the value computed with equation (3.80). Contours of the corresponding modelled flux, $\rho^{(6)} C_\kappa^{(6)} \Delta_6 \sqrt{k^{[6]}} |\boldsymbol{\nabla} k^{[6]}|$, are plotted in the left panel on the bottom of Figure 3.3. The remarkably good correlation to $|\boldsymbol{F}^{[6]}|$ is evident. Even surfaces at which the flux vanishes as pressure-diffusion cancels the TOM contributions are well reproduced. Therefore, we conclude that the gradient-diffusion closure is a fair *statistical* description of turbulent transport, which correctly accounts for the *magnitude* but not for the local direction of transport. Numerically calculated values of $C_\kappa^{(6)}$ for different DNS are listed in Table 3.2. It appears that there is a trend towards stronger diffusion for higher Mach number. Figure 3.1 shows the variation of $C_\kappa^{(n)}$ with the smoothing length scale Δ_n. As one can see, the parameter of diffusion is almost scale-invariant for $n \in 2, \ldots, 10$, which corresponds to the nearly inertial subrange.

Finally, it was tested whether turbulent diffusivity is correlated with the turbulent viscosity. Recall that $\kappa_{\text{sgs}} = \sigma_{\text{kin}} \nu_{\text{sgs}}$ with $\sigma_{\text{kin}} \sim 1$ is a commonly used hypothesis. To that end, the parameter $C_\nu^{(n)}$ was computed locally according to the similarity closure for production. Then the diffusivity was set equal to the viscosity for positive values of $C_\nu^{(n)}$ and equal to zero for negative values. Negative diffusivity in the SGSTE model would cause numerical instability as energy could pile up more and more in certain regions contrary to the mechanism of diffusion[11]. According to the numerical evaluation, the resulting diffusive flux is too low by an order of a magnitude. An exemplary 2D contour section is shown the bottom of Figure 3.3. Although the discrepancy can be lowered by choosing a higher kinetic Prandtl number σ_{kin}, the level of correlation is found to be unsatisfactory in any case.

[11] Apart from that, the second law of thermodynamics would be violated, because entropy could decrease arbitrarily.

Chapter 4

Deflagration in the Cube

But the hope that "homogeneous turbulence" would be a sensible model was dashed by Landau & Lifschitz 1953-1959, which notes that some regions are marked by very high dissipation, while other regions seem by contrast nearly free of dissipation. This means that the well-known property of wind, that it comes in gusts, is also reflected—in more consistent fashion—on smaller scales.

B. B. Mandelbrot, **The Fractal Geometry of Nature**

The senses' pleasure in colour and melody is the mind's pleasure in pictures and music, and they in turn most often (though not invariably, because the mind enjoys abstraction too) prompt thought.

A. C. Grayling, **The Reason of Things**

With the SGS turbulence energy model, we have one of the keys for tackling turbulent combustion numerically. A further prerequisite is a method of representing and tracking the flame front. In the code Telperion, flames are modelled as discontinuities by means of the *level set method*. This is an excellent approximation for thermonuclear deflagration in degenerate matter, because the typical thickness of the reaction zones is much smaller than the resolution of the numerical grid. In the following, the performance of different SGS models in simplified numerical experiments is investigated. Stochastically driven turbulence in a cube, as discussed in Chapter 2, is set up as the stage on which burning takes place. Due to the periodic boundary conditions, the average mass density in this setting remains constant and there is no explosion. The deflagration rather proceeds in the form of a *percolation process*. All fuel is gradually consumed, and the system eventually approaches a state in which degenerate carbon and oxygen is replaced by nickel and alpha particles in statistical nuclear equilibrium. Another crucial point is that gravity is not included in the simulations. According to the order-of-magnitude estimate in Section 2.3.3, this is a valid approximation on scales $l \ll 10^8$ cm. It is still controversial, whether SGS models, which do not account for gravity, are applicable to thermonuclear supernova. Some arguments in favour of

such a conjecture were given in Section 1.1.3, and further discussion will follow in the concluding Chapter. The major indicators which are used to compare different SGS models in LES of deflagration are the time evolution of the rate of burning and the SGS turbulence velocity. The single most important result obtained from these simulations is that the evolution of the burning process is significantly affected by the SGS model in use. This underlines the importance of choosing a faithful SGS model and certainly bears consequences on the simulation of deflagration in thermonuclear supernova. The most favoured SGS models emerging from the numerical studies is a semi-localised hybrid model, which encompasses a fully localised procedure for SGS turbulence production, a partially statistical method of calculating the dissipation and a purely statistical treatment of diffusion.

4.1 Burning and the Problem of Flame Tracking

In a LES, the total energy E_{tot} is given by the sum of resolved kinetic energy K_{res}, SGS turbulence energy K_{sgs} and internal energy E_{int}, the latter being itself a mass-weighted filtered quantity:

$$E = K_{\mathrm{res}} + K_{\mathrm{sgs}} + E_{\mathrm{int}} = \frac{1}{2}\rho(\underbrace{\widetilde{v_i v_i} + q_{\mathrm{sgs}}^2}_{\widetilde{\langle \rho v_i v_i \rangle}_{\mathrm{eff}}}) + E_{\mathrm{int}}. \tag{4.1}$$

Filtering the conservation law for the total energy in the ideal system and splitting up the resulting equation into a resolved and a SGS part, as in Section 3.1.3 for the kinetic energy, the following equation for the *resolved total energy*, $E_{\mathrm{res}} = K_{\mathrm{res}} + E_{\mathrm{int}}$, is obtained:

$$\frac{\partial}{\partial t}E_{\mathrm{res}} + \frac{\partial}{\partial x_k}(E_{\mathrm{res}} + P)\widetilde{v}_k = \rho f_k \widetilde{v}_k + B - \rho \frac{\mathrm{D}}{\mathrm{D}t}k_{\mathrm{sgs}}. \tag{4.2}$$

The source term B accounts for the rate of heat production due to thermonuclear fusion of degenerate carbon and oxygen. As will be explained below, thermal conduction is implicitly included in the treatment of flame propagation. For this reason, there is no explicit thermal diffusion term in the above equation. Furthermore, one faces the challenge of the hugely disparate length and time scales of the thermonuclear reactions in comparison to anything that can be resolved in a numerical simulation with integral scales of interest. This fact entails two problems. On the one hand, the flame must be either artifically made thick or modelled as discontinuity. Regarding the latter option, which is considered here, a supplementary evolution equation for the propagation of the discontinuity has to be solved. On the other hand, the flame dynamics cannot be computed explicitly on arbitrarily small scales. Consequently, the enhancement of the burning speed due to turbulence on unresolved scales larger than the Gibson scale must be taken into account. Thus, we are lead to the SGSTE model which provides the turbulent flame speed $s_{\mathrm{t}} \sim q_{\mathrm{sgs}}$ and determines the loss of mechanical energy to the subgrid scales, $\mathrm{D}k_{\mathrm{sgs}}/\mathrm{D}t$.

4.1.1 The Level Set Method

In the early studies of deflagration by Khokhlov [1995] and Niemeyer and Hillebrandt [1995b], a *reactive-diffusive* flame model with artifical diffusion and reaction rates was

utilised. In this approach, the thickness of the flame brush is artifically increased over several grid cells and the propagation speed is adjusted to a prescribed value. As a consequence of the high diffusivity, however, the flame front is rather inert against turbulent distortions. For this reason, the surface area and, thus, the energy generation rate remain too small in the course of the burning process. This shortcoming of the reactive-diffusive flame capturing method lead Reinecke, Hillebrandt, and Niemeyer [1999] to a front tracking method which describes the interface separating ash from fuel as a genuine discontinuity, corresponding to an infinitesimally thin flame front. Naturally, this is a sensible approximation if the physical flame thickness is very small compared to the Gibson scale. The interface is numerically represented by the set of all points for which a suitably chosen *distance function* vanishes, i. e., the zero level set. This *level set method* was proposed by Osher and Sethian [1988] and was later adopted for the problem of flame propagation in a flow.

Details of the implementation are discussed in Reinecke et al. [1999] for the two-dimensional case. The generalisation to three-dimensional flames is presented in Reinecke [2001]. In principle, a signed distance function $G(\boldsymbol{x}, t)$ with the property $|\boldsymbol{\nabla} G| = 1$ is introduced. The absolute value $|G(\boldsymbol{x}, t)|$ is equal to the minimal distance of the point $\boldsymbol{x}$ from the flame front at time t. The front itself is given by the constraint $G(\boldsymbol{x}, t) = 0$, i. e., it is represented by the zero level set $\Gamma(t) = \{\boldsymbol{x} | G(\boldsymbol{x}, t)\} = 0$. With the sign convention $G(\boldsymbol{x}, t) > 0$ in regions containing burned material, the unit normal vector pointing towards unburned material is given by $\boldsymbol{n} = -\boldsymbol{\nabla} G / |\boldsymbol{\nabla} G|$. The time evolution of the front $\Gamma(t)$ is implicitly determined by the total time derivative of $G(\boldsymbol{x}_\Gamma(t), t) = 0$. For a certain point at the front, $\boldsymbol{x}_\Gamma(t) \in \Gamma(t)$, we have

$$\frac{\mathrm{d}}{\mathrm{d}t} G(\boldsymbol{x}_\Gamma(t), t) = \frac{\partial G}{\partial t} + \dot{\boldsymbol{x}}_\Gamma \cdot \boldsymbol{\nabla} G = 0. \tag{4.3}$$

The speed function $\dot{\boldsymbol{x}}_\Gamma$ is given by the sum of two contributions. Firstly, the advection speed normal to the flame front, $\boldsymbol{v}_\mathrm{u} \cdot \boldsymbol{n}$, where $\boldsymbol{v}_\mathrm{u}$ is the velocity of the fuel immediately ahead of the front in an Eulerian frame of reference. And, secondly, the intrinsic propagation speed s of the flame front relative the fuel.

The local equation (4.3) can be formulated globally, without constraining the position $\boldsymbol{x}$ to the flame surface. Substituting the definition of the normal vector $\boldsymbol{n}$ and expressing the speed function in the form $\boldsymbol{v}_\mathrm{u} \cdot \boldsymbol{n} + s$, the evolution equation for the level set function at any point in space becomes

$$\frac{\partial G(x, t)}{\partial t} = [\boldsymbol{v}_\mathrm{u}(x, t) + s(x, t) \boldsymbol{n}(x, t)] |\boldsymbol{\nabla} G(x, t)|. \tag{4.4}$$

The advection part on the right-hand side can be treated with any finite-volume scheme like the PPM. However, the updated distance function has to be corrected after each time step, in order to preserve the property $|\boldsymbol{\nabla} G| = 1$. In the implementation of Reinecke et al. [1999], this is achieved with a method called *re-initialisation*. The intrinsic front propagation is usually calculated by means of an *entropy-satisfying upwind scheme*. In general, non-planar fronts will develop sharp corners and the corresponding level set must be a *weak solution*: information about the initial conditions is lost, once a cusp has formed, and the subsequent evolution is irreversible. The corresponding *entropy condition* can be formulated in the following way: once a certain fluid element is burned, it remains burned thereafter. In fact, this implies the equivalent *Huyghen's*

principle in optics for the propagation of the front over an infinitesimal interval of time [cf. Sethian, 1996, Section 5]. An illustration of cusp formation in a two-dimensional flame is given in panel (a) of Figure 4.1.

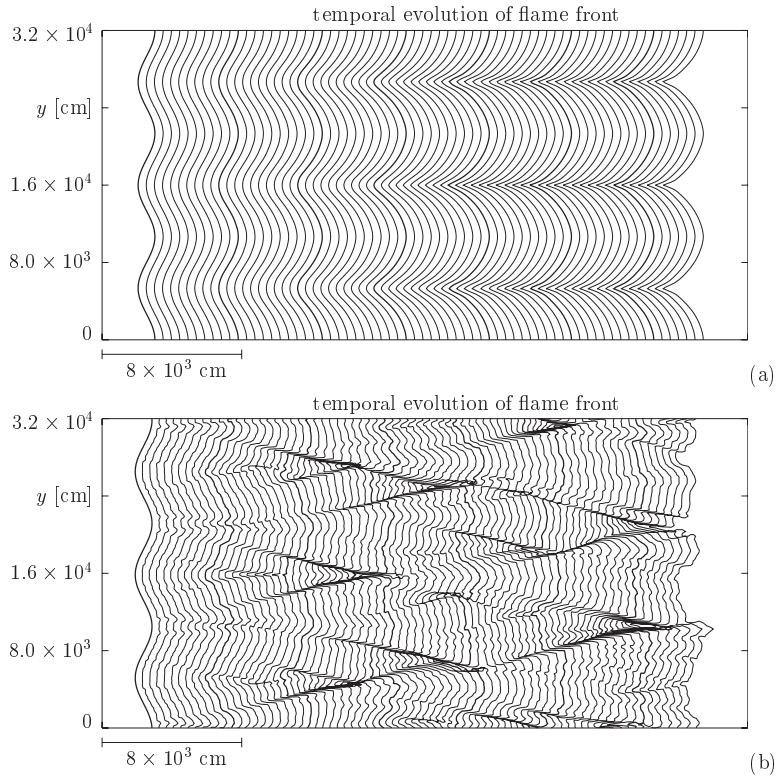

Figure 4.1: Evolution of perturbations in a two dimensional flame front. In the beginning, the perturbations are growing due to the Landau-Darrieus instability. Eventually, cusps begin to form and the flame stabilises. The panel on top shows a simulation of front propagation with complete reconstruction of the states, whereas the bottom panel shows the corresponding result obtained with the passive implementation. The density of the fuel is $5 \cdot 10^7$ g cm^{-3} [taken from Röpke et al., 2003].

For a *complete* implementation of the level set technique, both the burned and the unburned state in an intersected cell must be reconstructed from the jump conditions across the front. Assuming that there is a volume fraction of unburned material α, conservation of momentum imposes the constraint

$$\rho \boldsymbol{v} = \alpha \rho_\mathrm{u} \boldsymbol{v}_\mathrm{u} + (1 - \alpha) \rho_\mathrm{b} \boldsymbol{v}_\mathrm{b}, \tag{4.5}$$

given the finite-volume averages ρ and $\boldsymbol{v}$. Supplementing the momentum equation with the Rayleigh criterion (1.26), the Hugoniot jump condition (1.27) and the continuity constraint for the tangential velocity components, a non-linear system of equations is obtained, from which $\boldsymbol{v}_\mathrm{u}$, $\boldsymbol{v}_\mathrm{b}$ and the corresponding state variables can be determined. The volume fraction α can be calculated by linearly interpolating the discrete numerical values of the distance function G. However, the deviation of the interpolated front element from the exact smooth solution can introduce significant errors in the recon-

structed states. Due to the EOS of degenerate matter, it is sometimes impossible to reconstruct physically sound states. Moreover, one faces topological ambiguities for certain configurations. Reinecke et al. [1999] suggested to average over all possible values, whenever one of these rare cases is encountered. Although Röpke et al. [2003] have recently succeeded with the implementation of in-cell reconstruction in two dimensions, generalising the algorithm to three dimensions, unfortunately, would be much more challenging.

These difficulties are avoided in the so-called *passive* implementation, in which the difference between burned and unburned states is neglected and the advection speed is set equal to $\boldsymbol{v} \cdot \boldsymbol{n}$. The discrete values of G are then interpreted as cell-centred averages. This is a fair approximation in the limit of moderate density jumps between fuel and ash. A caveat of using the passive implementation for simulations of burning at low density is the generation of numerical artifacts. This is drastically demonstrated by panel (b) of Figure 4.1. The front becomes increasingly distorted by numerical noise and finally does not resemble the exact solution at all. Fortunately, these problems are mainly encountered for densities lower than about $10^8\,\mathrm{g\,cm^{-3}}$. We shall discuss this point further in Section 4.2. Apart from the systematic errors introduced by the averaged density and advection velocity, the burning zone is not properly represented as a discontinuity. There is a mixed phase between the regions containing pure fuel and ash, respectively. The width of the diffusive smearing of the flame is typically a few cells, which is still less than for the reaction-diffusion method. In conclusion, the passive implementation gives a satisfactory representation of flame fronts at high density and is robust even in three dimensions, as was demonstrated by numerous applications in type Ia supernova simulations [Reinecke et al., 2002]. The code Telperion features only the passive implementation and, thus, it was used for all simulations discussed in the following.

4.1.2 The Turbulent Flame Speed

The range of scales larger than the flame thickness δ_F can be divided into two regimes, in which the flame dynamics is markedly different. In the case $l \lesssim l_\mathrm{G}$, burning proceeds fast and is only weakly affected by turbulent velocity fluctuations. For $l \gtrsim l_\mathrm{G}$, on the other hand, turbulence wrinkles the flames. In a numerical simulation, the flame dynamics is fully resolved for a Gibson scale $l_\mathrm{G} \gtrsim \Delta_\mathrm{eff}$, where Δ_eff is the effective numerical scale (see Section 2.5.4). The intrinsic front propagation speed is, in first approximation, given by the *laminar* burning speed. However, setting $s = s_\mathrm{lam}$ does not account for the cellular structure of the flames due to instabilities on length scales comparable to l_G. If l_G is just slightly above the numerical resolution and, in particular, if the passive implementation of the level set method is used, the cellular flame texture is largely made smooth by numerical diffusion. This systematic error can be compensated by enhancing the propagation speed, $s = s_\mathrm{cell}$ [Niemeyer and Woosley, 1997].

On scales beyond the Gibson scale, flames are predominantly shaped by turbulence and the cellular regime breaks down. If $l_\mathrm{G} \ll \Delta_\mathrm{eff}$, a numerically computed flame front appears inevitably smoother than its physical counterpart. Consequently, the predicted burning rate would be underestimated, if the intrinsic propagation speed s were set equal to s_cell. This is where the notion of a turbulent flame speed comes in. Accord-

ing to the discussion in Section 1.1.3, an effective propagation speed $s_t(\Delta_{\text{eff}})$ can be associated with the surface area $A(\Delta_{\text{eff}})$ of the numerically resolved flame fronts, and, setting $s = s_t(\Delta_{\text{eff}})$, the total burning rate is preserved. Although the turbulent flame speed was introduced as an ensemble average, Niemeyer and Hillebrandt [1995b] proposed that $s_t(\Delta_{\text{eff}})$ is *locally* given by the magnitude of unresolved turbulence velocity fluctuations. In a way, this assumption is based on *self-similarity*, i. e.,the conservation of the burning rate for the flame as a whole should hold individually for pieces of the flame as well. Since the propagation speed cannot be less than the laminar flame speed, it was suggested to set

$$s_t(\Delta) = \max(s_l, q_{\text{sgs}}). \tag{4.6}$$

Certainly, this is a very limited approximation, which can be expected to hold in the regime of fully developed turbulence only. Even then it is not clear whether the constant of proportionality between $s_t(\Delta)$ and q_{sgs} is actually unity. In transient phases, the relation between turbulent flame speed and turbulence velocity might very well be different[1]. The right-hand side of the above relation ignores the transition from resolved laminar burning to unresolved turbulent burning. However, this transition progresses rather quickly at any particular location, and a correct description in the intermediate phase is probably not overly important. Despite these uncertainties, the relation proposed by Niemeyer and Hillebrandt [1995b] remains to be in use for numerical simulations.

A different turbulent flame speed model was derived theoretically by Pocheau [1994]:

$$\frac{s_t}{s_{\text{lam}}} = \left[1 + C_t \left(\frac{q_{\text{sgs}}}{s_{\text{lam}}}\right)^n\right]^{1/n}. \tag{4.7}$$

In the scale-invariant regime, with $q_{\text{sgs}} \gg s_{\text{lam}}$, the asymptotic form $s_t \simeq C_t^{1/n} q_{\text{sgs}}$ is obtained. Thus, the parameter C_t determines the asymptotic scaling of the turbulent flame speed for fully developed turbulence. The particular case $C_t = 1$ agrees with the asymptotic limit of equation (4.6). Kim et al. [1999], however, chose $C_t \approx 20$ for LES of gas turbine combustor flows. This value was inferred from laboratory experiments with hydrocarbon/air flames. As mentioned in Williams [1994, Section 7.4], the parameter C_t supposedly depends on thermodynamical properties of the system. Thus, one has to be careful with adopting any experimental values for LES of thermonuclear burning. If $q_{\text{sgs}} \ll s_{\text{lam}}$, the *Calvin-Williams* relation is obtained from Taylor series expansion of the right-hand side of equation (4.7) in the case $n = 2$:

$$\frac{s_t}{s_{\text{lam}}} = 1 + C_t \left(\frac{q_{\text{sgs}}}{s_{\text{lam}}}\right)^2. \tag{4.8}$$

The validity of this relation for weak turbulence is supported by some numerical results [cf. Im et al., 1997]. The heuristic relation (4.6), on the other hand, implies $s_t = s_{\text{lam}}$ if $q_{\text{sgs}} \leq s_{\text{lam}}$ and entails a discontinuity in the derivative of $s_t(q_{\text{sgs}})$ at the transition from laminar to turbulent burning.

[1] Im et al. [1997] mentioned a quadratic dependence on the turbulence velocity in the case of weak turbulence, whereas Röpke [2003] reported a linear relation, even for turbulence velocities which are only marginally larger than the laminar flame speed.

4.2 Transient Laminar Burning in a Developing Flow

To begin with, let us consider a simulation of stochastic deflagration, in which the flame dynamics is completely resolved. Since the Gibson scale is the lower cutoff scale, $l_\mathrm{G} \gtrsim \Delta_\mathrm{eff}$ is a sufficient condition, regardless of the Kolmogorov scale η_K. As before, Δ_eff is the effective numerical scale of the finite-volume scheme, namely, the PPM. The Gibson scale l_G is mostly determined by the initial density ρ_0 and the characteristic scales of turbulence. Assuming Kolmogorov scaling, one can estimate the magnitude of turbulent velocity fluctuations at a separation of the order to the Gibson length:

$$v'(l_\mathrm{G}) \sim V\,(l_\mathrm{G}/L)^{1/3}\,, \tag{4.9}$$

As in (Section 2.3.3, L and V are, respectively, the integral length and the characteristic velocity of fully developed turbulence. Setting $v'(l_\mathrm{G}) = s_\mathrm{lam}$, the scaling law for the Gibson scale becomes

$$l_\mathrm{G} \sim L\,(s_\mathrm{lam}/V)^3\,. \tag{4.10}$$

Obviously, the Gibson scale is very sensitive to the ratio of the laminar burning speed to the characteristic velocity of the flow. In the following, suitable parameters for a completely resolved simulation of thermonuclear deflagration in high-density C+O matter are identified and results from a DNS with these parameters are discussed.

4.2.1 Critical Parameters

For $N \sim 10^3$ grid cells in each dimension, the relation (4.10) implies $s_\mathrm{lam} \gtrsim 0.1V$, if the flame dynamics is to be resolved completely. In fact, the constraint becomes even tighter, if the ratio of the integral scale to the size of the computational domain, $\alpha = N\Delta/L$, and the ratio of effective numerical scale to the grid scale, $\beta = \Delta_\mathrm{eff}/\Delta$, are taken into account. With the effective Reynolds number $\mathrm{Re}_\mathrm{eff} = (N/\alpha\beta)^{4/3}$, it follows that

$$V \lesssim \mathrm{Re}_\mathrm{eff}^{1/4}\, s_\mathrm{lam} \tag{4.11}$$

is required for a DNS. Since $\mathrm{Re}_\mathrm{eff} \approx 400$ was found in the simulations of isotropic turbulence with 432^3 grid cells, at most $V \approx 4s_\mathrm{lam}$ would be admissible, if burning were included. For moderate densities, this would imply very low Mach numbers, which are computationally infeasible. The laminar burning speed is sufficiently large compared with the speed of sound only at high densities. For example, one obtains $s_\mathrm{lam} \approx 1.05{\cdot}10^7\,\mathrm{cm\,s^{-1}}$ at a density $\rho_0 = 100\rho_\mathrm{c} \approx 2.903{\cdot}10^9\,\mathrm{g\,cm^{-3}}$ via interpolation of the numerical values for the laminar burning speed in Table 3 of Timmes and Woosley [1992][2]. The speed of sound for this density is $c_0 \approx 9.70 \cdot 10^8\,\mathrm{cm\,s^{-1}}$. Choosing $V = 4s_\mathrm{lam} \approx 4.20 \cdot 10^7\,\mathrm{cm\,s^{-1}}$, the characteristic Mach number is $V/c_0 \approx 0.043$. This is quite small, but still computationally manageable with a fully compressible hydro code.

Choosing the aforementioned parameters, a DNS of thermonuclear burning was carried out with the code Telperion, including the passive level set implementation.

[2] Timmes and Woosley [1992] also gave a fit formula for s_lam, which was determined from their numerical data. However, the values obtained from this formula do not agree well with the tabularised values in certain cases.

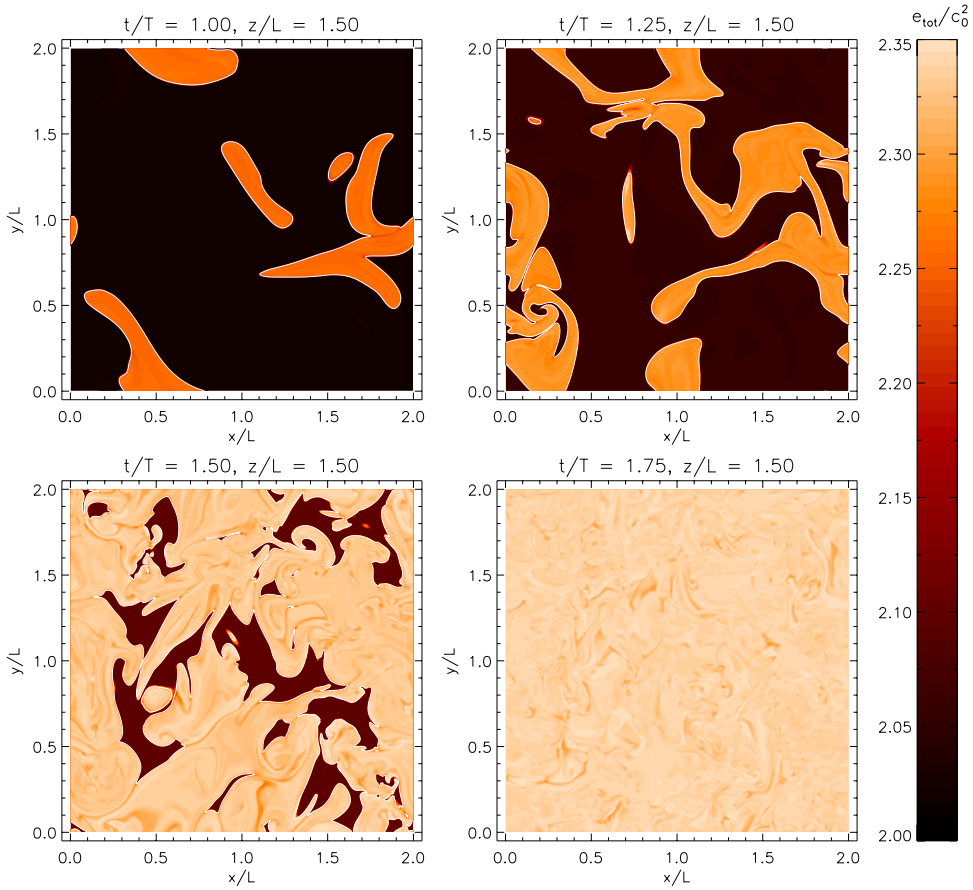

Figure 4.2: Simulation `dns432burn` of thermonuclear deflagration in C+O of density $\rho_0 \approx 2.903 \cdot 10^9\,\mathrm{g\,cm^{-3}}$ with $V/s_{\mathrm{lam}} = 4$ and a characteristic Mach number is $V/c_0 \approx 0.043$. Shown are 2D contour sections of the normalised specific energy $\tilde{e} = e/c_0^2$ at different stages of the burning process.

Subsequently, we shall refer to this simulation as `dns432burn`. In place of the complicated network of thermonuclear reactions, the fusion of equal mass fractions of ^{12}C and ^{16}O to ^{56}Ni and ^{4}He was used as representative reaction [cf. Steinmetz et al., 1992]. The integral length was set to half of the size of the computational domain ($\alpha = 2$) and turbulence was produced with purely solenoidal stochastic forcing. The Gibson length corresponding to $V = 4s_{\mathrm{lam}}$ and $L = 216\Delta$ is roughly $l_{\mathrm{G}} \approx 3.3\Delta$, which allows for some margin between l_{G} and Δ_{eff}. Since the Gibson scale is just within the range of resolved scales, the cellular flame structure induced by Landau-Darrieus instability will be largely smoothed out by numerical dissipation. Hence, $s = s_{\mathrm{cell}}$ would be the correct intrinsic propagation speed (see Section 4.1.2). However, this effect was ignored, as the purpose of the simulation in question is the study of level set propagation with constant intrinsic speed. Whether this speed is s or s_{cell} was not of much concern, because both are of the same order of magnitude. Regarding the numerical distortion introduced by the passive implementation, one should be on the safe side

for a mass density larger than $10^8\,\mathrm{g\,cm^{-3}}$. Apart from that, the randomisation caused by turbulence tends to diffuse any numerical artifacts. In this respect, simulating the propagation of symmetric flame fronts, say, nearly planar or spherical ones, is a more demanding task. Furthermore, flow maps prepared form the simulation data clearly show a tight correlation between the shape of the front and the flow structure. If there were significant spurious propagation or deformation, the evolution of the front should become increasingly uncorrelated to the flow. In conclusion, the simulations which will be discussed subsequently are likely to give a sound description of the flame dynamics, albeit the shortcomings of the level set method in the passive implementation.

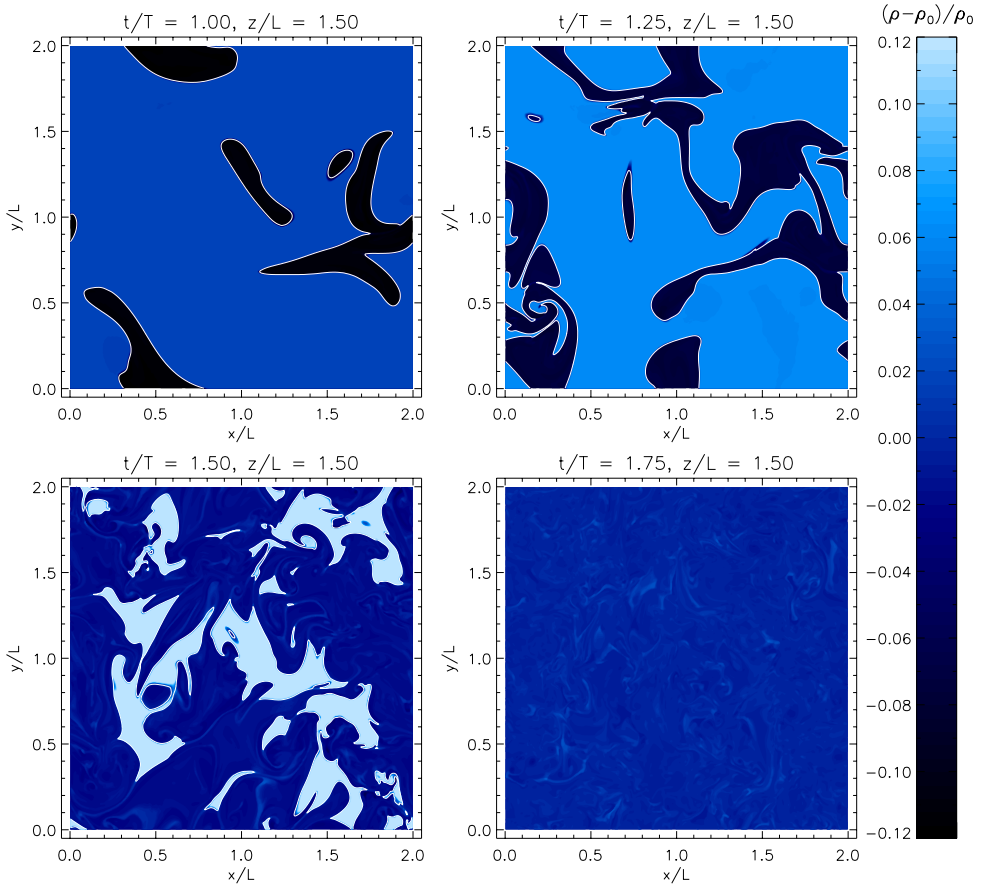

Figure 4.3: 2D contour sections of the relative density fluctuations $(\rho-\rho_0)/\rho_0$ in the simulation `dns432burn` corresponding to the panels shown in Figure 4.2.

4.2.2 Evolution of the Burning Process

The progression of the deflagration in the simulation `dns432burn` is illustrated by a sequence of contour plots in Figure 4.2. In this DNS, burning was ignited in eight small spherical regions, each one in the centre of a cubic subdomain of volume L^3 corresponding to one integral scale. The contours of the zero level set can be seen as

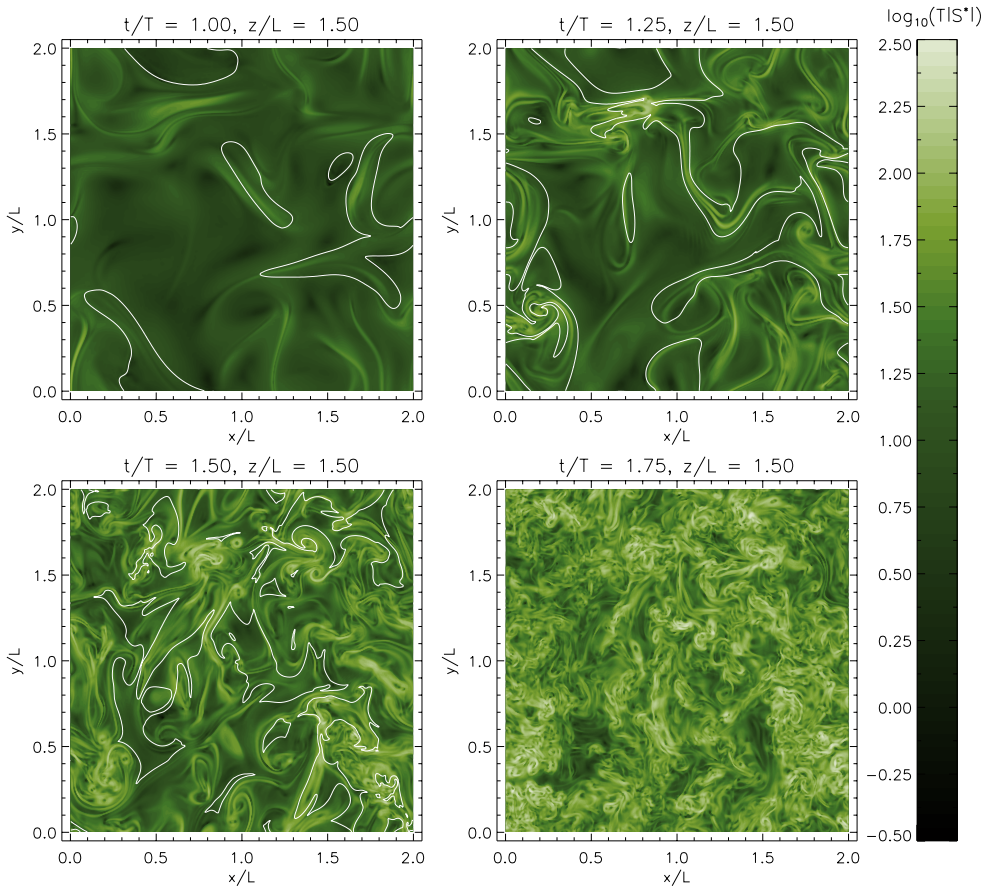

Figure 4.4: 2D contour sections of the logarithmic dimensionless rate of strain, $\log_{10}(T|S^*|)$, corresponding to the panels shown in Figure 4.2 and Figure 4.3.

thin white lines which separate dark regions containing unburned matter of low energy density from the brightly coloured regions containing processed material of high energy density. In the course of the first integral time T, the regions of burned material are expanding gradually. At the same time, they are stretched an folded by the vortical large-scale flow. From $\tilde{t} \sim 1.0$ onwards, vortices are generated on small scales. However, around $\tilde{t} \approx 1.5$ most of the fuel has already been consumed by the burning process, and the last fuel patches disappear quickly. Thus, the peak of burning is reached before turbulence is fully developed. Consequently, the front propagation is is not much affected by small-scale velocity fluctuations. In the top panel on the right of Figure 4.5, the mean burning rate $\langle B \rangle$. The rate of burning increases exponentially in the interval $0.3 \lesssim \tilde{t} \lesssim 1.2$. The peak of $\langle B \rangle$ at $\tilde{t} \approx 1.35$ marks the *percolation threshold*. Afterwards ash encloses fuel rather than the other way around. This threshold occurs significantly earlier than the peak of vorticity at time $\tilde{t} \approx 1.9$, which can be seen in the bottom right panel. For $V/s_{\mathrm{lam}} = 4$, two adjacent burning zones would merge within two integral time scales if they were not perturbed by the flow. However, since the advection increases the surface as compared to a spherical shape, flame fronts origi-

nating from different ignition zones are likely to collide earlier and burning proceeds faster. Furthermore, percolation entails a *density inversion*, as the ash gets compressed once most of the domain volume is burned. The inversion of the density is shown in Figure 4.3. Viewing the contour plots of the rate of strain in Figure 4.4, one can see that the flames appear elongated and shaped by the strain. Small-scale features of the flow affect the flame propagation only marginally, because of the high laminar flame speed. Apart from that, most of the fuel is burned before small vortices are formed appreciably. The statistics shown in the bottom panel on the right of Figure 4.2 also suggests that the growth of the burning rate prior to the percolation threshold correlates with the exponentially increasing RMS rate of strain.

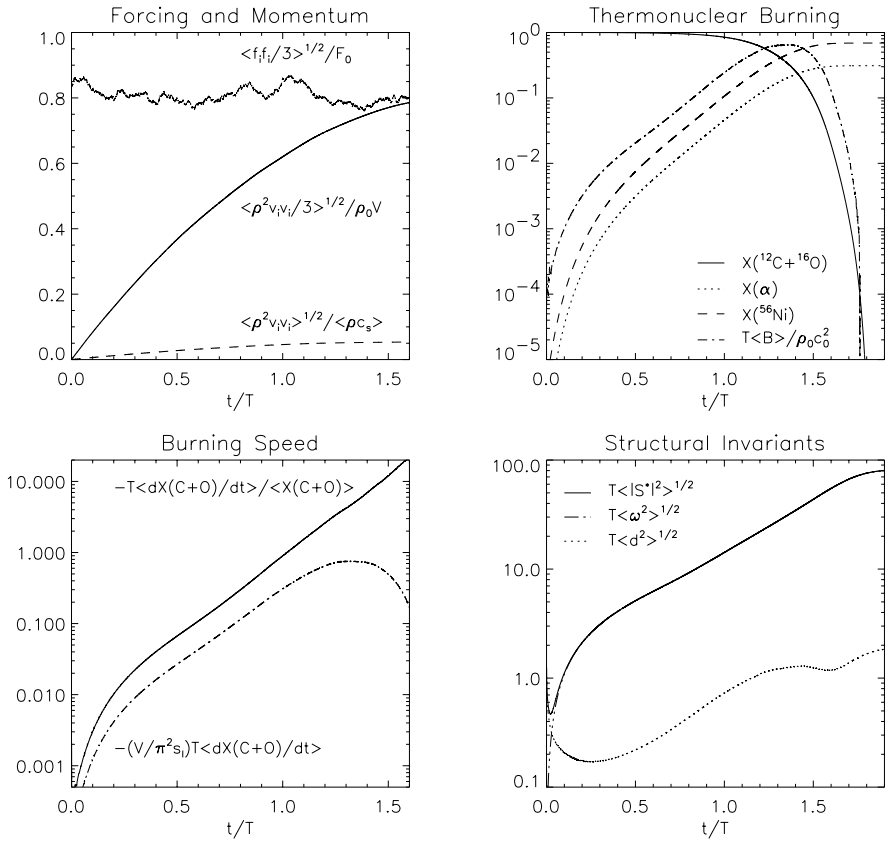

Figure 4.5: Evolution of dimensionless statistical moments for the simulation `dns432burn`. The panels show the RMS force, momentum and Mach number, the average rate of energy release due to burning and the chemical composition, the mean rate of energy production and dissipation, respectively, as well as averaged structural invariants.

The rate of change of the mean mass fraction of fuel, $\langle \dot{X}(\mathrm{C+O}) \rangle$, is also a measure of the burning speed. For an energy release ϵ_{nuc} per unit mass, the total energy generated by fusion of C+O in the whole cubic domain per unit time can be expressed as

$$(\alpha L)^3 \langle B \rangle = -\epsilon_{\mathrm{nuc}} M_{\mathrm{cube}} \langle \dot{X}(\mathrm{C+O}) \rangle, \tag{4.12}$$

where $M_{\rm cube} = \rho_0(\alpha L)^3$ is the total mass contained in the computational domain. On the other hand, the rate of energy production can be related to the total surface area of the flame fronts, $A_{\rm F}$, and the laminar propagation speed $s_{\rm lam}$, if compression effects are neglected:

$$(\alpha L)^3\langle B\rangle = \rho_0 \epsilon_{\rm nuc} A_{\rm F} s_{\rm lam}. \tag{4.13}$$

Combining equations (4.12) and (4.13) with $M_{\rm cube} = 8\rho_0 L^3$, the approximate total surface area is found to be

$$A_{\rm F} \simeq \frac{(2L)^3}{s_{\rm lam}}\langle \dot{X}({\rm C+O})\rangle. \tag{4.14}$$

The graph of the normalised surface area[3],

$$\tilde{A}_{\rm F} = \frac{A_{\rm F}}{8\pi^2 L^2} = -\frac{1}{\pi^2}\frac{V}{s_{\rm lam}}\langle T\dot{X}({\rm C+O})\rangle, \tag{4.15}$$

is shown in the left bottom panel of Figure 4.2. The exponential growth of the burning rate is manifest in this plot as well. At the peak, $\tilde{A}_{\rm F} \sim 1$. Thus, it appears that the flame surface does not significantly increase due to wrinkling in the course of the burning process. This agrees with the impression of rather smooth flames in Figure 4.2. Also plotted is the graph of $-\langle T\dot{X}({\rm C+O})\rangle/\langle X({\rm C+O})\rangle$, which is a measure of the ratio of the flame surface area to the amount of still unburned material[4]. There is sustained exponential behaviour even beyond the maximum burning rate, continuing almost to the end point of combustion, which demonstrates the invariance of laminar burning with respect to the amount of fuel.

4.3 Turbulent Burning

The laminar propagation speed decreases much faster towards lower densities than the speed of sound. For example, setting $\rho_0 = 10\rho_{\rm c} \approx 2.903 \cdot 10^8\,{\rm g\,cm^{-3}}$, which is by an order of a magnitude smaller than the density chosen in Section 4.2, $s_{\rm lam} \approx 9.78 \cdot 10^5\,{\rm cm\,s^{-1}}$ is obtained from interpolating the data in Table 3 of Timmes and Woosley [1992]. Choosing a characteristic velocity $V = 100 s_{\rm lam}$, we have a Mach number $V/c_0 \approx 0.15$, and an estimate of the Gibson scale is $l_{\rm G} \sim 10^{-6}L$. Thus, keeping the Mach number ~ 0.1, it is not possible to resolve the flame over the whole range of dynamical scales, and a numerical simulation of the burning process is necessarily a large-eddy simulation (LES). In this Section, LES of thermonuclear burning with the parameters outlined above are discussed. First the non-linear algebraic model is compared to the SGS turbulence energy model. Then several flavours of the turbulence energy model are investigated. In particular, a *semi-localised* variant is formulated and tested *a posteriori*.

4.3.1 The Algebraic vs. the Dynamical Model

The lowest-order algebraic closure for the SGS turbulence stress tensor implies that the corresponding turbulence energy is solely determined by the local rate of strain (see

[3] $8\pi^2L^2$ is the total surface area of eight spheres of radius $L/2$.

[4] Strictly, the volume of fuel left at a certain time would be given by $(\alpha L)^3\langle \rho X({\rm C+O})\rangle/\rho_0$. However, the mass-weighted fraction of C+O was not calculated in the simulation.

Section 3.1.2). According to equation 3.23 for the SGS turbulence velocity q_{sgs}, there is one closure parameter, C_{nl}, which is *a priori* undetermined. The other parameter of the model, namely, the linear Smagorinsky length scale, were determined from DNS data. In the following, we consider the simulation `les216nlk075` with $C_{\text{nl}} = 3/4$ and $\ell_{\text{S}} \approx 0.30\Delta$, the latter being an appropriate Smagorinsky length length for a Mach number ~ 0.1 (see Table 3.1). In the reference simulation `les216kinw`, the SGSTE model (3.45) with the constant closure parameters $C_\nu = 0.06$, $C_\epsilon = 0.48$ and $C_\kappa = 0.36$ from Section 3.2 was used. The pressure-dilatation term was neglected ($C_\lambda = 0$) and the effective numerical length scale $\Delta_{\text{eff}} = 1.8\Delta$ was chosen. Both simulations were computed with 216^3 grid cells of size $\Delta = 2 \cdot 10^3$ cm and an integral scale of the flow $L = 108\Delta = 2.16 \cdot 10^5$ cm.

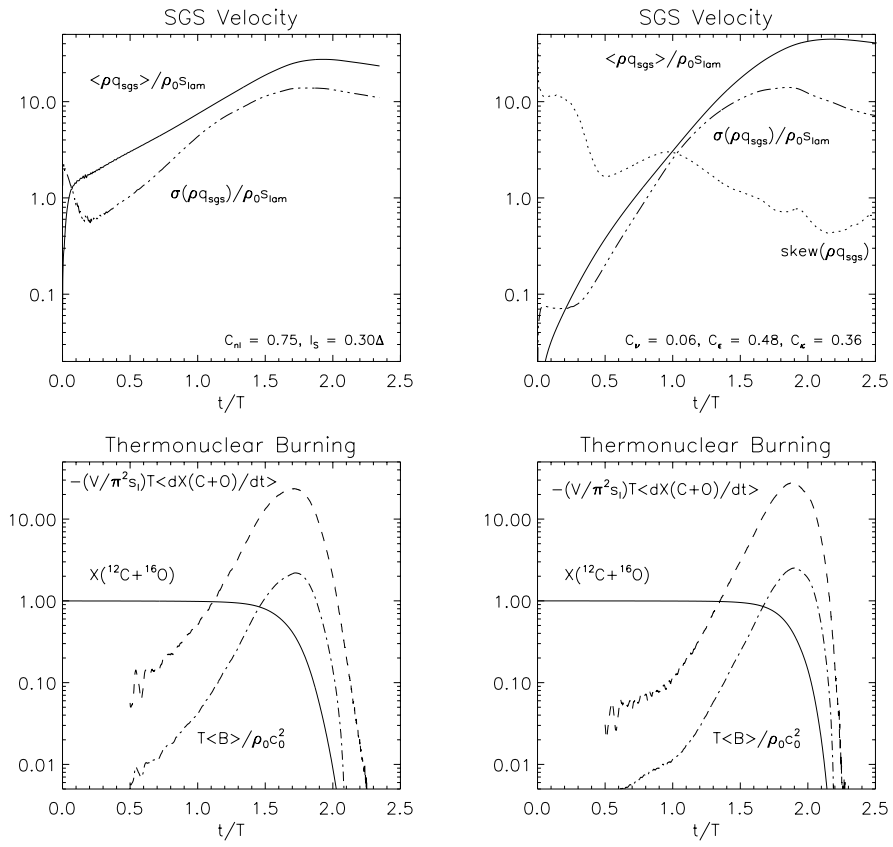

Figure 4.6: Comparison of the evolution of SGS turbulence and thermonuclear burning for the simulations `les216nlk075` and `les216kinw` with the non-linear algebraic and the SGS turbulence energy model, respectively.

The evolution of three statistical moments of the mass-weighted SGS velocity is shown in the top panels of Figure 4.6. These moments are the global mean $\langle \rho q_{\text{sgs}} \rangle / \rho_0$, the standard deviation $\sigma(\rho q_{\text{sgs}})/\rho_0$ and the *skewness*, which is defined by (cf. Lumley [1970], Section 2.1)

$$\text{skew}(\rho q_{\text{sgs}}) = \frac{\langle [\rho q_{\text{sgs}} - \langle \rho q_{\text{sgs}} \rangle]^3 \rangle}{\sigma^3(\rho q_{\text{sgs}})}. \tag{4.16}$$

Both the mass-weighted average and the standard deviation of q_{sgs} are plotted in units of the laminar propagation speed s_{lam}. For fully developed turbulence at time $\tilde{t} \gtrsim 2.0$, the mean SGS velocity is much larger than the laminar speed in both simulations. In the case of the algebraic SGS model, $\langle \rho q_{\mathrm{sgs}} \rangle / \rho_0$ is exponentially growing, proportional to the mean rate of strain. In comparison with the SGSTE model, there is more SGS turbulence in the early production phase, but less once the flow approaches stochastic equilibrium. The standard deviations are also quite different for both models. The relative fluctuations of q_{sgs} are definitely smaller for the SGSTE model. This is mainly a consequence of the absence of any diffusion mechanism in the algebraic model.

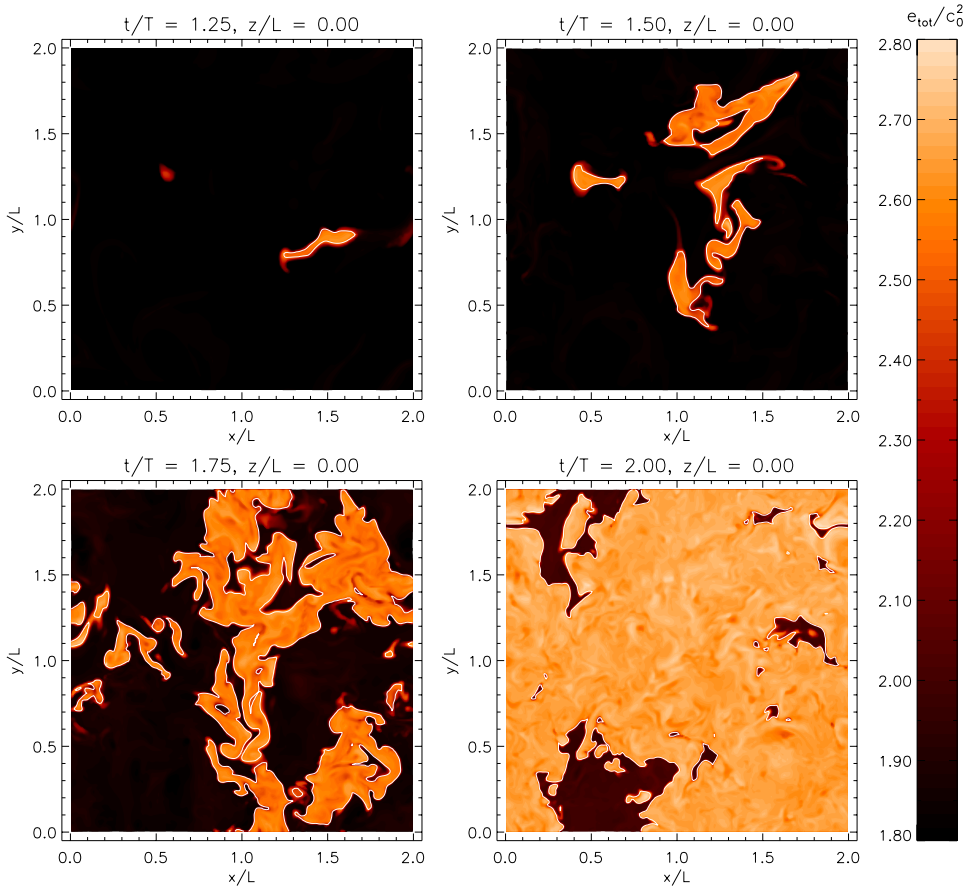

Figure 4.7: 2D contour sections of the normalised specific energy $\tilde{e} = e/c_0^2$ at $\tilde{z} = 0.0$ for `les216kinw`. In this simulation, the SGS turbulence energy model with constant closure parameters was used to calculate the turbulent flame speed.

In contrast, there is an exponential increase of the mean burning rate $\langle B \rangle$ from $\tilde{t} \approx 1.2$ to $\tilde{t} \approx 1.8$ in the case of `les216kinw`, as one can see in the right bottom panel of Figure 4.6. The non-linear algebraic model, on the other hand, predicts a slower growth of the burning rate in this time interval. However, since the burning proceeds faster in the beginning, the peak of $\langle B \rangle$ is shifted towards an earlier time. The maximum rate of energy release is of the order $\rho c_0^2 / T$, which indicates that the density of

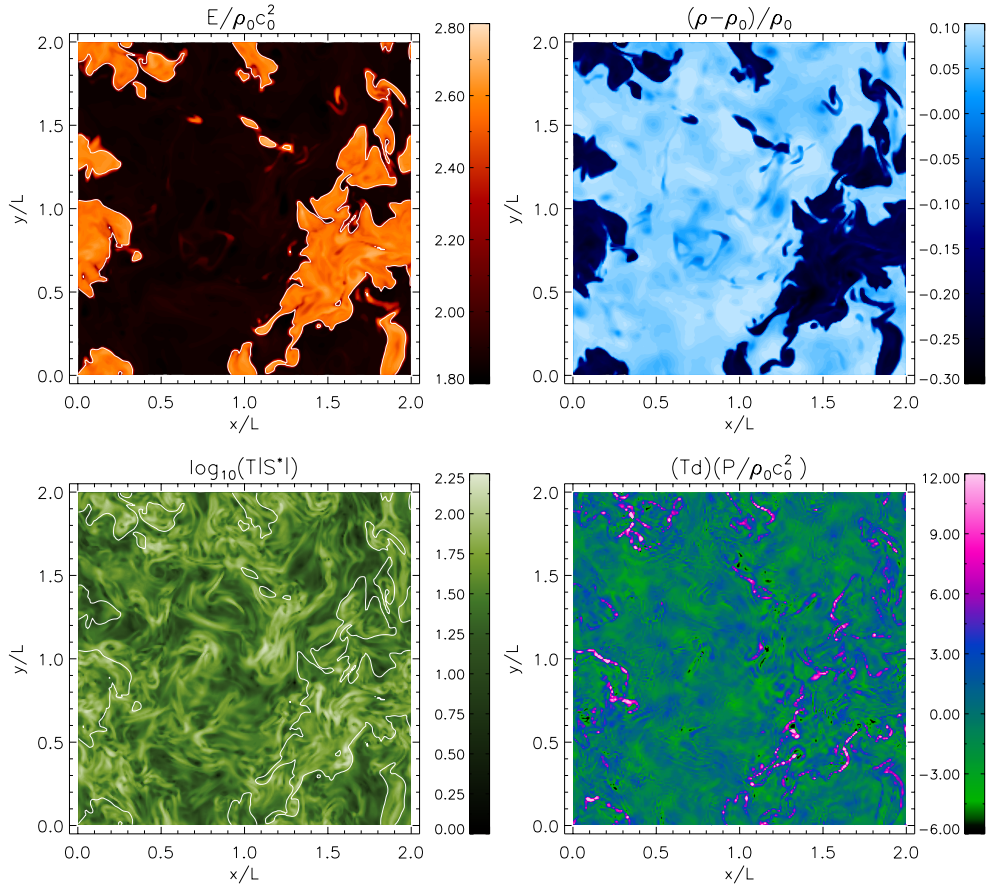

Figure 4.8: 2D contour sections of normalised energy, density fluctuations, rate of strain and pressure dilatation for `les216kinw` at time $\tilde{t} = 1.75$.

internal energy, $E_{\text{int}} \sim \rho c_s^2$, rises substantially in the course of the combustion process. In fact, the final mean internal energy is by a factor of about 1.5 greater than the initial energy. Furthermore, the mean mass fractions of fuel and the approximate flame surface areas according to equation (4.15) are plotted in the bottom panels. As opposed to the DNS of laminar burning, $\tilde{A}_{\text{F}} \sim 10$ at the time of most rapid burning, which implies that the flames are more folded and wrinkled. Indeed, the zero level set contours for simulation `les216kinw`, which are shown in Figure 4.7, are clearly more structured at small scales than those of model `dns432burn` (see Figure 4.2). There also appears to be a more pronounced leakage of energy into unburned material, as the errors in the passive implementation are larger at lower resolution and lower mass density. However, the energy diffusion extends only over a few numerical cells, and the separation between ash and fuel is basically maintained in the course of the whole burning process. Contour sections for several quantities at time $\tilde{t} = 1.75$ are shown Figure 4.8. Comparing the two panels on top, one can see that ash is contained in regions of high specific energy $\tilde{e} = e/c_0^2$, whereas the mass density of ash falls short of as much as 30 % compared to most of the unburned material. Such a large density contrast is not

encountered in thermonuclear supernovae. However, since the total volume is constant and mass must be conserved in a cube with periodic BCs, heated material compresses its surroundings and thereby enhances the density gradient. The bottom panel on the right depicts the corresponding normalised pressure dilatation, $\tilde{P}\tilde{d} = (P/\rho_0 c_0^2)(Td)$. In fact, the locus of significant expansion is the vicinity of the flames, while most of the fuel, but also some of the ash, are being compressed.

4.3.2 Statistical vs. Localised Closures

Independent of numerous attempts by engineers to localise turbulent-viscosity models, a method of including "wall effects" in simulations of stellar interiors was suggested by Clement [1993]. Bringing to mind that a steep density gradient in a turbulent stratified medium, such as the convection zone in a star, acts more or less like a wall, Clement found empirically that the ratio of internal energy to the turbulent kinetic energy, $e_{\rm int}/k_{\rm sgs}$, serves as an indicator of the local level of turbulence and the wall proximity. Thus, he suggested the following relations for the closure parameters of production and dissipation in the SGSTE model:

$$C_\nu = 0.1W, \text{ and } C_\epsilon = \frac{0.5}{W}, \tag{4.17}$$

where the *wall proximity function* W is defined by

$$W = \min\left[100, \max\left(0.1, 2\cdot 10^{-4}\,\frac{e_{\rm int}}{q_{\rm sgs}^2}\right)\right]. \tag{4.18}$$

As Supplementary relation, Clement set $C_\kappa = C_\nu$. These are the specifications of the SGS model which has been used in all simulations of thermonuclear supernovae starting with Niemeyer and Hillebrandt [1995b] up to the most recent models by Reinecke et al. [2002]. However, as was pointed out by Niemeyer and Hillebrandt, it is not all clear whether the numerical constants chosen by Clement [1993] for stellar interiors are also appropriate for supernova explosions. Actually, this is very doubtable. A more rigorous objection comes from the observation that turbulence production is inhibited close to a wall [cf. Meneveau and Katz, 2000, Fig. 2]. However, the production parameter $C_\nu = 0.1W$, with W given by equation (4.18), tends to become larger as the SGS turbulence energy decreases, which works against inhibition near a wall.

The evolution of statistical moments in a LES with the SGSTE model and Clement's rules for calculating the closure parameters are plotted in the left column of panels in Figure 4.9. A moderate resolution of 144^3 grid cells was chosen, the mass density, integral length scale and characteristic velocity are the same as before. The effective numerical scale was set equal to Δ in order to maintain consistency with earlier implementations of Clement's model. As one can see in the top panel on the very left, the ratio $\langle\rho q_{\rm sgs}\rangle/\langle|\rho\boldsymbol{v}|^2\rangle^{1/2}$ is nearly constant throughout the simulation. Moreover, $\langle\rho q_{\rm sgs}\rangle/\rho_0$ is large compared to the laminar burning speed almost right from the beginning. Accordingly, the rate of burning increases more or less gradually as one can see in the bottom panel. In the middle column of panels in Figure 4.9, the corresponding evolution for a simulation with the SGSTE model with the constant parameters $C_\nu = 0.06$, $C_\epsilon = 0.48$, $C_\kappa = 0.36$, $C_\lambda = -0.2$ and $\beta = \Delta_{\rm eff}/\Delta = 1.8$ is shown. Contrary to the LES with Clement's procedure, the SGS turbulence velocity is rising

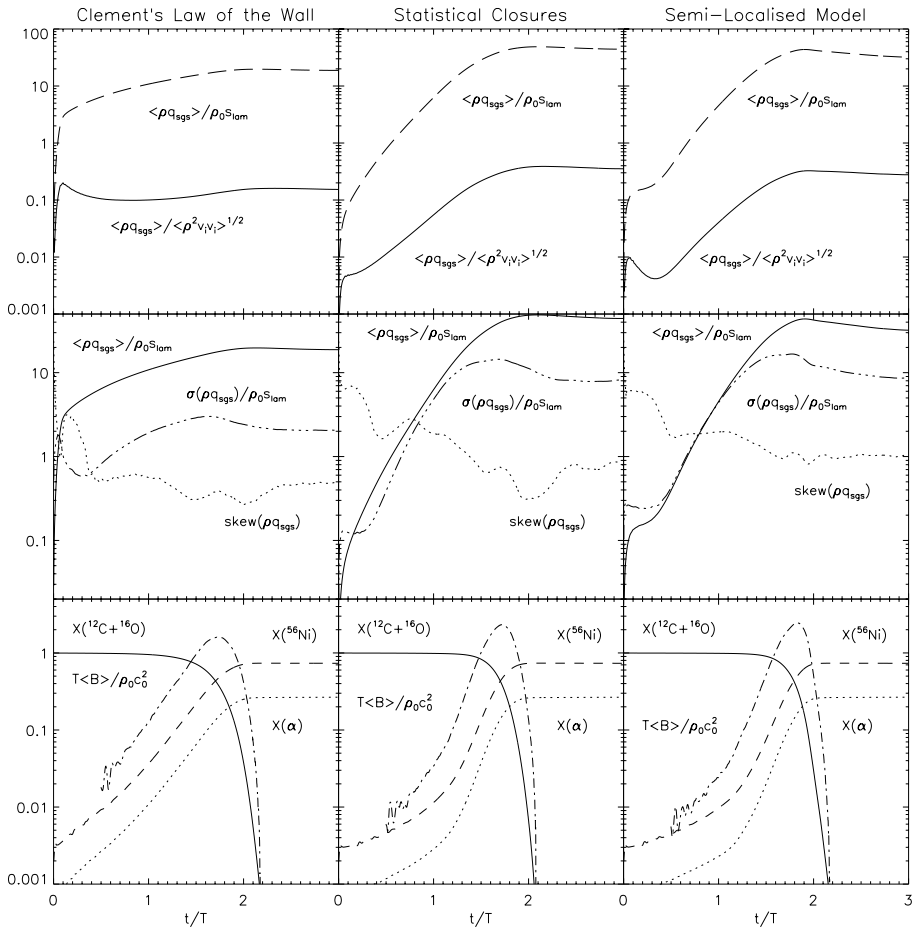

Figure 4.9: Comparison of the evolution of SGS turbulence and thermonuclear burning for different SGS models. In the first simulation, Clement's law of the wall was used to calculate the closure parameters, the second one was computed with constant statistical parameters and for the third simulation, the semi-localised model was applied.

much slower while turbulence is being produced. The maximum of $\langle \rho q_{\mathrm{sgs}} \rangle$ coincides with the peak of the rate of strain. In consequence, there is only little enhancement of the burning speed at first, but then it is rising ever faster as turbulence sets in and eventually becomes space filling. Note that the steep rise of the burning rate begins around $\tilde{t} \approx 1$, although the mean SGS turbulence velocity is of the same order as the laminar burning speed as early as $\tilde{t} \gtrsim 0.5$. This can be understood if one considers the standard deviation and skewness of the SGS turbulence velocity. In the production phase, there are large fluctuations in q_{sgs} and the distribution in space is quite inhomogeneous. Consequently, SGS turbulence is concentrated in certain regions, and the probability of the flame front crossing one of those is rather low. Once SGS turbulence becomes rather homogeneous, however, an increasing fraction of the flame surface is subject to turbulent acceleration. This impressively illustrates the *spatial intermittency* of turbulence, even though the system approaches a homogenous steady state at later

time. Intermittency is clearly ignored in Clement's law of the wall.

However, one has to keep in mind that the SGSTE model with constant closure parameters is not fully adequate either, when it comes to transient and intermittent systems. The statistical values for C_ν, C_ϵ and C_κ strictly apply to the case of developed isotropic turbulence only. Deflagration in a developing turbulent flow, however, is neither homogeneous nor steady. Moreover, the flames themselves introduce a kind of anisotropy, albeit a weak one, because the hydrodynamical quantities are only marginally affected by the burning process. For this reason, a semi-localised SGSTE model was formulated which is based upon the self-similarity closure for the production term. Diffusion is still treated statistically, with the constant parameter $C_\kappa = 0.36$, and so is pressure-dilatation. Dissipation, on the other hand, is computed in a semi-statistical fashion. Details of the model will be explained in Sections 4.3.3 and 4.3.4. For the time being, we shall merely contrast the outcome of a LES using the semi-localised model with the other models. The results are plotted in the very right column of panels in Figure 4.9. Regarding SGS turbulence and the evolution of burning, there are no pronounced differences compared with the purely statistical closures. Indeed, this does not come as a surprise, because of *local isotropy*. If there is only little SGS turbulence, incorrect values of the closure parameters merely influence something that is insignificant anyway. Once turbulence has developed in a certain region, it is locally isotropic. Only in between, in the course of the non-linear transition, a dynamical production parameter makes a difference. Does this imply that determining C_ν from local time-dependent properties of the flow is not essential? It depends what questions one intends to answer. Apart from that, in more complex scenarios, the localisation of closures is probably much more significant.

As a matter of fact, the physical conditions inside and outside of a flame are different. For example, averages of the production parameter C_ν over the three principal topological regions of the computational domain are shown in the top panels of Figure 4.10. The region *ash* corresponds to the bulk of cells in the interior, and *fuel* to those in the exterior with respect to the flame front. Cells in the vicinity of the zero level set constitute the *flame* region. On the left, the evolution of the mean values for Clement's law of the wall is plotted, and the corresponding graphs for the semi-localised model are shown on the right. With Clement's wall proximity function, large values are obtained in the early stage of production, whereas the dynamical procedure predicts initially small values of C_ν. Since $\beta = 1$ for the former, the averages of C_ν calculated according to Clements prescription are normalised by a factor $1/\beta \approx 0.56$. The asymptotic value of the mean characteristic length $\langle \ell_\nu \rangle$ is about the same for both models, which implies that Clement's rules are not too far off in the case of fully developed turbulence. Nevertheless, a higher rate of production is obtained with the semi-localised model and, consequently, a higher level of SGS turbulence energy in stochastic equilibrium. Furthermore, one can see from the standard deviations of q_{sgs}, which are plotted in Figure 4.9, that the distribution of SGS turbulence is more homogeneous in the case Clement's model. Apparently, variations of C_ν induced by localisation create patches of intense SGS turbulence, which contribute to a higher mean velocity. Remarkably, this happens despite the stronger diffusion in the semi-localised model. Recall that $C_\kappa = 0.36$, whereas following Clement, the parameter of diffusion is set equal to the parameter of production, a very poor approximation according to the tests performed upon DNS data in Section 3.2.4. Therefore, diffusion effects are

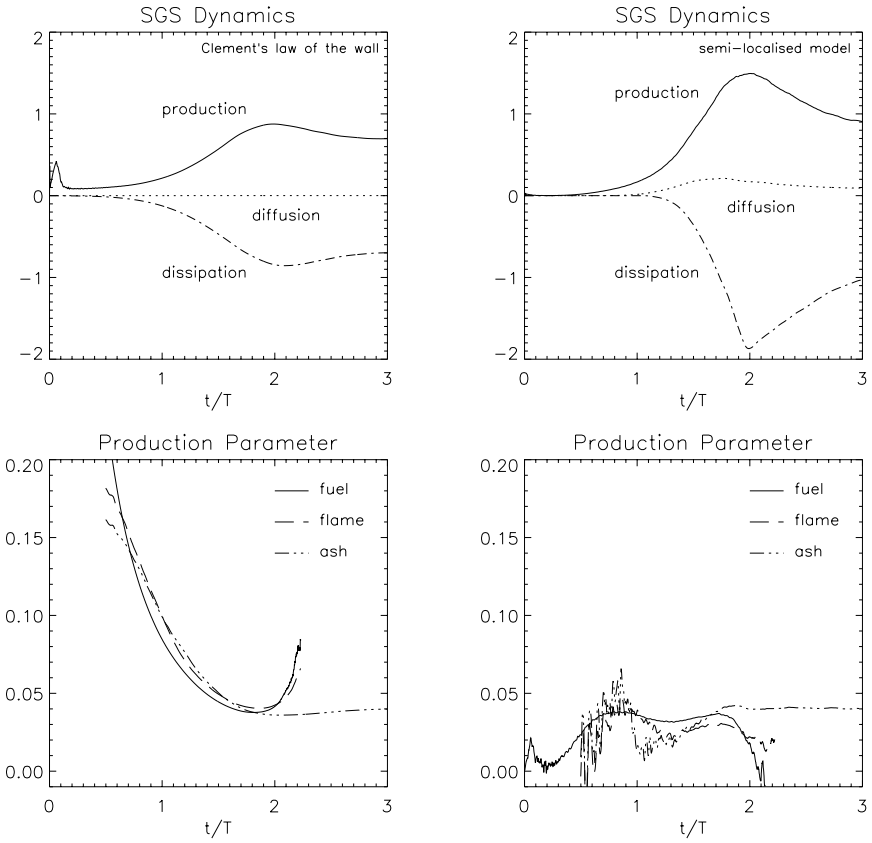

Figure 4.10: Contributions to the rate of change of the SGS turbulence velocity and the mean production parameters in ash, flames and fuel, respectively. In one case, Clement's law of the wall was used to calculated C_ν, in the other case, the localised self-similarity model for turbulence production.

seemingly over-compensated by locally enhanced production, owing to fluctuations in the dynamically computed production parameter.

4.3.3 The Similarity Closure for Production

The dynamical computation of the production parameter C_ν is based upon the filtering approach introduced by Germano [1992] in combination with the self-similarity closure. In Section 3.2.2, this closure was formulated with respect to a couple of Gaussian filters of characteristic length scales Δ_n and $\Delta_{n-1} > \Delta_n$, respectively. For a SGS model, the less smoothing filter corresponds to the implicit numerical filter with the associated length scale Δ_{eff}. The filter of larger characteristic length Δ_Γ is called the *test filter* and has to be applied explicitly. Since the implicit filter is, of course, not explicitly known, one cannot readily formulate a test filter which would be *similar* to the implicit filter. According to Carati and van den Eijnden [1997], this does not pose any difficulties if the production parameter C_ν is computed in the fashion of the Germano-Lilly procedure. In this case, the implicit filter is always formally similar to the *composition* of the implicit and the test filter. For the self-similarity procedure proposed by Liu, Men-

eveau, and Katz [1994], on the other hand, the test filter itself ought to be similar to the implicit filter. However, this cannot be implemented. In consequence, one is forced to abandon the similarity condition for the filters. Notwithstanding this caveat, we may assume that the de-correlation due to the dissimilarity of the implicit and the test filter, respectively, is not significant compared with the inherent inaccuracy of the turbulent-viscosity closure. For the SGS module in the code Telperion, a *discrete box filter* was utilised as test filter. Details of the implementation are described in Appendix A.1. A Gaussian filter, on the other hand, would be computationally too costly, and the action of a sharp cut-off filter is clearly very different from the gradual damping of modes due to numerical dissipation.

Applying the closure (3.35) with the turbulent viscosity (3.36) at the *test filter level*, the parameter of production is given by [cf. Kim et al., 1999]:

$$C_\nu = \frac{\tau^*_{\mathrm{T}}(v_i, v_k) S^{[\mathrm{T}]}_{ik}}{\rho_{\mathrm{T}} \Delta_{\mathrm{T}} k_{\mathrm{T}}^{1/2} |S^{*[\mathrm{T}]}|^2}, \tag{4.19}$$

where $\rho_{\mathrm{T}} = \langle \rho \rangle_{\mathrm{T}}$ is the test-filtered mass density, $S^{[\mathrm{T}]}_{ik} = \partial_{(i} \langle \rho v_{j)} \rangle_{\mathrm{T}} / \rho_{\mathrm{T}}$ the rate of strain of the smoothed velocity field, and $\tau^*_{\mathrm{T}}(v_i, v_k)$ is the trace-free part of

$$\tau_{\mathrm{T}}(v_i, v_k) = -\langle \rho v_i v_k \rangle_{\mathrm{T}} + \frac{1}{\langle \rho \rangle_{\mathrm{T}}} \langle \rho v_i \rangle_{\mathrm{T}} \langle \rho v_k \rangle_{\mathrm{T}}, \tag{4.20}$$

which specifies the intermediate stress exerted by turbulence on scales in the range between Δ_{eff} and Δ_{T}. The specific kinetic energy of velocity fluctuations associated with this range of scales is defined by

$$k_{\mathrm{T}} = -\frac{1}{2} \tau_{\mathrm{T}}(v_i, v_i). \tag{4.21}$$

Therefore, C_ν is locally determined by structural properties of the flow at the smallest resolved scales.

Substituting equation (4.19) into the closure for the SGS rate of production (3.29),

$$\Pi_{\mathrm{sgs}} \doteq \ell_\nu q_{\mathrm{sgs}} |S^*|^2 = \frac{\tau^*_{\mathrm{T}}(v_i, v_k) S^{[\mathrm{T}]}_{ik}}{\gamma_{\mathrm{T}} \rho_{\mathrm{T}}} \frac{|S^*|^2}{|S^{*[\mathrm{T}]}|^2} \sqrt{\frac{k_{\mathrm{sgs}}}{k_{\mathrm{T}}}}, \tag{4.22}$$

one can see that the result scales with the inverse of the *filter scaling ratio* $\gamma_T = \Delta_T / \Delta_{\mathrm{eff}}$. In consequence, it is crucial to find a reliable and robust estimate of γ_T. Δ_T is explicitly known for standard filters like the box filter, but determining the characteristic length Δ_{eff} of the implicit filter is non-trivial. In the following, we shall assume that $\Delta_{\mathrm{eff}} = \beta \Delta$, where β is given by equation (2.73). Although the values listed in the Tables 2.2, 2.3 and 2.4 suggest that β is almost universal, there is actually a trend towards larger values of β as the Mach number becomes smaller (see Table 4.1). Hence, there is some ambiguity in the dynamically computed production parameter, stemming both from the uncertainties in β and the filter scaling ratio γ_T.

The impact of varying γ_{T} was investigated *a posteriori* in a series of LES with different test filters. The chosen scaling ratios, which are listed in Table 4.2, are motivated in Appendix A.1. An increasing number of supporting nodes, $2N_{\mathrm{T}} + 1$, was included, in order to allow for larger length scales Δ_T. Statistical results from these simulations

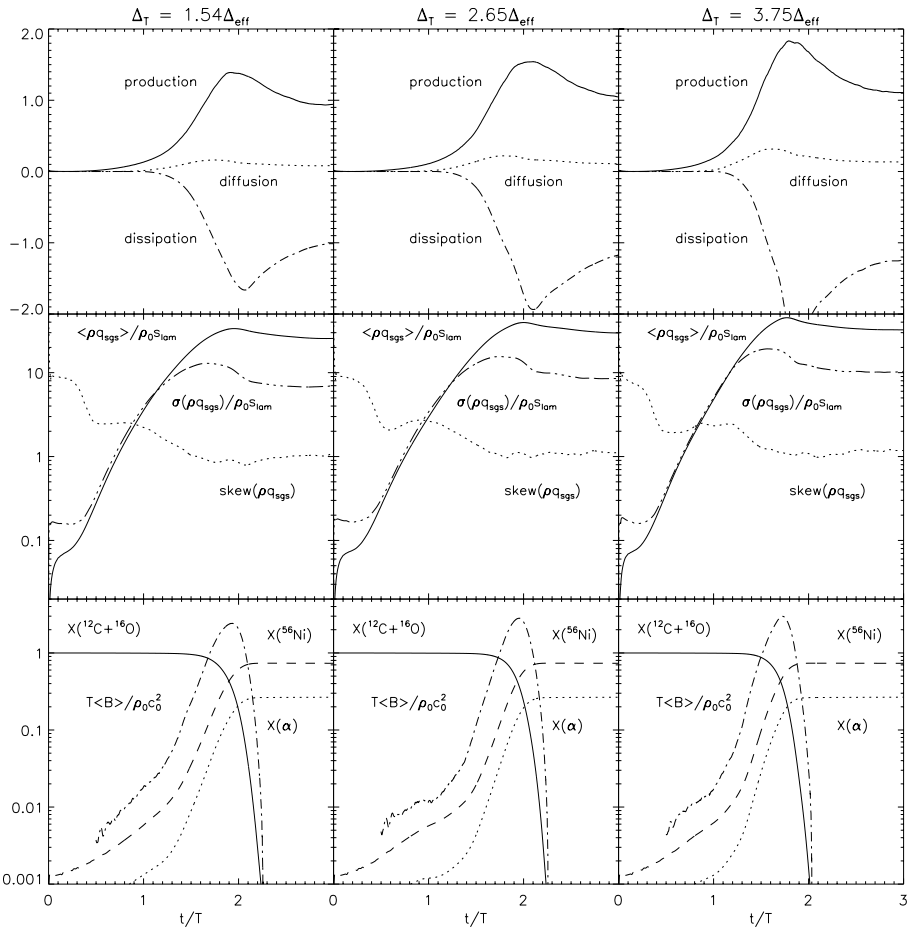

Figure 4.11: LES with the semi-localised SGSTE model (passive implementation): Comparison of the evolution of SGS turbulence and thermonuclear burning for test filters of varying characteristic length Δ_T (see Table 4.2).

are shown in Figure 4.11. Basically, the evolution of the burning process appears to be fairly robust with respect to the test filtering length. Only in the case of the maximal scaling ratio $\gamma_T \approx 3.75$, combustion proceeds somewhat faster. The flattening of the SGS turbulence velocity also sets in at an earlier time in this case. The average value of C_ν in the stationary regime is about 0.045 for the largest test filter length. This is within the range of values which was inferred from DNS data (see Table 3.3). It is also reasonably close to most values found in the literature [cf. Kim and Menon, 1996, Section 5.2]. In any case, the degree of uncertainty is comparable to that one of statistically determined closure parameters. However, one can clearly see that the level of production is less for a smaller characteristic length of the test filter. This is a rather worrisome fact, as SGS turbulence production is expected to be quite insensitive to the choice of the filter length. Actually, even if $\gamma_T \approx 6.74\Delta$, the test filter length scale is still smaller than the length scale of maximal dissipation, $l_\flat \sim 10\Delta$. Unfortunately,

V/c_0	$\langle\tilde{e}_{\mathrm{kin}}\rangle$	$\langle e^{\parallel}_{\mathrm{kin}}\rangle/\langle e_{\mathrm{kin}}\rangle$	$\eta_{\mathrm{eff}}/\Delta$	β	l_{p}/L
0.084	0.714	$1.36 \cdot 10^{-5}$	0.298	1.82	0.0740
0.42	0.728	$8.16 \cdot 10^{-3}$	0.261	1.62	0.0674
0.66	0.571	$1.87 \cdot 10^{-2}$	0.260	1.61	0.0659

Table 4.1: Mean energy, rate of dissipation and characteristic length scales for fully developed turbulence in the simulations `dns432ersl` `dns432nrsl` and `dns432nh75`.

$2N_{\mathrm{T}}+1$	$\Delta_{\mathrm{T}}/\Delta$	γ_{T}
5	2.771	1.54
7	4.773	2.65
9	6.742	3.75

Table 4.2: Specifications of the test filters in three LES with the semi-localised SGSTE model.

using a test filter with $\Delta_{\mathrm{T}} \gtrsim l_{\mathrm{p}}$ is computationally intractable[5]. In Section 4.3.5, we will see that this deficiency of the dynamical computation of C_ν can be cured, if the feedback of SGS turbulence onto the resolved momentum is included.

4.3.4 The Semi-Localised Model

In the variational approach of Ghosal et al. [1995], the parameter of dissipation C_ϵ is determined by subtracting the test-filtered SGS turbulence energy equation (3.28) from the corresponding equation for the unresolved kinetic energy $k_{\mathrm{sgs}} + k_{\mathrm{T}}$ at the level of the test filter. Taking up this idea, we shall formulate a *spatially averaged* difference equation. Upon averaging equation (3.28), we obtain

$$\left\langle \rho \frac{\mathrm{D}}{\mathrm{D}t} k_{\mathrm{sgs}} \right\rangle = \langle \tau_{ik} S_{ik} \rangle - \left\langle \rho(\lambda_{\mathrm{sgs}} + \epsilon_{\mathrm{sgs}}) \right\rangle . \tag{4.23}$$

The diffusion term cancels out, because integrating the divergence of the diffusive flux over a domain with periodic BCs yields zero. Furthermore,

$$\left\langle \rho \frac{\mathrm{D}}{\mathrm{D}t} k_{\mathrm{sgs}} \right\rangle = \left\langle \frac{\partial}{\partial t} \rho k_{\mathrm{sgs}} \right\rangle + \underbrace{\left\langle \frac{\partial}{\partial x_i} \rho v_i k_{\mathrm{sgs}} \right\rangle}_{=0} = \frac{\mathrm{d}}{\mathrm{d}t} \langle K_{\mathrm{sgs}} \rangle, \tag{4.24}$$

i. e., there is vanishing net advection over the whole domain of the flow. The turbulence energy at the characteristic scale of the test filter is defined by

$$-\frac{1}{2}\tau_{\mathrm{T}}(\overset{\infty}{v}_i, \overset{\infty}{v}_i) = -\frac{1}{2}\langle \tau_{ii} \rangle_{\mathrm{T}} + \frac{1}{2}\tau_{\mathrm{T}}(v_i, v_i) = \langle \rho k_{\mathrm{sgs}} \rangle_{\mathrm{T}} + \rho_{\mathrm{T}} k_{\mathrm{T}}, \tag{4.25}$$

[5] This would require component filters in excess of 20 supporting nodes. However, apart from unfavourable memory access, restrictions come from the limited number of ghost cells. Actually, only four ghost cells are available in Telperion. This number is hard-coded, and changing that would be a rather tedious endeavour.

and the corresponding averaged dynamical equation is[6]

$$\frac{\partial}{\partial t}\langle \rho K_{\rm sgs} + \rho_{\rm T} K_{\rm T}\rangle = \left\langle \tau_{\rm T}(\overset{\infty}{v}_i, \overset{\infty}{v}_k) S_{ik}^{[\rm T]} \right\rangle - \left\langle \rho(\lambda_{\rm sgs} + \epsilon_{\rm sgs}) + \rho_{\rm T}(\lambda_{\rm T} + \epsilon_{\rm T}) \right\rangle . \tag{4.26}$$

Equations (4.23) and (4.25) in combination with the Germano identity imply the following conservation law for the mean turbulence energy $K_{\rm T}$ on small resolved scales, $\Delta_{\rm eff} \lesssim l \lesssim \Delta_{\rm T}$:

$$\frac{\mathrm{d}}{\mathrm{d}t}\langle K_{\rm T}\rangle = \left\langle \tau_{\rm T}(v_i, v_k) S_{ik}^{[\rm T]} + \langle \tau_{ik}\rangle_{\rm T} S_{ik}^{[\rm T]} - \tau_{ik} S_{ik} \right\rangle - \langle \rho_{\rm T}(\lambda_{\rm T} + \epsilon_{\rm T})\rangle . \tag{4.27}$$

Substituting the turbulent-viscosity closures for the various production terms on the right-hand side, the above equation becomes

$$\begin{aligned} \frac{\mathrm{d}}{\mathrm{d}t}\langle K_{\rm T}\rangle \simeq & \underbrace{\left\langle \rho_{\rm T} C_\nu \Delta_{\rm T} \sqrt{k_{\rm T}}\, |S^{*[\rm T]}|^2 \right\rangle - \frac{2}{3}\left\langle K_{\rm T} d^{[\rm T]} \right\rangle}_{\rm (I)} - \langle \rho_{\rm T}\lambda_{\rm T}\rangle + \langle \rho_{\rm T}\epsilon_{\rm T}\rangle \\ & + \underbrace{\left\langle \langle \rho \nu_{\rm sgs} S_{ik}^*\rangle_{\rm T} S_{ik}^* - \rho \nu_{\rm sgs} |S^*|^2 \right\rangle}_{\rm (II)} - \frac{2}{3}\underbrace{\left\langle \langle K_{\rm sgs}\rangle_{\rm T} d^{[\rm T]} - K_{\rm sgs} d \right\rangle}_{\rm (III)} . \end{aligned} \tag{4.28}$$

Analogous to the rate of strain at the test filter level, the divergence $d^{[\rm T]}$ is given by $d^{[\rm T]} = \partial_i \langle \rho v_i\rangle_{\rm T}/\rho_{\rm T}$. The complete numerical computation of the production terms in the above equation would be rather demanding, in particular, the evaluation of the numerous tensor components at the test-filter level. For this reason, we shall putatively drop the contributions (II) and (III), while only retaining (I), which is intuitively the most significant production term. Then the rate of dissipation $\epsilon_{\rm T}$ is approximately given by

$$\langle \rho_{\rm T}\epsilon_{\rm T}\rangle \simeq -\frac{\mathrm{d}}{\mathrm{d}t}\langle K_{\rm T}\rangle + \left\langle \rho_{\rm T} C_\nu \Delta_{\rm T} \sqrt{k_{\rm T}}\, |S^{*[\rm T]}|^2 \right\rangle - \frac{2}{3}\left\langle \rho_{\rm T}(k_{\rm T} d^{[\rm T]} + \lambda_{\rm T}) \right\rangle . \tag{4.29}$$

In order determine the parameter C_ϵ from this balance equation, one can conceive of two alternatives: On the one hand, the closure (3.40) could be applied to the total rate of dissipation on the length scale $\Delta_{\rm T}$. In this case, the net rate of dissipation on intermediate scales would be given by

$$\langle \rho_{\rm T}\epsilon_{\rm T}\rangle \doteq \frac{C_\epsilon}{\Delta_{\rm T}}\left\langle \rho_{\rm T}\left(\frac{\langle \rho k_{\rm sgs}\rangle_{\rm T}}{\rho_{\rm T}} + k_{\rm T}\right)^{3/2} - \gamma_{\rm T}\rho k_{\rm sgs}^{3/2} \right\rangle . \tag{4.30}$$

On the other hand, one could set

$$\langle \rho_{\rm T}\epsilon_{\rm T}\rangle \doteq C_\epsilon \frac{\langle \rho_{\rm T} k_{\rm T}^{3/2}\rangle}{\Delta_{\rm T}} . \tag{4.31}$$

This expression can be regarded as limiting case of the other one for $\gamma_{\rm T} = \Delta_{\rm T}/\Delta_{\rm eff} \to \infty$, corresponding to $k_{\rm T} \gg k_{\rm sgs}$. From numerical tests, it became clear that using the more involved closure (4.30) is troublesome, because it introduces singularities and

[6] Here the relation $\langle\langle a\rangle_{\rm T} + b\rangle = \langle a + b\rangle$ is used.

can be either positive or negative. Thus, with the Deardorff closure for the intermediate pressure-dilatation,

$$\lambda_{\mathrm{T}} \doteq C_\lambda k_{\mathrm{T}} d^{[\mathrm{T}]}, \tag{4.32}$$

the dissipation parameter is, to the lowest order, determined by

$$C_\epsilon = -\frac{\Delta_{\mathrm{T}}}{\langle K_{\mathrm{T}} \sqrt{k_{\mathrm{T}}}\rangle}\left[\frac{\mathrm{d}}{\mathrm{d}t}\langle K_{\mathrm{T}}\rangle - \left\langle C_\nu \rho_{\mathrm{T}} \Delta_{\mathrm{T}} \sqrt{k_{\mathrm{T}}}\,|S^{*\,[\mathrm{T}]}|^2\right\rangle + \left(\frac{1}{3}+C_\lambda\right)\left\langle K_{\mathrm{T}} d^{[\mathrm{T}]}\right\rangle\right]. \tag{4.33}$$

As opposed to the statistical values estimated from DNS data, the above equation yields a spatially constant parameter evolving in time. This method of calculating C_ϵ in combination with the dynamical procedure for C_ν makes up the *semi-localised* SGSTE model. For the numerical implementation, two further modifications were added.

On account of the anisotropy in the vicinity of a flame front, it seems advisable to average over the principal topological subdomains introduced in Section 4.3.2, i. e., the interior, the exterior and the interface. The latter is identified by marking all grid cells which have a certain maximum distance to those cells in which the level set function G swaps its sign. In discrete steps, this maximal distance is set to $N_{\mathrm{T}}/2$. For example, if the component mesh filters had 9 supporting nodes (see Appendix A.1.1), ± 2 cells up or down any cell intersected by the zero level set would be included in the interface. With this procedure, the functions $C_\epsilon^{(\mathrm{a})}(t)$, $C_\epsilon^{(\mathrm{b})}(t)$ and $C_\epsilon^{(\mathrm{f})}(t)$ are obtained for the mean dissipation parameters in ash, the burning zone and fuel, respectively. However, these functions were empirically found to oscillate rapidly, especially, in the early stage of the burning process. This is presumably a consequence of the dissipation being very intermittent in developing flows. Apart from that, the closure relation for dissipation is based upon the notion of a turbulence cascade with Kolmogorov scaling. In the course of the transition from non-linear to turbulent flow, this closure is not really applicable, and equation (4.33) might be ill posed. As a pragmatic solution, which is surely contestable, a temporal filtering procedure was implemented in order to clear possible spurious effects. To that end, both the enumerator and dominator in equation (4.33) are separately smoothed via convolution with an exponential damping function, as described in Section A.1.2 of the Appendix. The characteristic time scale of smoothing is prescribed by the parameter T_ϵ.

An appropriate choice for the time scale T_ϵ has to be found *a posteriori*. Figure 4.12 shows results from three LES with 144^3 grid cells, using the method outlined above. The values 0.01, 0.05 and 0.25 for the dimensionless smoothing time scale $\tilde{T}_\epsilon = T_\epsilon/T$ were tested in these simulations. The smallest smoothing parameter encompasses roughly 10 time steps. As one can see from the evolution of the dissipation parameters $C_\epsilon^{(\mathrm{a})}(t)$, $C_\epsilon^{(\mathrm{b})}(t)$ and $C_\epsilon^{(\mathrm{f})}(t)$, there are still large fluctuations in the case of the shortest smoothing time, whereas most features are suppressed in the case of the $\tilde{T}_\epsilon = 0.25$. Fortunately, the influence of T_ϵ, which is a purely numerical parameter, on the evolution of the SGS turbulence is only marginal. Setting $T_\epsilon \approx 0.1$ appears to be a good choice in order to get well behaved functions $C_\epsilon^{(\mathrm{a})}(t)$, $C_\epsilon^{(\mathrm{b})}(t)$ and $C_\epsilon^{(\mathrm{f})}(t)$, without overly damping dynamical variations.

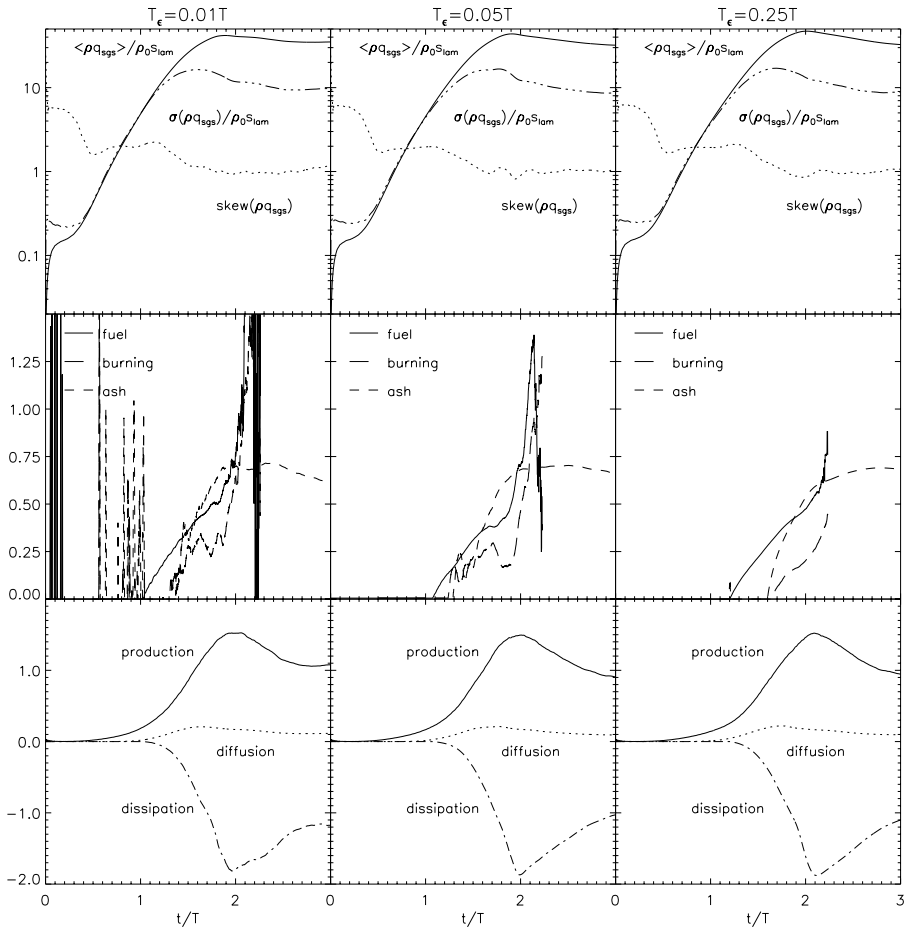

Figure 4.12: Evolution of SGS turbulence, the dissipation parameter C_ϵ and dynamical contributions to the rate of change of $q_{\rm sgs}$ for different choices of the smoothing time scale T_ϵ in the semi-localised SGS model.

4.3.5 Active Subgrid Scale Modelling

In the previously discussed LES, the SGS model merely yields the turbulent flame speed. Although the SGS turbulence energy is taken into account in the energy budget, the action of the turbulence stress is not included in the dynamical equation for the resolved momentum (3.3). In this mode, $q_{\rm sgs}$ is treated just as a passive scalar. For the justification of *passive* SGS modelling, usually *numerical dissipation* is invoked. The argument goes like this. If a finite-volume scheme produces dissipation, it will mimic, at least statistically, the energy transfer from resolved to subgrid scales. The turbulent stress terms in the equations of motion could be included, but it is not worth the trouble, because there is not going to be much improvement anyway. The combined action of numerical and SGS dissipation might even produce too much viscosity and influence the resolved flow in an unfavourable manner. Actually, there are numerical investigations in support of this view, for instance, by Rider and Drikakis [2002]. Of course, the DNS discussed in Chapter 2 bear on this very argument. No SGS model

was used for these simulations at all, despite the fact that the microscopic viscosity was much smaller than the putative numerical viscosity of to the PPM.

In most LES in engineering and geophysics, on the other hand, the SGS turbulence stress is actually acting on the resolved flow. There are several reasons for this *active* SGS modelling. In atmospheric or oceanic turbulence, measurements revealed features breaking scale-invariance on small scales, which cannot be resolved in contemporary simulations Kupka [2003]. In this case, the SGS model is the only possibility to account for such effects. In laboratory flows, inhomogeneities entail significant spatial variations of the SGS turbulence stress. Whether this could be reproduced solely with numerical dissipation seems to be rather questionable. Moreover, if the localised similarity closure for production is used, one can make another good case for including the explicit turbulence stress terms in the momentum equations. Since the parameter of production C_ν inevitably becomes negative in some regions, there is transfer of kinetic energy from unresolved to the resolved scales. This *backscattering* will locally contribute to an increase of the total resolved energy, $e_{\text{res}} = \frac{1}{2}|\boldsymbol{v}|^2 + e_{\text{int}}$. However, if the corresponding stresses in the momentum equation were neglected, the velocity would remain utterly unaffected by the process of backscattering. On account of this, the turbulence energy transfered to resolved scales would effectively be converted into *heat* which is palpably wrong, for backscattering must increase the resolved *kinetic* energy. The LES which have been discussed thus far suffer from this very inadequacy.

For this reason, the SGS turbulence stress terms in the qNSE (3.3) were modelled according to the turbulent-viscosity closure,

$$\begin{aligned}\frac{\partial}{\partial x_k}\tau_{ik} &\doteq 2\frac{\partial}{\partial x_k}\left(\rho\nu_{\text{sgs}}S^*_{ik} - \frac{1}{3}K_{\text{sgs}}\delta_{ik}\right)\\ &= 2\frac{\partial}{\partial x_k}\rho\ell_\nu q_{\text{sgs}}\left(S_{ik} - \frac{1}{3}d\delta_{ik}\right) - \frac{1}{3}\frac{\partial}{\partial x_k}\rho q^2_{\text{sgs}},\end{aligned} \tag{4.34}$$

and numerically implemented in order to facilitate active SGS modelling. The spatial derivatives in the above expression were discretised as fourth-order centred differences. This is of the same order of accuracy as for spatial derivatives in the PPM [cf. Colella and Woodward, 1984]. The performance of the active semi-localised model was investigated in a series of three LES, using 9-node component filters of varying characteristic length on a grid of 192^3 cells. In one case, the optimal length $\Delta_{\text{T}} \approx 3.75\Delta_{\text{eff}}$ was chosen, in the other simulations a larger length, $\Delta_{\text{T}} \approx 4.72\Delta_{\text{eff}}$, and a smaller one, $\Delta_{\text{T}} \approx 2.78\Delta_{\text{eff}}$. Some of the resulting statistics is plotted in Figure 4.13. The most striking result is that now the SGS dynamics appears to be fairly invariant with respect to the test filter, quite contrary to the simulations with the passive SGS model (see Figure 4.11). As one can see in the top panels, it appears that the parameter of production converges towards the same average value, independent of the characteristic length of the test filter. Thermonuclear burning evolves rather similar in all three LES, although the peak is slightly higher and narrower for $\Delta_{\text{T}} \approx 3.75\Delta_{\text{eff}}$. The temporal changes of mechanical energy production and dissipation, respectively, which are plotted in the bottom panels of Figure 4.13, indicate that stochastic equilibrium is approached faster for test filters of larger characteristic length. Combining all of these observations, we conclude that the active SGS model is preferable compared to the passive one, and a test filter of characteristic length $\Delta_{\text{T}} \approx 4\Delta_{\text{eff}}$ should be chosen. Note

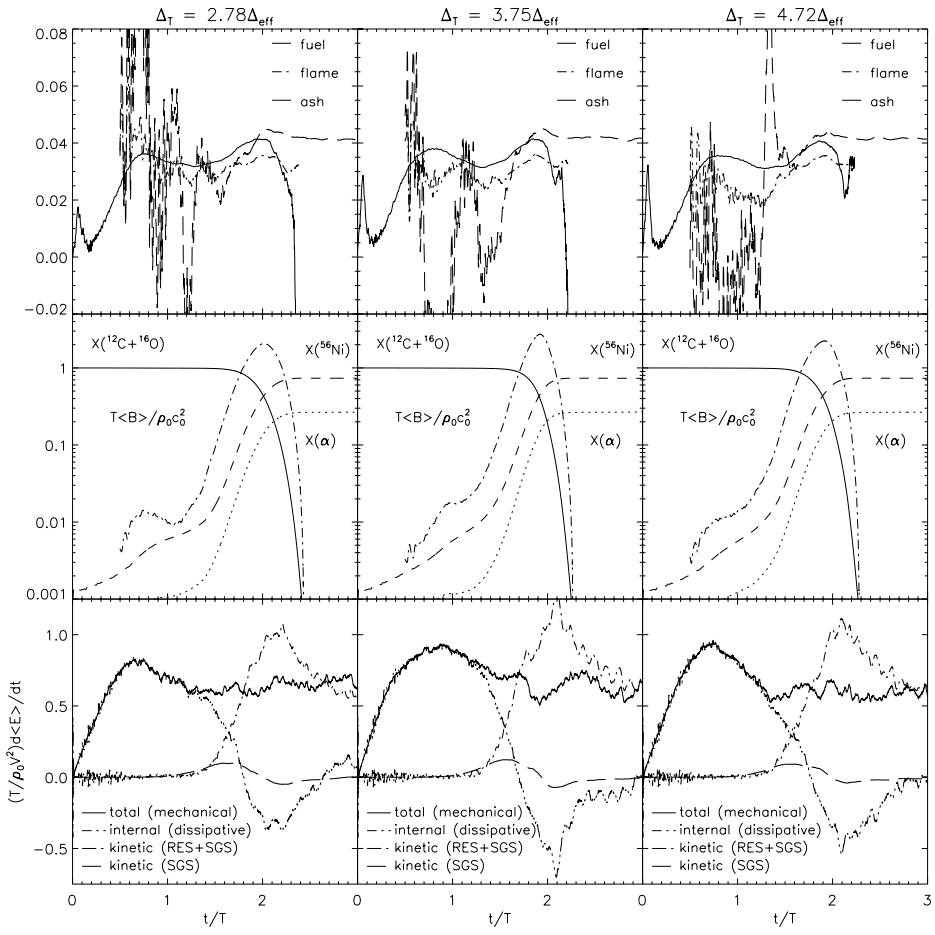

Figure 4.13: LES with active semi-localised SGSTE model: comparison of the evolution of the parameter C_ν, thermonuclear burning, mechanical production and dissipation rates. Each column of panels corresponds to a different characteristic length Δ_T of the test filter.

that the factor 4 is significantly larger than the scaling ratio $\gamma_T \approx 2$, which is recommended in most of the literature. However, in the case of PPM, it appears that such a small ratio is not a sensible choice.

As a further test of the reliability of the active semi-localised model, the numerical resolution was varied in a series of runs with a test filter of characteristic length $\Delta_T \approx 3.75\Delta_{\text{eff}}$. For a constant integral length scale $L = 2.16 \cdot 10^5$ cm, the numerical resolution N was, respectively, set to 144, 160, 192 and 216. The averaged values of the production parameter C_ν and the dissipation parameter C_ϵ in ash and flames, respectively, are plotted in Figure 4.14. The invariance with respect to the numerical resolution is thereby impressively demonstrated. The asymptotic mean values for steady turbulence are $\langle C_\nu \rangle \approx 0.042$ and $C_\epsilon \approx 0.65$. Of course, there are variations in the evolution due to different realizations of the stochastic stirring process in each simulation[7]. In particular, the behaviour of $C_\epsilon^{(f)}$ in the exponential growth phase prior

[7]Even if the same initialisation was used for the random number generator in each case, the resulting

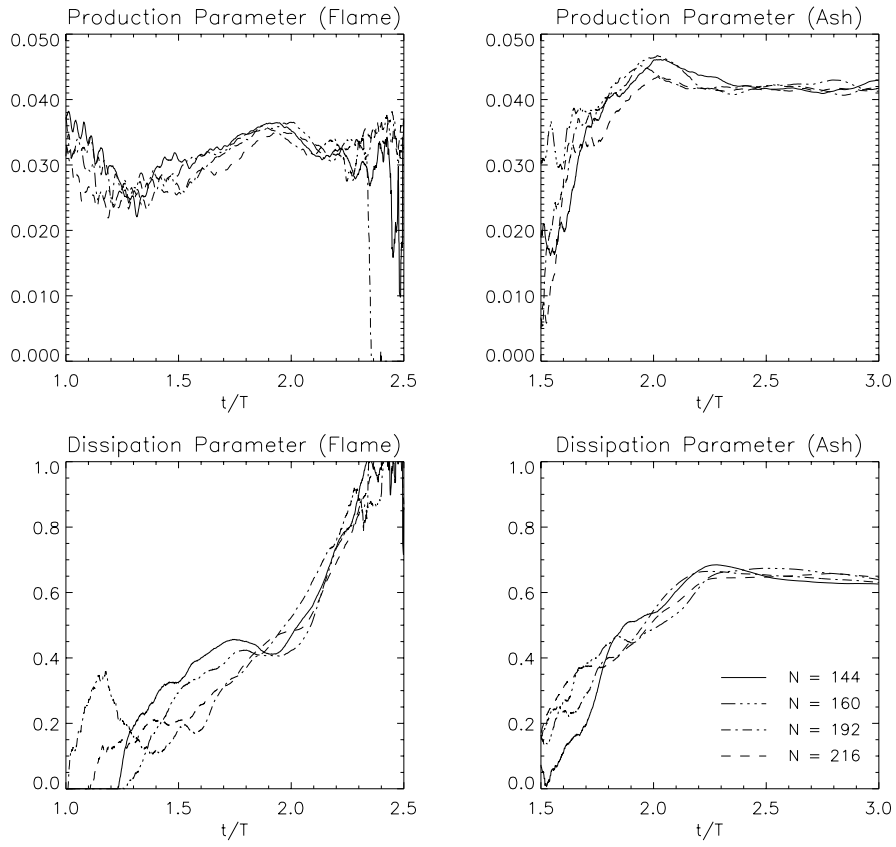

Figure 4.14: LES with varying resolution: mean production parameter C_ν and the corresponding dissipation parameter C_ϵ in regions containing thermonuclear ash and the burning zones, respectively.

to peak of the burning rate does not display any trend following the numerical resolution. This could reflect a sensitive dependence of $C_\epsilon^{(\mathrm{f})}$ on stochastic variations in the early flame fronts, but it might also indicate a shortcoming of the rather crude method of calculating the parameter of dissipation. The average rate of energy release and the composition as functions of time are shown in Figure 4.15. The maxima of $\langle B \rangle$ are found around $\tilde{t} \approx 2.0$ for each LES. This is a reasonable result, as one would intuitively expect that the peak of the burning rate coincides more or less with the complete homogenisation of turbulence, which was found to occur at the same time. Apart from that, some variations in the shape of the graphs for $\langle B \rangle$ can be seen, particularly, in the vicinity of the transition to turbulent burning. Cross-checking with the evolution of the mean momentum shows that these variations can largely be attributed to differences in the random driving forces. However, the bumps near $\tilde{t} \approx 1.0$ are probably numerical artifacts related to the anomalies in $C_\epsilon^{(\mathrm{f})}$.

Finally, different relations between the turbulent flame speed s_t and the SGS turbulence velocity q_{sgs} were numerically investigated. In Figure 4.16, statistical results

stochastic processes would still not be the same, because of the different time steps depending on the resolution.

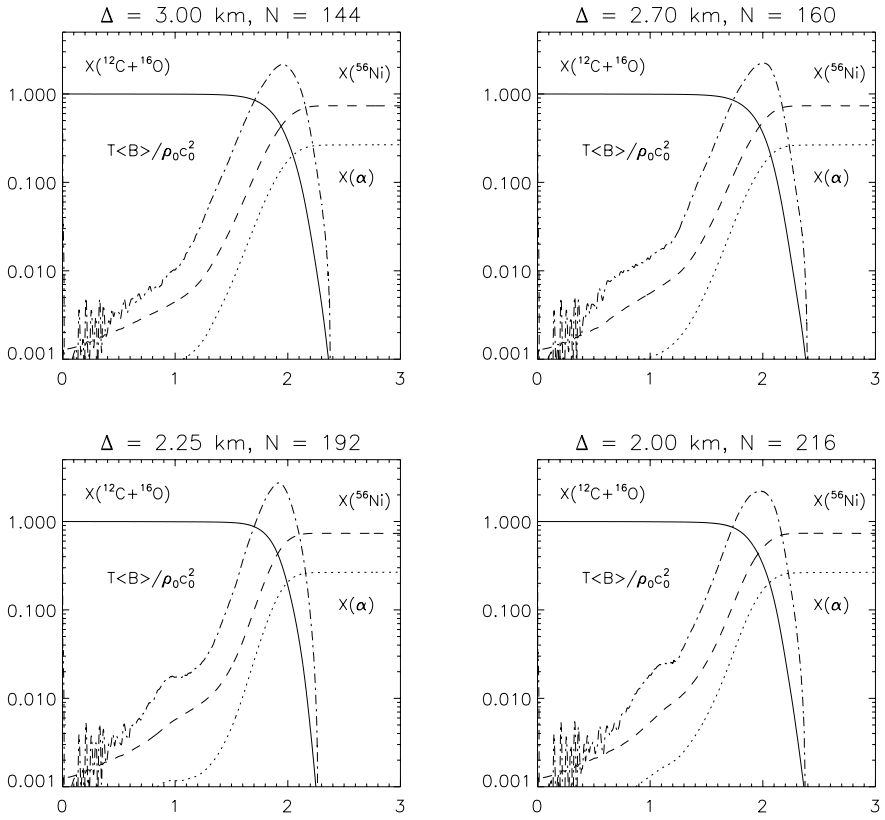

Figure 4.15: LES with varying resolution: evolution of the mean burning rate and nuclear composition.

from three LES are shown. The first simulation corresponds to the standard case, with s_t given by equation (4.6). For the other two LES, Pocheau's relation (4.7) with the exponent $n = 2$ was used to determine s_t. The values 4 and 16 were chosen for the parameter C_t, corresponding to the asymptotic relations $s_t \simeq 2q_{sgs}$ and $s_t \simeq 4q_{sgs}$, respectively, in the limit $q_{sgs} \ll s_{lam}$. As one can see from the plots of the burning statistics in the middle row of panels, the peak of the burning process is shifted towards earlier time for increasing C_t, but the shape of the graph is not significantly changed. It should be noted that even $C_t = 16$ is still smaller than the value proposed by Kim et al. [1999]. They adopted $C_t = 20$ from laboratory experiments with gaseous flames. The row of panels on the bottom of Figure 4.16 show the mean rate of production and dissipation for each simulation. A feature which comes to attention in the case of the LES with Pocheau's relation are the strong oscillations in $\langle \Pi - \epsilon \rangle$ and $\langle \epsilon \rangle$. This indicates alternating conversion of internal to kinetic energy and vice versa due to pressure waves, as discussed in the context of the supersonic flow simulated in `dns432nr20` (see Section 2.4.4). Although the characteristic Mach number in the LES of turbulent burning is ~ 0.1, the flow can locally become as fast as Mach 0.3. Given the low resolution of $N = 144$, the SGS turbulence velocity is possibly of the order $0.1c_s$ in some regions. Thus, in combination with the enhancing coefficient in

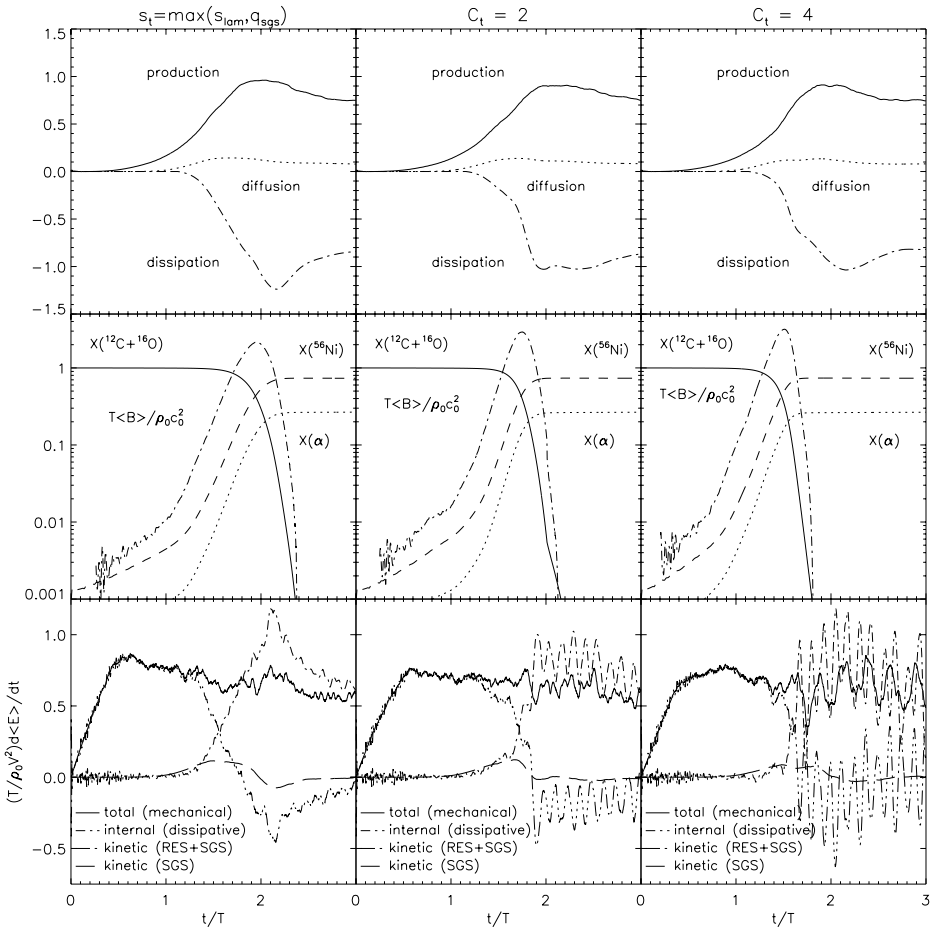

Figure 4.16: LES with different relations for the turbulent flame speed s_t. In one case, equation (4.6) was used to calculate s_t and for the other simulations equation (4.7), with the parameter C_t as specified on top of the corresponding columns of panels and the exponent $n = 2$.

Pocheau's flame speed relation, the turbulent propagation speed s_t might reach a significant fraction of the speed of sound during the late stage of burning. Moreover, as the remaining patches of fuel get compressed, significant disturbances in the pressure equilibrium might be generated. These results suggest that we actually face limitations of the turbulent flame propagation model. If Pocheau's relation is used, then probably both a higher resolution and a more precise treatment of SGS pressure dilatation are required. Otherwise, $C_t \approx 1.0$ appears to be the most sensible choice.

4.3.6 The Evolution of Turbulent Burning

Let us finally review the phenomenology of turbulent burning. The evolution of the burning process in a LES with 216^3 grid cells and active semi-localised SGS modelling is illustrated in the sequence of Figures 4.17, 4.18 and 4.19. In this case, the turbulent flame speed is modelled as $s_t = s_{\rm lam}\sqrt{1 + (q_{\rm sgs}/s_{\rm lam})^2}$, which follows from

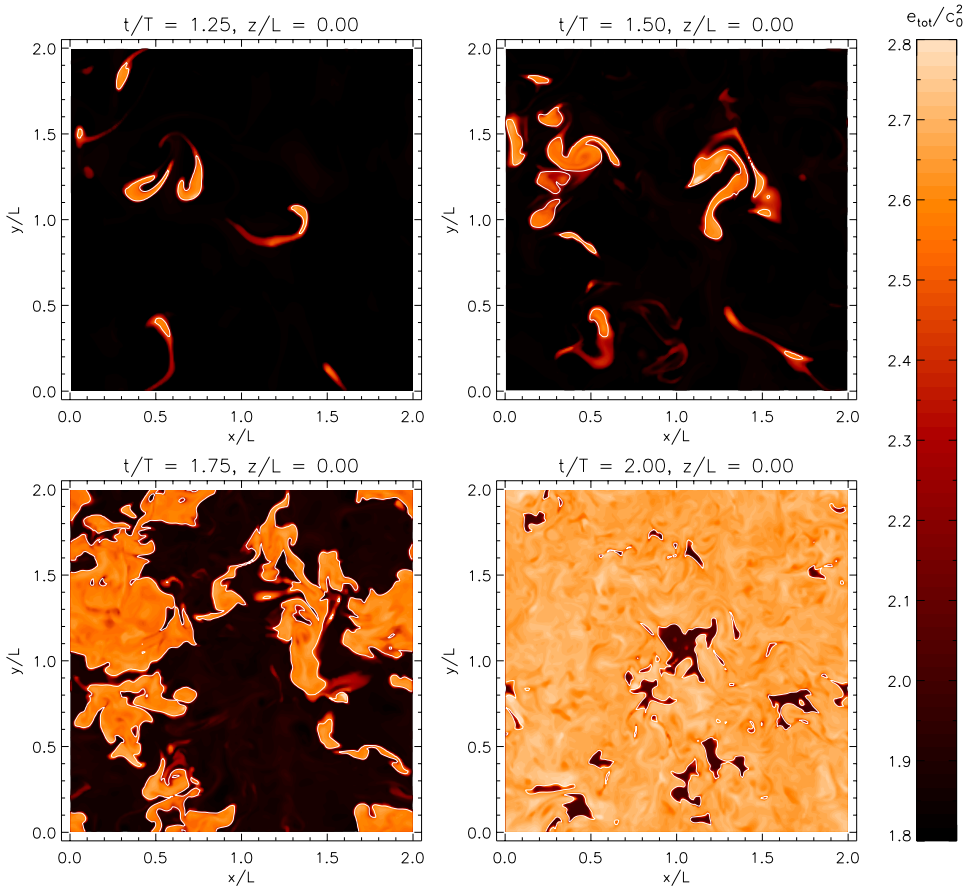

Figure 4.17: LES with the active semi-localised SGSTE model: 2D contour sections of the normalised specific energy $\tilde{e} = e/c_0^2$ at $\tilde{z} = 0.0$.

Pocheau's expression (4.7) with $C_t = 1$ and $n = 2$. The characteristic length of the test filter is $\Delta_T \approx 3.75\Delta_{\text{eff}}$, the smoothing time scale is $T_\epsilon = 0.1T$, and the physical parameters are the ones specified earlier for `les216kinw`. In comparison to the burning process in the LES with constant closure parameters, it appears that the shape and topology of the flame is even more complex and small-scale features are particularly pronounced if the semi-localised model is used. Supposedly, this can be attributed to the more complex interaction between resolved and subgrid scales if C_ν is computed *in situ*. From the visual impression alone, one should become aware that the localised self-similarity closure, indeed, makes a difference. The corresponding evolution of the SGS turbulence is illustrated in Figure 4.18, with contour sections of the ratio of q_{sgs} to the laminar speed, and Figure 4.19, which shows contours of the rate of SGS dissipation. For $\tilde{t} \lesssim 1.5$, the SGS turbulence energy is distributed very inhomogeneously in filamentary and eddy-like structures. Slightly later, pieces of flames are penetrating concentrations of turbulence and get accelerated. From this point onwards, the flame front is shaped by complex interaction with both resolved and subgrid-scale turbulence. Thereby, the burning rate increases exponentially, as one can see in the

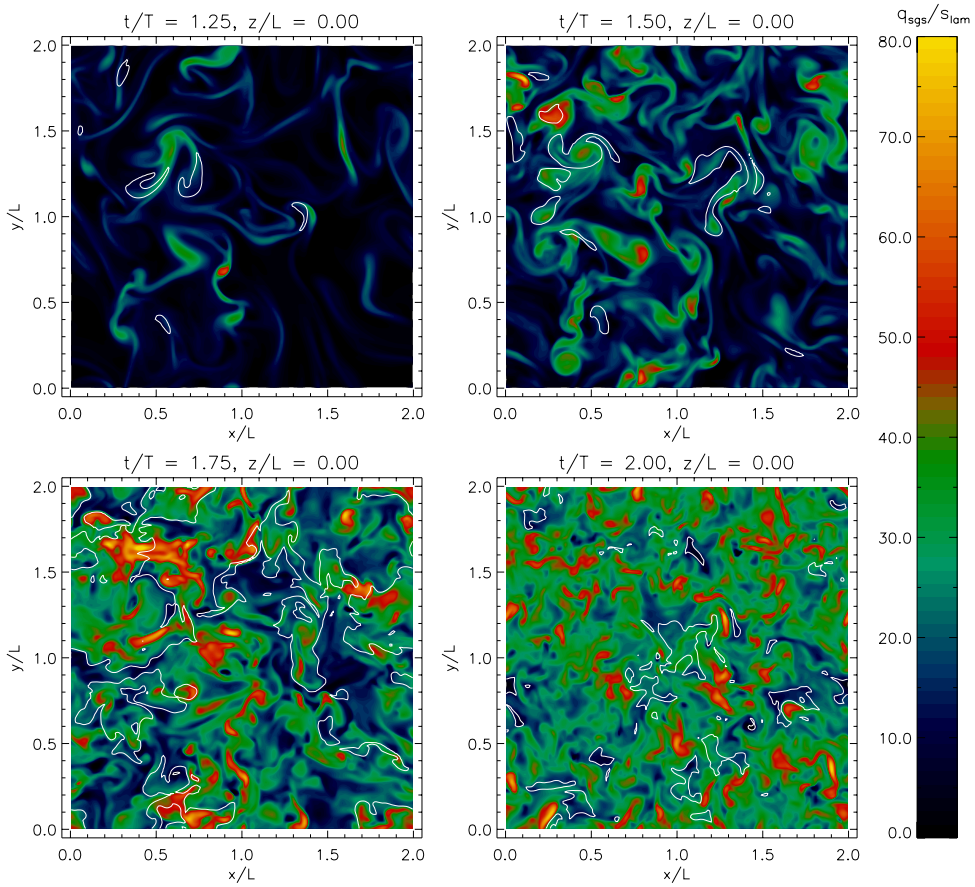

Figure 4.18: LES with the active semi-localised SGSTE model: contours of the ratio $q_{\mathrm{sgs}}/s_{\mathrm{lam}}$ corresponding to the panels in Figure 4.17.

plot of the mean burning rate $\langle B \rangle$ in Figure 4.20. One should also note that the bump around $\tilde{t} \approx 1$, which was found for the LES discussed in Section 4.3.5, is flattened considerably. Apparently, there is a smoother onset of turbulent burning, with s_t given by Pocheau's prescription. After two integral time scales have elapsed, turbulence is virtually space filling and the system is relaxing gradually into stochastic equilibrium. The equilibration is clearly demonstrated by the plots of $\langle \rho q_{\mathrm{sgs}} \rangle / \rho_0$ and the averages of C_ν as well as C_ϵ.

Moreover, the dynamics of SGS turbulence can be inferred from the middle panel on the right, which shows the RMS production, dissipation and diffusion of q_{sgs}. After the initial relaxation of the hot bubbles of ash, the SGS rate of dissipation vanishes and then re-emerges at time $\tilde{t} \approx 1.1$. Presumably, the physical dissipation is never altogether zero, but the trend seen for $\langle \epsilon_{\mathrm{sgs}} \rangle$ in the LES is basically correct. Around $\tilde{t} \approx 1$, the first small-scale vortices are formed and, as we have seen for the DNS in Section 2.4, this marks the onset of dissipation. With increasing vorticity of the flow, the rate of SGS dissipation grows, as one can see from the logarithmic contours of ϵ_{sgs} in the sequence of panels shown in Figure 4.19. In the early phase of turbulent burning,

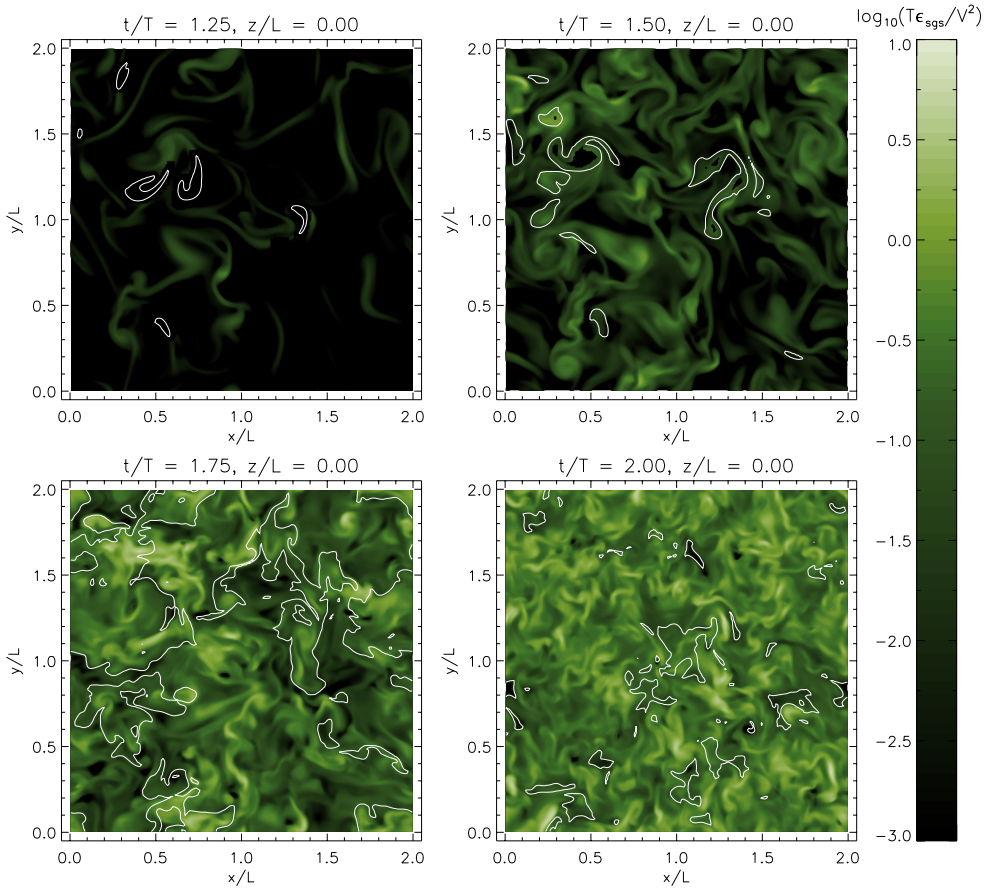

Figure 4.19: LES with the active semi-localised SGSTE model: logarithmic contours of the normalised SGS rate of dissipation, $T\epsilon_{\text{sgs}}/V^2$, corresponding to the panels in Figure 4.17.

dissipation vanishes in the vicinity of the flame or the interior regions. This entails discontinuities which are certainly unphysical. Nevertheless, one can expect that the three different values for the closure parameter C_ϵ account for inhomogeneities arising from the flames in a statistical manner. It is also interesting to note that even for nearly steady turbulence at time $\tilde{t} = 2.0$, SGS dissipation varies over roughly four orders of magnitude, which confirms the statement of Mandelbrot cited in the header of this Chapter. The energy injection due to stirring, the rate of change of kinetic energy on resolved and subgrid scales, respectively, as well the increase of internal energy due to dissipation is shown in the bottom panel on the left of Figure 4.20. There is a phase of rising SGS turbulence production accompanied by increasing dissipation of resolved kinetic energy, while the second large-eddy turn-over is elapsing. For$\tilde{t} \gtrsim 2$, the trend reverses and the system evolves towards a steady state.

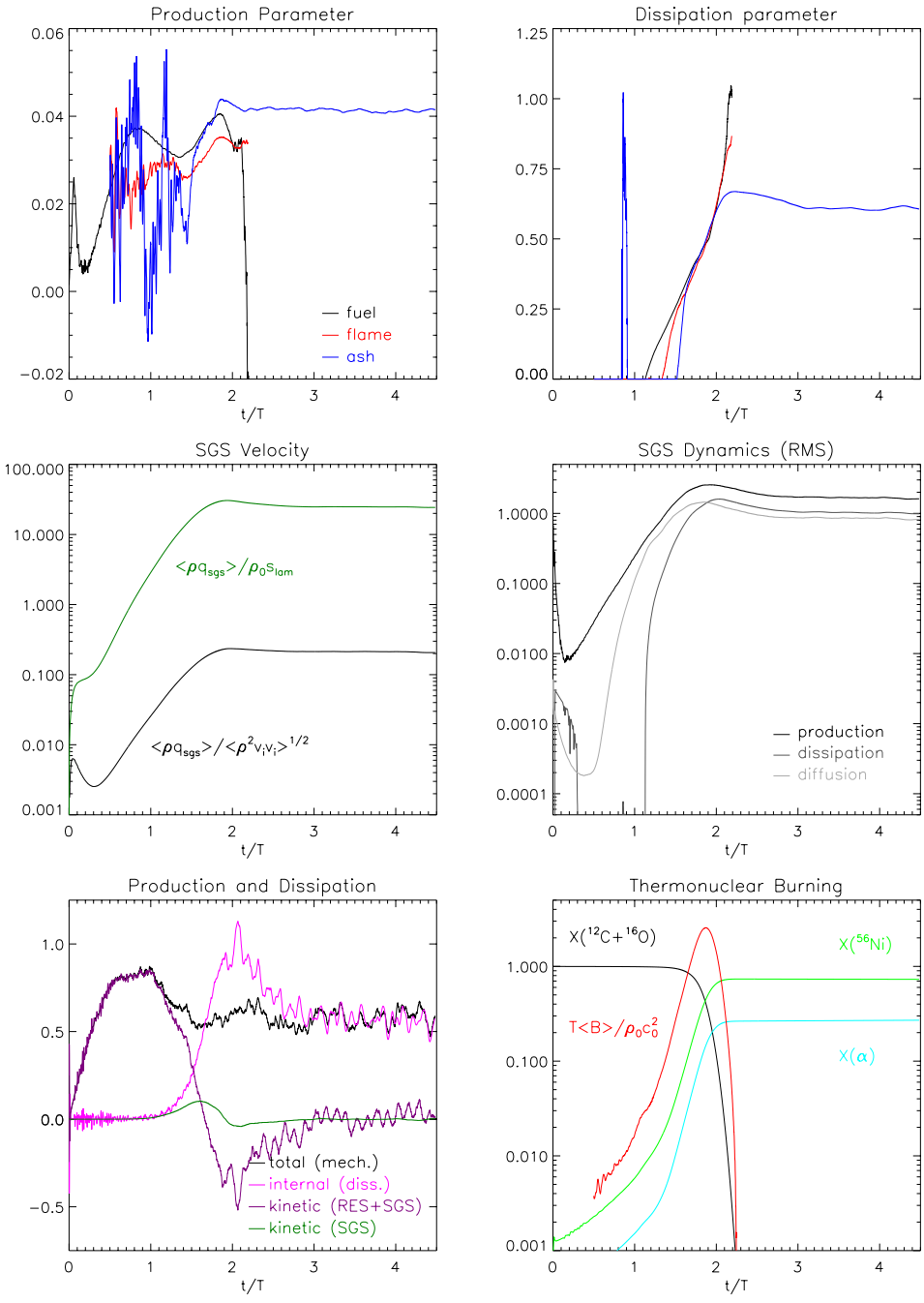

Figure 4.20: Statistics of the LES with the active semi-localised SGSTE model.

Chapter 5

Résumé

The question is not whether one model or the other is right. All models are wrong. They only help us to understand the physics.

Jens Niemeyer during coffee break in the Villa Tambosi

The investigation of purely hydrodynamical turbulence and turbulent deflagration presented in this Thesis has clearly demonstrated that the physical understanding of a complex phenomenon by means of computer simulations cannot be detached from numerical issues. This would be possible, if computers of infinite memory and unlimited speed were available. Since this is not the case, numerical simulations are tentative by their very nature. For the treatment of deflagration in the flamelet regime, the level set method in combination with a subgrid scale model to determine the intrinsic propagation speed in a turbulent flow are powerful tools. However, one faces many uncertainties regarding particular approximations. Whether a certain formulation of a numerical model is applicable to the problem at hand, is mainly a matter of the robustness of the physically relevant results with respect to the free model parameters. In the case of LES of burning in a cubic domain, one must ensure that the evolution of the burning statistics is largely independent of resolution and any prescribed SGS closure parameters. As for simulations of thermonuclear supernovae, the total amount of energy produced by the explosion, the final chemical composition and the distribution of elements in velocity space can be compared to observational data. In this concluding Chapter, a few comments on the results discussed in Chapters 2 and 4 are made, and it is pointed at possible directions of future research.

5.1 Concerning Turbulence

Turbulence has pushed to the frontiers in astrophysics in the course of recent years. It has been realised that turbulence plays a key role in many phenomena of interest. In the case of thermonuclear deflagration, a particularly intriguing example is found. It is actually turbulence which *drives* the burning process. Although LES of deflagration in a cube have produced valuable information, there are still a number of open issues, which are beyond the reach of this Thesis.

5.1.1 Localisation of the Subgrid Scale Closures

The main results emerging from the numerical studies discussed in Chapter 4 can be summarised as follows: First of all, the SGS turbulence energy model basically appears to perform very well in LES of turbulent deflagration. However, details of the burning process were found to be quite sensitive to the computation of the closure parameters C_ν, C_ϵ and C_κ for SGS production, dissipation and diffusion, respectively. Three different options were investigated: Firstly, an *ad hoc* procedure introduced by Clement [1993], secondly, constant statistical values determined from DNS data and, finally, a semi-localised model which, in part, follows the dynamical procedure proposed by Kim, Menon, and Mongia [1999]. From these three possibilities, only the statistical and the localised closures seem to be adequate. Whether the semi-localised model is indeed superior to the statistical model is difficult to answer purely on grounds of LES of isotropic turbulence with artificial forcing. In any case, one must be aware that the SGS closures introduce supplementary numerical parameters. Therefore, we can definitely *not* speak of parameter-free models. The discussion of the influence of different SGS parameters in Section 4.3 underlines this statement. In order to arrive at sound physical predictions, it is of the uttermost importance to study carefully what changes come about if some *particular* parameter assumes different values. From this point of view, it is encouraging that the semi-localised model is fairly robust with respect to changes in the numerical resolution, the characteristic length of the test filter and the temporal smoothing scale for dissipation.

It is actually the rate of SGS dissipation, from which the most difficult closure problem arises. This can be attributed to the fact that dissipation is spatially intermittent and most significant on scales of the order of the Kolmogorov scale η_K. Contrary to SGS production, which is mostly determined by the dynamics on scales in the vicinity of the numerical scale Δ_{eff}, similarity assumptions usually fail for closures of dissipation. Thus, the statistical approach outlined in Section 4.3.4 was applied. Basically, the parameter C_ϵ is calculated from the numerically resolved energy budget in the three distinct topological regions containing fuel, the flames and ash, respectively. Using this method in LES, the following is observed for the evolution of the dissipation statistics. During the first integral time, there is very little dissipation, as virtually no small-scale vortices are present. Then the rate of dissipation is rising sharply and subsequently settles into a plateau with $C_\epsilon \approx 0.6$. This value basically agrees with numerical or theoretical estimates in the literature and is about 20 % larger than the statistical result $C_\epsilon \approx 0.5$, which was computed from DNS data (see Section 3.2.3). On account of the uncertainties in both approaches and the significant scatter among cited values for closure parameters calculated with different methods, the result for C_ϵ appears to be satisfactory.

An entirely different ansatz is a two equation model in the spirit of the well known $k-\epsilon$ model. The basic idea is to formulate a supplementary dynamical equation for the rate of dissipation, which is obtained by dimensional multiplication of the equation for the SGS turbulence energy with the inverse time scale $\tau_\epsilon^{-1} = \epsilon_{\text{sgs}}/k_{\text{sgs}}$:

$$\frac{\mathrm{D}}{\mathrm{D}t}\epsilon_{\text{sgs}} - \frac{1}{\rho}\boldsymbol{\nabla}\cdot\left(\frac{\rho\kappa_{\text{sgs}}}{\sigma_\epsilon}\boldsymbol{\nabla}\epsilon_{\text{sgs}}\right) = -C_{\epsilon 1}\frac{\epsilon_{\text{sgs}}}{k_{\text{sgs}}}\Pi_{\text{sgs}} - C_{\epsilon 2}\frac{\epsilon_{\text{sgs}}^2}{k_{\text{sgs}}}, \tag{5.1}$$

where $C_{\epsilon 1} = 1.44$, $C_{\epsilon 2} = 1.92$, and $\sigma_\epsilon = 1.3$, if $\kappa_{\text{sgs}} = \nu_{\text{sgs}}$ [cf. Pope, 2000, Sec-

tion 10.4]. The source terms can be interpreted as non-linear relaxation of $\tilde{\tau}_\epsilon^{-1}$ towards the equilibrium value $\sim (\Pi_{\rm sgs}/\rho\nu_{\rm sgs})^{1/2} \sim |S^*|$. The diffusion term is completely analogous to $\mathfrak{D}_{\rm sgs}$, with an effective diffusivity $\kappa_{\rm sgs}/\tau_\epsilon$[1]. Canuto [1994] actually proposed to adopt the above second-order closure for the rate of dissipation in a SGS model. The implementation for LES of turbulent deflagration, however, did not succeed. In fact, the two-equation SGS model fails to converge, once turbulence is fully developed, which becomes manifest in a slow persistent growth of the SGS turbulence energy. The drift might be caused by deficiencies in the numerical scheme for the SGS equations. However, it could reflect an inherent inadequacy of the two-equation model as well. This issue certainly has to be investigated in the future.

Very little is known about the influence of gravity on small scales. On grounds of scaling arguments, it was argued in Section 1.1.3 that buoyancy effects should become asymptotically negligible towards length scales much smaller than the integral scale. However, this conclusion applies in the case of fully developed, steady turbulence only. Since a supernova explosion is a transient phenomenon, one can doubt the validity of the argument. The dominance of the turbulence cascade over Rayleigh-Taylor instabilities has actually been questioned by Khokhlov et al. However, so far they have not produced convincing evidence in favour of their conjecture. Anyhow, it would be important to investigate whether gravitational effects are significant on subgrid scales, by including the buoyancy terms in the SGSTE model. Firstly, scale separation in the filtering approach would imply the following modification of the SGS rate of production:

$$\Pi_{\rm sgs} = \tau_{ik} S_{ik} + \Gamma_{\rm sgs}, \tag{5.2}$$

where

$$\Gamma_{\rm sgs} \equiv -\tau(v_i, g_i) = \langle \overset{\infty}{\rho}\overset{\infty}{v_i}\overset{\infty}{g_i} \rangle_{\rm eff} - \rho v_i g_i \tag{5.3}$$

accounts for gravitational energy injection on unresolved scales. Secondly, an additional convective transport term would have to be included in the resolved energy conservation law. This term is given by the divergence of the flux $\langle \overset{\infty}{E}_{\rm int}\overset{\infty}{v_i} \rangle_{\rm eff} - E_{\rm int} v_i$. The closure for the convective flux is usually made in terms of an adiabatic temperature gradient [cf. Canuto, 1996], or it is modelled by a dynamical equation [cf. Canuto, 1994, Section 5]. In any case, it is hard to see how this could be carried over to the problem of turbulent deflagration. There are also indications that the rate of dissipation has to be modified under the action of gravity. For instance, Canuto and Minotti [1993] pointed out that gravity waves store kinetic energy lost by turbulent vortices in a stable stratification of fluid. This would lead to the *Lumley-Weinstock model* of dissipation. Of course, a supernova explosion is non-stationary and, therefore, the Lumley-Weinstock model appears not to be appropriate. However, once turbulence freezes out due to the expansion of the unbound white dwarf, so-called *fossil turbulence* is produced [cf. Gibson, 1999]. Possibly, this phenomenon plays a key role in the transition to ballistic expansion in the late stage of the explosion. One should note that the observable distribution of elements in velocity space is ultimately determined by the flow structure at freeze-out time.

[1] A tensor diffusivity proportional to τ_{ik} is discussed in Speziale [1991].

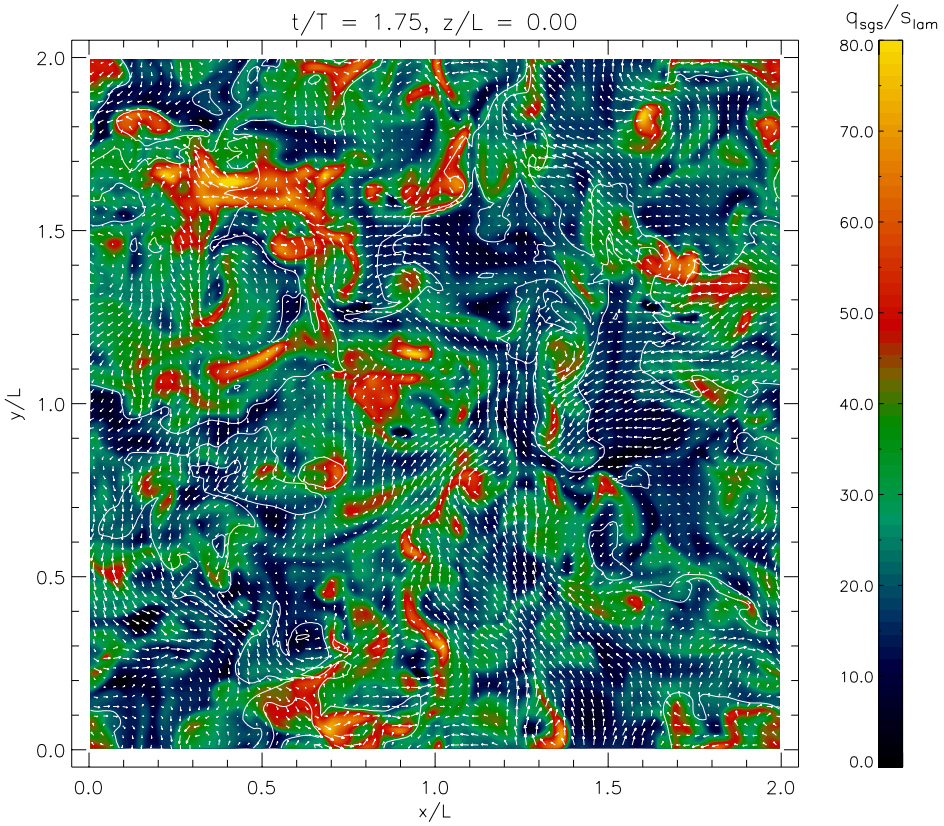

Figure 5.1: Filtered flow map with contours of the SGS turbulence velocity relative to the laminar burning speed in a 2D section at time $\tilde{t} = 1.75$. The numerical resolution is $N = 216$. The semi-localised SGS model with $\Delta_T = 6.74\Delta$ was actively coupled to the resolved flow in this simulation.

5.1.2 Flame Physics and the Level Set Method

The LES of turbulent deflagration presented in this Thesis impressively demonstrate that the level set method is indeed well suited for the representation of flame fronts. As an illustration, a 2D flow map with contours of $q_{\rm sgs}/s_{\rm lam}$ is shown in Figure 5.1 for a LES of turbulent deflagration with the semi-localised SGS model. In this simulation, the turbulent flame speed was defined by $s_{\rm t} = s_{\rm lam}\sqrt{1 + (q_{\rm sgs}/s_{\rm lam})^2}$. Nevertheless, some deficiencies of the current implementation remain a matter of concern. Firstly, there are limitations due to the passive implementation, in which differences between burned and unburned states are ignored. This makes simulations prone to significant numerical errors for burning at densities $\lesssim 10^7\,\mathrm{g\,cm^{-3}}$. Secondly, the algorithm for the re-initialisation of the level set is inefficient and eats away a lot of computing power. As for the first problem, complete reconstruction in 3D is the only reliable option. However, this might very well turn out to be computationally too involved. There are also alternatives to the re-initialisation method. Unfortunately, one particularly promising option, the so-call *fast marching method*, is not readily parallelisable [cf.

Adalsteinsson and Sethian, 1999].

Apart from the implementation of the level set technique, another crucial question concerns the relation between the intrinsic propagation speed s of the level set and the velocity scale q_{sgs} associated with SGS turbulence. Two different options were investigated. Firstly the naïve relation $s = \max(s_{\mathrm{lam}}, q_{\mathrm{sgs}})$ and, secondly, Pocheau's relation (4.7). The latter introduces the parameter C_{t}, which fixes the asymptotic ratio of s_{t} to q_{sgs}. From numerical experiments, it appears that $C_{\mathrm{t}} \simeq 1$ is preferable. Furthermore, one could include SGS effects in the dynamical equation (4.4) for the level set function. This was indeed investigated by Im et al. [1997]. They even suggested a dynamical procedure for the computation of C_{t} in the fashion of the localised closure for the production parameter C_{ν}. Whether this is advisable with the passive implementation, where numerical artifacts in the shape of the resolved level set could produce significant spurious contributions, is questionable. For this reason, it has not been attempted. In addition, there is a SGS transport term for the level set, which is of the form $\partial_k(\langle \overset{\infty}{v}_k \overset{\infty}{G} \rangle_{\mathrm{eff}} - v_k G)$ and effectively introduces *diffusion* of the level set due to SGS turbulence. However, Kim et al. [1999] argued that the contributions arising thereof are not particularly important and, in fact, cannot be determined within the available framework of SGS modelling. Yet another interesting proposal is to extend the methodology based upon the notion of a level set with a turbulent propagation speed to flames in the *thin-reaction-zone regime*, when the Gibson scale is comparable to the flame thickness. This regime is possibly important in the late stage of a thermonuclear supernova explosion. Kim and Menon [2000] suggested a generalised flame speed relation which accounts for turbulent broadening of the reaction zone in a deflagration front. Basically, small-scale turbulence enhances the transport of heat and, thus, preheating is more efficient than in the case of purely conductive transport. Implementing the generalised model, which was originally developed for engineering applications, might extend the interval of time over which a supernova explosion can reasonably be simulated.

5.2 Towards New Supernova Explosion Models

As follow-up action, the SGS model developed in the course of this Thesis will be applied to simulations of thermonuclear supernovae. This is not quite as straightforwards as one might think. One problem stems from the rapidly decreasing density at the surface of the white dwarf, which poses difficulties for a compressible SGS model. Even more important, however, is the feedback between burning and turbulence production in a supernova explosion. If SGS turbulence enhances the rate of burning, more ash is produced and buoyancy increases convection, which in turn generates more SGS turbulence. For this reason, it is possible that the semi-localised SGS model with dynamical treatment of production predicts a significantly accelerated progression of the deflagration, once convection is initiated. In the early phase, on the other hand, the burning process should proceed slower in comparison to Clement's model, because the production parameter of the localised model is initially small.

Whatever the outcome will be, the pure deflagration model for SNe Ia is pushed hard to accommodate recent observational facts. One issue is the observation of intermediate mass elements (IMEs) ejected at extraordinarily high velocity in SN 2002bo

[Benetti et al., 2003], which indicates that the burning zone penetrates into the outermost layers of the expanding white dwarf. At the same time, however, the mass of produced ^{56}Ni is comparable to those found in events with significantly smaller ejection velocities of IMEs. Therefore, the properties of SN 2002bo can not be understood solely on grounds of the explosion energetics. Moreover, evidence for polarisation in the spectra of SN 2001el points at a non-spherical structure of the explosion [Kasen et al., 2003]. For the time being, delayed detonations and, possibly, a significant rotation of the progenitor are favoured as explanations for these peculiarities. Even if this should put an end to the pure deflagration model, the thorough understanding of the physics of turbulent deflagration will still be essential, in order to model the early phase of a SN Ia explosion prior to the transition from deflagration to a detonation. The investigation of turbulent burning and the development of a more sophisticated SGS model presented in this Thesis will hopefully turn out to be a step in achieving such an understanding.

Bibliography

Adalsteinsson, D. and J. A. Sethian (1999, January). The Fast Construction of Extension Velocities in Level Set Methods. *Journal of Computational Physics 148*, 2–22.

Balberg, S. and S. L. Shapiro (2000). The properties of matter in white dwarfs and neutron stars. In M. Levy, H. Bass, and R. Stern (Eds.), *Handbook of Elastic Properties of Solids, Liquids, and Gases*, Volume 4, Chapter 15. Academic Press. Preprint `astro-ph/0004317`.

Bardina, J., J. H. Ferziger, and W. C. Reynolds (1983). Improved turbulence models based on large eddy simulation of homgeneous, incompressible, turbulent flows. Technical Report Report TF-19, Dept. Mechanial Engineering, Stanford University.

Baym, G., C. Pethick, and P. Sutherland (1971, December). The Ground State of Matter at High Densities: Equation of State and Stellar Models. *Astrophys. J. 170*, 299.

Benetti, S., P. Meikle, M. Stehle, G. Altavilla, S. Desidera, G. Folatelli, A. Goobar, S. Mattila, J. Mendez, H. Navasardyan, A. Pastorello, F. Patat, M. Riello, P. Ruiz-Lapuente, D. Tsvetkov, M. Turatto, P. Mazzali, and W. Hillebrandt (2003). Supernova 2002bo: inadequacy of the single parameter description. Accepted to MNRAS. Preprint `astro-ph/0309665`.

Blinnikov, S. I. and P. V. Sasorov (1995). Landau-darrieus instability and the fractal dimension of flame fronts. *Phys. Rev. E 53*(5), 4827–4841.

Branch, D. (1998). Type Ia Supernovae and the Hubble Constant. *Ann. Rev. Astron. Astrophys. 36*, 17–56.

Canuto, V. M. (1994, June). Large Eddy simulation of turbulence: A subgrid scale model including shear, vorticity, rotation, and buoyancy. *Astrophys. J. 428*, 729–752.

Canuto, V. M. (1996, August). Turbulent Convection: Old and New Models. *Astrophys. J. 467*, 385.

Canuto, V. M. (1997, June). Compressible Turbulence. *Astrophys. J. 482*, 827.

Canuto, V. M. and M. S. Dubovikov (1996, February). A dynamical model for turbulence. I. General formalism. *Physics of Fluids 8*, 571–586.

Canuto, V. M. and F. Minotti (1993, July). Stratified turbulence in the atmosphere and oceans - A new subgrid model. *Journal of Atmospheric Sciences 50*, 1925–1935.

Cao, N., S. Chen, and Z. She (1996, May). Scalings and Relative Scalings in the Navier-Stokes Turbulence. *Physical Review Letters 76*, 3711–3714.

Carati, D. and E. van den Eijnden (1997, July). On the self-similarity assumption in dynamic models for large eddy simulations. *Phys. Fluids 9*, 2165–2167.

Carroll, B. W. and D. A. Ostlie (1996). *An Introduction to Modern Astrophysics*. Addison-Wesley.

Carroll, S. M. (2003). *Measuring and Modeling the Universe*, Volume 2 of *Carnegie Observatories Astrophysics Series*, Chapter Why is the Universe Accelerating? Springer. Preprint astro-ph/0310342.

Center for Turbulence Research (1997). *Annual Research Briefs*. Center for Turbulence Research.

Chandrasekhar, S. (1931). The Maximum Mass of Ideal White Dwarfs. *Astrophys. J. 74*, 81.

Chorin, A. J. (1994). *Vorticity and Turbulence*, Volume 103 of *Applied Mathematical Sciences*. Springer.

Clark, R. A., J. H. Ferziger, and W. C. Reynolds (1979). Evaluation of sugrid-scale models using and accurately simulated turbulent flow. *J. Fluid Mech. 91*, 1–16.

Clement, M. J. (1993). Hydrodynamical simulations of rotating stars. I. A model for subgrid-scale flow. *Astrophys. J. 406*, 651–660.

Colella, P. and P. R. Woodward (1984). The piecewise parabolic method (PPM) for gas-dynamical simulations. *Journal of Computational Physics 54*, 174–201.

Damköhler, G. (1940). Der Einfluß der Turbulenz auf die Flammengeschwindigkeit in Gasgemischen. *Z. Elektrochem. 46*, 601–626.

Deardorff, J. W. (1973). The use of subgrid transport equations in a three-dimensional model of atmospheric turbulence. *ASME J. Fluids Engng.*, 429–438.

Dobler, W., N. Erland, L. Haugen, T. A. Yousef, and A. Brandenburg (2003). The bottleneck effect in three-dimensional turbulence simuations. Preprint astro-ph/0303324. Submitted to *Phys. Rev. E*.

Eswaran, V. and S. B. Pope (1988). Direct numerical simulations of the turbulent mixing of a passive scalar. *Phys. Fluids 31*, 506–520.

Fedorova, A. V., A. V. Tutukov, and L. R. Yungelson (2003). Type Ia Supernovae in semi-detached binary systems. *Astronomy Letters 29*(12). In press. Preprint astro-ph/0309052.

Filippenko, A. V. (2003). Evidence from Type Ia Supernovae for an Accelerating Universe and Dark Energy. In W. L. Freedman (Ed.), *Measuring and Modeling the Universe*, Volume 2 of *Carnegie Observatories Astrophysics Series*. Cambridge University Press. Preprint astro-ph/0307139.

Frigo, M. and S. G. Johnson (1998). FFTW: An Adaptive Software Architecture for the FFT. In *ICASSP conference proceedings*, Volume 3, pp. 1381–1384.

Fryxell, B. A., E. Müller, and W. D. Arnett (1989). MPA preprint 449.

Fureby, C., G. Tabor, H. G. Weller, and A. D. Gosman (1997, November). Differential subgrid stress models in large eddy simulations. *Phys. Fluids 9*, 3578–3580.

Gamezo, V. N., A. M. Khokhlov, E. S. Oran, A. Y. Chtchelkanova, and R. O. Rosenberg (2003, January). Thermonuclear Supernovae: Simulations of the Deflagration Stage and Their Implications. *Science 299*, 77–81.

Germano, M. (1992). Turbulence: the filtering approach. *J. Fluid Mech. 238*, 325–336.

Germano, M., U. Piomelli, P. Moin, and W. H. Cabot (1991, July). A dynamic subgrid-scale eddy viscosity model. *Phys. Fluids 3*, 1760–1765.

Ghosal, S., T. S. Lund, P. Moin, and K. Akselvoll (1995). A dynamic localization model for large-eddy simulation of turbulent flow. *J. Fluid Mech. 286*, 229–255.

Gibson, C. H. (1999). Fossil turbulence revisited. *J. Marine Sys. 21*, 147–167.

Gotoh, T. and D. Fukayama (2001, April). Pressure Spectrum in Homogeneous Turbulence. *Physical Review Letters 86*, 3775–3778.

Green, D. A. and F. R. Richardson (2003). *Supernovae and Gamma Ray Buersters*, Chapter The Historical Supernovae. Lecture Notes in Physics. Springer. In press. Preprint `astro-ph/0301603`.

Hachisu, I. (2002, January). Evolution of binaries producing Type Ia supernovae, luminous supersoft X-ray sources, and recurrent novae. In *ASP Conf. Ser. 261: The Physics of Cataclysmic Variables and Related Objects*, pp. 605.

Hamuy, M., M. M. Phillips, N. B. Suntzeff, J. Maza, L. E. González, M. Roth, K. Krisciunas, N. Morrell, E. M. Green, S. E. Persson, and P. J. McCarthy (2003, August). An asymptotic-giant-branch star in the progenitor system of a type Ia supernova. *Nature 424*, 651–654.

Han, Z. and P. Podsiadlowski (2003). The single degenerate channel for the progenitors of type Ia supernovae. Submitted to MNRAS. Preprint `astro-ph/0309618`.

Hillebrandt, W. and B. Leibundgut (Eds.) (2002). *From Twilight to Highlight: The Physics of Supernovae. ESO/MPA/MPE Workshop*. Springer.

Hillebrandt, W. and J. C. Niemeyer (2000). Type Ia supernova explosion models. *Ann. Rev. Astron. Astrophys. 38*, 191.

Hoyle, F. and W. A. Fowler (1960, November). Nucleosynthesis in Supernovae. *Astrophys. J. 132*, 565.

Im, H. G., T. S. Lund, and J. H. Ferziger (1997, December). Large eddy simulation of turbulent front propagation with dynamic subgrid models. *Phys. Fluids 9*, 3826–3833.

Kadanoff, L. P. (2001). Turbulent heat flow: structures and scaling. *Physics Today 54*(8), 34–39.

Kasen, D., P. Nugent, L. Wang, D. A. Howell, J. C. Wheeler, P. Höflich, D. Baade, E. Baron, and P. H. Hauschildt (2003, August). Analysis of the Flux and Polarization Spectra of the Type Ia Supernova SN 2001el: Exploring the Geometry of the High-Velocity Ejecta. *Astrophys. J. 593*, 788–808.

Kerstein, A. (1988). *Combustion Sci. Technol. 50*, 441.

Khokhlov, A. M. (1991, May). Delayed detonation model for type Ia supernovae. *Astron. & Astrophys. 245*, 114–128.

Khokhlov, A. M. (1995, August). Propagation of Turbulent Flames in Supernovae. *Astrophys. J. 449*, 695.

Kim, W. and S. Menon (1996). On the properties of a localized dynamic subgrid-scale model for large-eddy simulations. Draft.

Kim, W. and S. Menon (2000). Numerical Modeling of Turbulent Permixed Flames in the Thin-Reaction-Zones Regime. *Combust. Sci. and Tech. 160*, 119–150.

Kim, W., S. Menon, and H. C. Mongia (1999). Large-Eddy Simulation of a Gas Turbine Combustor Flow. *Combust. Sci. and Tech. 143*, 25–62.

King, A. R., D. J. Rolfe, and K. Schenker (2003, June). A new evolutionary channel for Type Ia supernovae. *Mon. Not. R. Astron. Soc. 341*, L35–L38.

Kolmogorov, A. N. (1962). A refinement of previous hypotheses concerning the local structure of turbulence in a viscous incompressible fluid at high Reynolds number. *J. Fluid Mech. 13*, 82–85.

Kosović, B. (1997, April). Subgrid-scale modelling for the large-eddy simulation of high-Reynolds-number boundary layers. *J. Fluid Mech. 336*, 151–182.

Kosović, B., D. I. Pullin, and R. Samtaney (2002, April). Subgrid-scale modeling for large-eddy simulations of compressible turbulence. *Phys. Fluids 14*, 1511–1522.

Kupka, F. (2003). Private Communication.

Landau, L. D. (1932). On the Theory of Stars. *Phys. Z. Sowjetunion 1*, 285.

Landau, L. D. and E. M. Lifshitz (1991). *Lehrbuch der theoretischen Physik*, Volume VI. Hydrodynamik. Akademie Verlag.

Leibundgut, B. (2000). Type Ia Supernovae. *The Astron. Astrophys. Rev. 10*, 179–209.

Leibundgut, B. and N. B. Suntzeff (2003). *Supernovae and Gamma Ray Buersters*, Chapter Optical Light Curves of Supernovae. Lecture Notes in Physics. Springer. In press. Preprint `astro-ph/0304112`.

Lesieur, M. and O. Métais (1996). New trends in large-eddy simulations of turbulence. *Annu. Rev. Fluid Mech. 28*, 45.

LeVeque, R. J. (2002). *Finite Volume Methods for Hyperbolic Problems*. Cambridge University Press.

Liebert, J. (1980). White Dwarf Stars. *Ann. Rev. Astron. Astrophys. 18*, 363–398.

Liu, S., C. Meneveau, and J. Katz (1994). On the properties of similarity subgrid-scale models as deduced from measurements in a turbulent jet. *J. Fluid Mech. 275*, 83–119.

Lumley, J. L. (1970). *Stochastic tools in turbulence*, Volume 12 of *Applied mathematics and mechanics*. Academic Press.

Lund, T. S. (1997). On the use of discrete filters for large eddy simulation. See Center for Turbulence Research [1997].

Lund, T. S. and E. A. Novikov (1992). Parametrization of subgrid-scale stress by the velocity gradient tensor. *Annual Research Briefs - Center of Turbulence Research*, 27–43.

McComb, W. D. (1990). *The Physics of Fluid Turbulence*. Oxford Science Publications.

Meneveau, C. and J. Katz (2000). Scale-Invariance and Turbulence Models for Large-Eddy Simulation. *Annual Review of Fluid Mechanics 32*, 1–32.

Moin, P., K. Squires, W. Cabot, and S. Lee (1991, November). A dynamic subgrid-scale model for compressible turbulence and scalar transport. *Phys. Fluids 3*, 2746–2757.

Müller, E. (2002). Weiße Zwerge, Neutronensterne und Schwarze Löcher: Physik kompakter astrophysikalischer Objekte. Vorlesung an der Techn. Universität München.

Nandkumar, R. and C. J. Pethick (1984, August). Transport coefficients of dense matter in the liquid metal regime. *Mon. Not. R. Astron. Soc. 209*, 511–524.

Nesis, A., R. Hammer, M. Kiefer, H. Schleicher, M. Sigwarth, and J. Staiger (1999, May). Dynamics of the solar granulation. VI. Time variation of the granular shear flow. *Astron. & Astrophys. 345*, 265–275.

Niemeyer, J. C. (1999). Can deflagration-detonation transitions occur in type Ia supernovae? *Astrophys. J. 523*, L57.

Niemeyer, J. C., W. K. Bushe, and G. R. Ruetsch (1999). Small-scale interaction of turbulence with thermonuclear flames in type Ia supernovae. *Astrophys. J. 524*, 290–294.

Niemeyer, J. C. and W. Hillebrandt (1995a, October). Microscopic Instabilities of Nuclear Flames in Type Ia Supernovae. *Astrophys. J. 452*, 779.

Niemeyer, J. C. and W. Hillebrandt (1995b, October). Turbulent Nuclear Flames in Type Ia Supernovae. *Astrophys. J. 452*, 769.

Niemeyer, J. C., W. Hillebrandt, and S. E. Woosley (1996, November). Off-Center Deflagrations in Chandrasekhar Mass Type Ia Supernova Models. *Astrophys. J. 471*, 903.

Niemeyer, J. C. and A. R. Kerstein (1997, June). Burning regimes of nuclear flames in SN Ia explosions. *New Astronomy 2*, 239–244.

Niemeyer, J. C., M. Reinecke, C. Travaglio, and W. Hillebrandt (2003). Small Steps Toward Realistic Explosion Models of Type Ia Supernovae. See Hillebrandt and Leibundgut [2002], pp. 151–157.

Niemeyer, J. C. and S. E. Woosley (1997). The thermonuclear explosion of Chandrasekhar mass white dwarfs. *Astrophys. J. 475*, 740–753.

Nomoto, K. and Y. Kondo (1991, January). Conditions for accretion-induced collapse of white dwarfs. *Astrophys. J. 367*, L19–L22.

Nomoto, K., F.-K. Thielemann, and K. Yokoi (1984, November). Accreting white dwarf models of Type I supernovae. III - Carbon deflagration supernovae. *Astrophys. J. 286*, 644–658.

Nomoto, K., T. Uenishi, C. Kobayashi, H. Umeda, T. Ohkubo, I. Hachisu, and M. Kato (2003). Type Ia Supernovae: Progenitors and Diversities. See Hillebrandt and Leibundgut [2002], pp. 115.

Osher, S. and J. A. Sethian (1988, November). Fronts propagating with curvature-dependent speed: Algorithms based on Hamilton-Jacobi formulations. *J. Comp. Phys. 79*, 12–49.

Padmanabhan, T. (2000). *Theoretical Astrophysics*. Cambridge University Press.

Perlmutter, S. (2003). Supernovae, Dark Energy, and the Accelerating Universe. *Physics Today 56*(4), 53–59.

Perlmutter, S., G. Aldering, G. Goldhaber, R. A. Knop, P. Nugent, P. G. Castro, S. Deustua, S. Fabbro, A. Goobar, D. E. Groom, I. M. Hook, A. G. Kim, M. Y. Kim, J. C. Lee, N. J. Nunes, R. Pain, C. R. Pennypacker, R. Quimby, C. Lidman, R. S. Ellis, M. Irwin, R. G. McMahon, P. Ruiz-Lapuente, N. Walton, B. Schaefer, B. J. Boyle, A. V. Filippenko,

T. Matheson, A. S. Fruchter, N. Panagia, H. J. M. Newberg, W. J. Couch, and The Supernova Cosmology Project (1999, June). Measurements of Omega and Lambda from 42 High-Redshift Supernovae. *Astrophys. J. 517*, 565–586.

Perlmutter, S. and B. P. Schmidt (2003). *Supernovae and Gamma Ray Buersters*, Chapter Measuring Cosmology with Supernovae. Lecture Notes in Physics. Springer. In press. Preprint `astro-ph/0303428`.

Phillips, M. M. (1993, August). The absolute magnitudes of Type Ia supernovae. *Astrophys. J. 413*, L105–L108.

Piomelli, U. (1993, June). High Reynolds number calculations using the dynamic subgrid-scale stress model. *Phys. Fluids 5*, 1484–1490.

Piomelli, U. and J. Liu (1995). Large-eddy simulation of rotating channel flows using a localized dynamic model. *Phys. Fluids 7*(4), 839.

Pocheau, A. (1994, February). Scale invariance in turbulent front propagation. *Phys. Rev. E 49*, 1109–1122.

Pope, S. B. (2000). *Turbulent Flows*. Cambridge University Press.

Porter, D. H., A. Pouquet, and P. R. Woodward (1992, May). Three-dimensional supersonic homogeneous turbulence - A numerical study. *Physical Review Letters 68*, 3156–3159.

Porter, D. H., A. Pouquet, and P. R. Woodward (1994, June). Kolmogorov-like spectra in decaying three-dimensional supersonic flows. *Phys. Fluids 6*, 2133–2142.

Porter, D. H. and P. R. Woodward (1994, July). High-resolution simulations of compressible convection using the piecewise-parabolic method. *Astrophys. J. 93*, 309–349.

Porter, D. H., P. R. Woodward, and A. Pouquet (1998, January). Inertial range structures in decaying compressible turbulent flows. *Phys. Fluids 10*, 237–245.

Potter, D. (1973). *Computational Physics*. Wiley.

Röpke, F. K., J. C. Niemeyer, and W. Hillebrandt (2003, May). On the Small-Scale Stability of Thermonuclear Flames in Type Ia Supernovae. *Astrophys. J. 588*, 952–961.

Reinecke, M., W. Hillebrandt, and J. C. Niemeyer (1999, July). Thermonuclear explosions of Chandrasekhar-mass C+O white dwarfs. *Astron. & Astrophys. 347*, 739–747.

Reinecke, M., W. Hillebrandt, and J. C. Niemeyer (2002, September). Three-dimensional simulations of type Ia supernovae. *Astron. & Astrophys. 391*, 1167–1172.

Reinecke, M. A. (2001). *Modeling and simulation of turbulent combustion in type Ia supernovae*. Ph. D. thesis, Technical University of Munich, Physics Department.

Richardson, L. F. (1922). *Weather Prediction by Numerical Process*. Cambridge University Press.

Rider, W. J. and D. Drikakis (2002). *Turbulent Flow Computation*, Chapter High Resolution Methods for Computing Turbulent Flows. Kluwer Acad. Publ.

Riess, A. G. and A. V. Filippenko (2001). Evidence from Type Ia Supernovae for an Accelerating Universe. In *Identification of Dark Matter*, pp. 30. Preprint `astro-ph/0008057`.

Röpke, F. K. (2003). *On the stability of thermonuclear flames in type Ia supernova explosions*. Ph. D. thesis, Technical University of Munich, Physics Department.

Ruiz-Lapuente, P. (2003). Cosmology with Supernovae. In D. B. et al. (Ed.), *3K, SNs, Clusters: Hunting the Cosmological Parameters*. Kluwer Acad. Publ. Invited review presented at the JENAM 2002 (Porto, Portugal). Preprint `astro-ph/0304108`.

Rutgers, M. A., X. Wu, and W. I. Goldburg (1996, September). The onset of two-dimensional grid generated trubulence in flowing soap films. *Phys. Fluids 8*(9), S7. Photographs can be downloaded from `home.earthlink.net/~marutgers`.

Sagaut, P. (2001). *Large Eddy Simulation for Incompressible Flows*. Springer.

Schmidt, B. P., N. B. Suntzeff, M. M. Phillips, R. A. Schommer, A. Clocchiatti, R. P. Kirshner, P. Garnavich, P. Challis, B. Leibundgut, J. Spyromilio, A. G. Riess, A. V. Filippenko, M. Hamuy, R. C. Smith, C. Hogan, C. Stubbs, A. Diercks, D. Reiss, R. Gilliland, J. Tonry, J. Maza, A. Dressler, J. Walsh, and R. Ciardullo (1998, November). The High-Z Supernova Search: Measuring Cosmic Deceleration and Global Curvature of the Universe Using Type Ia Supernovae. *Astrophys. J. 507*, 46–63.

Schmidt, H. and U. Schumann (1989, March). Coherent structure of the convective boundary layer derived from large-eddy simulations. *J. Fluid Mech. 200*, 511–562.

Sethian, J. A. (1996). *Level Set Methods*. Number 3 in Cambridge monographs on applied and computational mathematics. Cambridge University Press.

Shapiro, S. L. and S. A. Teukolsky (1983). *Black Holes, White Dwarfs and Neutron Stars*. John Wiley & Sons.

She, Z. and E. Jackson (1993, July). On the universal form of energy spectra in fully developed turbulence. *Phys. Fluids 5*, 1526–1528.

Speziale, C. G. (1991). Analytical methods for the development of Reynolds-stress closures in turbulence. *Annual Review of Fluid Mechanics 23*, 107–157.

Speziale, C. G., G. Erlebacher, T. A. Zang, and M. Y. Hussaini (1988, April). The subgrid-scale modeling of compressible turbulence. *Phys. Fluids 31*, 940–942.

Steinmetz, M., E. Müller, and W. Hillebrandt (1992, February). Carbon Detonations in Rapidly Rotating White Dwarfs. *Astrophys. J. 254*, 177.

Sytine, I. V., D. H. Porter, P. R. Woodward, S. W. Hodson, and K. Winkler (2000, March). Convergence Tests for the Piecewise Parabolic Method and Navier-Stokes Solutions for Homogeneous Compressible Turbulence. *Journal of Computational Physics 158*, 225–238.

Thoroughgood, T. D., V. S. Dhillon, S. P. Littlefair, T. R. Marsh, and D. A. Smith (2001, November). The mass of the white dwarf in the recurrent nova U Scorpii. *Mon. Not. R. Astron. Soc. 327*, 1323–1333.

Timmes, F. X. and S. E. Woosley (1992). The conductive propagation of nuclar flames. I. Degenerate C+O and O+Ne+Mg white dwarfs. *Astrophys. J. 396*, 649–667.

Tonry, J. L., B. P. Schmidt, B. Barris, P. Candia, P. Challis, A. Clocchiatti, A. L. Coil, A. V. Filippenko, P. Garnavich, C. Hogan, S. T. Holland, S. Jha, R. P. Kirshner, K. Krisciunas, B. Leibundgut, W. Li, T. Matheson, M. M. Phillips, A. G. Riess, R. Schommer, R. C. Smith, J. Sollerman, J. Spyromilio, C. W. Stubbs, and N. B. Suntzeff (2003, September). Cosmological Results from High-z Supernovae. *Astrophys. J. 594*, 1–24.

Vasilyev, O. V. and T. S. Lund (1997). A general theory of discrete filtering for les in complex geometry. See Center for Turbulence Research [1997].

Warsi, Z. (1993). *Fluid Dynamics : Theoretical and Computational Approaches*. CRC Press.

Williams, F. A. (1994). *Turbulent reacting flows*. Academic Press.

Woosley, S. E., S. Wunsch, and M. Kuhlen (2003). Carbon Ignition in Type Ia Supernovae: An Analytic Model. Submitted to ApJ. Preprint `astro-ph/0307565`.

Yoshizawa, A. (1986, July). Statistical theory for compressible turbulent shear flows, with the application to subgrid modeling. *Phys. Fluids 29*, 2152–2164.

Zel'dovic, Y. B. (1966). An effect shich stabilizes the curved front of a laminar flame. *J. of Appl. Mech. and Tech. Phys. 1*, 68–69. English translation.

Appendix A

Numerical Techniques

A.1 Implementation of Discrete Filters

In general, a filtering operation $\langle\ \rangle_F$ on a field $q(\boldsymbol{x}, t)$ is defined by a convolution product:

$$\langle q\rangle_F(\boldsymbol{x}, t) = \int_{-\infty}^{t} \mathrm{d}t' \int \mathrm{d}^3x'\, q(\boldsymbol{x}', t')F(\boldsymbol{x} - \boldsymbol{x}', t - t'), \tag{A.1}$$

where F is called the *filter kernel*. The filter is called *spatial*, if the kernel is of the form

$$F(\boldsymbol{x} - \boldsymbol{x}', t - t') = G(\boldsymbol{x} - \boldsymbol{x}')\delta(t - t'). \tag{A.2}$$

On the other hand,

$$F(\boldsymbol{x} - \boldsymbol{x}', t - t') = \delta(\boldsymbol{x} - \boldsymbol{x}')H(t - t') \tag{A.3}$$

is the kernel of a *temporal* filter. Note that the upper boundary of the interval of time integration preserves causality. In spectral space, filtering is a merely a multiplication:

$$\langle\hat{q}\rangle_F(\boldsymbol{k}, \omega) = \hat{F}(\boldsymbol{k}, \omega)\hat{q}(\boldsymbol{k}, \omega). \tag{A.4}$$

The hat on top of a symbol indicates the Fourier transform of the corresponding quantity in physical space and in the time domain. The wave vector $\boldsymbol{k}$ and the frequency ω are dual to $\boldsymbol{x}$ and t, respectively. In the context of LES, only *low-pass spatial* filters are relevant, which suppress modes of high frequency and wavenumber. The most common of these filters are discussed in Sagaut [2001, Chapter 2]. For the numerical implementation, either discrete Fourier transforms are applied, or the convolution integral in physical space is discretised. In the former case, the filtering operation itself is trivial, but the computation of Fourier transforms is costly, both in terms of CPU time and memory. In the second case, the major challenge is the numerical integration. If the filter kernel is of local support in physical space, the computation of the convolution integral will be significantly less demanding than the Fourier transformation. Apart from that, it is also a matter of the application, which option is preferable. For the post-processing of DNS data, as discussed in Sections 2.5.4 and 3.2, Gaussian filters are particularly useful. Since a Gaussian filter operation is not bounded in physical space, the computation is most easily carried out in spectral space. To that end, the implementation *FFTW* of the discrete fast Fourier transform algorithm was utilised

[cf. Frigo and Johnson, 1998][1] . For the test filter in the semi-localised subgrid scale model, on the other hand, a discretised box filter was applied. The numerical implementation of this filter as well as a temporal smoothing procedure are briefly outlined in the following.

A.1.1 Spatial Filtering

Discrete spatial filters for the application in LES are discussed in Vasilyev and Lund [1997]. In one dimension, the kernel of a discrete filter is defined by a series of *weights* for each grid node:

$$\frac{1}{\Delta} G\left(\frac{x_i - x'}{\Delta}\right) = \sum_{l=-N_G}^{N_G} w_{il}\,\delta(x_{i+l} - x'). \tag{A.5}$$

If a dynamical quantity $q(x)$ is numerically represented by the discrete sequence of values $\{q_i\}_{i=1}^{N}$, then the filter operation is defined by

$$\overline{q}_i = \sum_{l=-N_G}^{N_G} w_{il} q_l, \qquad i \in \{1, \ldots, N\}. \tag{A.6}$$

The cells with indices $i - N_G, \ldots, i + N_G$ are the *supporting nodes* for filtering q_i, and $(2N_G + 1)$ is the number of supporting nodes. Obviously, one must impose boundary conditions in order to determine the *ghost values* for $-N_G \le l < 1$ and $N < l \le N_G$. Moreover, the weights w_{il} must satisfy the normalisation condition

$$\forall i \in \{1, \ldots, N\} : \sum_{l=-N_G}^{N_G} w_{il} = 1. \tag{A.7}$$

Here we will exclusively consider *homogeneous* filters on *equidistant* grids. In this case, $\forall i \in \{1, \ldots, N\} : w_{il} = w_l$, i. e., the weights are uniquely given by the offset l from the central supporting node. Moreover, if $w_{-l} = w_l$, then the filter is *symmetric*.

In the framework of finite-volume schemes, a particularly suitable kind of filter is the *box filter*. In one dimension, this is basically the average over an interval:

$$\overline{q}(x) = \frac{1}{\overline{\Delta}} \int_{-\overline{\Delta}/2}^{\overline{\Delta}/2} q(x')\mathrm{d}x' \tag{A.8}$$

where $\overline{\Delta}$ is the characteristic length of the box filter. Appropriate filter weights can be found by means of a Fourier analysis. Suppose, a symmetric mesh filter with $2N_G + 1 = 5$ supporting nodes acted upon a harmonic function $q_i = Q\exp(\mathrm{i}kx_i)$, then

$$\overline{q}_i = Q \sum_{l=-2}^{2} w_l \exp(\mathrm{i}kx_l) = (w_0 + 2w_1 \cos k\Delta + 2w_2 \cos 2k\Delta) q_i. \tag{A.9}$$

Hence, the spectral representation of a 5-node filter is given by

$$\begin{aligned} \hat{G}^{(5)}(k) &= 1 - 2w_1(1 - \cos k\Delta) - 2w_2(1 - \cos 2k\Delta) \\ &\simeq 1 - (w_1 + 4w_2)k^2\Delta^2 + \frac{w_1 + 16w_2}{12} k^4\Delta^4 + \mathrm{O}(k^6\Delta^6). \end{aligned} \tag{A.10}$$

[1] The acronym *FFTW* stands for *Fastest Fourier Transform in the West*. *FFTW* is a library which was developed at MIT by M. Frigo and S. G. Johnson. It can be downloaded from `www.fftw.org` for free.

For an analytic box filter of characteristic length $\bar{\Delta} = \gamma\Delta$, on the other hand, we have [cf. Pope, 2000, Table 13.2]

$$\begin{aligned}\hat{G}_{\gamma\Delta}(k) &= \left(\frac{\gamma\Delta}{2}\right)^{-1} \sin\left(\frac{\gamma\Delta}{2}\right) \\ &\simeq 1 - \frac{\gamma^2}{24}k^2\Delta^2 + \frac{\gamma^4}{1920}k^4\Delta^4 + \mathrm{O}(k^6\Delta^6)\end{aligned} \tag{A.11}$$

Matching the Taylor expansions of $\hat{G}^{(5)}(k)$ and $\hat{G}_{\gamma\Delta}(k)$, respectively, the discrete filter weights can be expressed in terms of the scaling ratio γ:

$$w_0 = 1 - \frac{5\gamma^2}{48} + \frac{\gamma^4}{320}, \qquad w_1 = \frac{\gamma^2}{6}\left(\frac{1}{3} - \frac{\gamma^2}{80}\right), \qquad w_2 = \frac{\gamma^2(3\gamma^2 - 20)}{5760}. \tag{A.12}$$

Naturally, $\gamma \in [1, 5]$ for a filter with 5 supporting nodes. In fact, setting $u_i = 1/5$ for $-2 \le i \le 2$, no consistent solution which would satisfy all of the above equations can be found for γ.

γ	w_0	w_1	w_2
2.0	0.6333	0.1889	-0.0056
2.5	0.4710	0.2658	-0.0014
3.0	0.3156	0.3313	0.0109
3.5	0.1929	0.3679	0.0356
4.0	0.1333	0.3556	0.0778
4.5	0.1721	0.2707	0.1433
5.0	0.3490	0.0868	0.2387

Table A.1: Weights for a 5-node mesh filter of characteristic scale $\gamma\Delta$.

A sample of weights for $2 \le \gamma \le 5$ is listed in Table A.1. If the monotonicity constraint $w_2 < w_1 < w_0$ is imposed for strictly positive weights, then there remains only a narrow range of possible values for γ around 2.7. Actually, there is a particular value, for which the discrete and the analytical kernels agree at the grid cut-off wavenumber π/Δ, i.e., $\hat{G}^{(5)}(\pi/\Delta) = \hat{G}(\pi/\Delta)$. With this constraint, the remaining degree of freedom can be eliminated, and numerically $\gamma = 2.77108$ is found. The corresponding weights are $w_0 = 0.38438$, $w_1 = 0.30376$ and $w_2 = 0.00405$. We shall call this the *optimal* filter, because a particularly good agreement between discrete and analytical box filter is found in the whole range of numerically relevant wave numbers $k \le \pi/\Delta$. The procedure outlined thus far may also be applied to mesh filters with a larger number of supporting nodes. Since the mathematical expression become increasingly complicated, it is convenient to resort to software for symbolic computation. The weights and scaling factors for the optimal mesh filters with 7 and 9 nodes, respectively, were calculated with MATHEMATICA (see Table 4.2). Last but not least, it is very easy to construct multidimensional discrete box filters from homogeneous 1D filters, if the grid is equidistant. This is trivial by the separability of the analytic box filter, $G_{\bar{\Delta}}(x, y, z) = G_{\bar{\Delta}}(x)G_{\bar{\Delta}}(y)G_{\bar{\Delta}}(z)$, in a 3D Cartesian coordinate system. Therefore, we consider 1D mesh filters to be the *component filters* of homogeneous, discrete 3D box filters.

A.1.2 Temporal Filtering

In order to smooth a time-dependent function $f(t)$ on a time scale T, the convolution of f with an exponential damping function is computed, and the result is normalised with the integral of the damping function:

$$\bar{f}(t) = \frac{\int_0^t f(t')\mathrm{e}^{-(t-t')/T_\epsilon}\mathrm{d}t'}{\int_0^t \mathrm{e}^{-(t-t')/T_\epsilon}\mathrm{d}t'}. \tag{A.13}$$

This is a modified *time low-pass filter* [cf. Sagaut, 2001, Section 2.1.4]. Note that the convolution integral preserves causality. The discretised counterpart of the above equation is straightforward. Let f^m be the value of f at time t_m, then

$$\bar{f}^n = \frac{f^0\mathrm{e}^{-(t_1-t_0)/T_\epsilon}T_\epsilon + \sum_{m=1}^n f^m\mathrm{e}^{-(t_n-t_m)/T_\epsilon}(t_m - t_{m-1})}{\mathrm{e}^{-(t_1-t_0)/T_\epsilon}T_\epsilon + \sum_{m=1}^n \mathrm{e}^{-(t_n-t_m)/T_\epsilon}(t_m - t_{m-1})}. \tag{A.14}$$

The discrete equation is equivalent to a system of recursion rules, which makes the calculation of the smoothed functions particularly easy:

$$\bar{f}^0 = f^0, \qquad \bar{f}^n = \frac{1}{N_n}\left[N_{n-1}\bar{f}^{n-1}\exp\left(-\frac{t_n - t_{n-1}}{T_\epsilon}\right) + f^n\left(\frac{t_n - t_{n-1}}{T_\epsilon}\right)\right], \tag{A.15}$$

$$N_0 = 1, \qquad N_n = N_{n-1}\exp\left(-\frac{t_n - t_{n-1}}{T_\epsilon}\right) + \frac{t_n - t_{n-1}}{T_\epsilon}. \tag{A.16}$$

A.2 Implementation of Subgrid Scale Diffusion

The dynamical equation (3.45) for the SGS turbulent speed is a non-linear parabolic PDE, which is both explicitly and implicitly coupled to the resolved state and flow variables. Explicit coupling is introduced by the rate of strain S_{ik} and the divergence d. Moreover, the resolved flow influences SGS turbulence dynamics in a more subtle way through a localised production parameter. A systematic analysis of these complex interactions is certainly not feasible. This is why stability with regard to the source terms in the semi-localised model can only be established *a posteriori* in numerical simulations. As for diffusion, a simple numerical scheme is employed, for which a stability analysis can be carried out on the assumption of constant SGS parameters.

For brevity, we shall consider the one-dimensional problem. The scheme outlined here carries over to three dimensions via operator splitting. Let q_i be the turbulent speed in the i-th cell. The *diffusive fluxes* through the interfaces to the adjacent cells are naturally given by [cf. LeVeque, 2002, Section 4.2]

$$F_{i+1/2} = \kappa_{i+1/2}\frac{q_{i+1} - q_i}{\Delta}, \qquad F_{i-1/2} = \kappa_{i-1/2}\frac{q_i - q_{i-1}}{\Delta}, \tag{A.17}$$

assuming an equidistant grid. The above expressions follow from the discrete formulation of *Fick's law* of diffusion. However, the diffusivities $\kappa_{i\pm1/2}$ are actually functions of the quantity being transported. Hence, SGS diffusion is nonlinear, with the mean diffusivity in the i-th cell given by $\kappa_i \propto \rho_i C_\kappa q_i$, where C_κ is the constant closure parameter for turbulent diffusion. The simplest possibility of defining $\kappa_{i\pm1/2}$ is by averaging

over the corresponding couples of adjacent cells:

$$\kappa_{i+1/2} = \frac{C_\kappa}{2}\left(\rho_i q_i + \rho_{i+1} q_{i+1}\right), \tag{A.18}$$

$$\kappa_{i-1/2} = \frac{C_\kappa}{2}\left(\rho_{i-1} q_{i-1} + \rho_i q_i\right). \tag{A.19}$$

The increment of q_i corresponding to diffusion over the time step δt^n is explicitly given by the following Euler-forward step:

$$\delta q_i^{(\mathrm{D1})n} = \frac{1}{\rho_i^n}\frac{\delta t^n}{\Delta}\left(F^n_{i+1/2} - F^n_{i-1/2}\right) \tag{A.20}$$

For linear diffusion, this scheme is subject to a rather restrictive stability constraint: $\delta t < \min(\rho_i \Delta^2/\kappa_i)$. Consequently, implicit schemes like the *Crank-Nicholson method* are usually preferred to solve diffusion equations. The problem of non-linear diffusion we are concerned with, on the other hand, can be treated quite well with the scheme outlined above. This can be shown analytically by means of a Fourier stability analysis for the simplified case of an incompressible flow. Even in the general case, however, the performance of the scheme in various simulations has not given any indication of instability.

If a Fourier mode of wavenumber k is substituted, $q_i = Q\mathrm{e}^{\mathrm{i}kx_i}$, and the density is constant, then the *amplification factor* for this mode is given by[2]

$$g_i = \frac{\sqrt{2}C_\nu \Delta_{\mathrm{eff}}\delta t}{\Delta^2} Q \sin \Delta k = \frac{\sqrt{2}C_\nu \beta \delta t}{\Delta} Q \sin \Delta k. \tag{A.21}$$

The numerical scheme for diffusion is stable if $|g_i| < 1$, which implies

$$\delta t < \frac{\Delta}{\sqrt{2}C_\nu \beta Q} \sim \frac{10\Delta}{Q} \tag{A.22}$$

Thus, the grid spacing Δ constrains the time step linearly and not quadratic as in the case of linear diffusion. Since δt is basically determined by the CFL condition $\delta t < \min(\Delta/c_i)$, where c_i is the speed of sound in the i-th cell, the above condition for the maximal SGS turbulence energy is effectively $Q < 0.1 \max(c_i)$. This is almost certainly fulfilled for moderate Mach numbers and sufficient resolution.

The quadratic gradient term, which originates from reducing the conservation law for SGS turbulence energy to an equation for $q_{\mathrm{sgs}} = \sqrt{2k_{\mathrm{sgs}}}$, is spatially symmetric, i. e., this term depends on the *magnitude* of the gradient $\boldsymbol{\nabla} q_{\mathrm{sgs}}$, but it is independent of direction. For this reason, centred differences appear to be appropriate for the discretisation:

$$\delta q_i^{(\mathrm{D2})n} = C_\kappa \left(\frac{q^n_{i+1} - q^n_{i-1}}{2\Delta}\right)^2. \tag{A.23}$$

[2]The method of calculating amplification factors of Fourier modes in finite difference schemes is introduced in the book of Potter [1973].